REPORT DOCUMENTATION PAGE	Form Approved OMB NO. 0704-0188

Public reporting burden for this collection of information is estimated to average 1 hour per response, including the time for reviewing instructions, searching existing data sources, gathering and maintaining the data needed, and completing and reviewing the collection of information. Send comment regarding this burden estimates or any other aspect of this collection of information, including suggestions for reducing this burden, to Washington Headquarters Services, Directorate for information Operations and Reports, 1215 Jefferson Davis Highway, Suite 1204, Arlington, VA 22202-4302, and to the Office of Management and Budget, Paperwork Reduction Project (0704-0188), Washington, DC 20503.

1. AGENCY USE ONLY (Leave blank)	2. REPORT DATE 8/20/98	3. REPORT TYPE AND DATES COVERED Final Progress Report, 07/01/1995-06/27/1998

4. TITLE AND SUBTITLE Spray Deposition Processing of Al/SiC MMC Armor Materials and Ta Alloys for Army Applications	5. FUNDING NUMBERS DAAH04-95-1-0424

6. AUTHOR(S)

E.J. Lavernia and F.A. Mohamed

7. PERFORMING ORGANIZATION NAME(S) AND ADDRESS(ES) Department of Chemical and Biochemical Engineering and Materials Science University of California, Irvine Irvine, 92697	8. PERFORMING ORGANIZATION REPORT NUMBER

9. SPONSORING / MONITORING AGENCY NAME(S) AND ADDRESS(ES) U.S. Army Research Office P.O. Box 12211 Research Triangle Park, NC 27709-2211	10. SPONSORING / MONITORING AGENCY REPORT NUMBER ARO 34374.25-MS

11. SUPPLEMENTARY NOTES

The views, opinions and/or findings contained in this report are those of the author(s) and should not be construed as an official Department of the Army position, policy or decision, unless so designated by other documentation.

12a. DISTRIBUTION / AVAILABILITY STATEMENT Approved for public release; distribution unlimited.	12b. DISTRIBUTION CODE

13. ABSTRACT *(Maximum 200 words)*

In this research program, the spray atomization and deposition technique was both experimentally and numerically studied to process ceramic particulate reinforced (including functionally graded reinforcement distributions) Al alloy metal matrix composites (MMCs) as armor materials and Ta alloys for Army applications such as shaped charged liners and explosively formed projectiles. In this final progress report, the aforementioned experimental and numerical results are described and discussed in five individual sections, which are described as follows: investigation of thermal residual stresses in layered SiC/Al composite using the finite element method and X-ray diffraction; spray forming and co-injection of particle reinforced TiAl/TiB$_2$ composites; spray atomization and deposition of tantalum alloys; low pressure spray forming; modeling of porosity during spray forming; and a summary on the investigation on creep behavior of Al alloys and SiC/Al composites.

DTIC QUALITY INSPECTED 4

19981222 072

14. SUBJECT TERMS Spray atomization and deposition; spray forming; metal matrix composites; SiC/Al; layered composites; residual stress; Tantalum alloy; low pressure spray forming; porosity	15. NUMBER OF PAGES
	16. PRICE CODE

17. SECURITY CLASSIFICATION OF REPORT UNCLASSIFIED	18. SECURITY CLASSIFICATION OF THIS PAGE UNCLASSIFIED	19. SECURITY CLASSIFICATION OF ABSTRACT UNCLASSIFIED	20. LIMITATION OF ABSTRACT UL

Spray Deposition Processing of Al/SiC MMC Armor Materials and Ta Alloys for Army Applications

FINAL REPORT

Submitted to:

Dr. Kathryn Logan
U.S. Army Research Office
4300 S. Miami Blvd.
Research Triangle Park, North Carolina 27709-2211

Submitted by

Enrique J. Lavernia, Professor

and

Farghalli A. Mohamed, Professor

July 1, 1995-June 27, 1998

U.S. ARMY RESEARCH OFFICE

20283

Grand Number: DAAH04-95-1-0424

Department of Chemical and Biochemical Engineering and Materials Science
University of California, Irvine
Irvine, CA 92697

TABLE OF CONTENTS

LIST OF TABLES

LIST OF FIGURES

FOREWORD

The objective of this research program is in twofold. The first is to use spray deposition technique to process ceramic particulate reinforced Al alloy MMCs as armor materials with optimum combinations of high penetration resistance and other mechanical properties, and to examine the feasibility of improving the ballistic behavior and other mechanical properties of MMCs by using spray deposition technique to process SiC particulate reinforced 6061 Al ($6061Al/SiC_p$) MMCs with a layered geometrical arrangement. The second is to use spray deposition technique to process Ta alloys for attractive combinations of microstructure, mechanical properties and ballistic properties. The relevance of the proposed program to the Army will be on assessing the potential applications of ceramic particulate reinforced Al alloy MMCs in applications requiring high penetration resistance and light weight and the potential application of spray formed Ta alloys as shaped charged liners and explosively formed projectiles.

This final report summarizes both experimental and theoretical results on the processing particle reinforced composites and refractory alloys by using spray atomization and deposition.

I. INTRODUCTION

Particulate reinforced metal matrix composites (MMCs) have attracted considerable attention as a result of their feasibility for mass production and promising mechanical properties. The particulate reinforced MMCs are cost-effective and exhibit substantially improved mechanical properties when compared with their corresponding monolithic matrix alloys [1-3]. In particular, particulate reinforced MMCs exhibit near-isotropic properties and are easy to process using conventional processing techniques such as casting. To develop high penetration resistance armor materials, the MMC processing provides an approach to tailor ballistic property and mechanical properties to meet Army performance requirements. However, current MMCs as armor materials only possess a comparable or slightly higher penetration resistance than that of conventional armor Al alloys. Therefore, a novel processing technique should be developed as a feasible means to further improve the ballistic performance of armors. More recently, it has been demonstrated that it is possible to achieve a layered structure in particulate reinforced MMCs using a spray atomization and deposition approach [4, 5]. A spray deposition processing approach to produce layered structures (similar to those with a laminated geometry) is attractive because it involves significantly fewer steps when compared to available layering techniques in manufacturing layered MMCs. One of objectives of the present work is to examine the feasibility of improving the ballistic properties of particulate reinforced MMCs by using spray deposition technique to process SiC particulate reinforced 6061 Al (6061Al/SiC$_p$) MMCs with a layered geometrical arrangement.

Tantalum and its alloys combine ductility and toughness with a strong resistance to chemical attack by many liquid metals, which are attractive for applications requiring high strength, thermal stability, corrosion resistance and high density [6, 7]. However, the properties of refractory metal alloys are extremely sensitive to processing conditions [8-11]. As a result, some limitations have been imposed on our ability to take full advantage of the attractive properties of Ta alloys, and consequently, restrict the complete development of this important class of materials. It is one of the objectives to study alternative fabrication processes to overcome the present drawbacks aiming at the potential applications for Army.

In this research program, spray atomization and deposition was studied both experimentally and numerically for processing particle reinforced composite materials and Ta alloys.

Functionally gradient materials (FGMs) are a relatively new class of composite materials that exhibit continuous or discontinuous variation in composition, structure, and properties as a function of position in the materials. Consequently, FGMs have the potential to be utilized in a wide range of engineering applications since the compositional gradient can be tailored to meet specific performance requirements. Some of the processing routes for FGMs include chemical vapor deposition [12], plasma spray technique [13], and various powder metallurgy techniques

[14]. Among the techniques available, spray atomization and co-deposition [15] is of considerable interest as an attractive route to fabricate FGMs because of several advantages. First, its ability to expose the reinforcement to relatively low processing temperatures, thus minimizing any potential reactions between the matrix and the reinforcement. Second, because of its potential to synthesize difficult-to-form materials into near-net shapes, minimizing the costly joining and machining operations that are typically required after conventional forming. Third, its ability to minimize surface oxidation and other deleterious surface reactions because processing is performed under environmentally controlled conditions. Currently, using spray atomization and co-deposition technology, FGMs consisting of aluminum alloy matrices, and reinforced with SiC and other reinforcements are being successfully fabricated [16]. There exist dissimilar thermal expansion coefficients in FGMs, which can generate significant thermal residual stresses during fabrication. There exist two types of thermal residual stresses to be considered in FGMs. One type is the macro-residual stresses that develop by differential contraction of the alternating layers and the constraints imposed on each layer by its neighbors. The other type is the micro-residual stress that develop by differential contraction of the matrix and the reinforcement in the composite layers. The macro- and micro-residual stress distribution often plays an important role in determining and understanding the mechanical behavior of the fabricated material when it is subjected to its intended service loads and environment. In some cases, such stresses may be unavoidable due to the nature of the processing conditions, and may be very detrimental. In other cases, they may be purposely introduced for beneficial effects. In any event, their effective control depends critically on the investigators' ability to detect their presence and their distribution accurately within FGMs. Therefore, by judiciously tailoring the microstructure of heterogeneous materials, thermal residual stresses can be dispersed and minimized during the fabrication process. In the present study, thermal macro- and micro-residual stresses that develop in a layered 2024Al/SiC composite fabricated by spray atomization and co-deposition process are investigated using thermo-elastoplastic finite element analysis. X-ray diffraction is also used to measure the residual stresses. The numerically calculated values from finite element analysis are compared with those obtained using X-ray diffraction.

Gamma TiAl is of interest due to its inherent low density (~3.8 g/cm^3) and high melting temperature, and its excellent elevated temperature mechanical properties, such as high strength, high creep resistance, and high modulus [17-19]. Gamma TiAl based composites, both continuously and discontinuously reinforced, are also being actively investigated in an effort to tailor the mechanical properties of monolithic gamma TiAl intermetallics [20-23]. These endeavors include the incorporation of ductile reinforcement phases to improve fracture toughness and the addition of hard ceramic particles or fibers to further increase its high temperature strength and creep resistance. It is well documented that spray forming and co-injection has been successfully

employed to synthesize Al based composites and Ni₃Al based composites, with improved physical and mechanical properties [24-26]. The application of the spray forming technique in synthesis of titanium based composites, however, lags well behind other metallic systems, mainly because of the high chemical reactivity associated with the molten titanium based alloys. Recently, with the advent of skull melting/spray forming technique, spray forming of titanium aluminides, including Ti₃Al, TiAl, and TiAl₃, is being actively explored [27-31] However, the application of this technique to synthesize titanium aluminide based composites has not been reported thus far. As a result, the work was motivated to explore the possibility of spray forming and co-injecting a TiAl/TiB₂ composite, and to investigate, experimentally and numerically, the microstructural characteristics of the spray formed and co-injected TiAl/TiB₂ composite. Selection of TiB₂ is prompted by its availability, and its compatibility with TiAl [32-34]. Compatibility between the matrix and the reinforcement, at the projected use temperature, is essential since at high temperatures the kinetics of possible reactions are extremely fast and can result in degradation of the reinforcement phase [24].

To elucidate the feasibility of spray atomization and deposition to process Ta alloys, an investigation was conducted to obtain some preliminary characterization of the resulting deposited material. Furthermore, the study aims at gaining some insight concerning the physical processes (e.g. liquid metal flow at impact, solidification heat transfer) controlling these characteristics. To this end, numerical simulation is used to complement the experiments and provide information where measurements are impractical.

The presence of some porosity in the as-deposited materials is inevitable. For instance, porosity has been reported to vary from 1 to 10% for a variety of Al alloys [35]. The presence of porosity in deposited materials brings about at least two challenges. First, the material properties, especially those at elevated temperatures, may degrade due to the presence of porosity [36-38]. Second, secondary working, such as extrusion, rolling, forging and HIPing, are required to achieve full or near full density, which in turn limits the applicability of spray forming as a flexible near net-shape manufacturing processing. As a consequence, research efforts have been initiated to better understand the formation mechanisms of porosity and to find ways to control and/or minimize porosity level either by manipulating the processing parameters or exploring alternative approaches. The formation of porosity during spray forming is influenced by many factors, such as: processing parameters, thermodynamic properties of materials, thermodynamic properties of atomization gases, as well as considerations pertaining to apparatus design [37, 39-42]. Accordingly, influences of these factors on porosity must be assessed in order to determine optimal conditions yielding minimal amount of porosity. In this research program, both experimental and numerical approaches were used to study. Experimentally, a novel technique, namely low pressure spray forming (LPSF), has been developed in an effort to reduce the porosity present in

as-deposited materials. The amount of porosity in spray formed 2024 Al alloy was significantly reduced. Numerically, a porosity model was developed based on particle packing theory, fluid mechanics, and heat transfer of droplets. By using this model, influences of processing parameters such as melt flow rate; atomization gas pressure; deposition distance; and melt superheat, which are readily manipulated during spray forming, were investigated. Furthermore, the influences of atomization gas chemistry and alloy composition on porosity were also addressed.

In this final progress report, the aforementioned experimental and numerical results are described and discussed in four individual sections, which are described as follows: investigation of thermal residual stresses in layered SiC/Al composite using the finite element method and X-ray diffraction; spray forming and co-injection of particle reinforced TiAl/TiB$_2$ composites; spray atomization and deposition of tantalum alloys; low pressure spray forming; modeling of porosity during spray forming, and a summary on the investigation on creep behavior of Al alloys and SiC/Al composites.

II. BACKGROUND

2.1. Ballistic Properties of Armor Materials

The ballistic performance of a material is generally described in terms of the penetration ability of penetrators or projectiles and the protection capacity of targets or armors. The penetration of a projectile into an armor is essentially a kinetic energy transfer process [43-49]. However, the penetration process typically involves a transient impact or a rapid plastic deformation under high loading rate conditions and therefore the kinetic energy transfer during penetration becomes a complicated process. In the presence of plastic deformation, the local strain rate can exceed 10^6 sec^{-1} with associated strain energies and superimposed stresses that can be significantly greater than the yield strengths of both penetrator and target materials. During penetration, a penetrator defeats an armor by tunneling a crater through the target. Accordingly, both armor and penetrator materials experience extensive plastic deformation during impact. As a result, the armor material surrounding the crater is pushed aside by the penetrator, while the penetrator itself is forced backwards or back extruded and eroded at the moving boundary between penetrator and target. This process continues until the penetrator is either decelerated to a complete stop or completely consumed.

The ballistic behavior of a material is usually characterized in terms of a penetration depth (P). To that effect, numerous theoretical and experimental studies have been performed in an effort to predict penetration depth and to provide insight into the mechanisms of penetration [50-53]. Among currently available models, the Forrestal model [54] has been shown to accurately predict the cylindrical cavity expansion for a spherical tipped rod penetrating a semi-infinite, elastic-perfectly plastic metallic target. According to the Forrestal model, the penetration depth is given by [54]

$$P = \frac{m}{2\beta} \ln\left(1 + \frac{\beta V^2}{\alpha}\right) \tag{2.1}$$

where

$$\alpha = \frac{2}{3}\pi a^2 Y_D (1 + \frac{\pi}{2}\mu)\left\{1 + \ln\left[\frac{E}{3(1-\nu)Y_D}\right]\right\} \tag{2.2}$$

and

$$\beta = 1.041\frac{\pi}{2}a^2\rho(1 + \frac{\pi}{4}\mu) \tag{3.3}$$

where E, v, ρ are the Young's modulus, Poisson's ratio, and density of the target materials, respectively; m, a and V are the projectile mass, radius and velocity, respectively; μ is the coefficient of friction at the projectile/target interface; Y_D is the dynamic yield strength. The above model has been successfully used to predict the penetration depth and residual velocity for steel and tungsten penetrators fired into 6061-T651 and 5083-H131 Al target materials [50].

Armors or targets are typically fabricated of ballistic protection materials in order to resist the impact of projectiles and absorb the associated kinetic energy during the deformation of both target and projectile. In the case of targets made out of hard materials, such as ceramics, the projectile may elastically collide on the target surface and the hard target may undergo brittle fracture during impact. The kinetic energy of projectile is dissipated by the work of fracture due to the creation of crack surfaces and pulverization of the fragments into smaller pieces. As a result of their extreme hardness and high elastic modulus, ceramic materials can damage the high velocity projectile during impact; in turn, the ceramic target itself shatters and needs to be replaced thus limiting its use to single impact applications. Accordingly, for ballistic protection applications, ceramic materials have to be combined with a ductile material, which may be a metal alloy such as Al. The ductile material provides structure to support the ceramic material during projectile impact thereby absorbing a portion of the kinetic energy of the projectile [50-53, 55-57].

In the case of metallic materials, the kinetic energy of an incoming projectile is dissipated during the plastic deformation of the target material. Perforation of the target takes place by ductile cavity formation, which involves radial flow of the target material. It has been noted that there are four primary factors that influence the penetration resistance of target materials, namely: dynamic yield strength, dynamic modulus, dynamic fracture toughness and ductility. Hence, the higher the dynamic yield strength, modulus, and fracture toughness, the greater the penetration resistance. Due to their high fracture toughness and ductility, metals are attractive materials for ballistic applications.

In the development of high performance armor materials, metal matrix composites (MMCs) provide a unique opportunity to combine reinforcement properties (e.g., strength and modulus) with matrix properties (e.g., ductility and toughness). MMCs are being increasingly used in civil and military applications since they can be tailored to develop relatively high stiffness and low coefficient of thermal expansion (CTE) over a wide range of temperatures while preserving high strength and toughness. All these advantages are achieved at no increase in unit weight in comparison with conventional matrix materials. Currently, a number of structural elements in lightweight armor vehicles can be designed using MMCs. Before being used to replace conventional materials in armor vehicle structural applications, however, MMC parts have to be demonstrated to possess a comparable or higher ballistic resistance relative to that of conventional monolithic materials.

Recent studies have explored the potential of utilizing particulate reinforced MMCs as armor materials through ballistic testing and dynamic property assessments. The results of these testing programs support the hypothesis of increased ballistic protection of particulate reinforced MMCs. Alcan International (Kingstown, Canada), for example, conducted a systematic testing program to evaluate the ballistic property of SiC particulate reinforced Al alloy MMCs which were manufactured using spray atomization and deposition and ingot casting metallurgy processes [51-53]. It was found that the projectile's nose geometry, impact velocity and material properties significantly affected the penetration process. Al/SiC MMCs exhibited a substantial improvement in penetration resistance when compared with conventional Al armor alloys in semi-infinite penetration experiments. The enhanced performance of the MMCs was attributed to the improved the dynamic flow strength (yielding strength) and the erosion characteristics of the SiC particulate reinforcement. Other relevant studies also demonstrated that the dynamic yield strength and elastic modulus played an important role in the improvement of ballistic penetration resistance.

More recently, the US Army Research Laboratory studied the ballistic properties of powder metallurgy (P/M) processed Al/SiC MMCs and ingot cast Al/SiC and Al/Al_2O_3 MMCs [51-53]. It was found that the P/M processed 2024 Al, 2124 Al, 6061 Al, 7090 Al and 7091 Al based MMC plates were equivalent in terms of ballistic performance and all offered superior ballistic resistance to that of 5083 Al armor alloy. It was also noted that the ballistic performance of theses P/M processed MMCs was independent of volume fraction of SiC particulates in the range of 20 vol.% to 40 vol.%. The ingot cast Al/SiC, Al/Al_2O_3, and 2024 Al/Al_2O_3 MMCs exhibited a comparable ballistic resistance to that of 2519 Al armor alloy but superior to that of 6061 Al/SiC MMCs with the same volume fraction of reinforcement, under different heat treatment conditions (O, T6, T8, and T9). It was noted that the ballistic resistance of the MMCs increased with increasing yielding strength. The best combinations of strength and ballistic performance were achieved with cold working after hot deformation and aging (T9).

2.2. Tantalum and Ta Alloys

Of the refractory metals family, tantalum (Ta) is attractive candidate for structural applications, as a result of its attractive combinations of chemical inertness and high toughness [7, 58-61]. The physical properties of tantalum are summarized in Table 2.1 [7]. Tantalum's high atomic weight makes it a good candidate material for applications requiring high density. In addition, tantalum exhibits extremely high ductility (>30%) as a result of its BCC crystal structure. This characteristic is attractive from the standpoint of metal working operations. For example, tantalum parts can be cold worked 95% without failure. Some of the mechanical properties of tantalum are summarized in Table 2.2. Furthermore, because of its high melting point (2996°C), tantalum is used for

heating elements, heat shields and other components in high temperature vacuum furnaces. Tantalum and its alloys have been used in specialized aerospace and nuclear applications and have found increasing used in military components [58]. Because of its corrosion resistance to body fluids, it is used in prosthetic devices and in surgical staples. Tantalum is also used as an alloying element in superalloys. Among Ta alloys, Ta-10W alloy (9 to 11wt.% W, balance Ta) is most widely used in aerospace and military applications in high temperature environment [58]. Ta-10W alloy can be used at temperature up to 2480°C such as hot gas metering valves, rocket engine extension skirts, complex manifold assemblies, and fasteners. Chemical process industry applications include machined solid valves, internal seats and plugs for large valves, liners requiring abrasion and corrosion resistance, and disks used in patching glass-lined steel vessels; also used for tubing in some nuclear applications.

Table 2.1. Physical Properties of Tantalum [7]

Atomic Weight	180.95
Density	16.6 g/cc
Melting Point	2996° C
Boiling Point	5431° C
Coefficient of Thermal Expansion (RT)	$6.5 \times 10^{-6}/°C$
Electrical Resistivity	13.5/cm
Electrical Conductivity	13.9% IACS
Specific Heat	0.140 J/g
Thermal Conductivity	0.544 J
Crystal Structure	bcc
Thermal Neutron Cross Section	21.3b

2.3. Spray Atomization and Deposition

For years, spray deposition processing has been proven to be an able technique to process SiC particulate reinforced Al alloy (Al/SiC$_p$) MMCs in the Materials Lab at the University of California at Irvine. It was found that spray deposition processed Al/SiCp MMCs exhibited a higher modulus than that of their corresponding monolithic matrix alloys and showed an improved strength. It was also found that spray deposited and layered Al/SiCp MMCs exhibited a relatively high fracture toughness. These observations, according to Eq. (2.1), demonstrate that spray deposition technique may be used to develop high ballistic performance armor materials.

Table 2.2.   Mechanical Properties of Tantalum [7]

<u>Annealed</u>	
Ultimate Tensile Strength	285 MPa(41 ksi)
Yield Strength	170 MPa (25 ksi)
% Elongation	30% +
% Reduction in Area	80% +
<u>Cold Worked</u>	
Ultimate Tensile Strength	650 MPa (95 ksi)
% Elongation	5%
<u>Hardness</u>	
Annealed	90 HV
Cold Worked	210 HV
<u>Poisson's Ratio</u>	0.35
<u>Strain Hardening Exponent</u>	0.24
<u>Elastic Modulus</u>	
Tension	186 GPa (27 x 10^6 psi)
<u>Ductile Brittle</u>	
<u>Transition Temperature</u>	$<75°K$
(Significantly affected by	
increasing interstitial contents.)	
<u>Recrystallization Temperature</u>	900-1200°C

2.3.1. Development of Spray Atomization and Deposition

Spray processing methodology, which was originally developed by Singer [62], has resulted in the development of the Osprey process, controlled spray deposition (CSD), spray forming or spray casting, liquid dynamic compaction (LDC) and variable co-deposition of multiphase materials, although the general principle is the same in these processes [63, 64]. A superheated liquid metal is delivered to an atomizer through a ceramic delivery tube where the liquid metal is disintegrated into a distribution of micron-sized droplets by the inert gas jets. The atomization gas not only absorbs the thermal energy that is released by the metal, but also accelerates the droplets. At a pre-selected flight distance where the average solid fraction in the overall distribution of droplets reaches a predetermined value (generally, 0.5 to 0.8 [63]), the mixture of solid, liquid and partially solidified droplets is collected on a substrate or mold, leading to the formation of a preform. To circumvent the inherent manufacturing limitations that are associated with an atomized

distribution of droplets that exhibits a Gaussian-like geometry, such as that typically present during spray atomization and deposition, a variety of experimental arrangements have been developed. For example, spraying onto a rotating substrate which is being displaced horizontally enables a solid cylindrical billet to be fabricated. Spraying onto a rotating mandrel or tube allows for the fabrication of a solid cylindrical preform, or simply a coating. Other experimental arrangements include spray rolling, spray forging, centrifugal spray deposition, and simultaneous spray peening [64].

Spray atomization and deposition offers a potentially attractive manufacturing route for several reasons. First, the highly efficient heat convection that is present during atomization ensures the maintenance of a relatively low processing temperature which limits large scale segregation and coarsening phenomena. Second, the inert conditions that are generally used for atomization and deposition minimize surface oxidation and other deleterious surface reactions. Third, spray atomized and deposited materials reportedly exhibit some of the characteristics associated with rapid solidification and semisolid metal forming, such as, fine spheroidal grain morphology, increased solid solubility, non-equilibrium phases, small sized precipitates, and modified morphology of secondary phases. Most significantly, spray atomization and deposition processes may be used potentially for near net shape manufacturing of difficult-to-form materials, such as superalloys, MMCs and IMCs (intermetallic matrix composites).

Over the last two decades, this processing approach has received considerable attention [5, 15, 63-66] as an alternative route for the synthesis of highly reactive alloys, such as those based on Mg and Al, for the synthesis of high temperature and high performance materials, such as those based on Ni, Fe, Cu, Ti, Ni_3Al and TiAl intermetallics, and more recently, for the synthesis of discontinuously reinforced MMCs and IMCs [64]. Commercial application of spray atomization and deposition technology is being pursued actively, with notable examples available in Europe, Scandinavia, and Japan. Sandvik Steel (Sandviken, Sweden) for example, is currently operating an Osprey plant to produce tubes from stainless steels and selected nickel alloys [64]. A variety of tube geometries can be manufactured, including lengths of up to 8 m, wall thicknesses between 25 and 50 mm and external diameters of up to 400 mm. In this application, the principal advantage offered by the Osprey technology is the ability to fabricate tubes directly from the melt in a single step. The as-spray formed tubes exhibit mechanical properties that are at least equivalent to those of the corresponding wrought alloys, and thus may be used directly without further hot or cold working. Using a 300 kg vacuum melting furnace [64], turbine ring blanks up to 800 mm in diameter by 500 mm in length and forging billets up to 250 mm diameter have been successfully spray formed and evaluated by Howmet Inc. (Plymouth, MI, USA) for a wide range of alloy compositions, including: IN100, IN718, Rene80, Rene125, Rene41, Rene95, Rene88DT, Merl76, Waspalloy and AF2-1DA-6. In this particular application, spray atomization and

deposition processing reduces manufacturing complexity, and minimizes the reactivity problems that are associated with fine powders. COSPRAY Advanced Aluminum Materials, (Alcan International, Banbury, UK) reported that Al alloys such as Al-Si, 2000 and 7000 series have been successfully spray formed as billets up to 400 mm in diameter by 1.3 m in length [64]. Significant improvements in damage tolerance of the spray formed Al alloys were reported, and were attributed to the refinement of both grain structure and the primary phase distribution, particularly in alloys that are sensitive to the presence of iron-containing intermetallic phases.

Spray atomization and deposition has attracted considerable interest as a viable manufacturing approach for the synthesis of MMCs and IMCs, as a result of the inherent simplicity and flexibility that are provided by this approach [5, 15, 63-66]. For example, incorporation of ceramic particulates or platelets into the spray of atomized droplets may be used effectively to form discontinuously reinforced MMCs and IMCs [5, 15, 63-66]. Moreover, if instead of using an inert gas, a reactive gas is used to atomize metal or intermetallic matrices, it is possible to promote the formation of in-situ dispersoids such as carbides, nitrides and oxides. It is also possible to synthesize continuous fiber reinforced MMCs and IMCs by directing the atomized droplets onto prearranged fibers located on the deposition surface. Clad composite tubes and billets can also be manufactured by spray atomization and deposition by spraying a highly alloyed materials onto an existing roll and mandrel . The clad composite approach is being evaluated as a possible means for producing gun barrels by spray depositing a highly alloyed material onto a mild steel bar, pre-machined with rifling grooves.

Inspection of the available scientific literature reveals that the matrix microstructure of MMCs and IMCs exhibits certain characteristics (e.g., grain morphology, segregation patterns) that are similar to those of the spray deposited unreinforced matrix counterparts. It is also evident, however, that the introduction of reinforcing phases during atomization and deposition leads to scientifically interesting and technologically important modifications to the matrix microstructure. The section that follows describes the various approaches that have been used to introduce the reinforcing phases into the matrix during spray deposition, paying particular attention to critical issues, such as reinforcement volume fraction.

2.3.2. Spray Deposition Processing of MMCs

Spray deposition processing of MMCs involves the atomization of a molten alloy, injection of ceramic reinforcements, and subsequent co-deposition of fine, semi-solid droplets of the alloy and the reinforcements on a substrate [5, 15, 63-66] . The process is conducted in an environmental chamber filled with a nitrogen atmosphere. Inside the chamber, the molten metal or alloy is energetically disintegrated into micrometer-sized droplets by high velocity jets of nitrogen through

an atomizer. Simultaneously, the ceramic particulate reinforcement, carried by a separate flow of nitrogen, is co-injected via four nozzles, perpendicular to the outline of the atomization cone. The injection nozzles are located at a predetermined flight distance to the atomizer, where the average solid fraction in the overall distribution of droplets reaches a predetermined value (generally, 0.25) according to numerical analysis [63]. The reinforcing particulates and partially solidified droplets then continue to travel under the combined effects of drag forces and gravity until they impinge on a water-cooled copper substrate.

Spray deposition processing has been developed as an able manufacturing approach for processing metals, alloys and MMCs. A wide variety of particulate reinforced Al alloy MMCs have been synthesized by using spray deposition for structural applications. Gupta et al. [66] processed SiC particulate reinforced Al-2.1Li, Al-5Cu, Al-7Si, and Al-1Ti (all compositions in wt. %) matrix composites. They reported that the volume fraction of SiC particulates up to 15% and a homogeneous distribution of the SiC particulates throughout the Al alloy matrix could be reached. In related studies, Wu and Lavernia [[67-69], successfully processed SiC and TiB_2 particulates reinforced Al-Si alloy with volume fraction of 20%. Regarding commercialization of these types of MMCs processed using spray deposition, COSPRAY Advanced Aluminum Materials (Alcan International, Banbury, UK) have successfully produced numerous Al alloys reinforced with up to 20 vol. % of SiC or Al_2O_3 particulates [64]. The COSPRAY reported that the spray deposited MMCs exhibited the improved mechanical properties, including stiffness, wear resistance, and CTE, in comparison with those of the unreinforced matrix materials [64].

2.3.3. Injection of Reinforcing Particulates and Co-Deposition

Early experiments on spray atomization and co-deposition for the synthesis of MMCs involved the tangential injection of particulates in the region between the liquid stream and the atomizing gas [70]. The rationale for selecting this co-injection approach was to reduce the loss of reinforcing particulates. Another approach studied is to inject the reinforcing particulates directly into the atomization region through a central tube located inside a liquid metal delivery tube [70]. These methods, however, are difficult to carry out in practice due to low flow rates of the co-injected particulates [70]. Hence, on the basis of the available experimental findings, it appears that the most effective means to introduce the reinforcements into the matrix is to inject the particulates directly into the atomization cone. Accordingly, the matrix material is disintegrated into a dispersion of droplets using an atomizing gas, while one or more streams of reinforcement particulates are injected into the atomized spray at a previously determined spatial location [64, 70]. The problem posed by the introduction of ceramic particulates into a dispersion of droplets that are experiencing a phase change (e.g., solidification) has been addressed by several investigators [70].

On the basis of these studies, it is evident that a finite amount of thermal energy will be transferred from the droplets to the reinforcement particulates, with concomitant changes in the microstructure. Moreover, the available results suggest that by carefully selecting the co-injection distance, it is possible to avoid interfacial reactions that would otherwise occur under equilibrium conditions [64, 70]. A more detailed discussion of the fundamental thermal and solidification mechanisms that are associated with the interactions between atomized droplets and co-injected ceramic particulates will be presented in a later section.

In practice, injection of the reinforcement particulates into the dispersion of droplets is accomplished generally by utilizing a gas medium to entrain the particulates and accelerate them towards the droplet dispersion [5, 15, 63-67, 69, 71]. The particulate mass flow may be stabilized by several means, such as mechanical agitation of the particulates during entrainment [67, 69, 71]. This approach has also been demonstrated to effectively increase the mass flow rate of the particulates. The reinforcement particulates that are generally used for co-injection are ceramics, such as SiC, Al_2O_3, TiB_2, and TiC, or non-metals such as graphite. It is also possible, to co-inject secondary types of metallic particulates into metallic materials to form multi-phased composites. The morphology of the co-injected ceramics may be equiaxed particulates, whiskers or chopped fibers [70]. A wide range of particulate sizes, generally from 1 μm to 120 μm, can be readily incorporated into spray deposited materials. Regarding reinforcement volume fraction, inspection of available results reveals that particulate volume fractions ranging from 0 - 20 vol.% may be achieved. Although volume fractions as high as 30-40 vol.% have been reported, these are difficult to reproduce in a reliable manner, and segregation of the particulates throughout the spray deposited matrix is often noted [70].

As early as 1985, Singer et al. [62] reported that up to 36 vol.% of SiC, Al_2O_3, chilled iron, graphite, and sand particles, and mixtures of these, 75-120 μm in size, could be incorporated successfully into pure Al and Al-5Si alloy matrixes by spray atomization and co-deposition. Singer noted that all of the different particulates were distributed homogeneously throughout the matrix, regardless of the extreme differences in density and/or morphology. Moreover, in this study, Singer reported that the as-spray deposited MMCs could be hot rolled to produce composite strips for examination and testing.

More recently, a wide variety of matrix Al alloys and reinforcement particulates have been synthesized by spray atomization and co-deposition due to interest in this class of materials for structural applications. In related studies, Al-2.1wt.%Li, Al-5wt.%Cu, Al-7wt.%Si, and Al-1wt.%Ti matrix composites reinforced with SiC particulates were processed [64]. In these studies, the SiC volume fraction ranged from 5 to 15 vol.%, and the particulates appeared to be homogeneously distributed throughout the alloy matrix. Moreover, it was reported consistently that the matrix microstructure in the MMCs consisted of spheroidal grains for a spray deposited Al-

2.1wt.%Li/SiC$_p$ MMC. In addition, using X-ray diffraction, it was showed that a spray atomized and deposited Al-4 wt.% Ti material retained 0.88 wt.% Ti in solid solution, whereas the corresponding spray atomized and co-deposited Al-2.3 wt.% Ti/SiC material retained up to 1.3 wt.% Ti in solid solution. In related studies [5, 15, 63-66], Al alloys 6061 and 2519 co-injected with graphite, SiC, and Al$_2$O$_3$ particulates were processed using spray atomization and co-deposition. It was reported that the MMCs exhibited relatively high damping capacities, due to the incorporation of the particulates and accompanying modifications to the matrix microstructure. In addition, SiC and TiB$_2$ particulates were successfully co-injected into an Al-Si matrix [5, 15, 63-66].

Metal matrices other than Al alloys have also been used in spray atomization and co-deposition experiments. Mathur et al. [72], for example, reported that W particulates with an average size of 6 μm and Al$_2$O$_3$ particulates smaller than 45 μm were injected into pure Cu during spray atomization and deposition to form Cu matrix composites. It was observed that a large fraction of the W particulates penetrated and were embedded in the Cu droplets, hence leading to the formation of a uniform distribution of dispersed W particulates in the Cu/W MMC [72]. In a related investigation [26], Ni$_3$Al was spray atomized and co-deposited with both SiC and TiB$_2$ particulates to form Ni$_3$Al IMC. The SiC particulates exhibited an average size of 3 μm and the TiB$_2$ exhibited a size of 10 μm. Total volume fraction of reinforcement particulates in this IMC was measured to be 12.7 %, and the microstructure exhibited a relatively homogeneous distribution of particulates.

In terms of commercial interest in these types of MMCs, COSPRAY Advanced Aluminum Materials (Alcan International, Banbury, UK) has successfully produced numerous 2000, 6000, 7000 Al alloys and 8090 Al-Li alloys reinforced with up to 20 vol.% of SiC or Al$_2$O$_3$ particulates, using spray atomization and co-deposition technology [64]. The spray atomized and co-deposited MMCs reportedly exhibit physical and mechanical properties, including stiffness, wear resistance, and coefficient of thermal expansion, that are superior to those of the unreinforced matrix materials.

2.4. Functionally Gradient Materials Processed Using Spray Deposition

A functionally gradient material (FGM) exhibits a progressive change in composition, microstructure and properties as a function of position within the material [73-78]. Thus problems associated with interfaces due to abrupt changes in composition or structure may be avoided. The constitutional gradation can be tailored for specific requirements. The related properties are not only mechanical (static and dynamic strength, hardness, wear resistance), but also thermal (heat conductivity and isolation) and chemical (corrosion and oxidation resistance). The gradation is introduced intentionally and quantitatively controlled in order to optimize material properties for use

in real environment by place-to-place control of composition and microstructure.

Among currently used FGM processing approaches to fabricate FGM components. CVD, laser processing, self-propagating high-temperature synthesis (SHS) and powder metallurgy (P/M) have been developed for different manufacturing purposes [73-78]. CVD and laser processing are particularly suited for modifying the near surface regions of components. SHS is developed for joining and thermal barrier coatings. P/M processing is capable of producing structural FGMs. However, P/M processing involves handling fine powders (sieving, classification, mixing, cold or hot pressing), which degrades the cost-effectiveness of this processing approach.

More recently, Spray deposition processing may achieve a layered structure in particulate reinforced MMCs [5, 79]. Spray deposition processing approach to produce layered structures (similar to those with a laminated geometry) is attractive because it involves significantly fewer steps when compared to available layering techniques in manufacturing layered MMCs. The layered geometrical arrangement in the spray deposition processed MMCs was produced by alternating droplet deposition and particulate injection on a rotating substrate at a controlled rotation which was accomplished using a hydraulic system. This layering effect seems to be more prominent as the rotation speed of the substrate decreases. Thus, it is postulated that the rotation of the substrate creates a layered structure by maximizing the time differential between the impinging droplets and particulates at particular location.

In the studies reported in Ref. [79], efforts were aimed at producing different layered geometrical arrangements using spray deposition processing approach. The results obtained from these preliminary studies are very encouraging. For example, Figure 2.1 [79] shows the layer distribution within the spray deposited and layered 6061Al/SiCp MMC. The layer thickness was determined using image analysis by the following procedure. Particulates were counted every 200 μm interval along the deposited MMC height using image analysis and the data were graphed in Figure 2.1. From the figure, the amplitude of each layer was delineated and the width of the region was approximated accordingly to be 4.13 mm. As shown in Figure 2.1, no definitive interfaces formed as otherwise found in other layered MMCs. Instead, a half sinusoidal wave-like pattern delineated the progressive accumulation of reinforcement within the 6061Al/SiCp MMC. The spray deposited and layered 6061Al/SiCp MMC was actually a FGM. It was demonstrated that the 6061Al/SiCp MMC exhibited much higher fracture toughness than that of other layered MMCs with similar volume fraction of reinforcement (Table 2.3 and Figure 2.2 [79]). One distinct feature observed in the 6061Al/SiC/15p MMC is the absence of macroscopic interfaces. The reinforcement distribution within the spray deposited and layered MMC is continuous with a wave-like pattern. Without an abrupt change in material properties, the load can be transferred more efficiently from reinforced regions to ductile regions. Consequently, more regions in the MMC participate in resisting fracture process and result in an improvement in the overall fracture

toughness of the 6061Al/SiC/15p MMC. The unreinforced regions in the 6061Al/SiC/15p MMC are able to locally arrest the growing crack (load drop and closing crack) and with proper interfacial bonding the stress is sustained by the reinforcement regions before particulate fracture occurs. A decrease in load after reaching maximum load indicates the onset of extensive particulate fracture and the dominance of matrix ductile rupture.
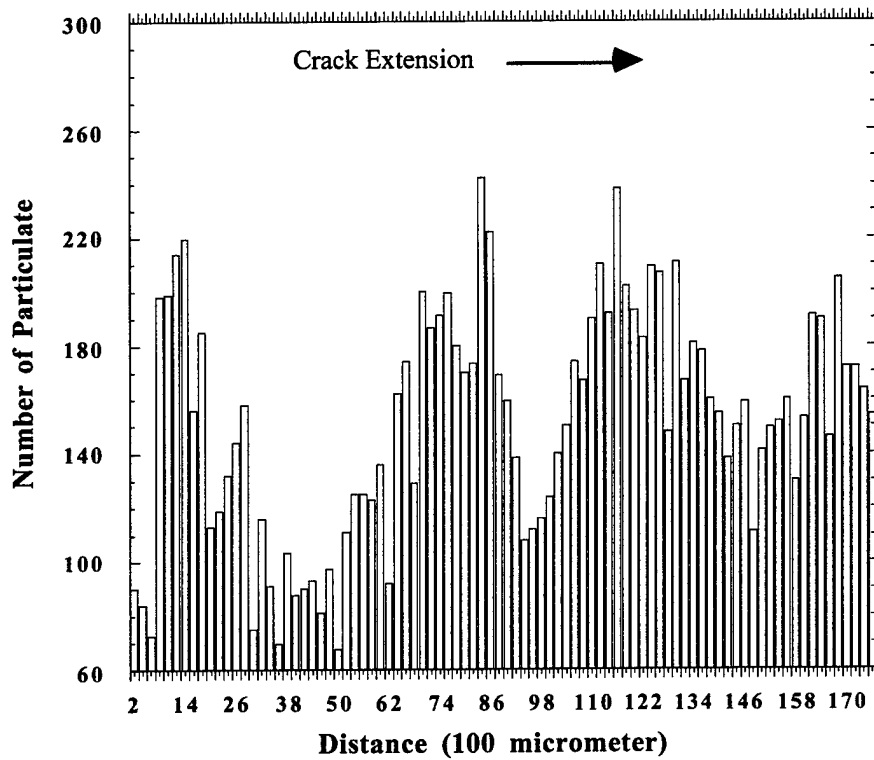
Figure 2.1. Particulate distribution in layered structures of 6061Al/SiCp MMCs [79, 80].

2.5. Elevated Temperature Properties

Dispersion strengthened Al alloys derive their strength and thermal stability at elevated temperatures from the presence of a dispersion of nanometer-size particles that effectively impede dislocation motion during deformation. The strengthening characteristics of these particulates at high temperatures depend on their ability to resist coarsening; thus low diffusivities and limited or no equilibrium solid solubility are desirable. The relatively high solidification cooling rates present during spray atomization and deposition have allowed investigators to utilize this synthesis approach to process high temperature Al alloys containing a fine dispersion of relatively insoluble phases [64].

Table 2.3. Comparison of fracture and mechanical properties for selected layered MMCs

Materials	J_{IC} (kJ/m^2)	E (GPa)	σ_y (MPa)	σ_u (MPa)	El. (%)	Remarks
6061Al/SiC/15p MMC	18.3 (40)*	81	187.5	290.5	3.3	T4 [79]
MB85Al/SiC/15p+6061 Al bilayer MMC	9	---	---	---	---	1:3 thickness ratio of 6061 Al to MB85/SiCp MMC [80]
6061Al/SiC/25p+5182 Al multilayer MMC	(48)	---	232	333	7.2	Equal thickness for 6061Al/SiCp MMC and 5182 Al [81]
X2080Al/SiC/20p+X20 80 Al bilayer MMC	(24.4)	--	---	---	---	[82]
6061Al/SiC/25p MMC	(15.8)	99	345	410	4.4	P/M, T6 [83]
6061Al/Al$_2$O$_3$/15p MMC	(24.7)	---	221	289	7	[84]

* The data in the parentheses denote K_{IC} or K_Q in MPa $\sqrt{m}$.
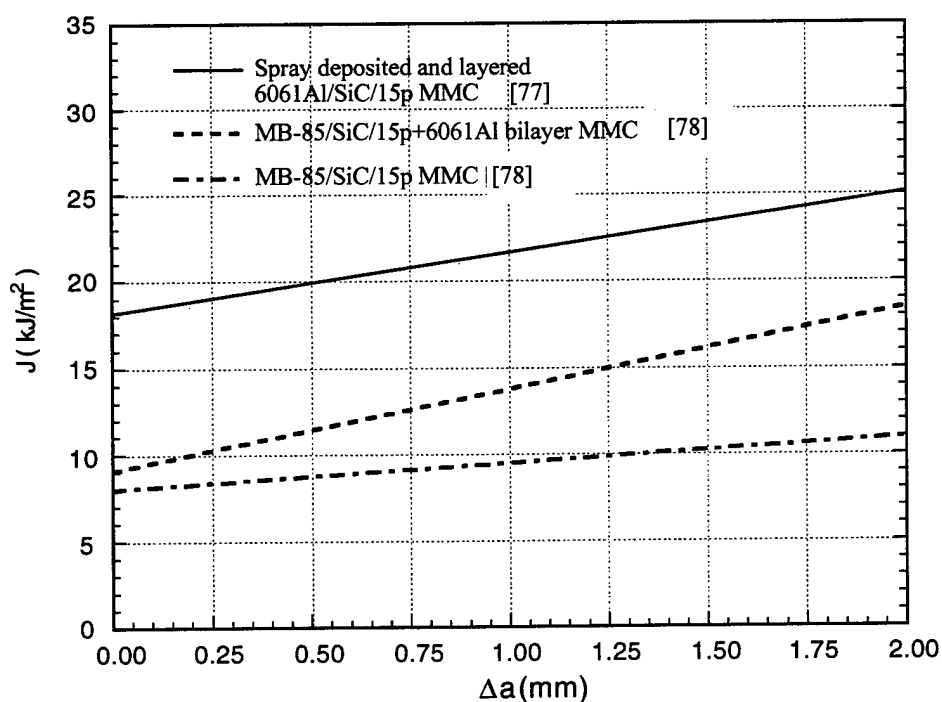
Figure 2.2. Comparison of fracture toughness among three selected MMCs [79, 80]

Among the family of transition metal high temperature Al alloys, Al-Ti alloys are actively being studied as a result of their attractive combination of elevated temperature properties [85]. These materials derive excellent strength, ductility, and creep resistance from their fine grain structure and dispersion of Al_3Ti particles, in combination with the low solid solubility (0.8 a/o) and low diffusivity (3.86×10^{-15} cm^2/sec) of Ti in α–Al [86]. In order to curtail the formation of coarse primary Al_3Ti, rapid solidification must be employed to extend the solid state solubility of Ti in Al. Gupta et al. [87], for example, noted that the amount of Ti in solid solution in Al could be increased over that achievable by equilibrium solidification, by using spray atomization and co-deposition. A summary of the elevated temperature mechanical behavior of the spray deposited and hot extruded Al-Ti alloys reported in this study is shown in Table 2.4, and compared to those of equivalent materials prepared by powder metallurgy and mechanical alloying. The results shown in this table for the Al-4wt.%Ti and Al-2.3wt.%Ti-SiC$_p$ materials were obtained after a 99 hour anneal, followed by mechanical testing at the designated temperature. The results in Table 2.4 show that the elevated temperature properties of the spray deposited materials compare favorably with those of the powder metallurgical materials, are superior to those of the ingot materials, but are inferior to those of the mechanically alloyed material (although the elongation behavior of the mechanically alloyed materials was not reported). The higher thermal stability of the spray atomized and deposited materials, relative to the cast ingot and extruded material, was attributed to the faster quench rates, with concomitant microstructural refinement resulting from the spray deposition stage. This is supported by the sharp reduction in grain size and the absence of the primary Al_3Ti phase observed for the spray deposited MMC, relative to that of the cast Al-Ti ingot.

In related studies [88], the creep behavior of a Ni_3Al IMC reinforced with both SiC and TiB_2 particulates and processed by spray atomization and co-deposition, was investigated. The creep rupture time of a material is generally governed by the nucleation, growth and coalescence of grain boundary cavities, which in turn leads to intergranular fracture. Microstructural examination of the fracture surface from the ruptured Ni_3Al/SiC/TiB_2 IMC showed that the cavities lie primarily on the grain boundaries and confirmed that the creep rupture process was governed by grain boundary cavitation. At a higher magnification, it appeared that these cavities nucleated at fine carbides (possibly resulting from the decomposition of SiC particulates) that were present on the Ni_3Al matrix grain boundaries. This suggestion may account for the longer lifetimes for the hot-extruded monolithic Ni_3Al, as compared to those of the hot-extruded Ni_3Al/SiC/TiB_2 IMC, since a large number of carbides existed on the grain boundaries in the Ni_3Al/SiC/TiB_2 IMC. The nucleation of grain boundary cavities on carbides also suggested poor interface bonding strength between these carbides and the Ni_3Al matrix. On the other hand, the absence of cavity nucleation at Ni_3Al/TiB_2 interfacial reaction zones indicated a relatively high interface bonding strength between Ni_3Al and

TiB$_2$.

Table 2.4. Elevated Temperature Mechanical Properties of Spray Atomized and Extruded Al-Ti/SiC Composites[85-87].

Material	Temperature (°C)	σ_{UTS} (MPa)	σ_{YS} (MPa)	Elongation (%)
Al-2.3Ti-SiC$_p$	25	200	198	7
	250	130	116	11
(Spray deposited)	350	51	48	18
(6 - 8 v/o)	450	24	22	32
Al-4.0Ti*	25	250	235	7
	250	127	106	24
(Spray deposited)	350	57	51	23
	450	20	18	40
Al-4.0Ti	25	180	145	23
	200	100	95	22
(Powder Metallurgy)	300	65	59	30
	400	42	35	30
Al-4.0Ti	25	--	320	--
	160		--	280
(Mechanical Alloying)	240	--	190	
	290	--	170	--
	350	--	150	--

2.6. Porosity During Spray Forming Processes

The presence of porosity in spray formed materials is inevitable, which has been consistently demonstrated by a variety of experimental studies. On the basis of a review of available literature on porosity during spray forming, several phenomena can be summarized as follows. First, the amount of porosity in as-deposited materials is generally larger than 1%, but in some materials it can be lower than 1%. For example, Table 2.5 summarizes the level of porosity reported for a variety of spray formed Al alloys, showing that porosity generally varies from 1 to 10%, whereas Benz et al. [36] reported less than 1% porosity for a René 95 superalloy. Second, the distribution of porosity in as-deposited materials is typically non-uniform. High porosity is frequently observed at the regions close to either substrate or top surface. For example, Bewlay and Cantor

[89] reported that in an as-deposited 316L stainless steel, porosity bands were observed in the region close to a refractory substrate and in the region close to top surface. Between these two regions, porosity was seldom observed. They reported that depths of porosity bands observed in deposited steel strip decreased with increasing melt flow rate [89]. Annavarapu et al. [90] observed similar bands adjacent to the bottom surface (substrate) in a spray formed steel strip. They also noted that porosity varies with flight distance. With shorter flight distance, a distinctive porosity band was observed, whereas with longer flight distance, the porosity distribution through the thickness of the sprayed strip tended to be uniform (Figure 2.3) [90]. Bewlay and Cantor [91] observed that the amount of porosity in spray formed Sn-38 wt.%Pb and Sn-15 wt.%Pb alloys decreases with increasing distance from the bottom of deposited materials to a distance at which porosity reaches minimum; beyond this distance, the amount of porosity increases and pore sizes increases as well [91]. In related studies, Underhill et al. [92] reported that porosity in as-deposited 2618 Al alloys was high at the initial stage of deposition; once the steady state cooling conditions were achieved, the level of porosity was low and pores distributed more uniformly. Similarly, Grant et al. [93] reported that porosity at the onset of deposition was highest across the deposit thickness (Figure 2.4). One exceptional example was reported by Ebalard and Cohen [94] for a cast iron in which porosity increased with increasing deposit thickness. The level of porosity varied from a minimum of 0.9% to a maximum of 1.6% with the average value being 1.3%; the size of the pores was typically in the range of 5 to 40 μm [94]. Third, porosity varies with radial distance in deposited materials. For example, Lavernia et al. [95] observed that the porosity at the center region of a spray formed 2020 Al alloys was lower than that at peripheral region, as shown in Figure 2.5. Fourth, pores exhibited different geometries. For example, Annavarapu and Doherty [96] observed two types of porosity present in an as-deposited Cu-6Ti alloy. The first type was interconnected, irregularly shaped, which was observed either in the region adjacent to substrate or the regions between subsequent deposition layers caused by incorrect substrate motion. The second type was large spherical pores, formed by the coalescence of entrapped atomization gases, which was commonly observed when the fraction of solid was high [96]. Gupta et al. [97] observed that micro-sized pores exhibited a near elliptical morphology. Finally, porosity was observed to be preferentially located at grain boundaries in a variety of alloys, such as in Weldalite 049 (Al-Cu-Li-Ag-Mg-Zr) [98], MERL-76 superalloy [99] and Al-Li-Mg-Ge-Zr alloy [97] and 2020 Al alloys (with Li additions) [95].

Table 2.5.   Porosity in As-deposited Aluminum Alloys

Alloy	Porosity (%)	Ref.
2020	3 - 5	[95]
2024	6 - 9	[100]
2618	5 - 30	[92]
6061	4.72 - 9.61	[38]
7075	1.5 - 2.9	[101]
7075	4.9 - 9.7	[102]
7075	5	[103]
7075 (+5.4wt.%Zn)	3-4	[5]
7150	2.5 - 2.7	[104]
7150 (+0.6wt.%Fe + 0.5wt.%Si)	< 8	[105]
Al-20wt.%Si-5wt.%Fe	1.2	[106]
Al-4wt.%Cu	2.5 - 9	[93]
Al-8 wt.% Fe -4wt.%Ce	11	[103]
Al-Cu-Li-Ag-Mg-Zr (Weldalite 049)	4-6	[98]
Al-Li-Mg-Ge-Zr	8	[97]
Al-Li-Mn-Zr	1.6	[107]
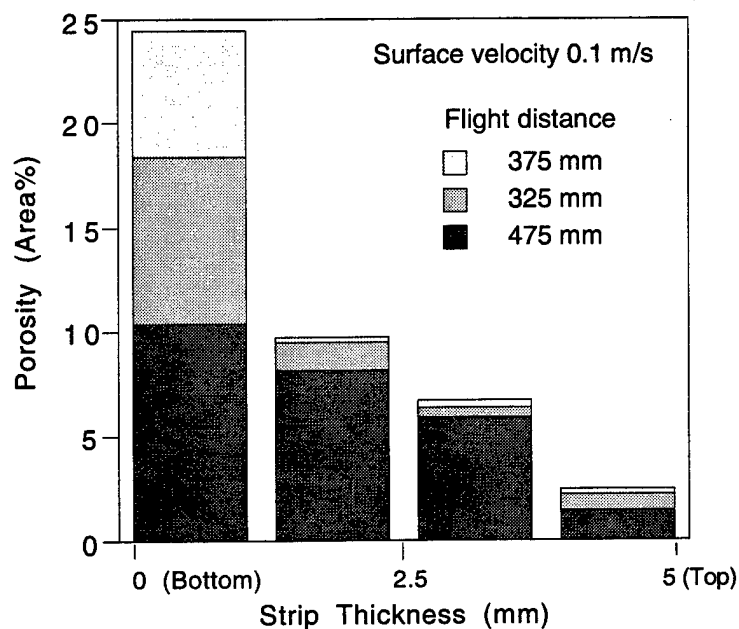
Figure 2.3.   Variation of porosity with thickness of AISI 1026 strip [90].
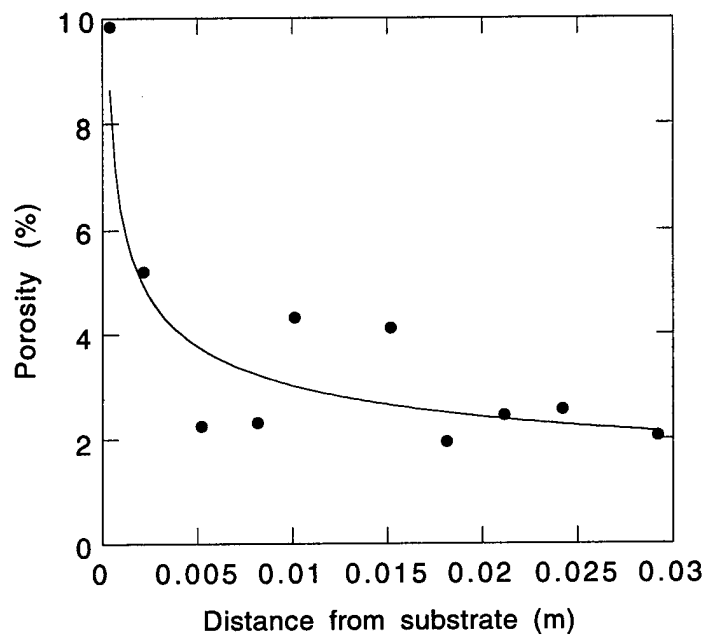
Figure 2.4. Measured porosity in spray formed Al-4wt.% Cu as a function of distance from substrate [93].
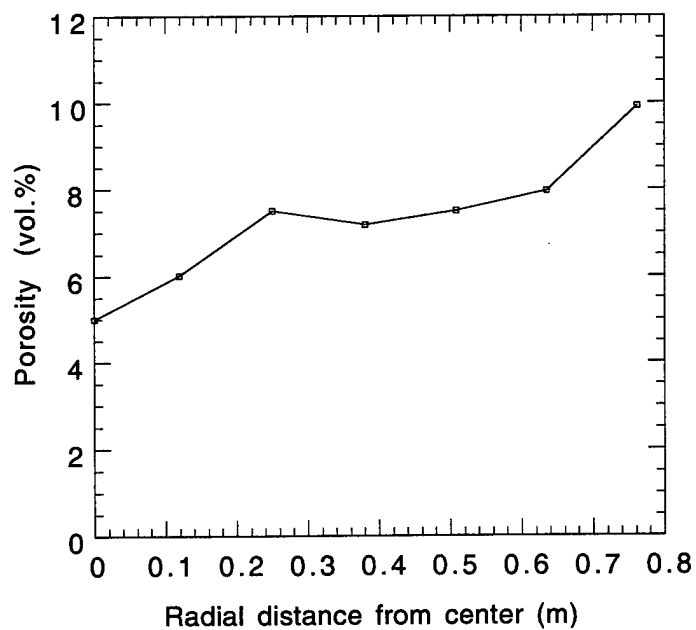
Figure 2.5. The variation of porosity with radial distance from the center in a spray formed 2020 Al alloy (data from reference [95]).

Spray forming processes are generally comprised of three steps, i.e., atomization, deposition, and solidification. Accordingly, porosity produced during gas atomization and solidification processes should be inevitably responsible for a proportion of porosity formed during spray forming. Unfortunately, porosity resulting from gas atomization has seldom been investigated during spray forming. Solidification shrinkage and gas porosity play a limited roles in the formation of porosity except under certain conditions. For example, it has been suggested that if the spray forming conditions are such that there is an excessive fraction of liquid present at the deposited surface, solidification shrinkage and gas porosity may play a significant role in the formation of porosity [108], which can be rationalized as follows. First, when excessive liquid is present, the solidification of deposited materials is similar to that in casting processes [40, 109]. Accordingly, solidification shrinkage and gas entrapment, the governing mechanisms of porosity formation in castings, would contribute a large proportion of porosity. Second, turbulent interactions between liquid and atomization gas can occur due to the presence of excessive liquid [108], which lead to serious gas entrapment during impingement. For example, large spherical pores have been reported when too much liquid is present [94, 96]. The presence of excess amounts of liquid phase during impingement may result from: coarse droplet sizes; high deposition temperatures; and remelting of solid phases caused by high enthalpy conditions.

Nevertheless, another mechanism, i.e., interstitial porosity is widely suggested to play a critical role in porosity formation during spray forming [40, 96, 108-111]. The formation of interstitial porosity can be envisaged as follows. Upon impingement, solidified individual droplets overlap each other, forming interstices. If the fraction of liquid in the incident spray is too low, these interstices will not be completely filled by the liquid, which gives rise to formation of porosity [109]. This mechanism is consistent with the observed correlation between deposition conditions and the amount of porosity present throughout the deposited materials [89, 90, 95, 99]. For example, lower porosity observed in the center region (Figure 2.5) has been attributed to the elevated mass flux of droplets in the region relative to the periphery [108]. These droplets contain elevated fraction of liquid, effectively filling the interstices between droplets. In contrast, the high level of porosity that generally observed in the periphery of the spray deposited materials results from a large proportion of small, presolidified droplets. Moreover, the high porosity that is frequently observed at regions adjacent to either substrate or top surface of deposited materials in several investigations [89, 90, 96] has also been attributed to the amount of liquid in incident spray. At the onset of deposition the fraction of solid is high due to the efficient cooling condition of substrate. Interstices are not sufficiently filled and irregular pores are formed. With the progress of deposition, the fraction of liquid increases and the level of porosity is reduced [93]. At the end of deposition, gas cooling leads to a low fraction of solid and therefore a high level of porosity. The phenomenon described above has also been explained on the basis of thermal history (enthalpy

extraction) of deposited materials [91]. At the beginning of deposition, the rate of enthalpy input from the spray is lower than the rate of enthalpy extraction. As deposition continues, the temperature of the substrate increases and the enthalpy extracted by the substrate decreases. During the last stage, the fraction of liquid is insufficient as a result of the decreased enthalpy input, leading to high porosity. In view of the irregular geometries of interstices, interstitial porosity is also irregularly shaped. This is consistent with observations made by a number of investigators [93, 96-98].

The formation of porosity during spray forming is influenced by many factors such as processing parameters, thermodynamic properties of the materials, thermodynamic properties of the atomization gases, as well as design considerations pertaining to apparatus design [37, 39-42, 112]. For example, the chemistry of the gaseous environment during atomization is known to play an important role on the formation of porosity. Results from experimental studies suggest that this phenomenon is related to the solubility of gases in the melt [39]. In related studies, Mathur et al. [40] indicated that the thermal properties of the deposition substrate play an important role in the formation of porosity in spray formed materials. For example, they reported that the porosity present in the near substrate region is higher when a high thermal conductivity substrate (i.e., Cu) is used, as compared with the case when an insulating substrate (i.e., refractory material) is used. Furthermore, it has been reported that an improperly designed substrate can induce a turbulent swirling gas flow pattern during deposition and thereby promote a higher level of porosity in the as-deposited materials [99]. Investigations on the influences of processing parameters on porosity are limited. One of the few available studies was made by Payne et al. [113]. They used artificial neural networks to predict effects of processing parameters on porosity during spray forming processes based on an approximate relationship between porosity and surface roughness of the deposited materials. Their results indicated that porosity decreases as the gas to metal flow rate ratio decreases, but increases with decreasing the melt superheat [113]. Moreover, Underhill et al. [92] reported that porosity approximately decreases as atomization gas pressure increases for a 2618 Al alloy.

III. INVESTIGATION OF THERMAL RESIDUAL STRESSES IN LAYERED COMPOSITE USING FINITE ELEMENT METHOD AND X-RAY DIFFRACTION

3.1. EXPERIMENTAL

3.1.1. Spray Atomization and Co-deposition

A SiC particulate-reinforced 2024 aluminum matrix composite with a layered structure was processed using spray atomization and co-deposition. The 2024 aluminum alloy used as the matrix in the present study was of commercial-quality grade with the nominal composition: Al-4.4Cu-1.5Mg-0.6Mn (in wt.%). The reinforcement used in the present study was α-phase SiC particulates with an average particulate size of 13 μm.

Spray atomization and co-deposition processing of the layered 2024Al/SiC composite was conducted in an environmental chamber which was filled with nitrogen to an over-pressure of 0.5 MPa to avoid oxidation (Figure 3.1). During processing, a typical charge of 3 kg of 2024Al was melted and superheated to 850 °C (1123 K) in a ceramic crucible. Then the melt was disintegrated into a fine dispersion of micrometer-sized droplets using nitrogen gas at a pressure of 1.2 MPa through an atomizer. Simultaneously, SiC particulates were carried by a separate flow of nitrogen at a varied pressure (0.07-0.31 MPa) and injected through two injection nozzles. The two nozzles were positioned perpendicularly to the spray atomization cone at a pre-determined distance from the atomizer. The layered structure in the 2024Al/SiC composite was produced by alternating droplet deposition and particulate injection on a rotating substrate. The substrate was rotated at 45 RPM using a hydraulic system. The primary processing parameters were determined on the basis of numerical analysis of the droplet temperature and solidification behavior [5, 63, 64]. The geometrical shape of the final co-deposited material obtained from the experiment exhibited a contour akin to the Gaussian distribution of droplets impinging on the substrate, as shown in Figure 3.2. After the process was completed, the height and the bottom diameter of the co-deposited material were measured to be 4.8 and 20 cm, respectively.

To eliminate the porosity typically associated with spray atomized and co-deposited materials, the as-sprayed layered 2024Al/SiC composite was densified using hot isostatic pressing (HIP) under the condition of 510 °C (783 K) and a maximum pressure of 206.4 MPa for 2 hours. After the HIP process, the porosity in the composite was measured to be approximately 10 vol.%. The HIP'ed 2024Al/SiC composite sample was then examined using optical microscopy to characterize the microstructural features such as particulate distribution and layer thickness.
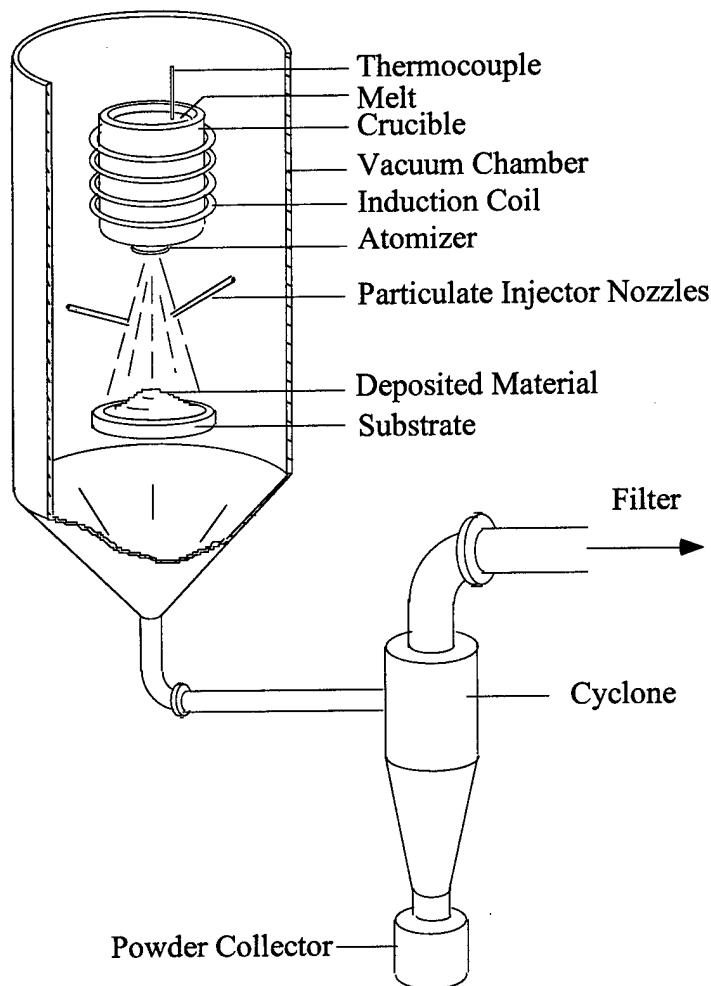
Figure 3.1.   A schematic diagram of spray atomization and co-deposition apparatus.

3.1.2. X-Ray Diffraction

The X-ray diffraction technique has been extensively used to measure the residual stress state in polycrystalline materials [114-117]. The determination of stresses by X-ray diffraction is based on the measurement of lattice spacings of particularly oriented sets of grains using Bragg's law [118]. The standard diffractometer method to measure residual stresses in the present study is often called the two-exposure method, because two plane-spacing measurements are made, one of d_n at $\psi=0°$ and one of d_i at $\psi=45°$ as shown in Figure 3.3. Here, d_n is the spacing of planes parallel to the surface, and d_i is the spacing of planes whose normal is inclined along OB. An expression for the calculation of the magnitude of the stress σ_ϕ using the two-exposure method is given as

$$\sigma_\phi = K_1(2\theta_n - 2\theta_i) = K_1(\Delta 2\theta) \qquad (3.1)$$

where

$$K_1 = \frac{E \cot \theta_n}{2(1+v)\sin^2 \psi} \tag{3.2}$$

E is the elastic modulus, v is the Poisson's ratio, $2\theta_n$ is the observed value (in radians) of the diffraction angle in the normal measurement (ψ=0°), and $2\theta_i$ is the value in the inclined measurement (ψ=45°). The constant K_1 is termed the stress constant.
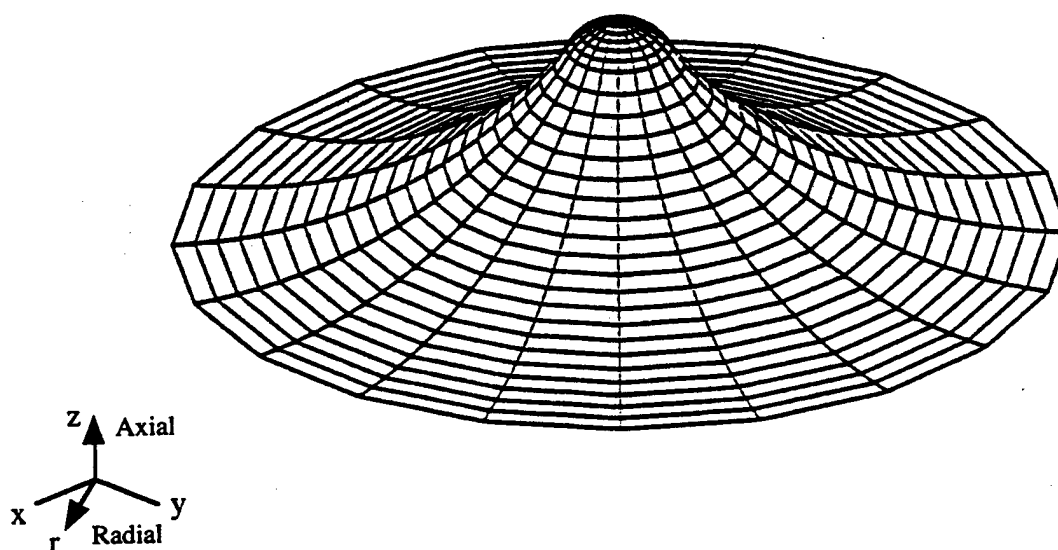
Figure 3.2.   The geometrical shape of co-deposited material from spray atomization and co-deposition.
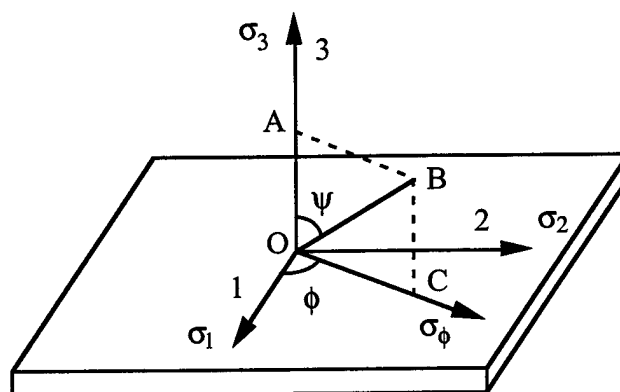
Figure 3.3.   Stresses corresponding to the surface of a stressed body.

In the present study, the diffraction angles were measured with a Siemens D5000 diffractometer using Cu Kα1 radiation with a wavelength (λ) of 0.15406 nm. To reduce systematic errors, a high angle diffraction peak was selected. The X-ray diffraction sample of the spray 2024Al/SiC deposited material was prepared such that it covers the entire range of the deposited material from top to bottom, for the purpose of measuring residual stresses as a function of deposition thickness. The dimension of the sample was typically limited by the sample holder of the X-ray diffractometer. Therefore, the sample was sectioned into three pieces to be fitted in the X-ray sample holder. In addition, the surfaces to be exposed to the X-ray for the measurement were electropolished in order to eliminate the residual stresses induced by the sectioning and machining. The residual stress measurement was made at six equally spaced locations along the deposition thickness.

3.2. Finite Element Analysis

3.2.1. Approach

Continuum models were used to compute the strains and stresses that develop in the layered 2024Al/SiC composite as it is cooled from the co-deposition temperature to the ambient temperature. Two different finite element models were considered in the present study. One was to investigate the macro-residual stresses that develop in the aluminum and the SiC rich composite layers, and the other was to investigate the micro-residual stresses that develop in the SiC particulates and the aluminum matrix. ABAQUS uses a finite element numerical approach to obtain solutions to the partial differential equations of equilibrium. Since the material response in the present study involves nonlinear plastic behavior, solutions were obtained as a series of cooling increments, allowing iteration within each increment to obtain equilibrium.

3.2.1. Material Model

Elastoplastic response was permitted in the aluminum matrix and the composite layers: a von Mises yield condition and isotropic hardening were assumed. Material behavior was assumed to be independent of time. The properties of 2024 aluminum and SiC are shown in Table 3.1 [119, 120]. The properties of 2024 aluminum are temperature dependent, and the properties of SiC are assumed to be independent of temperature.

Table 3.1.   Properties of 2024 Al and SiC [119, 120].

	2024 Al		SiC
Elastic Modulus (GPa)	72.4	··· 297 K	410
	69.1	··· 373 K	···
	66.5	··· 422 K	···
	63.7	··· 477 K	···
	60.2	··· 533 K	···
	57.3	··· 589 K	···
	54.5	··· 644 K	···
	51.1	··· 673 K	···
	47.6	··· 775 K	···
Yield Strength (MPa)	393	··· 297 K	···
	372	··· 373 K	···
	248	··· 422 K	···
	131	··· 477 K	···
	62	··· 533 K	···
	41	··· 589 K	···
	28	··· 644 K	···
	18	··· 673 K	···
	12	··· 775 K	···
Coefficient of Thermal Expansion (μm/m ·K)	21.1	··· 293 K	4.3
	22.9	··· 373 K	···
	23.8	··· 473 K	···
	24.7	··· 573 K	···
	25.6	··· 673 K	···
	26.5	··· 775 K	···
Density (kg/m ^{3})	2770		3100
Thermal Conductivity (W/m ·K)	151		83.6
Specific Heat (J/kg ·K)	875		1040

Stress-strain constitutive parameters for the composite layers with different volume fractions of reinforcement were computed using a modified rule-of-mixtures that was first proposed by Tamura *et al.* [121] and is illustrated schematically in Figure 3.4. The composite stress-strain curves were constructed by dividing both the stress and strain among the constituents in the ratio of their volume fractions, as follows,

$$\sigma_c = V_\alpha \sigma_\alpha + V_\beta \sigma_\beta \qquad (3.3)$$

$$\varepsilon_c = V_\alpha \varepsilon_\alpha + V_\beta \varepsilon_\beta \qquad (3.4)$$

where V_α and V_β are the ceramic and metal volume fractions, σ_α, ε_α and σ_β, ε_β are the corresponding stress and strain of the ceramic and metal, respectively, and σ_c and ε_c are the flow stress and strain of the composite. Since Eqs. (3.3) and (3.4) do not specify the absolute amount of stress and strain transfer, an additional equation,

$$q = \frac{\sigma_\alpha - \sigma_\beta}{\varepsilon_\alpha - \varepsilon_\beta} \qquad (3.5)$$

which defines the ratio of stress to strain transfer, is required. As illustrated in Figure 3.4, q is the slope of the correspondence line on the stress-strain curve, with large slopes approaching the isostrain condition ($\varepsilon_\alpha = \varepsilon_\beta = \varepsilon_c$) and small slopes approaching the isostress condition ($\sigma_\alpha = \sigma_\beta = \sigma_c$). In general, the value of q depends on many factors, including composition, flow stress ratio and hardening of the constituent phases, and their microstructural arrangement. The exact nature of this dependence, however, is not well known. Fishmeister and Karlsson [122] found that application of the modified rule-of-mixtures using a constant q value yielded a reasonable comparison with experiments over a wide range of volume fractions and applied strains for several systems involving two-phase microstructures comprised of hard and soft constituents. Williamson et al. [123] recently investigated the sensitivity of the stress calculated to the value of q varying from 1.0 GPa to 15.0 GPa in Al2O3-Ni composite material. In their study, they found that the residual stress calculations are not highly sensitive to the parameter q. Therefore, in the present study a q value of 4.5 GPa was used to calculate the stress-strain constitutive response. Other physical properties of composite materials, such as density, thermal conductivity, and coefficient of thermal expansion, were calculated using a volume fraction-based linear interpolation.

3.2.2. Geometry and Computational Mesh

As a result of the difficulties involved in modeling the transient problem posed by a growing deposited material during spray atomization and co-deposition, the fully grown deposited material

at the end of co-deposition was modeled in the present study. Accordingly, the present model formulation (*i.e.,* initial conditions) for the macro-residual stress analysis begins immediately following the completion of the co-deposition stage.
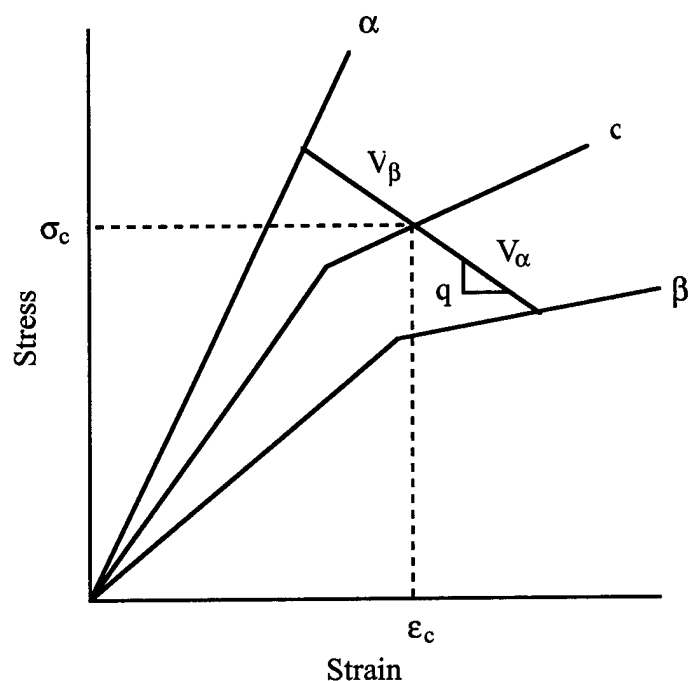
Figure 3.4.   Schematic illustration of the rule-of-mixtures approach for obtaining stress-strain constitutive data for composite materials.

As shown in Figure 3.2, the deposited material exhibits an axisymmetric shape. Therefore, the three-dimensional deposited material could be modeled using axisymmetric elements. Figure 3.5 shows the axisymmetric finite element mesh used for modeling the layered material to calculate the macro-residual stresses. The dimension of the finite element model was based on that of experimentally spray deposited material. A total of 3150 four-noded temperature-displacement elements were used. The layered material was treated as a series of perfectly bonded alternating 2024 aluminum layer and SiC rich composite layer. The layer thickness used in the finite element model was based on the graphically determined results obtained from the image analysis of the spray deposited material.

Node Number

Top Layer

1 2 3 4 5

Middle Layer

Aluminum layer

SiC rich layer

Bottom Layer

45 46

z

r
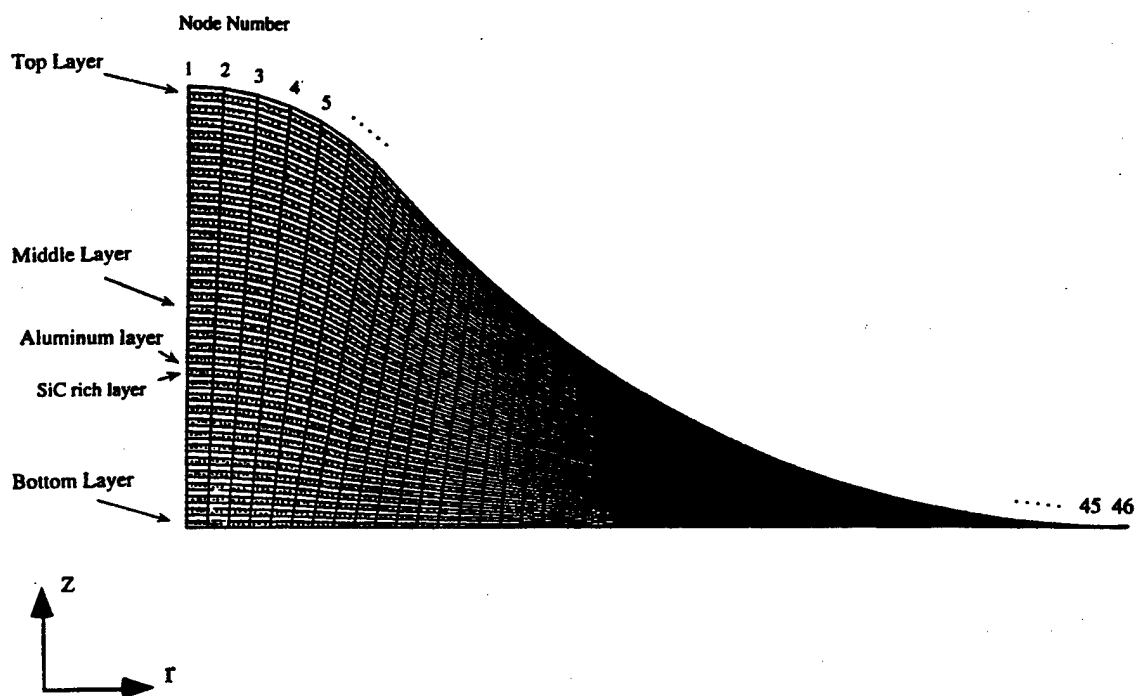
Figure 3.5.   Axisymmetric finite element mesh for the macro-residual stress analysis.

For the micro-residual stress analysis, it was assumed that the SiC rich composite layers are of a periodic array of SiC particulates embedded throughout the matrix using square packing arrangement. The particulates were assumed to be spherical and have the same diameter of 13 μm. In square packing arrangement, the particulates occupy the diagonal corners of a square matrix as shown in Figure 3.6 (a), and this type of arrangement is widely used for the finite element formulation of composite materials for the micro-stress analysis [124, 125]. Due to the difficulties involved in the modeling of entire composite layers using a micro-sized geometry, only single unit cell containing one-eighth of particulate at eight corners was considered in the present study under the assumption that the thermal boundary condition is uniform in the entire composite layers. Like the case for determining the layer thickness for macro-residual stress analysis, the dimension of the unit cell for the finite element model of micro-residual stress analysis was based on the experimentally determined volume fraction of particulates from the image analysis. Due to the symmetrical geometry and boundary conditions, only one-eighth of the unit cell could be modeled using a total of 216 eight-noded three-dimensional solid elements. The three-dimensional finite element mesh for the micro-residual stress analysis is shown in Figure 3.6 (b).
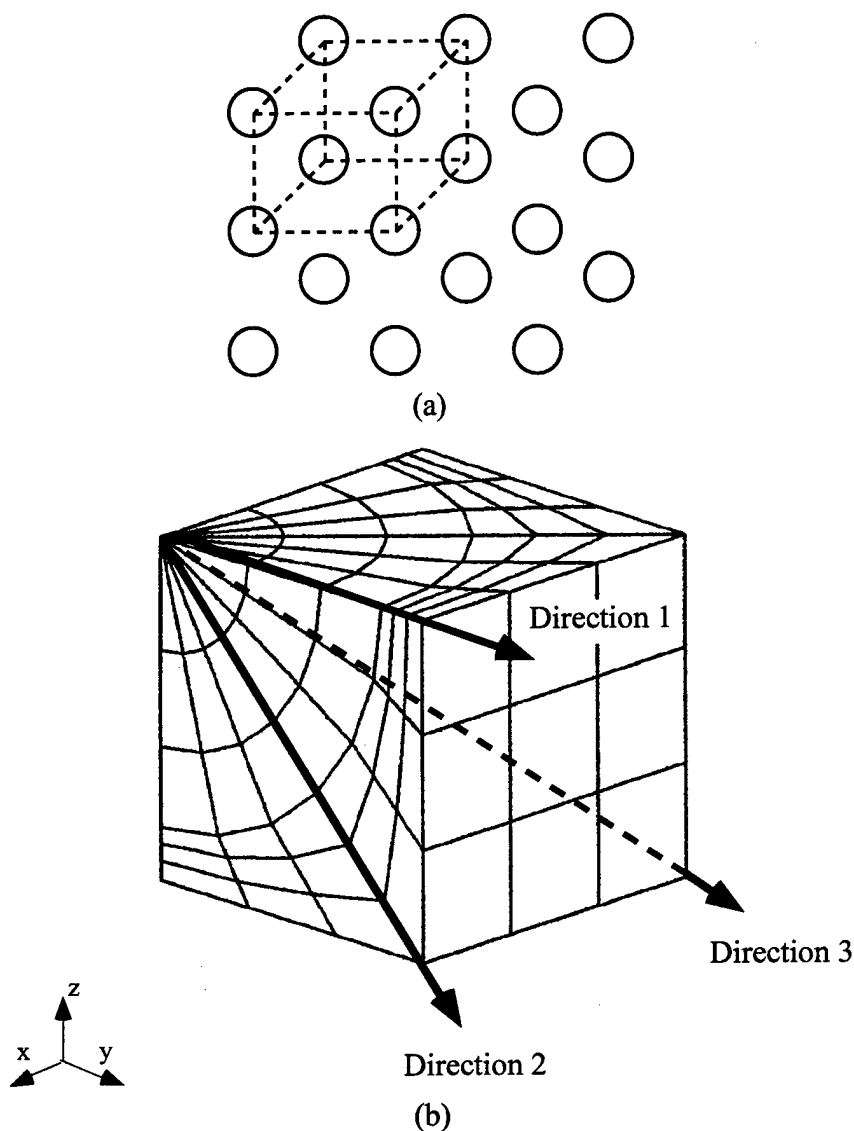
Figure 3.6. (a) Square packing arrangement and (b) three-dimensional finite element mesh for the micro-residual stress analysis.

3.2.3. Boundary and Initial Conditions

Throughout the modeling, symmetric boundary conditions were imposed such that every symmetric line and surface is constrained in its normal direction to represent the effect of the rest of the material. For the initial temperature condition of the model formulation for the macro-residual stress analysis, the temperatures at the top and bottom surfaces of the deposited material were assumed to be 775 and 600 K, respectively, since the top surface of the deposited material was covered with partially solidified droplets with a solidus temperature of 775 K at the end of the co-

deposition process, and the bottom surface of the deposited material was cooled down during the process and assumed to have a temperature of 600 K, when the co-deposition process was completed. The temperature inside the deposited material was then linearly interpolated.

During the spray atomization and co-deposition process, the co-deposited material loses thermal energy through a combination of three heat transfer processes: a) conduction to the low temperature substrate, b) convection to the atomization gas, c) radiation to the environment [63]. On the basis of thermal flux measurements, Mathur *et al.* [110] concluded that the heat transfer process during the initial stage of deposition was very high and that the corresponding thermal conductive heat transfer coefficient between deposited material and substrate was approximately 10^5 W/m^{2}K. Following a brief transient period, the magnitude of the heat transfer coefficient decreases to approximately 550 W/m^{2}K under steady state conditions for copper substrate cooled by water. The convective heat transfer coefficient from the top surface of the deposited material to the atmosphere at the end of deposition is assumed to be at least one order of magnitude smaller than the conductive heat transfer coefficient from the bottom surface of the deposited material to the substrate [126]. Therefore, in this study, heat transfer coefficients of 21 and 550 W/m^{2}K were used for the top and bottom surfaces of the deposited material, respectively. The radiative heat transfer was not considered in this study, since its effect becomes significant only when the temperature of the deposited material is extremely high [63]. The ambient temperature was assumed to be 300 K.

For the micro-residual stress analysis, a simplified thermal boundary condition was used to make the posed problem tractable. The thermal strains that develop from a uniform temperature change from 775 to 300 K in the model were considered. The analysis considered in the present study was a static analysis with thermal loads, and the heat transfer analysis was not taken into account.

3.3. Results And Discussion

An optical micrograph of the spray 2024Al/SiC deposited material is shown in Figure 3.7. In accordance with ASTM E 1245-89, the area fraction of SiC particulates in the sample surface as a function of deposition thickness was evaluated, and this is shown in Figure 3.8. The area fraction was then assumed to be equivalent to the volume fraction of SiC particulates in the present study. As shown in Figure 3.7 and 3.8, interfaces between the aluminum layers and the SiC rich layers were not well defined. Instead, small fraction of SiC particulates could be found even in the aluminum layers. The average volume fraction of SiC particulates in the SiC rich layers and the aluminum layers were estimated to be 31.5 and 3.8 %, respectively. On the basis of estimated 31.5 vol.% SiC particulates in the SiC rich composite layers, the length of the unit cell was

calculated to be 15.4 μm for the finite element model of composite layers. In addition, the thickness of each layer was determined to be 0.75 mm approximately.
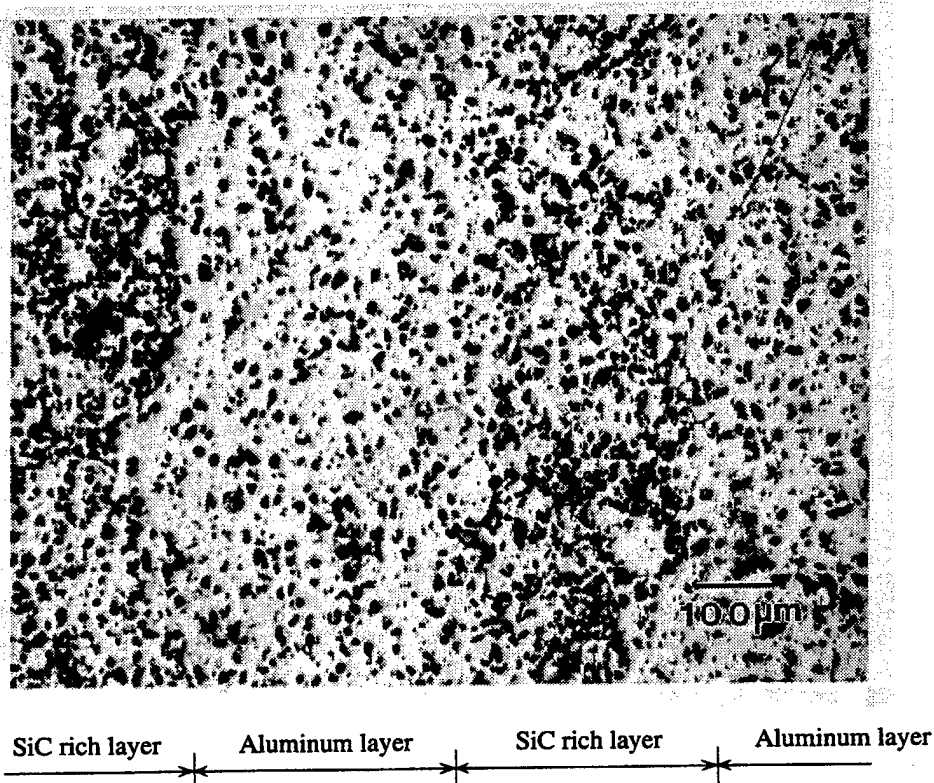
Figure 3.7.   Optical micrograph of the spray 2024Al/SiC deposited material.

Based on the information obtained from the image analysis, the finite element models for the macro- and the micro- residual stress analysis were created and analyzed. Figure 3.9 shows the numerically computed macro-axial residual stress as a function of distance along the z direction at the center of the deposited material from the top to bottom along with the values obtained using X-ray diffraction. It is noted that Figure 3.9 shows the calculated macro-residual stresses, whereas the X-ray diffraction measurement yields the total of macro- and micro-residual stresses. The macro-axial stress is found to be compressive both in the aluminum and the SiC rich layers for the entire center region of the deposited material. It is also found that the macro-axial stress for the upper region of the deposited material has lower magnitude as compared with that for the lower region. The residual stresses from X-ray diffraction and finite element analysis are in a very good agreement. The difference in magnitude of the residual stresses could be attributable to the fact that the X-ray diffraction measurement yielded the total residual stresses and that the samples for the X-ray measurement were exposed to the HIP process whereas the finite element model did not take

the HIP process into account. Under the isostatic loading condition during HIP process, the local stress field is not necessarily isotropic, hence plastic flow may take place in the material during application of the pressure. As a result, additional residual stresses may be introduced in the material [127]. In a related study, Li et al. [128] investigated residual stresses developed in the HIP process of various metals and ceramics. In their study, they calculated residual stresses using various processing parameters. They found that residual stresses are large enough to cause cracking in ceramic materials and shape change in ductile materials.
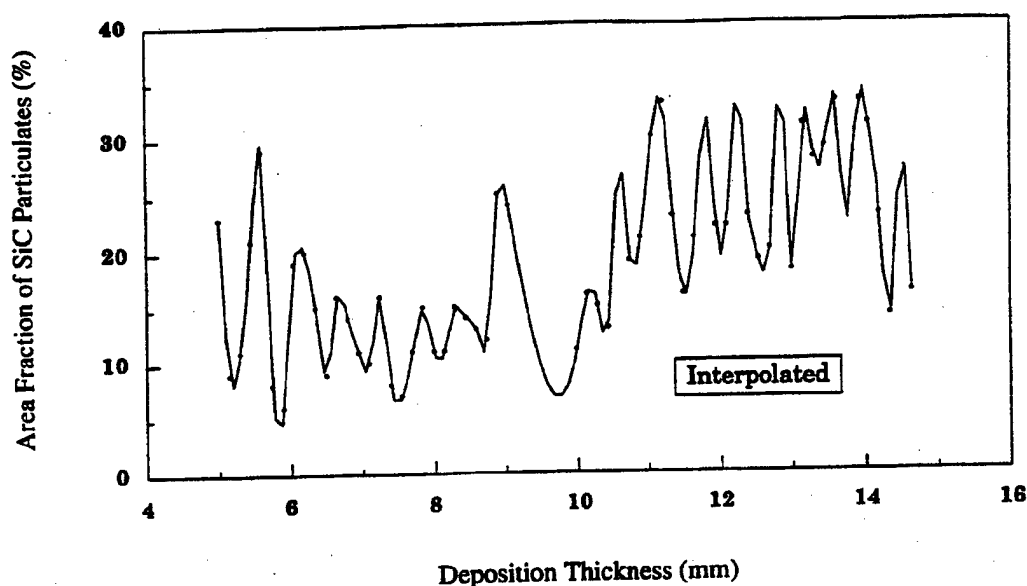
Figure 3.8.   Area fraction of SiC particulates as a function of deposition thickness.

Contrary to the continuous macro-axial stress distribution between the aluminum and the SiC rich layers, the macro-radial stress is very discrete for the aluminum and the SiC rich layers as shown in Figure 3.10. The macro-radial stress is found to be tensile in the aluminum layers and compressive in the SiC rich layers. This can be attributed to the fact that the aluminum layers tend to contract more than the SiC rich layers in the radial direction during cool down from the co-deposition temperature to ambient temperature, which results in the tensile state in the aluminum layers and the compressive state in the SiC rich layers in order to maintain continuity between layers. Also, as shown in Figure 3.11, the aluminum layers have higher macro-von Mises' stress for the upper center region of the deposited material as compared with that of the SiC rich layers. However, for the lower region of the deposited material, this trend is reversed.
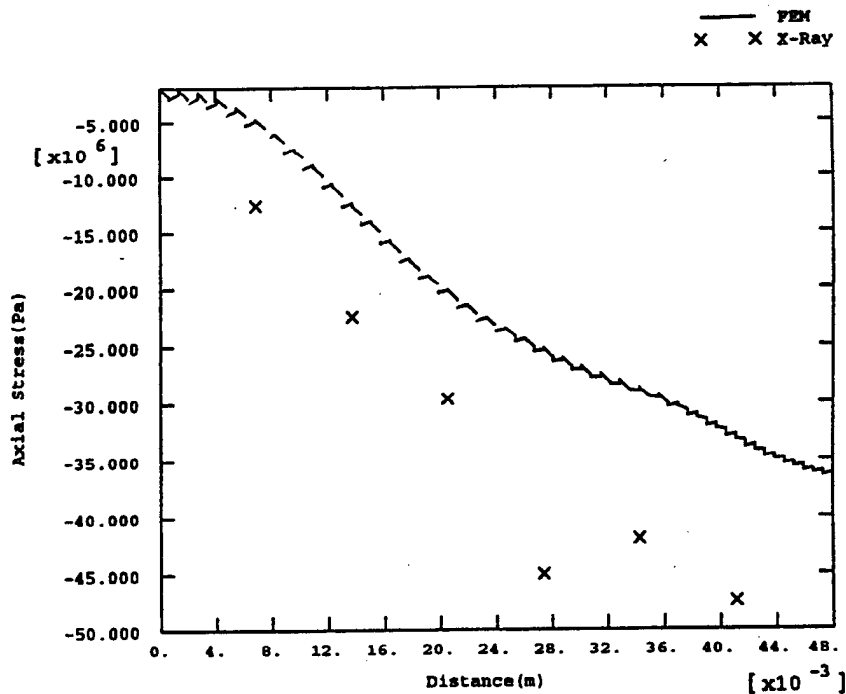
Figure 3.9.   The macro-axial stress from finite element method (FEM) and X-ray diffraction as a function of distance along the z direction at the center of the deposited material from the top to bottom.
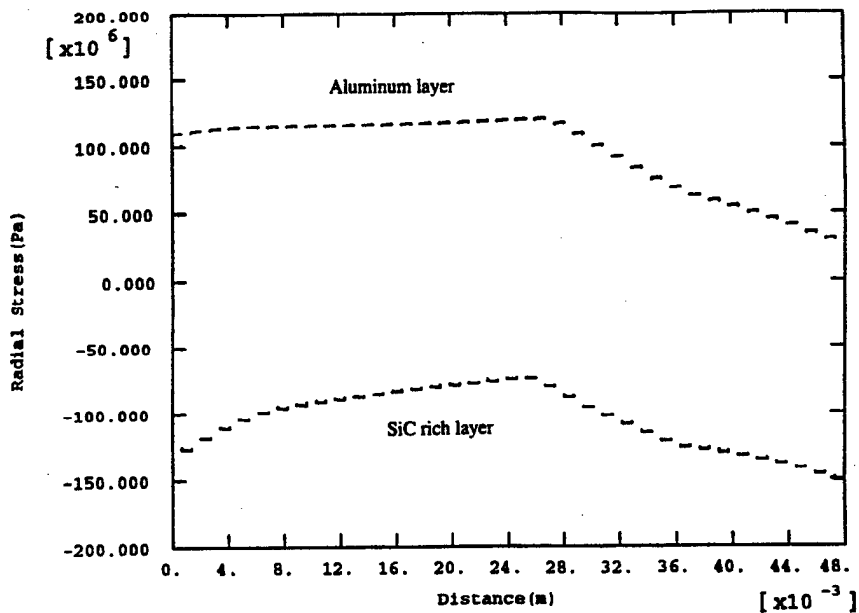
Figure 3.10.   The macro-radial stress at the center of the deposited material as a function of distance along the z direction from the top to bottom.
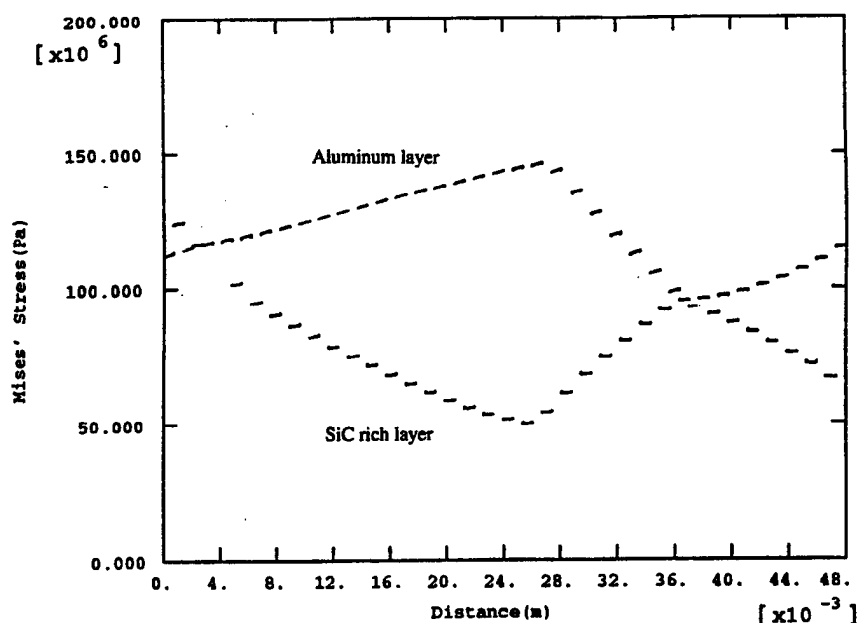
Figure 3.11. The macro-von Mises' stress at the center of the deposited material as a function of distance along the z direction from the top to bottom.

Figures. 3.12, 3.13, and 3.14 show the macro-axial, radial, and von Mises' stresses along the top, middle, and bottom layers in the deposited material as indicated in Figure. 3.5. Along the upper half of the entire deposited material, the macro-axial stress is mostly tensile only in the aluminum layer. As the region of the interest goes down below the lower half of the deposited material, the macro-axial stress becomes compressive both in the aluminum and the SiC rich layers, and the difference in magnitude of the macro-axial stress between the aluminum and the SiC rich layers becomes smaller. Based on Figure 3.13, it is found that for the entire region of the deposited material the macro-radial stress is tensile in the aluminum layers and compressive in the SiC rich layers. Again, this is due to the tensile state in the aluminum layers and the compressive state in the SiC rich layers in order to maintain continuity between layers during cool down. Figure 3.14 reveals that the macro-von Mises' stress in the aluminum layers for the entire region of the deposited material exhibits a flatter distribution as compared with that in the SiC rich layers. The macro-von Mises' stress in the SiC rich layers at the outer edge of the deposited material has the highest value, and this can be explained by the fact that the outer region experiences the most severe cooling rate due to the small deposition thickness.

For the micro-residual stress analysis in the composite materials, most of the analytical models are based on Eshelby's equivalent inclusion method [129, 130]. Eshelby first pointed out that the stress disturbance due to the presence of an inhomogeneity can be simulated by an eigenstress caused by an inclusion when the eigenstrain is chosen properly. Here, eigenstrain is a generic

name given to such nonelastic strains as thermal expansion, phase transformation, initial strains, plastic, or misfit strains. Eigenstress is a generic name given to self-equilibrated internal stresses caused by one or several of these eigenstrains in bodies which are free from any other external forces and surface constraints. Eigenstress is called thermal stress when the thermal expansion is a cause of the corresponding elastic stress field. According to Eshelby, the stress field in the inclusion in a infinitely extended body is obtained as

$$\sigma_{ij} = (S_{kkmn}e_{mn}^{**} - e_{kk}^{**})\lambda\delta_{ij} + 2\mu(S_{ijmn}e_{mn}^{**} - e_{ij}^{**}) \qquad (3.6)$$

where $\lambda = 2\mu v/(1-2v)$, $\mu = E/[2(1+v)]$, δ_{ij} is the Kronecker delta, and S_{ijkl} is the Eshelby's tensor, which is a function of elastic moduli C_{ijkl} and the geometry of the inclusion. In Eq. (3.6), e_{ij}^{**} is the total eigenstrain and defined as

$$e_{ij}^{**} = \alpha^* + e_{ij}^* \qquad (3.7)$$

where α^* is the strain due to the mismatch of thermal expansion coefficients between the inclusion and the matrix and e_{kl}^* is the equivalent eigenstrain. Once the stress within the inclusion $\sigma_{ij}^{(in)}$ is computed, the stress just outside the inclusion $\sigma_{ij}^{(out)}$ can be obtained by the following relation [131]:

$$\sigma_{pq}^{(out)} = \sigma_{pq}^{(in)} + C_{pqmn}\left[-C_{klij}e_{ij}^{**}n_l n_n \frac{(\lambda+2\mu)\delta_{km} - (\lambda+\mu)n_k n_m}{\mu(\lambda+2\mu)} + e_{mn}^{**}\right] \qquad (8)$$

where $\sigma_{pq}^{(in)}$ is given by Eq. (3.6), and n_i is the ith component of the unit vector outward normal to the surface of the inclusion. Even though the Eshelby's method provides significant insight, it is often limited to the problems with simplified geometry and boundary conditions and can only account for the stress field in an approximate manner. Recently, Ho [132] calculated the stress field that develops around a single inclusion due to a temperature change using the Eshelby's method. He also compared the analytical values from the Eshelby's method with those from the finite element analysis and found a good agreement between them.
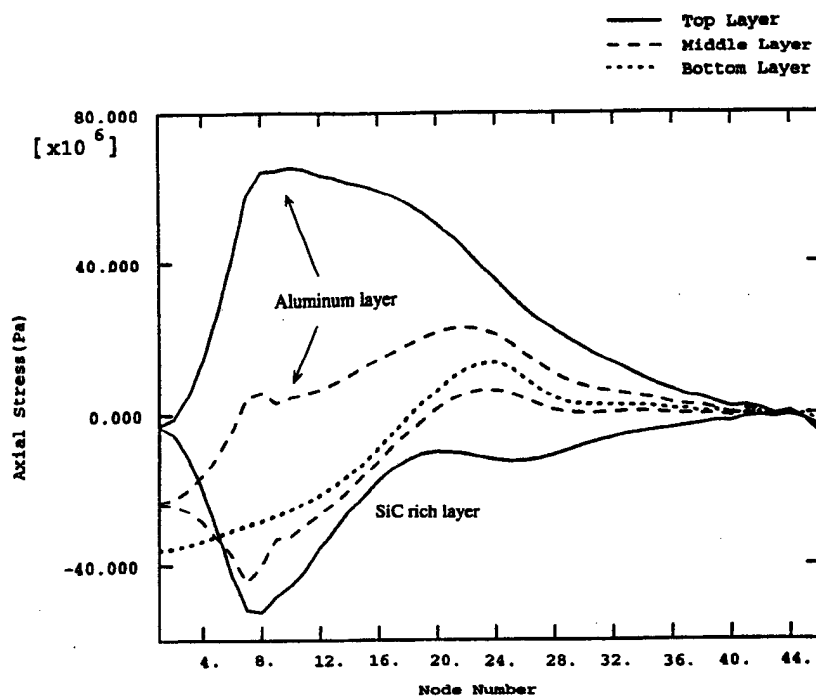
Figure 3.12. The macro-axial stress along the top, middle, and bottom layers in the spray deposited material.
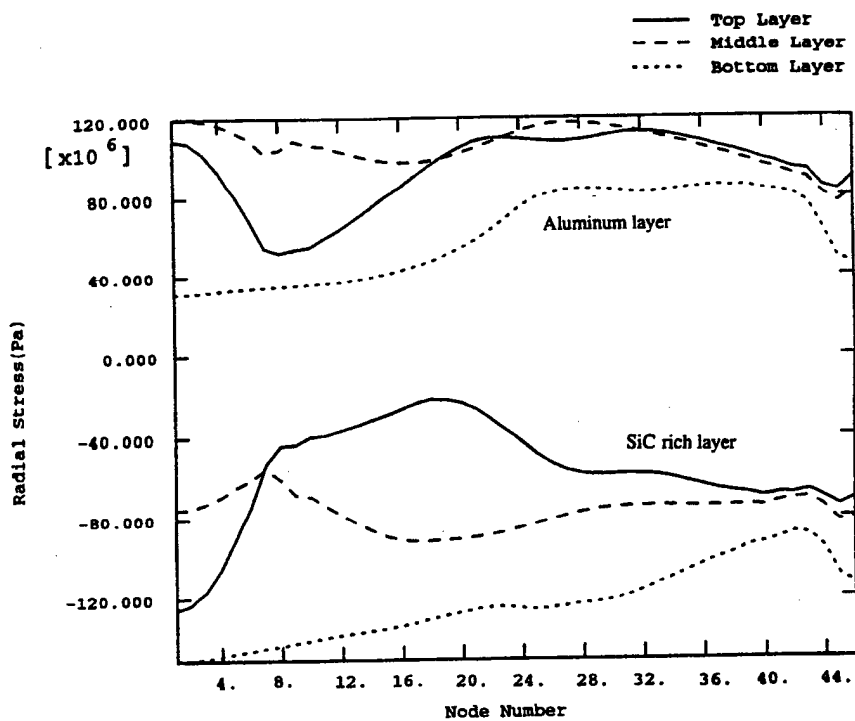
Figure 3.13. The macro-radial stress along the top, middle, and bottom layers in the spray deposited material.
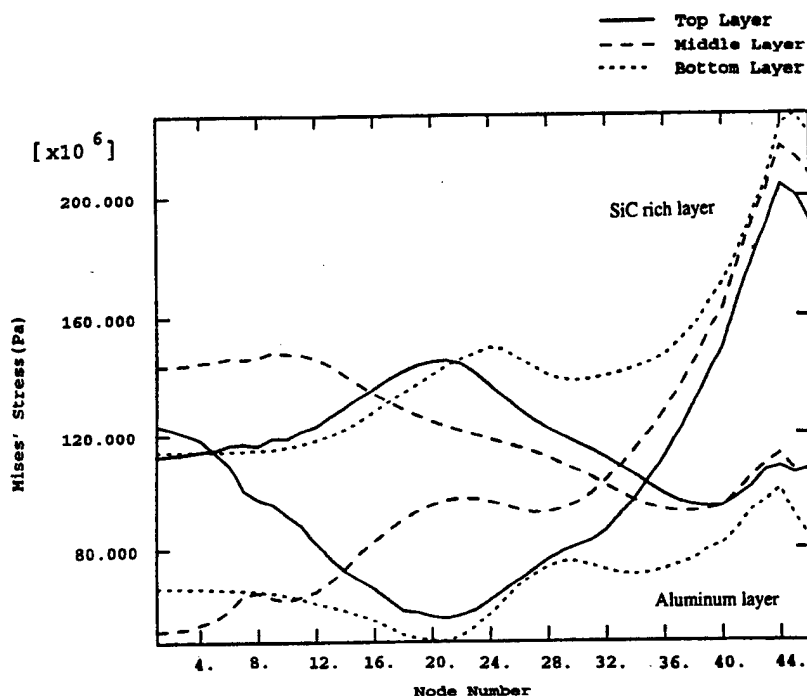
Figure 3.14.   The macro-von Mises' stress along the top, middle, and bottom layers in the spray deposited material.

Numerically calculated micro-residual stresses using the finite element analysis in the composite layers along the three directions as indicated in Figure 3.6 (b) are shown in Figures 3.15, 3.16, and 3.17.   The micro-radial stress is found to be compressive in the entire SiC particulate and have the average value of 260 MPa. It is also found that the aluminum matrix in the vicinity of the SiC particulate exhibits compressive micro-radial stress and this compressive micro-radial stress becomes tensile for the aluminum matrix farther away from the SiC particulate. The SiC particulate exhibits compressive micro-hoop stress, whereas the aluminum matrix exhibits tensile micro-hoop stress as shown in Figure 3.16. The results obtained in the present study are consistent with those from other investigators. For example, Suery et al. [133] calculated the thermal micro-residual stresses in 15 vol.% SiC particulate-reinforced 1100Al matrix composite. In their study, the SiC particulate had a diameter of 15 μm. They found that the radial stress is compressive in the particulate and the matrix. The micro-radial stress of -55 MPa was found in the matrix at the interface between the particulate and the matrix when the composite cooled down from 933 to 293 K. The micro-stress component in the circumferential direction was found to be positive. In a similar study, Smith et al. [134] investigated the micro-residual stresses in 20 vol.% SiC particulate-reinforced 1100Al matrix composite using X-ray diffraction and finite element analysis. The SiC particulate diameter in their study was 0.5 μm. They found that the SiC

particulate has a compressive micro-radial stress of 222 MPa when the composite is annealed at 800 K for 12 hours and furnace cooled.

The aforementioned behaviors of micro-radial and hoop stresses in the SiC particulate and the aluminum matrix can be explained by the fact that the aluminum matrix shrinks in all directions relative to the SiC particulate, when the composite experiences a temperature decrease. Thus, relative to its stress-free state, the aluminum matrix must stretch in order to maintain continuity with the SiC particulate. As a result, the SiC particulate experiences a compressive micro-stress state in the radial and the circumferential directions, and the aluminum matrix experiences a compressive micro-stress state in the radial direction and a tensile micro-stress state in the circumferential direction. Figure 3.17 reveals that the micro-von Mises' stress has the highest value at the interface between the SiC particulate and the aluminum matrix and it decreases as the distance from the interface increases. It is also found that the micro-von Mises' stress decreases significantly in the regions where the thickness of aluminum matrix surrounding the SiC particulate is large.
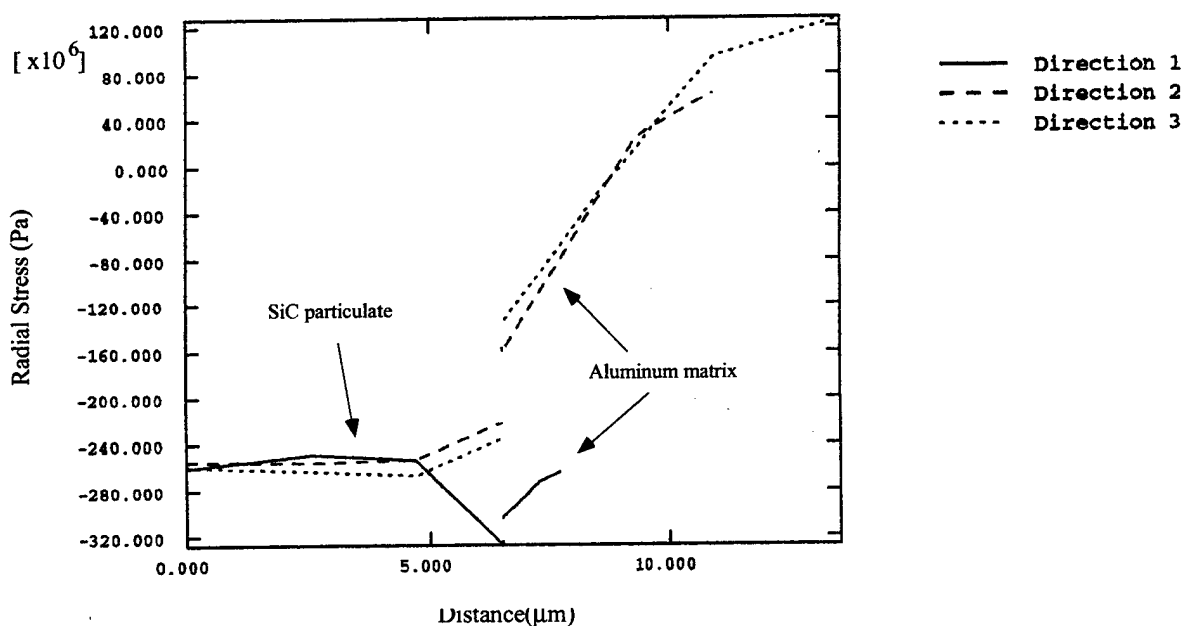
Figure 3.15. The micro-radial stress in the SiC particulate and the aluminum matrix along the three directions.
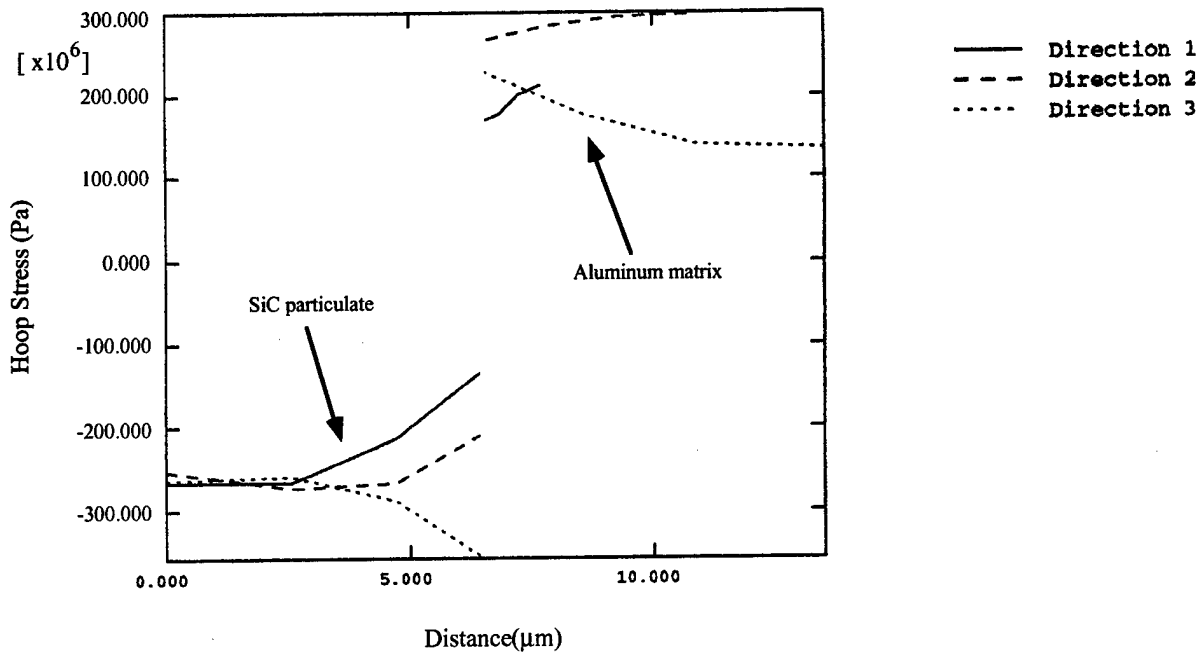
Figure 3.16.   The micro-hoop stress in the SiC particulate and the aluminum matrix along the three directions.
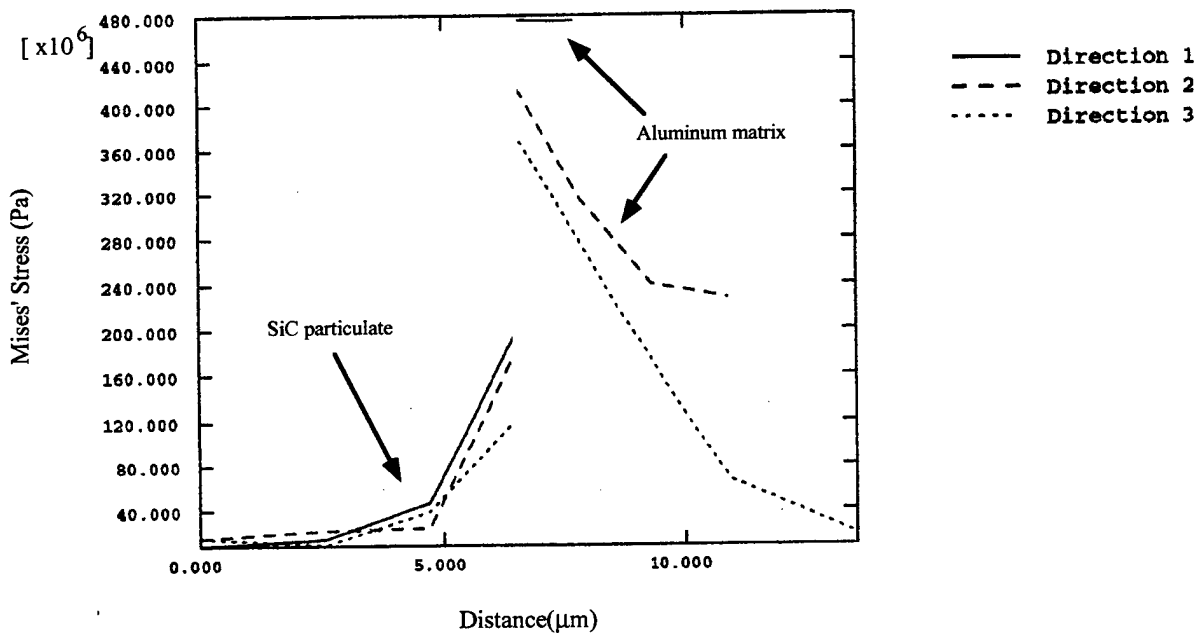
Figure 3.17.   The micro-von Mises' stress in the SiC particulate and the aluminum matrix along the three directions.

IV. SPRAY FORMING AND CO-INJECTION OF PARTICULATE REINFORCED TiAl/TiB$_2$ COMPOSITES

4.1 EXPERIMENTAL

4.1.1. Materials

The intermetallic matrix used in the present study was Ti-47 at.%Al (referred to as Ti-47Al hereafter); the chemical composition is summarized in Table 4.1. The reinforcement phase was commercially pure (99.5%) TiB$_2$ powders purchased from CERAC Inc. (Milwaukee, WI). The powder sizes are smaller than 45 μm, with typical values equal to 10 μm or less.

Table 4.1. Chemical composition of Ti-47 at.%Al ingot

Element	Ti (at. %)	Al (at. %)	C (wt. %)	N (wt. %)	O (wt. %)	H (wt. %)
As-cast	Bal.	46.86	100 ppm	24 ppm	480 ppm	26 ppm

4.1.2. Spray Forming and Co-Injection

The induction skull melting/spray forming and co-injection facility utilized for the synthesis of TiAl/TiB$_2$ composites in the present study is schematically shown in Figure 4.1. The experimental procedure may be briefly described as follows. The skull crucible is first charged with as-received Ti-47Al alloy. The cooling system in the skull crucible assures the formation of a layer of Ti-Al skull on the inside wall of the crucible when the molten Ti-47Al alloy contacts the cold crucible wall. The formation of the Ti-Al skull prevents the reaction between the chemically reactive molten Ti-47Al and the crucible. Once the central part of the charge was completely melted, the skull crucible was tilted down, and molten Ti-47Al was poured into a synchronously heated tundish (1973 °K, or 1700 °C). The molten Ti-47Al was then delivered through a nozzle and was atomized into a dispersion of micro-sized droplets. Following atomization, as the partially solidified Ti-47Al droplets traveled towards the water cooled substrate under the combined forces of gravity and fluid drag, two delivery tubes, which were symmetrically positioned on a plane across the spray cone (see Figure 4.1) with the central line of the spray cone being the symmetrical axis and the apex angle equals approximately to 110 °, injected TiB$_2$ particles at a pressure of 345 kPa into the spray cone (see Figure 4.1). At the end of spray atomization and deposition, a highly dense TiAl/TiB$_2$ composite preform, which exhibits a Gaussian profile with a maximum thickness of approximately 10 mm and a bottom diameter of about 10 cm, was obtained on the substrate. Simultaneously,

some powders, which will be referred to as oversprayed powders, are carried by the gas flow into the cyclone and collected in the container attached to the cyclone. To prevent extensive oxidation of the materials during processing, all experiments were conducted in an environmental chamber, which was evacuated down to a pressure of 66 Pa (0.5 torr) and back filled with argon gas to a pressure of 1×10^5 Pa prior to melting and atomization. A summary of the relevant processing parameters is provided in Table 4.2.
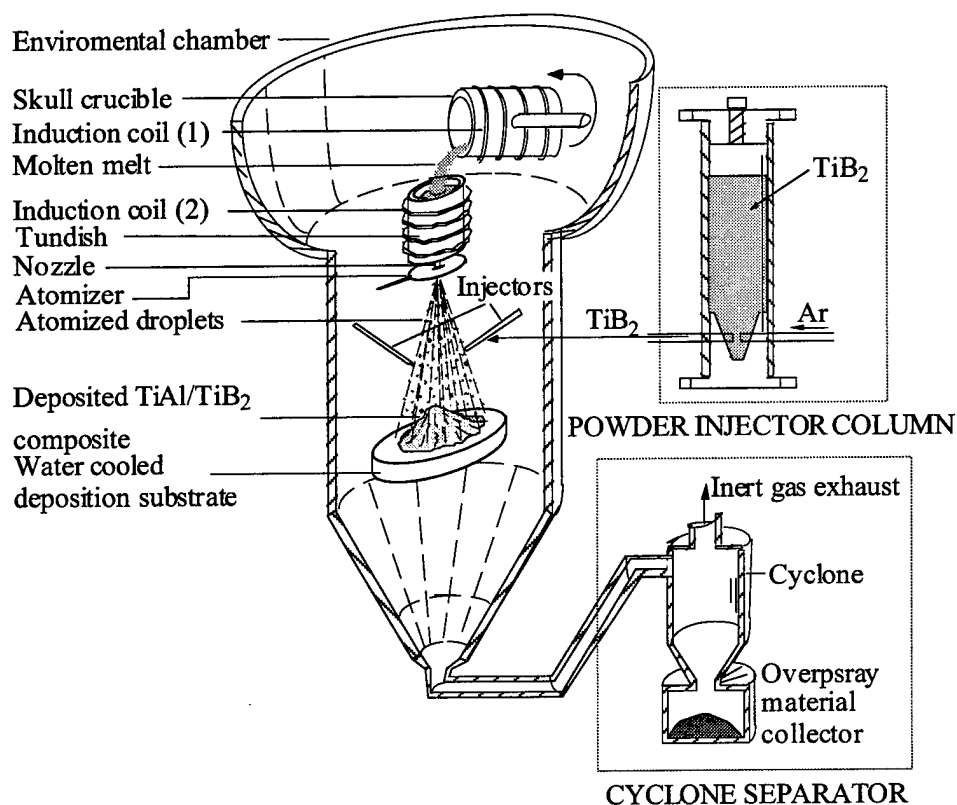
Figure 4.1.   Schematic representation of the induction skull melting/spray forming and co-injection facility.

4.1.3. Characterization

Spray formed bulk $TiAl/TiB_2$ composite was subjected to optical observation and X-ray diffraction analysis. Optical observation was carried out both for etched (grain structures) and unetched (reinforcement phase distributions) coupons of spray formed $TiAl/TiB_2$ composite prepared using standard metallographical procedures. The etchant used was Kroll's reagent with the following composition: 1 part HF, 2 parts HNO_3 and 50 parts H_2O. The microstructural characteristics and the volume fraction of TiB_2 were examined quantitatively using an ImageSet image analysis system developed by Dapple Systems Incorporated (Sunnyvale, CA). X-ray

diffraction was conducted on a SIEMENS D5000 diffractometer, using $CuK_{\alpha 1}$ radiation with a wavelength of $\lambda = 1.5406$ Å.

Table 4.2. Primary processing parameters used in spray forming and co-injection of TiAl/TiB$_2$ composite.

Variable	Value
Injection pressure (kPa)	345
Atomization pressure (MPa)	1.38
Atomization gas	Argon
Co-injection gas	Argon
Mass flow rate of atomization gas (kg/sec)	2.37×10^{-2}
Mass flow rate of co-injection gas (kg/sec)	1.57×10^{-3}
Substrate to atomizer distance (m)	0.35
Injector exit to atomizer distance (m)	0.11
Co-injection angle	55°
Tundish temperature (K)	1973
Metal delivery tube diameter (m)	4.394×10^{-3}

Oversprayed TiAl/TiB$_2$ composite powders were subjected to size distribution analysis, and microstructural analysis (both scanning electron microscopic and optical). The size distribution was established from sieving experiments in accordance with ASTM Standard B:214 and MPIF Standard 5. In order to study the effect of powder size on the microstructure characteristics, the oversprayed powders were sieved into groups of the various size ranges (refer to Table 4.3) and metallographically mounted. SEM analysis was carried out on a XL-30FEG Philips scanning electron microscopy.

4.2. Results

4.2.1. Phase Composition

Figure 4.2 shows the X-ray diffraction pattern on the spray formed and co-injected TiAl/TiB$_2$ composite. It consists of α_2 (hcp) Ti$_3$Al, γ (fcc) TiAl and TiB$_2$ phases. The Ti-Al phases, α_2 and γ, constitute the lamellar structure, as will be shown in section 3.1.3. On the basis of the detection limit of the X-ray diffraction analysis, no other phases were observed.

4.2.2. Distribution of TiB_2 in the Deposit

Optical observation of the unetched and metallographically polished specimens reveals that there is a thin layer (approximately 1.5 mm) on the bottom of the deposit which is almost free of TiB_2 reinforcement particulate. Excluding this thin layer, the distribution of TiB_2 in the deposit is roughly uniform, with the volume fraction of reinforced TiB_2 particulate determined by the Image analysis to be approximately 35 vol. %. Figure 4.3 shows the transient region from the TiB_2 free layer to TiB_2 reinforced area.

Table 4.3.   Penetration of particle in TiAl powders as a function of droplet size

Powder size range (μm)	Average powder size (μm)	Total powders examined	Particle penetrated powders	Percentage of particle penetrated powders (%)
-38	19	539	83	15.4
38-45	41.5	475	117	24.6
45-53	49	352	121	34.4
53-63	58	520	209	40.2
63-75	69	505	231	45.7
75-90	82.5	532	265	49.8
90-106	98	450	302	67.1
106-125	115.5	434	300	69.1
125-150	137.5	431	325	75.4
150-180	165	589	439	75.5
180-250	215	320	282	88.1
250-300	275	495	397	80.2
300-425	362.5	302	251	83.1
425-600	512.5	92	75	81.5

The characteristics of the TiB_2 distribution in the reinforced region are evident in Figures 4.4(a), (b) and (c). One of the characteristics is the preferential distribution of TiB_2 particles along the directio parallel to the substrate surface, resulting a layered like structure in the deposit (Figures 4.4(a) and (b) As will be discussed later, this may be associated with the preferential deformation of the spherica droplets along the direction perpendicular to the substrate surface upon their arrival onto the top surface of the deposit, and the aggregation of the ceramic particles on the exterior region of the droplets. Anothe characteristic is the presence of nearly spherical prior droplet boundaries delineated out by the cerami particles (Figures 4.4(a) and (c)), which provides direct support for rationalizing the distribution of TiB

in the deposit on the basis of the TiB_2 distribution in the droplets or oversprayed powders.
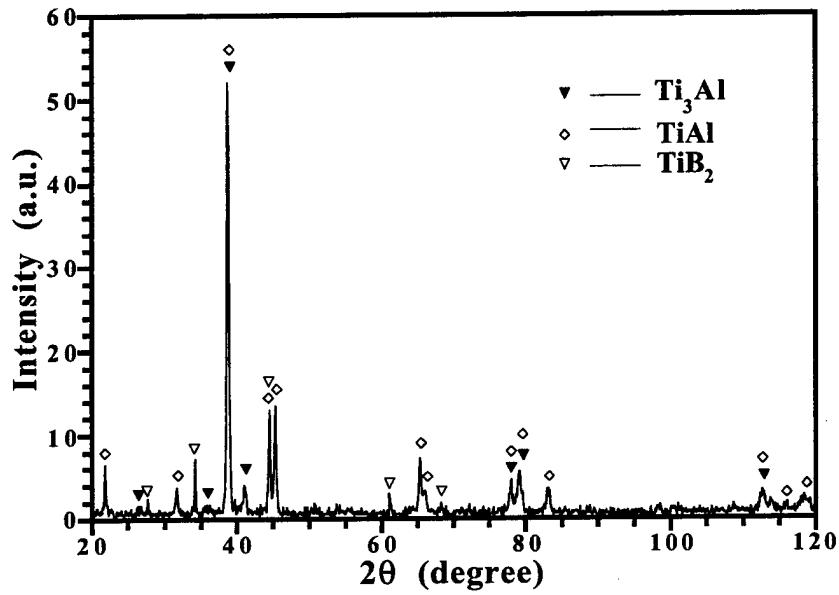
Figure 4.2.   X-ray diffraction patterns of the spray formed $TiAl/TiB_2$ composite bulk material.
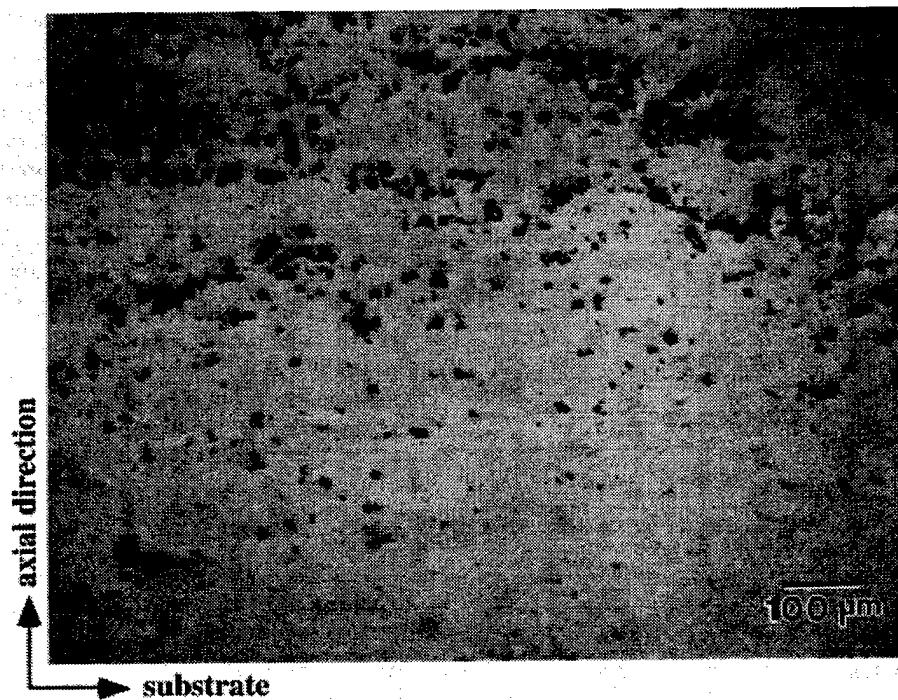
Figure 4.3.   The unenforced/reinforced transient region in the spray formed $TiAl/TiB_2$ composite bulk materials.
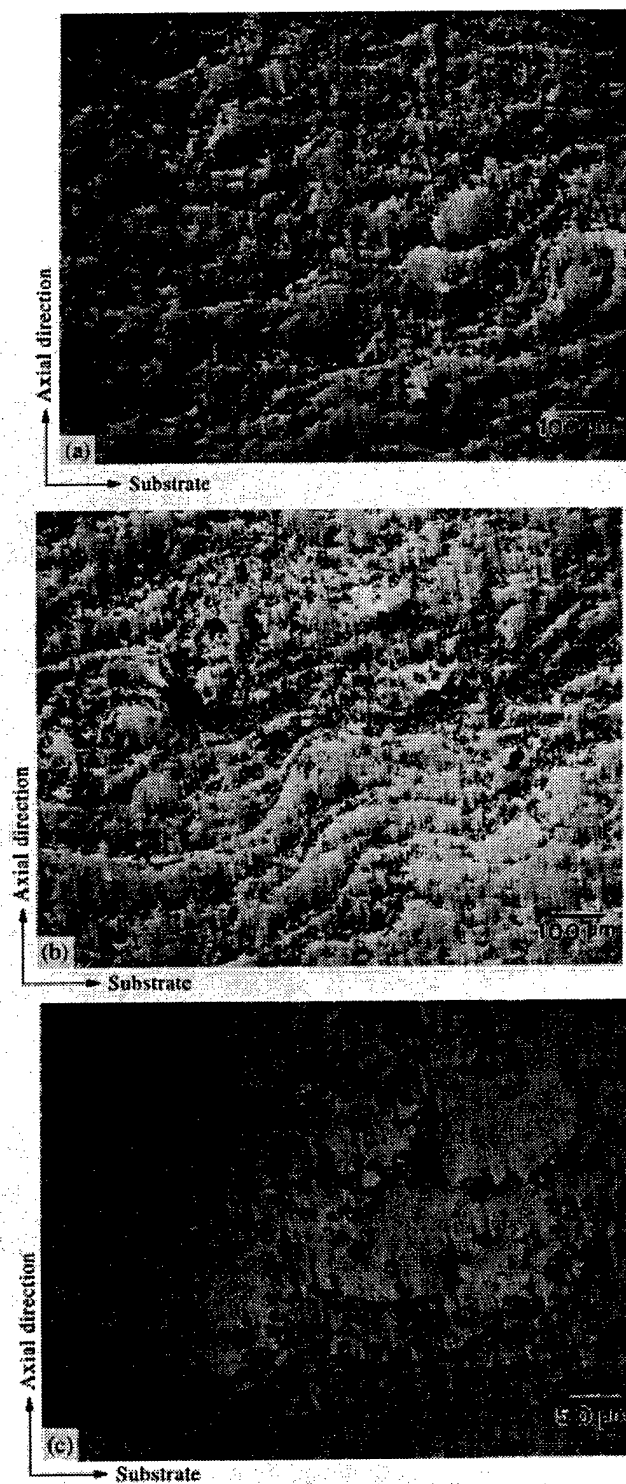
Figure 4.4.   Distribution of TiB$_2$ particles in the reinforced region of spray formed TiAl/TiB$_2$ composite bulk materials: (a). layered structure and spherical prior droplet boundaries; (b). layered structure; (c). spherical prior droplet boundaries in (a) at higher magnification.

The porosity percentage in the spray formed composite is also evaluated from the metallographically polished/unetched specimens, with determined value of approximately 0.47 %. This is highly dense compared with the TiAl based particulate reinforced composites fabricated by other techniques, such as combustion reaction synthesis (~30% of pores) [135].

4.2.3. Microstructure Characteristics

Figure 4.5(a) shows the microstructure of spray formed TiAl/TiB$_2$ bulk materials. The microstructure of the spray formed composite is characterized by fine grained equiaxed fully lamellar structures, with an average linear grain size of approximately 40 µm. For comparison purposes, the microstructure of the TiB$_2$ free thin layer was also shown in Figure 4.5(b). It is evident from Figure 4.5(b) that the characteristic microstructure is still equiaxed fully lamellar structure. However, the grain size was coarser (~160 µm) relative to that of the TiB$_2$ reinforced region.

4.2.4. Oversprayed Powders

Oversprayed powders are those atomized/co-injected droplets which were not collected into the deposit. Since the spray forming and co-injection inherently involves interaction/penetration between the reinforcement particulates and the atomized droplets, distribution of TiB$_2$ in the oversprayed powders and the size distribution of the oversprayed powders are of great significance in providing insight into the understanding of the fundamental mechanisms for incorporation of reinforcement particulate into the metallic/intermetallic matrix during spray forming and co-injection.

4.2.5. Distribution of TiB$_2$ Particulate in the Powders

The distribution of TiB$_2$ in the oversprayed powder may be categorized into three distinct cases, as revealed in Figure 4.6: i). powders free of TiB$_2$, ii). powders with exterior penetrated by TiB$_2$ and the interior free of TiB$_2$; and iii). powders with TiB$_2$ uniformly distributed in the exterior and interior of the droplets. From a practical point of view, the first case should be avoided since it does not contribute to the incorporation of TiB$_2$ particulates into the metallic matrix. The second case does contribute to the incorporation of reinforcement into the matrix. However, the segregation of reinforcement particulates to the exterior region of the powders (or the droplets prior to complete solidification) leads to segregation of the reinforcement particulates in the spray formed composite. The third situation is highly preferred, since it contributes to the incorporation of particulate reinforcement, and also enables the homogeneous distribution of the particulates in the deposit. In order to investigate the effect of powder size on the presence of these three cases, the

powders were sieved into groups of various size ranges and optically examined. The presence of the first case (i.e., powders devoid of TiB_2) decreases with increasing powder size range, as demonstrated in Table 4.3 and Figure 4.7. Moreover, it is evident from Figure 4.7, as the powder size range increases to 125-150 μm (average 135.5 μm), the presence of TiB_2 free powders level off at approximately 15%, instead of 0%. This may be associated with the presence of the TiB_2 free thin layer in the deposit, which suggests that approximately 15% of the powders traveled across the injection point before the co-injector start injecting TiB_2 particles. It is anticipated that, as the spray forming time increases, the time fraction of the injection delay will be greatly decreased, and the limiting fraction of TiB_2 free powder will approach 0%. Table 4.3 and Figure 4.7 also indicate that the combined probability of presence of cases 2 and 3 increases with increasing size ranges. It is somewhat difficult, however, to separate quantitatively the effect of the powder size on the presence of case 2 from that of case 3. Qualitatively, there is no other distinctive general trend observed except that case 3 is much more frequently observed in all size ranges studied.

TEM observation reveals the adherence of particulates on the surface of the powders, as shown in Figure 4.8(a). Powders with surfaces free of ceramic particles were also observed (see Figure 4.8(b)). Consistent with the optical observations, as the powder size decreases, the presence of powders with TiB_2 adhered to its surface decreases.

4.2.6. Powder Size Distribution

The size distribution characteristics of the $TiAl/TiB_2$ composite powders, along with the characteristic powder sizes d_{16}, d_{50}, and d_{84}, are important input parameters in the numerical analysis of the solidification and particulate penetration behavior of the atomized spray of micron-size droplets. These parameters were conventionally obtained from sieving experiments on the oversprayed powders. The sieving data of the oversprayed powders in the present study are summarized in Table 4.4. Interpretation of the experimental sieving data is complicated by the presence of the fine unreinforced TiB_2 particles in the oversprayed materials, since in this case the cumulative weight undersize is the sum of two terms: cumulative weight undersize of $TiAl/TiB_2$ composite powders and cumulative weight undersize of unreinforced TiB_2 particles. It is worth noting, however, that the diameter of the as-received TiB_2 particles is exclusively less than 45 μm. In order to obtain insight into the size distribution of the $TiAl/TiB_2$ composite powders, two limiting cases were considered herein: i). all of the oversprayed powders with size less than 45 μm are TiB_2; and ii). all of the oversprayed powders with size less than 45 μm are $TiAl/TiB_2$, with no unreinforced TiB_2 powders present. Accordingly, the experimental sieving data in Table 4.4 were modified on the basis of these two assumptions; and the results were summarized in Table 4.4 and graphically presented in Figure 4.9. As evident from Figure 4.9, the powder size distributions for

these two cases obey log-normal distribution statistics. The real size distribution of the $TiAl/TiB_2$ composite powders should fall between these two limiting cases, and hence also obeys log-normal distribution. In the present study, the characteristic powders sizes for these two limiting cases were determined, and the average characteristic sizes, which are 54, 130, and 333 μm for d_{16}, d_{50}, and d_{84}, respectively, were assigned to the real size distribution of the $TiAl/TiB_2$ composite. The corresponding real size distribution (log-normal) is provided in Figure 4.9.
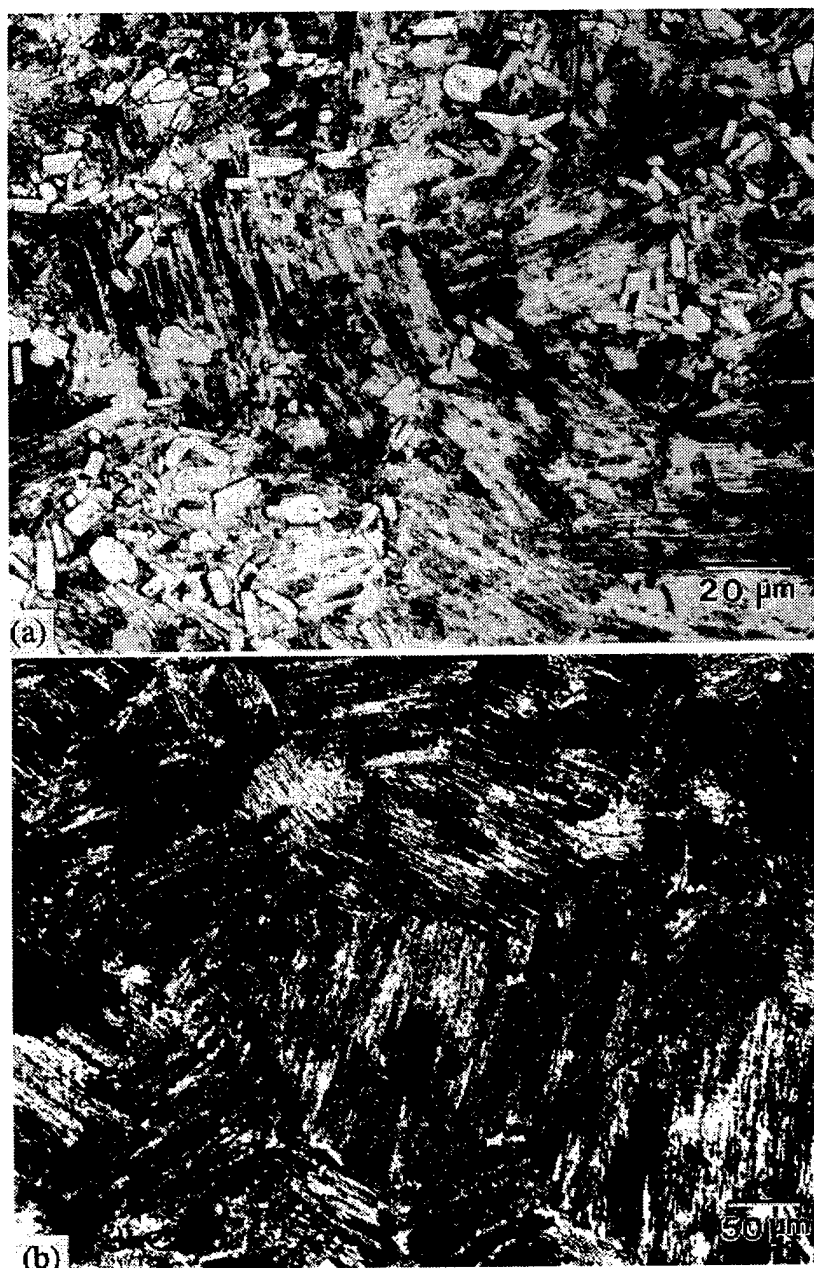
Figure 4.5.　Microstructure of the spray formed $TiAl/TiB_2$ composite bulk material: (a) reinforced region; (b) unreinforced region.
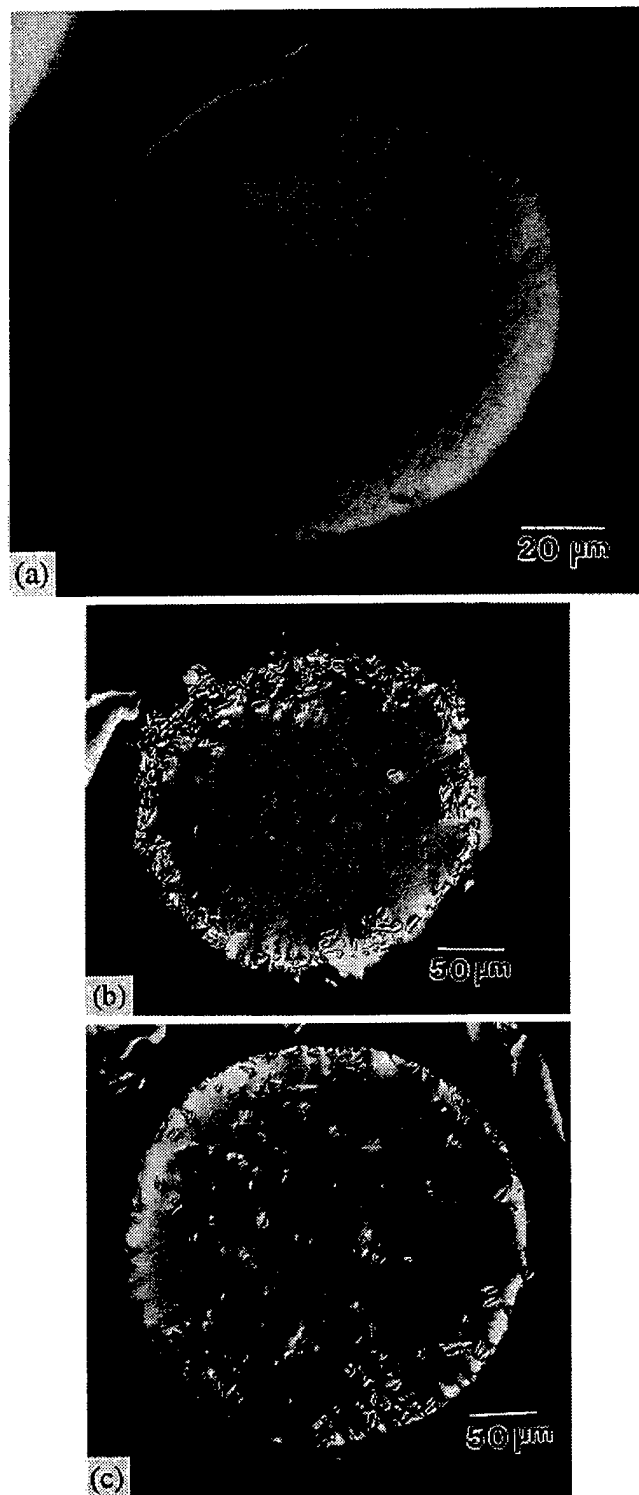
Figure 4.6.   Distribution of TiB2 particles in the oversprayed TiAl/TiB2 composite powders: (a). powder free of TiB2; (b). powder with exterior penetrated by TiB2 and the interior free of TiB2; and (c). powder with TiB2 uniformly distributed in the exterior and interior of the droplets.
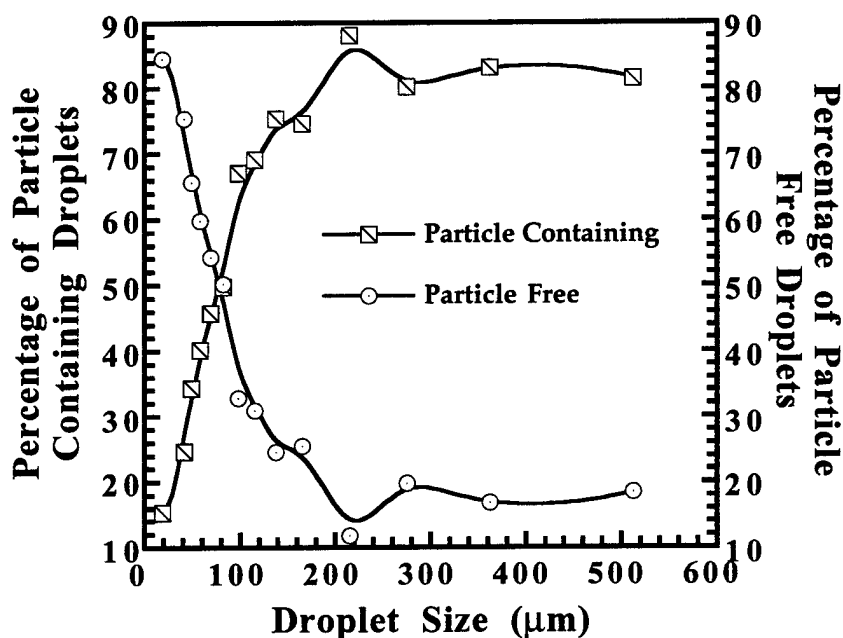
Figure 4.7.   Percentage of TiB2 reinforced/unreinforced TiAl powders as a function of the powder size.

4.3. Discussion

As mentioned earlier, compared with other processing techniques, spray forming and co-injection is potentially capable of incorporating more uniformly the reinforcement particulates into the metallic or intermetallic matrix, since it allows penetration of ceramic particulate into the micro-sized metallic/intermetallic droplets. It has been demonstrated in the previous sections that TiB2 reinforcement particulates were effectively incorporated into the TiAl matrix using the spray forming and co-injection technique. It is also evident, however, that a large proportion of TiB2 powders are segregated on the exterior region of the powders (or the prior-droplet-boundaries in the deposit). In the following sections, an effort will be made to provide insight into the fundamental mechanisms associated with the behavior of particles and droplets during spray forming and co-injection.

Spray forming and co-injection involves the momentum transfer between the atomization gas and the melt stream, which allows disintegration of the melt stream into micron size droplets; the momentum transfer between the atomization gas and the droplets, which governs the displacement of the droplets towards the bottom of the environmental chamber and the collecting substrate; the heat exchange between the atomization gas and the droplets, which enables the cooling and subsequent solidification of the droplets while they travel down the chamber; the penetration of the reinforcement particulates into the solidifying droplets; and the collection/deposition of the mixture

of solid, liquid and partially solidified droplets on the substrate [37]. The incorporation of the reinforcements into the droplets, and the deformation of the droplets upon arrival onto the top surface of the deposit, strongly depend on the velocity, temperature, and fraction of solid in the droplet. The computation of droplet velocity, temperature and fraction of solid is described in the next section.
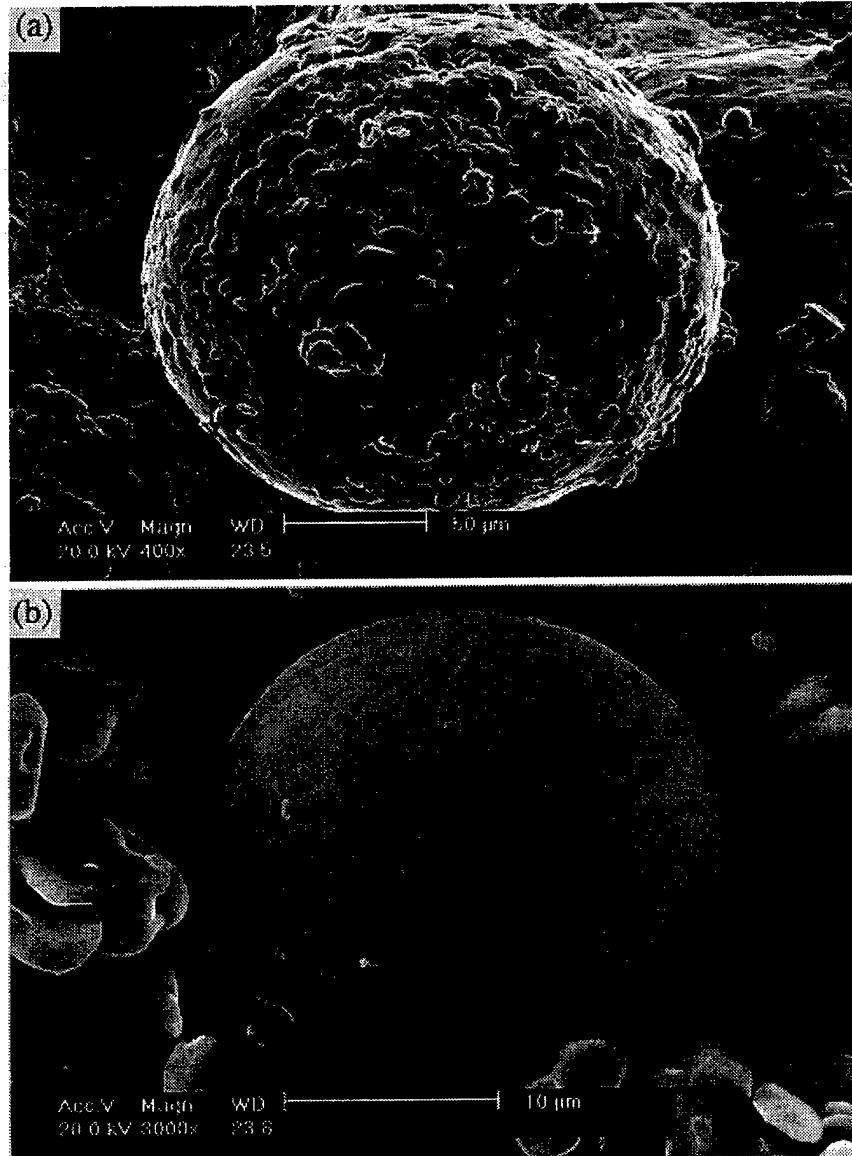
Figure 4.8.   SEM micrographs revealing: (a). adhering of TiB_2 particles on the surface of TiAl powders; (b) no adhering of TiB_2 particles on the surface of TiAl powders.

57

Table 4.4. Sieving data on oversprayed TiAl/TiB$_2$ composite +
unreinforced TiB2 powders

Powder Size (μm)	Cumulative Experimental data	Weight (g) Assuming no TiB$_2$ under 45 μm	Undersize Assuming all TiB$_2$ under 45 μm
38	12	—	—
45	28.33	—	—
53	32.86	4.53	32.86
63	41.76	13.43	41.76
75	46.61	18.28	46.61
90	53.2	24.87	53.2
106	61.34	33.01	61.34
125	70.8	42.47	70.8
150	78.78	50.45	78.78
180	87.3	58.97	87.3
250	101.22	72.89	101.22
300	108.69	80.36	108.69
425	116.83	88.5	116.83
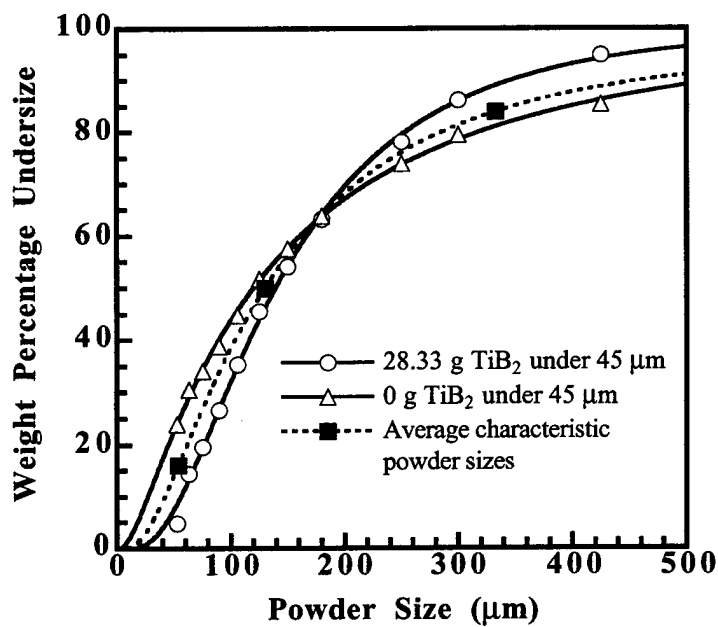
Figure 4.9.   Size distribution of oversprayed TiAl/TiB$_2$ powders.

4.3.1. Momentum Profile and Thermal History of Atomized Droplets

The governing equations for calculation of the momentum profile and the thermal history of the atomized droplets are:

$$\rho_d V_d \frac{d\upsilon_d}{dt} = V_d \rho_d g - V_d \rho_g g + (A_d/8)C_{drag}\rho_g(\upsilon_g - \upsilon_d)|\upsilon_g - \upsilon_d| \qquad (4.1)$$

for the momentum exchange between gas and the droplets, and

$$-\rho_d V_d [C_{pl}(1-f) + C_{ps}f - H_f \frac{df}{dT}]\frac{dT}{dt} = h(T - T_0)A_d + \varepsilon\sigma(T^4 - T_0^4)A_d \qquad (4.2)$$

for the heat transfer between gas and the droplets, where V_d and A_d are the volume and surface area of droplet, respectively; υ_g and υ_d are the gas and droplet velocity, respectively; C_{drag} is the drag coefficient; f is the fraction of solid in the droplets; and h is the convection heat transfer coefficient (The definition of any variables which are not described in the text may be found in the Table 4.6). The left hand side (LHS) of equation (4.1) represents the momentum changes of the droplet, and the right hand side (RHS) of equation (4.1) represents the contribution of three different driving forces, including the gravitational force (the 1st term), the buoyant force (the 2nd term), and the drag force due to the velocity difference between the droplet and the gas flow (the 3rd term). In equation (4.2), the RHS represents the heat loss from the droplet to the environment gas due to heat transfer (the 1st term) and radiation (the 2nd term), while the LHS describes the temperature changes of the droplet resulting from the heat loss. The explicit forms of equations (4.1) and (4.2), and their application to specific problems involve the evaluation of the drag coefficient (C_{drag}) and the heat transfer coefficient (h); and the detailed knowledge on the gas velocity profile, the gas properties, the solidification path/kinetics of the droplet, the related processing parameters, and the characteristic of the problem (i.e., one dimensional, two dimensional, or three dimensional), as have been studied intensively by several research groups [110-112, 136-138] Especially, the solidification path/kinetics of the droplet is further determined by the undercooling a droplet will experience, necessitating a reasonable estimate on this property. In the present study, the one dimensional momentum profile and thermal history (including calculation of the undercooling) of the atomized Ti-47Al droplets along the axial direction (i.e., from the atomizer to the substrate, see Figure 4.1) were calculated on the basis of the governing equations formulated in reference [138], with some modifications on the selection of atomization gas properties based on our most recent numerical results, as summarized in Table 4.5. The related physical parameters used in the calculations are provided in the Appendix. Droplets with five different diameters, including the three characteristic sizes (54, 130, 333 μm) and two limiting sizes normally

encountered in spray forming techniques (20 and 500 µm), were investigated. The results are summarized in Figures 4.10, 4.11, and 4.12 for the velocity profile of the atomization gas and droplets, the thermal history of the droplets, and the solidification behavior of the droplets, respectively.

Table 4.5. Physical properties of the atomization gas (Ar)

Properties	Value	Ref.
Velocity decay (m/s)	$v_{ga}(z) = \begin{cases} v_{ga}^e & z \leq 0.02m \\ v_{ga}^e \exp[-(z-0.02)/0.15] & z > 0.02m \end{cases}$	[126]
Density (kgm⁻³)	$\rho_g = \begin{cases} \rho_{g0} & z \geq 0.00422m \\ J/[\pi(1.62 \times 10^{-3} + 0.414z)^2 v_{ga}] & z < 0.00422m \end{cases}$ J —— atomization gas flow rate: 2.37×10^{-2} kgs⁻¹	—
Thermal conductivity (Wm⁻¹K⁻¹)	$k_g / k_{g0} = 0.061 + 3.9 \times 10^{-3} T_{flm}$ $\qquad -1.77 \times 10^{-6} T_{flm}^2 + 4.3 \times 10^{-10} T_{flm}^3$ T_{flm} —— gas/droplet film temperature (K): $\qquad T_{flm} = 0.42 T_0 + 0.58T$ T —— droplet temperature (K). T_0 —— gas temperature (K): $\qquad T_0 = 437 - 200\exp(-z/\alpha)$ $\qquad \alpha = 0.1$ m	[139, 140]
Viscosity (kgm⁻¹s⁻¹)	$\mu_g / \mu_{g0} = 0.1 + 3.75 \times 10^{-3} T_{flm}$ $\qquad -1.77 \times 10^{-6} T_{flm}^2 + 4.7 \times 10^{-10} T_{flm}^3$	[139, 140]

Figure 4.10 indicates that at a flight distance corresponding to the position of the injector, the 20, 5‹ 130, 333 and 500 µm droplets achieved a velocity of 269, 188, 135, 96, and 81 m/s, respectively. By th time they reach the substrate/bottom of the chamber, fine droplets (20, 54, and 130 µm) were decelerate by the atomization gas to smaller velocities, while the velocities of coarse droplets (333 and 500 µm remained at almost the same magnitudes as those at the point of injection. Figure 4.11 reveals that the 13 µm droplet has already completed cooling in the liquid state and recalescence (the sudden temperatur increase) stages, and is experiencing segregated solidification, with a temperature of 1785 K and a fractio of solid equal to 0.23. At a flight distance corresponding to the injection point, the temperatures of 33 and 500 µm droplets remain above the liquidus temperature of Ti-47Al due to slower cooling rat associated with coarser droplets; hence no solid is present in these droplets (see Figure 4.12). Compare

with the 130 μm droplet, the 54 μm droplet reached a lower temperature (~1485 K) at this poin However, due to the larger undercooling (387 K) which may be achieved by the 54 μm droplet relative t the 130 μm droplet (36 K), it is still in the stage of cooling in the liquid state, prior to recalescence; hen there is no fraction of solid in the 54 μm droplet at this point (see Figure 4.12). For the 20 μm droplet, i achievable undercooling is the largest among all of the five different droplet sizes investigated herei However, its cooling rate is also extremely high. Accordingly, at the point of injector exit, it finishe cooling in the liquid state, recalescence, segregated solidification, and peritectic solidification stage experiencing cooling in the solid sate, with the fraction of solid in it being unity (see Figure 4.12). Upo further flight to the substrate or the bottom of the chamber, the temperature of these droplets decrease further, with a corresponding increase in fraction of solid. In summary, the numerical results reveal th following: the completion of solidification for 54 and 130 μm droplets before they reach the substrate an the bottom of the chamber, respectively; and the absence of solid in the 500 μm droplet when it reaches th substrate (see Figure 4.12). The influence of the momentum and thermal profile of the droplets on th penetration of TiB$_2$ particles into the droplets will be addressed in the following sections.
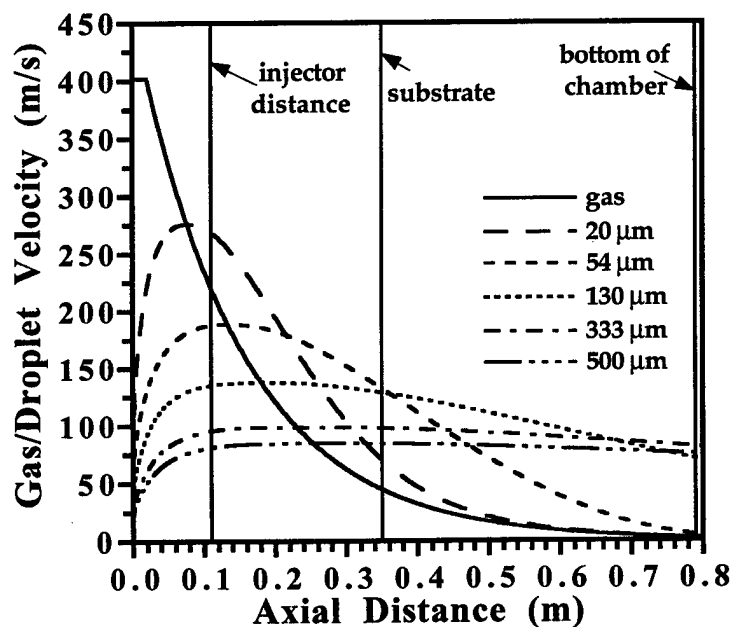
Figure 4.10. Velocity profile of the atomization gas and the spray atomized Ti-47 Al droplets.

Table 4.6. Thermophysical parameters used in the present investigation

Parameter	Description	Value	Units
ρ_d	density of Ti-47Al droplet	3200	kgm^{-3}
ρ_{g0}*	density of atomization gas (Ar)	1.654	kgm^{-3}
ρ_p	density of TiB$_2$	4560	kgm^{-3}
μ_d	viscosity of Ti-47Al droplet at liquidus	3x10^{-3}	kgm^{-1}s^{-1}
μ_{g0}*	gas viscosity (Ar)	2.125x10^{-5}	kgm^{-1}s^{-1}
k_d	thermal conductivity of droplet	56	Wm^{-1}K^{-1}
k_{g0}*	thermal conductivity of gas (Ar)	0.01634	Wm^{-1}K^{-1}
C_{pl}	specific heat of liquid Ti-47Al	825	Jkg^{-1}K^{-1}
C_{ps}	specific heat of solid Ti-47Al	723	Jkg^{-1}K^{-1}
C_{pg}	specific heat of gas (Ar)	519	Jkg^{-1}K^{-1}
T_L	liquidus temperature of Ti-47Al	1796	K
T_P	peritectic temperature of Ti-47Al	1764	K
T_I	initial temperature of the droplet	1896	K
H_f	latent heat of fusion for Ti-47Al droplet	28.4	kJmol^{-1}
γ	solid-liquid interface energy	0.185	Jm^{-2}
Ω	atomic volume of Ti-47Al droplet	2.42x10^{-5}	m^{3}mol^{-1}
R_{LS}	solid/liquid interface mobility	0.01	ms^{-1}K^{-1}
σ_m	surface tension of droplet at the liquidus	1.2	Nm^{-1}
ε	emissivity of the surface	0.5	—
υ_{ga}^e	exit velocity of atomization gas (Ar)	402	ms^{-1}
υ_{gi}^e	exit velocity of co-injection gas	31	ms^{-1}
υ_{pe}	exit velocity of injection TiB$_2$ particles	31	ms^{-1}
ω	injection angle for TiB$_2$	55	$^\circ$
g	gravitational constant	9.8	ms^{-1}
R	gas constant	8.314	JK^{-1}mol^{-1}
k	Boltzmann's constant	1.38x10^{-23}	JK^{-1}

*Properties at 298 K and atmospheric pressure.
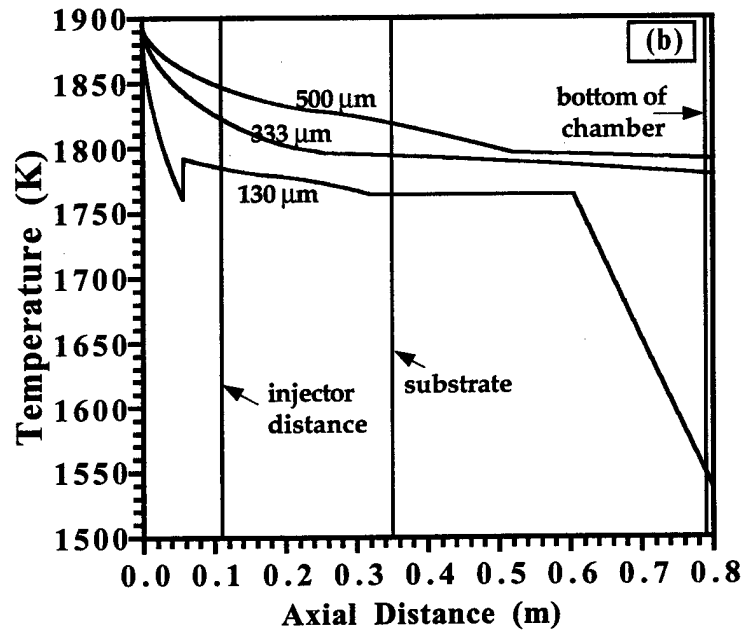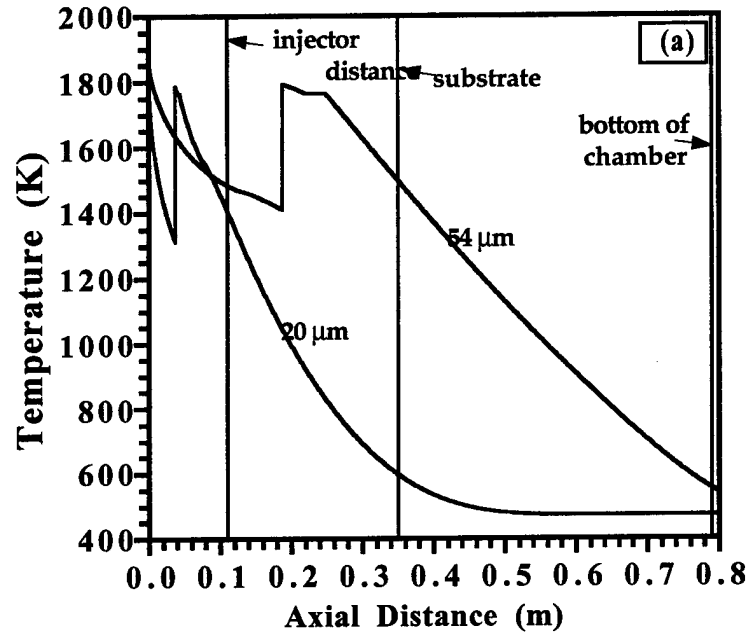
Figure 4.11. Thermal history of the spray atomized Ti-47Al droplets: (a) 20 and 45 μm; (b) 130, 333, and 500 μm.
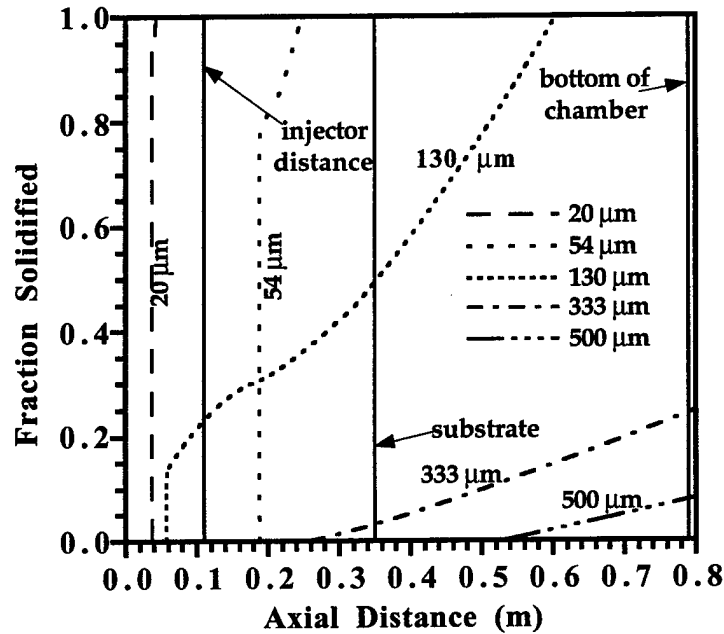
Figure 4.12.   Solidifcation behavior of the spray atomized Ti-47Al droplets;

4.3.2. Penetration into a Liquid Droplets with T=T_L

In general, penetration of a ceramic particle into a moving liquid droplet involves the competition between, and finally the balance of, the driving and the resistance forces. The origin and accordingly the explicit forms of these forces, however, depend on the direction of penetration. In the present study, the penetration of the TiB$_2$ particles in Ti-47Al droplets is divided into two terms: radial penetration and axial penetration, as schematically illustrated in Figure 4.13. These two terms will be evaluated individually in the following sections. It is worth noting that, in order to maintain the problem tractable, the geometry of the TiB$_2$ particles is assumed to be spherical in Figure 4.13 and the following sections.

Radial penetration

As described earlier, in the radial direction, the velocity of the droplet is assumed to equal to zero. Accordingly, the driving force for penetration of a ceramic particle into a liquid droplet originates from its kinetic energy (E_k) imparted by the co-injection gas, which is:

$$E_k = 0.5\rho_p V_p (\upsilon_{pe} \sin\omega)^2 \qquad (4.3)$$

where ρ_p is the density of the ceramic particle (TiB$_2$), V_p is the volume of the particle, and υ_{pe} is the velocity of the particle at the injector exit.
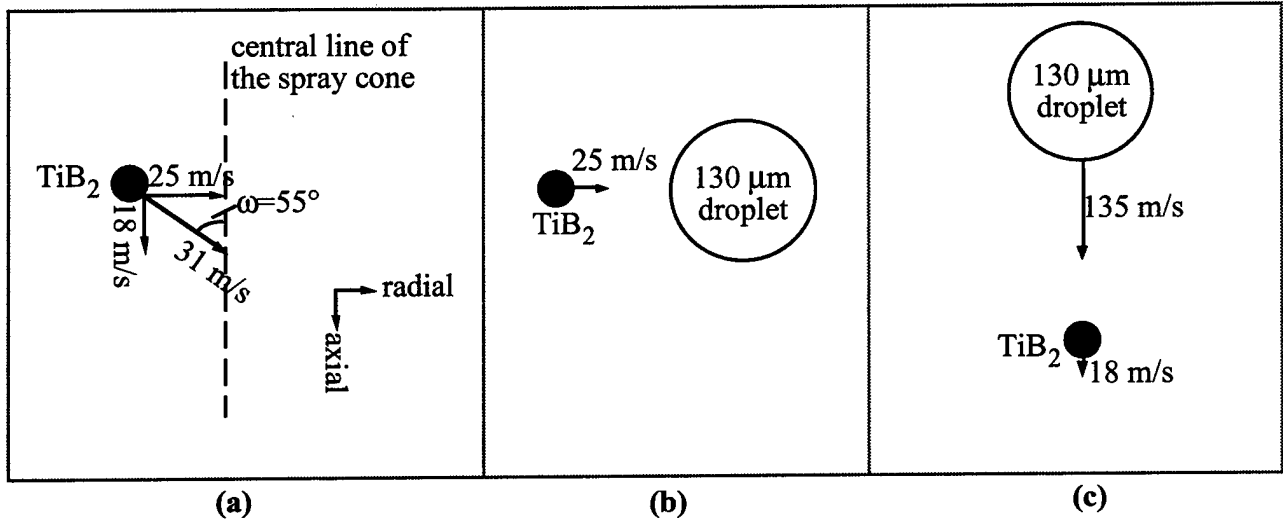
Figure 4.13. Schematic representation of the penetration direction of TiB2 particle into Ti-47Al droplets: (a) decomposition of penetration direction; (b) radial penetration; (c) axial penetration (upwards).

The resistance force for penetration are the surface energy change of the droplet caused by the interaction with the particle (ΔE_s), and the drag force exerted on the particle by the viscous melt in the droplet. The explicit forms of ΔE_s may be described as follows:

$$\Delta E_s = -A_p \sigma_m \cos\theta \qquad (4.4)$$

where A_p is the surface of the particle, σ_m is the surface tension of the liquid droplet, and θ is the wetting angle between TiB2 and Ti-47Al. Due to the unavailability of the wetting angle between TiB2 and Ti-47Al in the literature, two extreme cases will be considered here: no wetting ($\theta=180°$) and complete wetting ($\theta=0°$).

The penetration problem will be evaluated through two closely related steps in the present study. First, the kinetic energy, E_k, will be compared with the surface energy change, ΔE_s. If E_k is smaller than ΔE_s, which suggests that the kinetic energy of the particle is not large enough to circumvent the required surface energy changes, the penetration will be considered to be incomplete; and for simplicity, a penetration depth of zero will be assigned. If E_k is larger than ΔE_s, the penetration will be considered to be complete. Its further penetration into the droplet, which is defined as the penetration depth, will be determined by taking into account the drag force exerted on the particle by the viscous melt in the droplet. With the drag force exerted on it, the particle will be decelerated to be stagnant in the droplet as follows (refer to equation (4.1)):

$$\rho_p V_p \frac{d\upsilon_p}{dt} = -(A_p / 8)C_{drag}\rho_d\upsilon_p^2 \qquad (4.5)$$

where υ_p is the velocity of the particle in the droplet, and C_{drag} is the drag coefficient, which may be evaluated as [139]:

$$C_{drag} = \begin{cases} 24 / N_{Re} \dots\dots\dots 0 < N_{Re} < 1 \\ 24 / N_{Re}^{0.646} \dots\dots 1 \le N_{Re} < 400 \\ 0.5 \dots\dots\dots 400 \le N_{Re} < 3 \times 10^5 \end{cases} \qquad (4.6)$$

with the Reynolds number, $N_{Re} = D_p\rho_d|\upsilon_p - \upsilon_d|/\mu_d$, where D_p is the particle size, μ_d is the Ti-47Al melt viscosity, and υ_d is the droplet velocity. In the penetration problem, the droplet is a stagnant reference system; hence υ_d is always zero in calculation of the Reynolds number, N_{Re}.

The initial condition in solving equation (4.5) is the velocity of the particle immediately following its completion of penetration, υ_{p0}:

$$0.5\rho_p V_p\upsilon_{p0}^2 = E_k - \Delta E_s \qquad (4.7)$$

The penetration depth may be accordingly calculated as:

$$L = \int_{t=0}^{t=t_1} \upsilon_p dt \qquad (4.8)$$

where t=0 corresponds to the moment $\upsilon_p = \upsilon_{p0}$, and t_1 the moment that υ_p decays to zero.

Using equations (4.3) and (4.4), and the related thermophysical parameters provided in the Appendix, E_k, ΔE_s, and ($E_k - \Delta E_s$) were calculated as a function of the particle size, with the results summarized in Figure 4.14 for the case where θ=180°. As evident from Figure 4.14, when the particle size is smaller than 5.1 μm, ($E_k - \Delta E_s$) are negative, indicating the kinetic energy of the particle is not large enough to circumvent the surface energy change; hence penetration is incomplete. As the particle size increases beyond 5.1 μm, ($E_k - \Delta E_s$) becomes positive and increases dramatically with further increase in particle size, suggesting that penetration of liquid droplets by particles with diameter larger than 5.1 μm is completed. For particles larger than 5.1 μm, the velocity profile in the droplet and the penetration depth were calculated, with the results summarized in Figures 4.15(a) and (b), respectively. As the particle size increases the velocity decay generally decreases (see the change of the slope of the curves in Figure 4.15(a)), consistent with what equation (4.5) predicts. As the particle size increases, the initial velocity in the droplet also increases (see Figure 4.15(a)). The two factors together lead to an increase in penetration depth with increasing particle size (Figures 4.15(a) and (b)). For the other extreme case where θ=0°, the surface energy change is negative, and hence no longer plays as an resistance force.

Rather, it contributes to the driving force for penetration. Accordingly, similar to the case with $\theta=180°$, the velocity profile in the droplet and the penetration depth were calculated for particles with size ranging from 1 to 10 µm. The calculated penetration depth as a function of the particle size were provided in Figure 4.15(b). As expected, the penetration depths for this case are generally larger (~12 µm) than those obtained with $\theta=180°$.
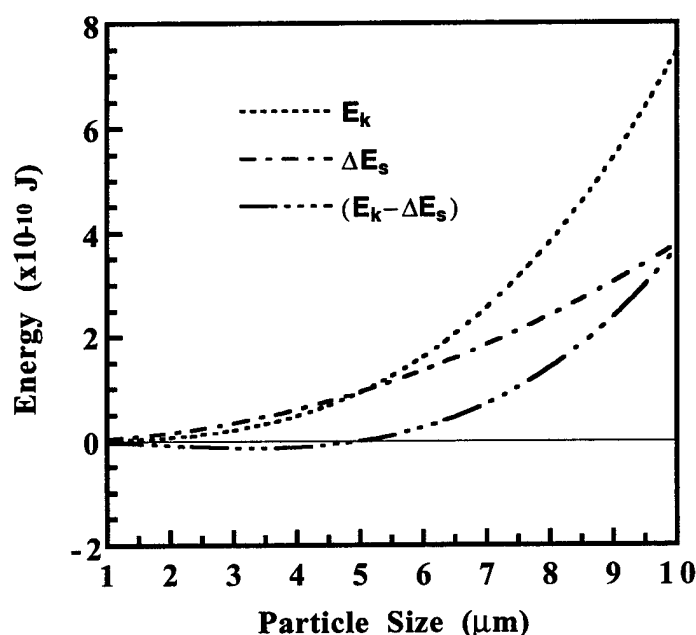
Figure 4.14.   Comparison of the kinetic energy of TiB2 in the radial directiion with the required surface energy change upon penetration when q=180°.

An important result which may be inferred from Figure 4.15 is that, if the particles are penetrating coarse droplets, such as 333 and 500 µm droplets (their radii are 166.5 and 250 µm, respectively), the particles cannot reach the center of the droplets, since the maximum penetration depth in Figure 4.15(a) is 35.6 µm for a 10 µm particles when $\theta=180°$. Accordingly, segregation of particles in the exterior region of the droplets will occur in 333 and 500 µm droplets. If the particles are penetrating fine droplets, such as 20, 54 µm droplets (the radii are 10 and 27 µm, respectively), most of the particles may reach the center of the droplets. For fine droplets, however, at the point of injector exit, they either contain significant proportion of solid in it, or are highly undercooled, with the temperature generally lower than the liquidus (see Figures 4.11 and 4.12). In an undercooled melt, the surface tension, σ_m, in equation (4.4), and the viscosity, μ_d, in equation (4.6) are expected to increase dramatically [141, 142], making the penetration of a particle into droplets much more difficult. The presence of solid in the droplet would also increase the surface tension and the viscosity [143]. Moreover, presence of solid provides an additional

resistance force for penetration: the strength of a solid. To that effect, it has been demonstrated that the penetration depth of a particle into a solid droplet is generally much less than the diameter of the particle, even though the penetration depth in the liquid droplet is more than ten times larger than the droplet diameter [67]. Although the analysis there [67] is somewhat simplified in the sense that it does not take into account the effect of temperature on the yield strength of the solid droplet, it does illustrate the difficulty encountered in penetrating a solid droplet compared with that in a liquid droplet.
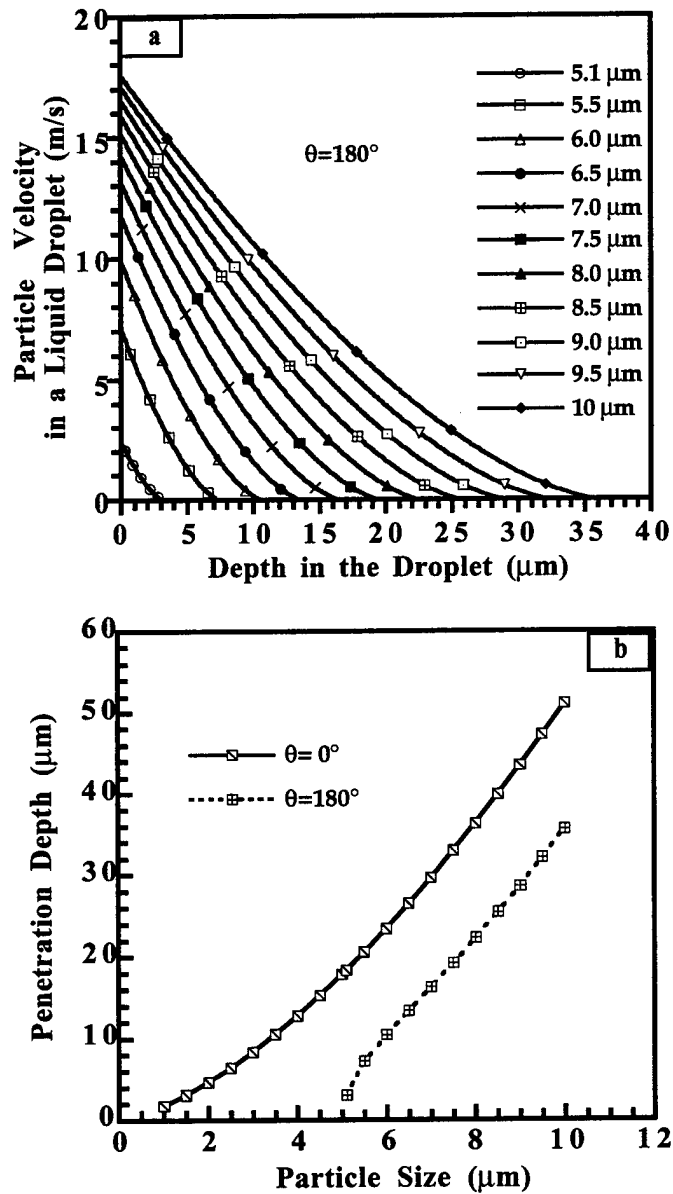
Figure 4.15.   Radial penetration: (a) TiB2 particle velocity profile in Ti-47Al droplets when θ=180°; (b) penetration depth as a function of particle size for θ=180° and θ=0°.

Axial penetration

The penetration problem in the axial direction may be addressed essentially the same way as that in the radial direction, except for some modifications on equation (4.3) and (4.5) as follows:

$$E_k = 0.5\rho_p V_p (\upsilon_{pe} \cos\omega - \upsilon_{dp})^2 \qquad (4.3a)$$

and

$$\rho_p V_p \frac{d\upsilon_p}{dt} = -(A_p / 8)C_{drag}\rho_d \upsilon_p^2 - \rho_p V_p g + \rho_d V_p g \qquad (4.5a)$$

where υ_{dp} is the velocity of the droplet at the penetration point. Equation (4.3a) incorporated the fact that the droplets are moving along the axial direction; hence the kinetic energy contributing to the driving force of the particle penetration should be evaluated using the relative velocity between the droplet and the particle in the axial direction. Equation (4.5a) incorporated the effect of the gravitational force and the buoyant force. Since the velocities of the 20~500 μm droplets are larger than the particle velocity in the axial direction at the penetration point, the penetration into all these droplets would be upwards. In this case, the gravitational force acts as a resistant force, while the buoyant force a driving force. If the particle velocity in the axial direction is larger than that of the droplet, the penetration, would be downwards. Accordingly, the role played by these two forces will be reversed relative to that described in equation (4.5a).

The calculated penetration depth values for different particles with $\theta=180°$ are summarized in Figure 4.16(a). The penetration depth in the axial direction is generally larger relative to that of radial penetration. Moreover, the penetration depth in a liquid droplet depends on the droplet size (see Figure 4.16(a)), originating from the dependence of the relative velocity between particle and the droplet on the droplet velocity in the axial direction, which in turn is a function of the droplet size. Figure 4.16(b) shows the penetration depth normalized by the droplet radius as a function of the particles size. As the droplet size increases from 20, 54 to 130 μm, the minimum particle size required for it to penetrate into the center of the droplet increases from 1.6, 3.5 to 7.3 μm. For 333 and 500 μm droplets, particles with size not exceeding 10 μm cannot reach the center of the droplets. The maximum penetration depth, which correspond to a 10 μm particle size, are 40% and 20% of the droplet radius for 333 and 500 μm droplet, respectively. The penetration depth for different particles with $\theta=0°$ were also calculated. However, since the surface energy changes are relatively small compared with the kinetic energy in the axial direction, the change of penetration depth resulting from the change of the wetting angle, θ, from 180° to 0° were found to be negligible.
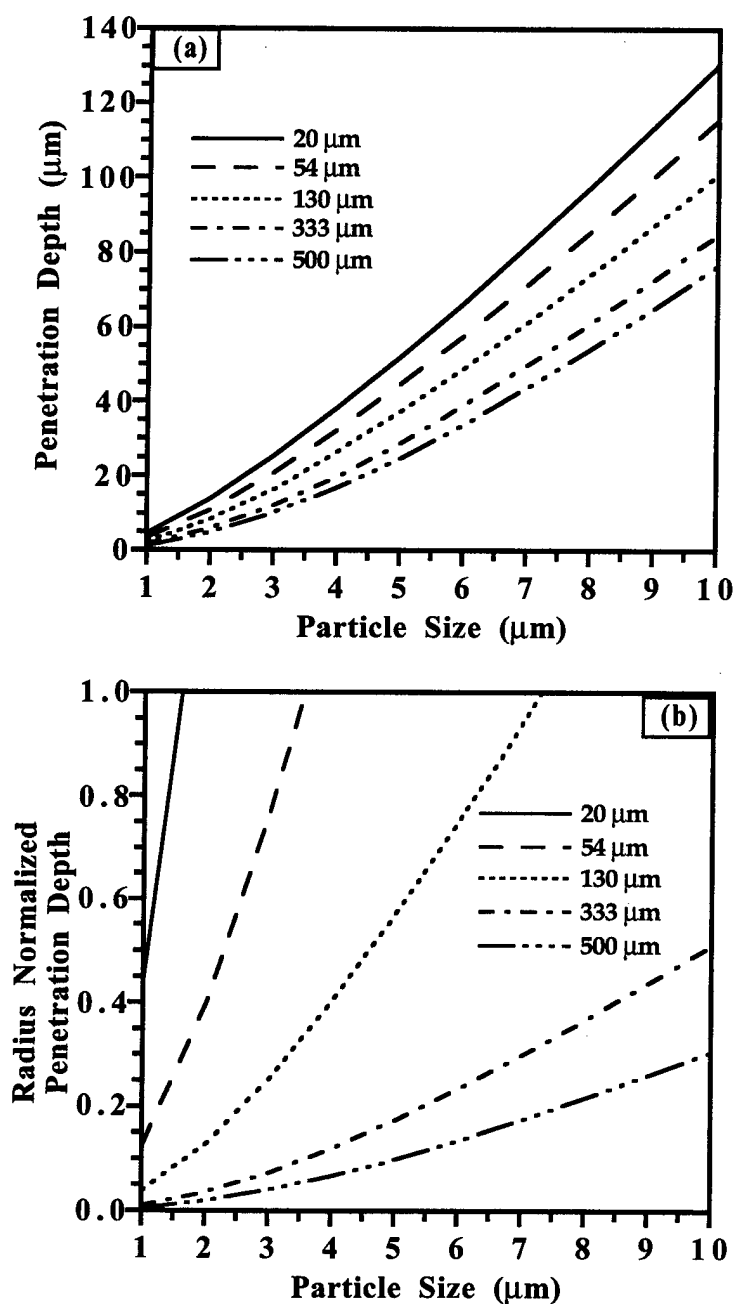
Figure 4.16. Axial penetration (θ=180°): (a) penetration depth of TiB2 particles into Ti-47Al liquid droplets; (b) comparison of the penetration depth with the radius of Ti-47Al droplets.

4.3.3. Correlation of the Numerical Results With The Experimental Observations

Figures 4.15 and 4.16, along with Figures 4.11 and 4.12, indicate that, for droplets in the

liquid state with temperatures above the liquidus (333 and 500 μm), the TiB$_2$ reinforcement particles are unable to reach the center of the droplets, since the droplets are coarse. This limits the TiB$_2$ particles to the exterior region of the droplet. This is consistent with the experimental observations that a large proportion of TiB$_2$ particles are segregated to the exterior regions of the droplets. However, the consistency of the numerical analysis with the experimental observation is limited to qualitative level in the sense that the experimentally observed segregated exterior regions in the droplets (15~20% of the droplet radius) are much less than the numerical results (~51% and 31% of the droplet radius for 333 and 500 μm droplets, respectively). Numerical prediction of the penetration behavior may be improved by extending the entire problem from one dimension to two dimensions. Two dimensional modeling of the momentum exchange and heat transfer between the droplets and the atomization gas indicated that the fraction of solid in the spray cone at any axial distance increases from the center to the edge of the cone [138], which will further limits the penetration of the particles into the center of the droplets.

The observed TiB$_2$ particle segregation in the exterior region of the droplets may be associated with the layered structure observed in the spray formed TiAl/TiB$_2$ composite bulk material. Figure 4.12 indicates that there are significant proportions of liquid phase in the 333 and 500 μm droplets when they reach the substrate. This allows significant deformation of these droplets along the direction normal to the surface of the substrate, resulting in disc like splats in the deposit [144]. Under optical microscopy, the two dimensional nature of the metallographic technique will reveal these disc like splats as plates if the cross section of the specimen under examination is parallel to the axial direction (from the atomizer to the substrate), which is the case for Figure 4.4. Furthermore, if the exterior region of the droplets are decorated with the TiB$_2$ particles, as revealed from the numerical results and the observation of the oversprayed powders, the TiB$_2$ particles will be preferentially distributed along the direction parallel to the substrate surface, leading to the formation of layered structures.

In order to improve the homogeneity of the distribution of TiB$_2$ particles in the droplet and the deposit, the following methods may be considered in the order of priority:

i). Move the injector closer to the atomizer. This adjustment enables fine particles to remain at higher temperature and contain more liquid at the penetration point, increasing the penetration depth of particles into fine droplets. As evident from Figures 4.15 and 4.16, when the fine (20, 54 and 130 μm) droplets are in liquid state with temperature above the liquidus, coarser (>5 μm) TiB$_2$ particles are able to reach the center of the droplets, improving the homogeneity of TiB$_2$ distribution in the droplet and consequently in the deposit.

ii). Increase the atomization pressure, which will increase the droplet velocity; hence increase the relative droplet/particle velocity, which in turn increases the particle penetration depth. Moreover, this adjustment will decrease the average droplet size, reducing the presence of coarse

droplets. As has been discussed above, it is more difficult for a TiB$_2$ particle to reach the center of a coarse liquid droplet than a fine liquid droplet (T=T$_L$). It is worth noting changes in atomization pressure also influence the thermal history of the droplets in a complex manner.

iii). Increase the co-injection pressure. This will increase the radial velocity of the particles; hence increase the radial penetration depth.

iv). Increase the particle size. It is evident from Figures 4.15 and 4.16 that coarser particles may penetrate deeper onto the droplets; hence increasing the particle size may increase the chance for particles to reach the center of the droplet. However, large particle size may adversely affect the mechanical behavior of the final product: the spray formed and co-injected composite.

V. SPRAY ATOMIZATION AND DEPOSITION OF TANTALUM ALLOYS

5.1. Experimental Set-Up

The present study focuses on the investigation of spray atomization and deposition of a Ta-Fe alloy with a nominal composition of 14.6 wt.% Fe. Ultimately, materials of interest will include Ta and Ta-W. However, Ta-Fe was selected as an intermediate investigation material because of its relatively low melting point and simpler phase structure (i.e. eutectic).

The alloy was first prepared using an vacuum non-consumable arc melting furnace (System VII, manufactured by Vacuum Industries, Inc.). The procedure is described as follows. Pure Ta (99.9%) and Fe (commercial purity) are weighted and placed in a water-cooled copper crucible. Then, the furnace is pumped down to 10-1 mmHg and purified Argon is backfilled up to 350 mmHg. Finally, the electric arc is activated and Ta and Fe are melted together.

Once the alloy was prepared, the spray forming phase was undertaken using an induction skull melting (ISM) spray forming facility as schematically illustrated in Figure 4.1. The ISM spray deposition facility is designed for the spray atomization and deposition of reactive alloys (e.g., Ti) and refractory metals (e.g., Ta). The experimental procedure is described as follows. First, a Ta-Fe alloy is charged in the skull melting crucible. The use of a skull melting crucible can effectively prevent the reaction between the charge and the crucible due to a skull forming on the water-cooled crucible wall once the charge is melted [145, 146]. Second, the atomization chamber is evacuated down to 0.6 torr and then backfilled with argon gas. Third, power is applied to the crucible using a 250 kW Ajax Magnethermic power supply for induction melting. Once the charge is completely melted, the molten Ta-Fe alloy is poured into a graphite tundish that is maintained at constant temperature (17000°C) using a 20 kW Inductotherm apparatus. The melt is then delivered to an atomizer that is located below the tundish, where it is disintegrated into a fine dispersion of micron-sized droplets by high velocity inert gas jet. Following atomization, the mixture of rapidly quenched, partially solidified droplets is deposited on a water-cooled copper substrate, eventually collecting as a coherent preform, the microstructure of which is largely dictated by the solidification conditions during impact. A summary of the relevant processing parameters is provided in Table 5.2.

The spray-formed Ta-Fe alloy and oversprayed powders were then subjected to microstructural observation and phase analysis using optical microscopy, X-ray diffraction and scanning electron microscopy (SEM/EDX). The metallographic samples were prepared using standardmetellographicc methods. The size of the pores present in the as-spray-formed Ta-Fe alloy was determined by using computerized image analysis. X-ray Diffraction and EDX were

used to identify the phases present in the spray formed Ta-Fe alloy. In order to allow qualitative comparisons with the numerical simulations of single droplet solidification, the oversprayed powder was collected and studied. The powder was first sieved in accordance with MPIF standard 05. Then, the powder morphology andmicrostructure were examined using optical microscopy and SEM.

Table 5.1.   Physical Properties of Tantalum [7]

Atomic Weight	180.95
Density	16.6 g/cc
Melting Point	29960 C
Boiling Point	54310 C
Coefficient of Thermal Expansion (RT)	6.5x 10-6/0 C
Electrical Resistivity	13.5/cm
Electrical Conductivity	13.9% IACS
Specific Heat	0. 140 J/g
Thermal Conductivity	0. 544 J
Crystal Structure	bcc
Thermal Neutron Cross Section	21.3b

Table 5.2.   Processing parameters

Atomization Pressure (MPa)	2.2
Atoniization Gas	Argon
Deposition Distance (mm)	254
Melt Temperature (OC)	~1750
Tundish Temperature (OC)	1700

5.2.   Numerical Formulation

At the moment of impact the thermal and solidification conditions of the droplet distribution depends, a priori, on a great number of parameters including: (a) the thermodynamic properties of the material, such as: (i)liquidus temperature, (ii) solidus temperature, (iii) melting temperature, (iv) density, (v) thermal conductivity, (vi) surface tension, (vii) heat capacity, and (viii) heat of fusion; (b) the thermodynamic properties of the gas, such as: (i) density, (ii) heat capacity, (iii) viscosity, and (iv) thermal conductivity, and (c) the processing parameters, such as: (i)atomization gas pressure, (ii) nozzle/substrate flight distance, and (iii) metal/gas flow ratio. The multiplicity of the parameters involved and the complexity of their coupling is a substantial obstacle to a physical

comprehension of this phenomenon. The numerical simulations described next constitute an effort to investigate the mechanisms controlling the deposition/solidification process and therefore to gain such a fundamental understanding.

5.2.1. Fluid Dynamics

Given the relatively high droplet impact velocity (from 20 to 70m/s) of the process studied here, this analysis focuses on the fluid dynamics aspects of the droplet behavior. Therefore, the model used here combines a Navier-Stokes solver (Ripple [147]) with a multi-directional solidification model [148] recently developed. This model is outlined below. Additional model information can be found in Refs. [149] and [147].

The equations for transient, two- dimensional, incompressible fluid flow with surface tension on free surfaces of general topology:

$$\nabla \cdot \left(\theta \overline{V} \right) = 0 \tag{5.1}$$

$$\theta \frac{\partial \overline{V}}{\partial t} + \nabla \cdot \left(\theta \overline{V} \overline{V} \right) = -\frac{\theta}{\rho} \nabla p + \frac{\theta}{\rho} \nabla \cdot \tau + \theta \overline{g} + \theta \overline{F_b} \tag{5.2}$$

are solved using a two step projection method [147]. Internal obstacles are represented using a characteristic function, 0. The position of the free surface is obtained by solution of a Volume of Fluid transport equation:

$$\frac{\partial}{\partial t} (\theta F) + \nabla \cdot \left(\theta F \overline{V} \right) = 0 \tag{5.3}$$

Surface tension effects are described using the Continuum Surface Force (CSF) approach [150].

5.2.2. Multi-Directional Solidification Model

Previous studies [149, 151] have shown that liquid-jet overflow is a possible mechanism for the formation of porosity in the near -substrate region. After impact, the liquid droplet deforms, spreads, and solidifies. Liquid-jet overflow occurs when the liquid detaches from the solidifying solid and re-attaches at a further radial location. A multi-directional model was proposed to simulate the solidification process in this case. This model is used herein. It is only outlined below, more details may be found in Ref [149].

The multi-directional solidification model is based on the application of a locally ID energy balance in the direction normal to the solid/liquid interface. Uni-directional models [42, 151, 152] only allow growth orthogonally to the substrate. The solid/fluid interfaces are tracked using

uniform- distributed markers. The algorithm allows for complex interface morphology representation as well as interface merging simulation. The markers move continuously as the solid layer grows and are not necessarily located on mesh lines. The 1-D Stefan solution is used locally to evaluate the growth rate:

$$\frac{\partial S}{\partial t} = \frac{2\lambda^2 \alpha_s}{S} \tag{5.4}$$

where the solidification constant, A, is obtained from the heat balance at the interface:

$$\lambda = \frac{1}{\sqrt{\pi}} \left\{ \frac{Ste_s}{erf[\lambda]\exp(\lambda^2)} - \frac{Ste_s\sqrt{\alpha_l/\alpha_s}}{erf[\lambda\sqrt{\alpha_s/\alpha_l}]\exp(\lambda^2 \alpha_s/\alpha_l)} \right\} \tag{5.5}$$

where Stes, and Stel are the solid and liquid Stefan numbers.

The Lagrangian/Eulerian character of the solid front tracking algorithm introduces an inherent bias resulting from the conversion of the marker data to a solid fraction field. Furthermore, because of the Eulerian nature of the free surface tracking algorithm used here some numerical smearing of the interface is unavoidable. The resulting mass conservation discrepancy has been shown to be typically below 10%.

5.2.3. Droplet Dynamics

The model described above requires the knowledge of the droplet velocity and size at impact. For a given size, velocity can be estimated using a simplified Lagrangian droplet dynamics equation. It is assumed that the spray is sufficiently dilute that droplets do not interact. Furthermore, the Basset history term and the lift force are neglected [126, 153]

$$\frac{dv_d}{dt} = g\left(1 - \frac{\rho_g}{\rho_d}\right) + \frac{3}{4}\frac{C_D}{d}\frac{\rho_g}{\rho_d}|v_d - v_g|(v_d - v_g) \tag{5.6}$$

The gas velocity v_g is estimated using experimental data such as that of Bewlay et al. [154]. In order to evaluate the drag force in a simple manner, the droplet is assumed to be spherical and to have a constant size. CD is then assumed to be a function of the Reynolds number only, it is evaluated using an improved approximation [153] of the standard drag curve. This equation is solved using a Runge-Kutta-Fehlberg algorithm.

5.3. Results and Discussion

5.3.1. Characterization of Oversprayed Powders

The atomized Ta-Fe powders exhibits a spherical morphology, which is consistent with a variety of gas atomized metal powders such as Al alloys [108] and Ni_3Al [155]. The size distribution of the oversprayed Ta-Fe powders, from a sieve experiment, is shown in Figure 5.1. The mean and median powder size (d_{10}, d_{50}), estimated from this distribution, are approximately 90 μm and 210 μm respectively. The microstructural examination revealed that the atomized powder exhibits a typical rapid solidification microstructure consisting of fine dendrites (Figure 5.2). The secondary dendrite arm spacing (SDAS) for solidified drops with a size corresponding to the mean size (90μm) is approximately 1.05 μm, which indicates a cooling rate of up to 10,5 K/s [155]. Figures 5.3(a) and 5.3(b) show the morphology of an oversprayed Ta-Fe splat.

5.3.2. Microstructure of Spray Formed Ta-Fe Alloy

The microstructures of a spray atomized and deposited Ta-Fe alloy in the lower (close to the substrate) and upper sections are significantly different. Figure 5.4(a) shows the microstructure in the upper section and no significant features can be distinguished. One possible explanation for the observed morphology is the remelting of dendrite arm fragments after impact. Pores were seldom observed in this region. On the contrary, the lower section exhibits a dendrite morphology distinctly consistent with that of the primary phase, with a fine eutectic microstructure in the inter-dendrite regions (Figure 5.4(b)). The presence of a dendrite morphology similar to that observed for oversprayed powders (Figure 5.2) indicates that the deposited materials in this region experienced rapid cooling, which is consistent with the results in numerous numerical [37, 156-158] and experimental [91, 159, 160] studies. It is worth noting, however, that secondary dendrite arms were seldom present in the lower region (Figure 5.4(b)). This may be a result of dendrite arm fragmentation, occurring during the droplet impingement on the substrate [37, 91, 155]. The Ta-Fe binary phase diagram (Figure 5.5) indicates that the two phases observed are most likely to be the primary FeTa and the Ta-Fe eutectic phase. This is confirmed by X-ray diffraction and EDX analysis. The X-ray diffraction spectrum (Figure 5.6) shows that at least four phases are present in the spray formed Ta-Fe alloy. They are Ta, μ-phase (TaFe), tantalum carbide (Ta_2C) and iron carbide (Fe-C). The presence of tantalum carbide and iron carbide is probably due to the use of graphite tundish. Furthermore, EDX analysis demonstrated that the approximate composition of the dendrite phase is 77wt.%Ta and 23wt.% Fe which falls in the range of p-phase composition, 21-24wt.% Fe (Figure 5.5). A few pores were observed in the cross section of the spray formed Ta-Fe alloy. The pore size ranges from 3 to 115 μm, with a mean at 40 μm.
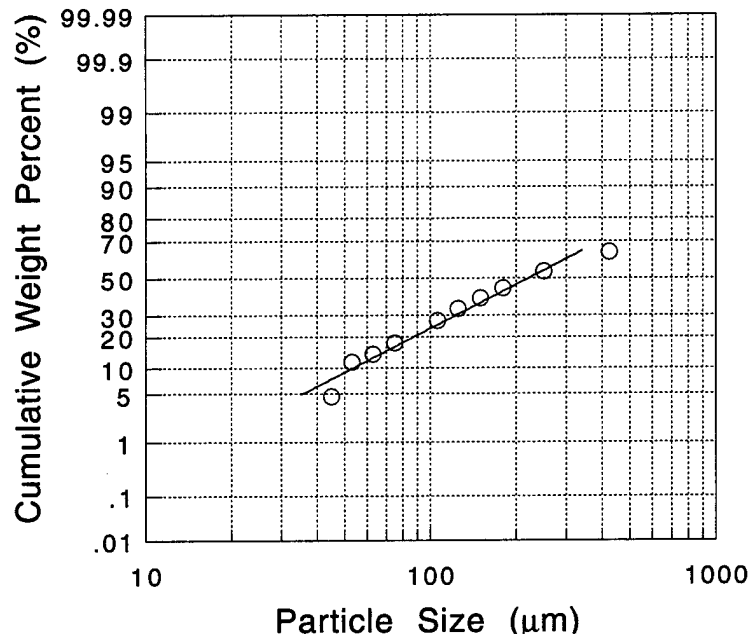
Figure 5.1. Size distribution of oversprayed Ta-Fe powders.
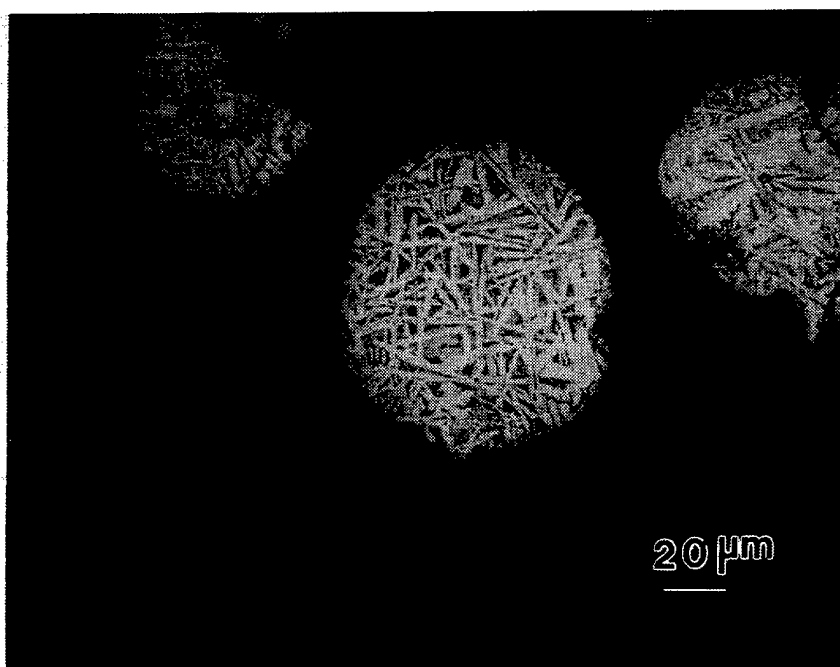
Figure 5.2. Microstructure of oversprayed Ta-Fe powder.
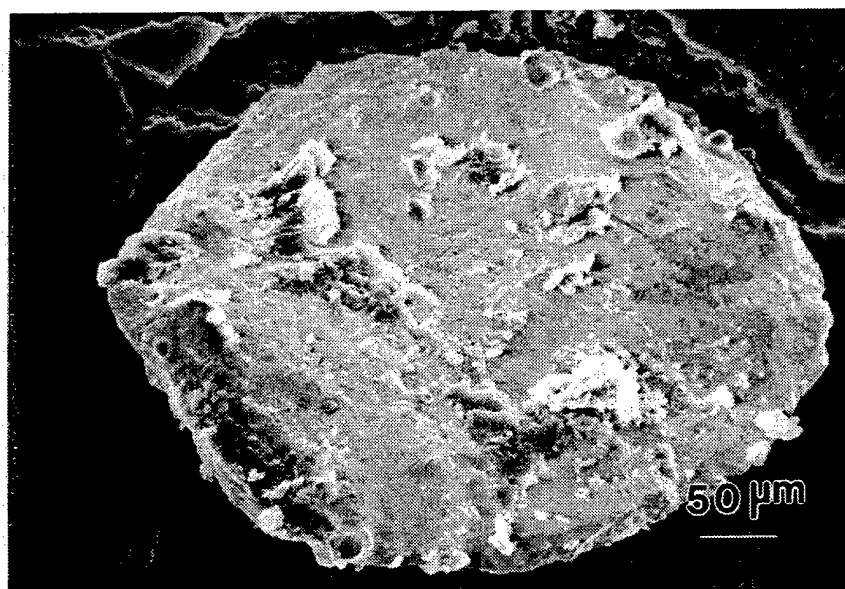
(Top View)
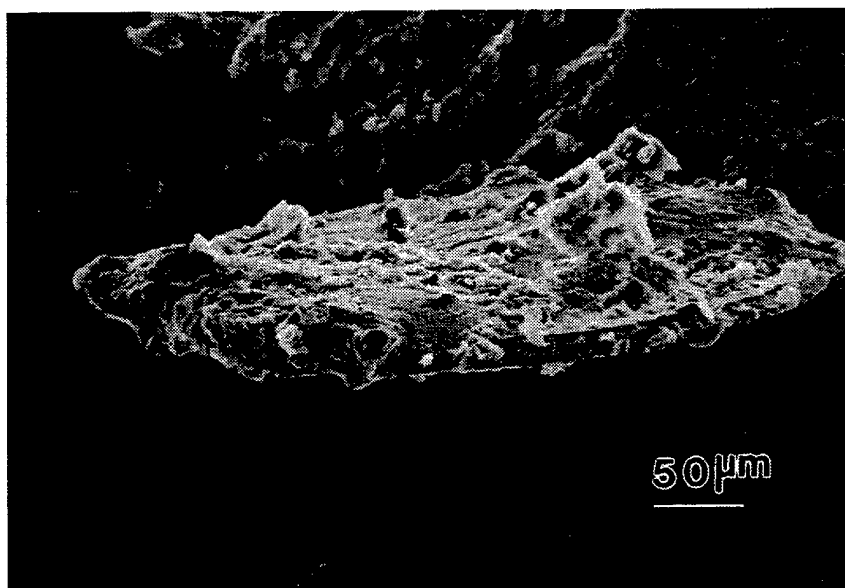
(Side View)

Figure 5.3. Morphology of an oversprayed Ta-Fe splat.
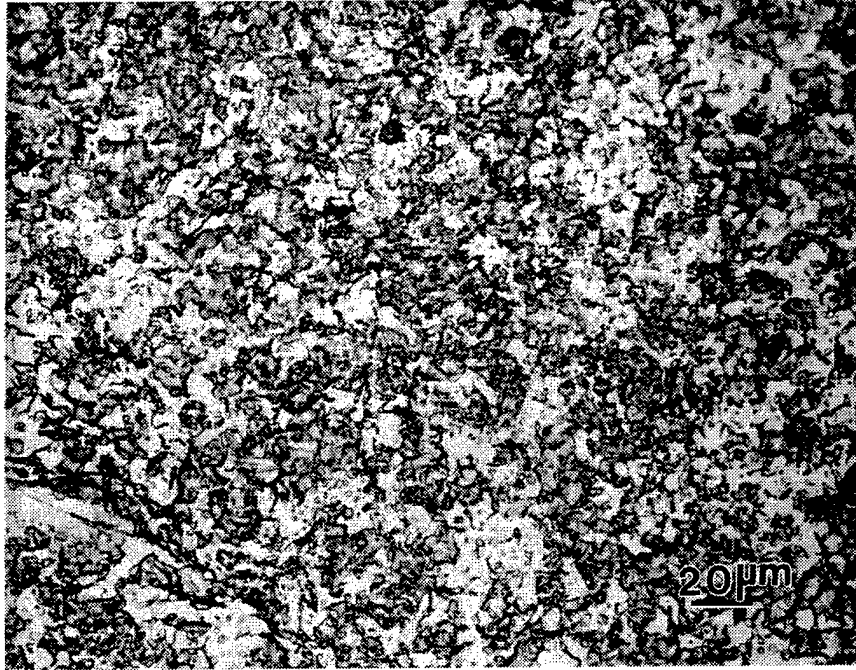
(a)

(b)

Figure 5.4. Microstructure of spray-formed Ta-Fe alloy. (a) Upper section, (b) lower section of the deposit.
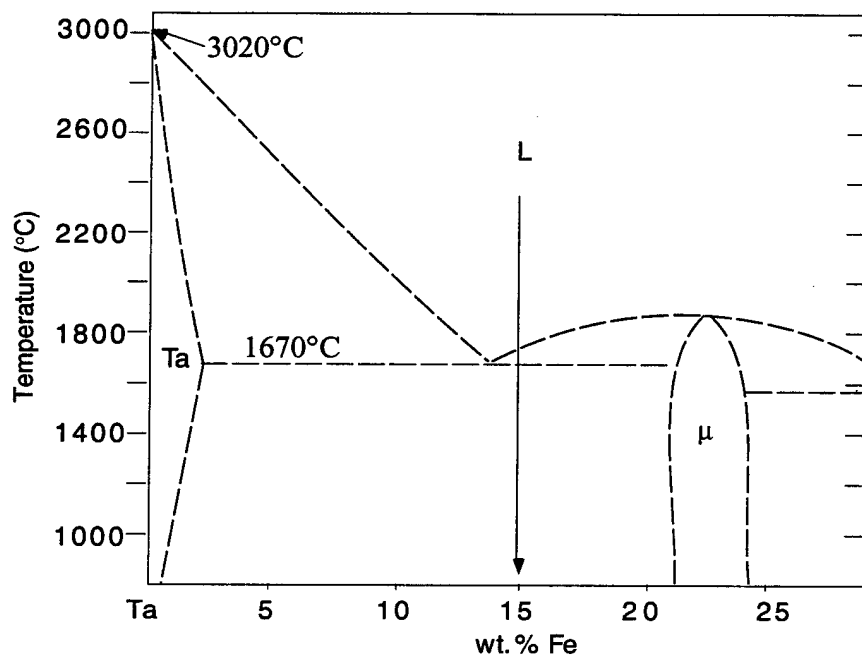
Figure 5.5. Ta-Fe binary phase diagram.
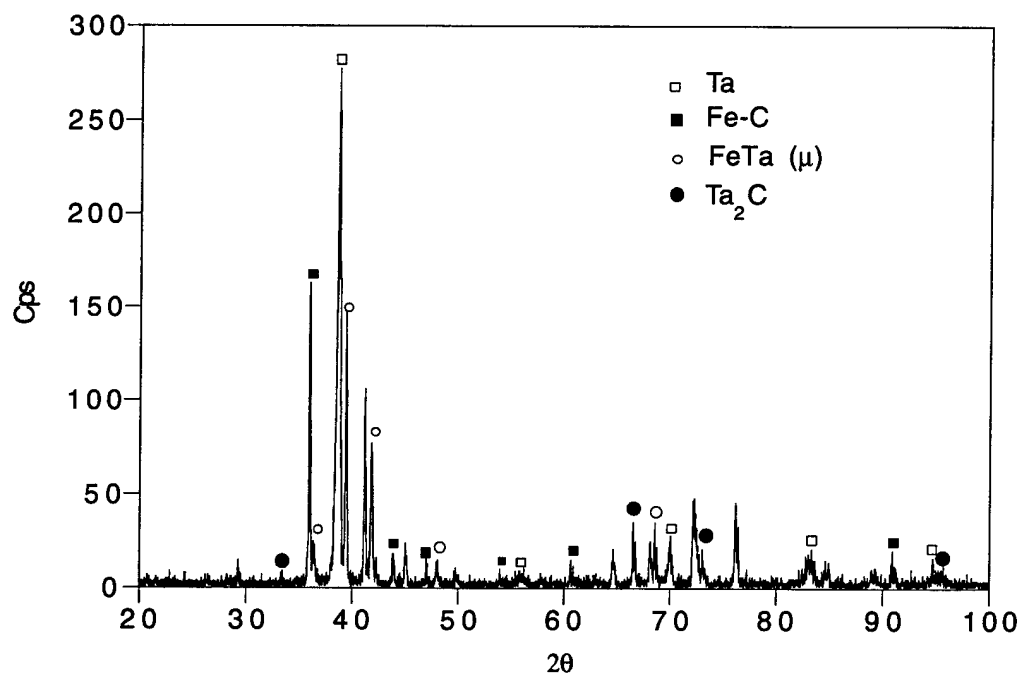
Figure 5.6. X-ray diffraction pattern of spray-formed Ta-Fe alloy.

5.3.3. Ta-Fe Droplet Impact Simulation

A reference case was defined to investigate numerically the impact spreading and solidification of a Ta-Fe droplet. These simulations aim at providing a detailed (sub droplet scale) description of the fluid dynamics aspects of this process which cannot realistically be obtained experimentally. Furthermore, comparison of the numerical predictions with the measured macroscopic features of the solidified droplets will yield important information regarding the representativity of the model.

A Ta-Fe droplet with a size equal to the measured mean size of the oversprayed powder (90 µm) is considered. The droplet temperature at impact is 1973 K. It impinges on a flat surface maintained at 300 K and located 254 mm below the atomizer. In order to obtain a realistic case, the droplet impact velocity is not arbitrarily prescribed but rather calculated using the droplet dynamic equation (Eq. 5.6). This equation requires the gas velocity as a function of the axial position (z). The exponential expression proposed by Liang and Lavernia [126], based on data by Bewlay et al. [154], is used here. The atomization gas is Argon. It exits the atomizer at 150 m/s, while the liquid stream is taken to exits at 2 m/s. Equation 5.6 can then be solved for any droplet size to yield the corresponding odometric function, $v_g(z)$. The results obtained for selected sizes are plotted in Figure 5.7.
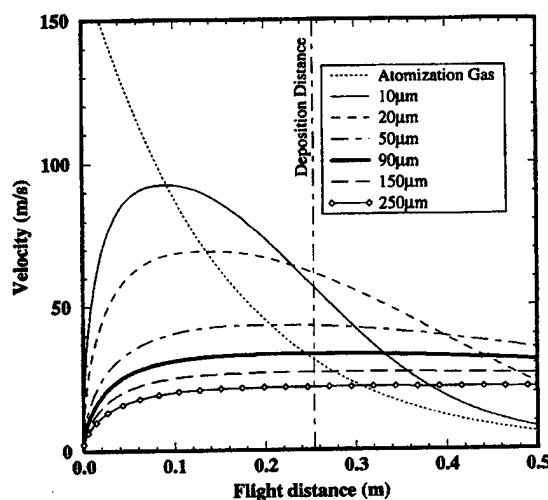
Figure 5.7. Computed Droplet Trajectories.

This plot shows the gas velocity decreasing, as prescribed, exponentially from 150 m/s to 30 m/s at the deposition distance (L_{dep}). The droplets are initially accelerated by the faster atomizing gas until their velocity exceeds that of the gas. Then, the droplets start decelerating. Smaller droplets, with smaller Stokes numbers ($St = \rho l D^2 v_g z_o / 18 \mu_g L_{dep}$), tend to follow the dynamics imposed by the ambient gas velocity more closely than larger droplets, with larger St, which tend

to be driven mainly by their inertia. For droplets with diameters from 10 to 250 Mm, the velocity at the deposition distance (254 mm) predicted to be between 20 and 62 m/s. In particular, the impact velocity of droplets having a size equal to the measured mean size (90 Mm) is estimated to be 38 m/s. Hence, the Reynolds and Weber number for this base case are 16330 and 760 respectively.

The simulated spreading and solidification history of a Ta-Fe droplet corresponding to the base case described above is presented in Figure 5.8. In this plot, the solid line is a VOF contour line at VOF=0.9. Although this line gives a good approximation of the droplet free surface location, it should not be confused with it. As the computations proceed some numerical smearing of the initially sharp interface is unavoidable [161], even though the numerical algorithm used here is designed to minimize this artifact [147]. Hence, the numerical representation of the physical interface is a transition region where the values of the Volume of Fluid function are between 0 and 1. Therefore, the small perturbations appearing on the VOF contour line at the end of the computations are representative of the thickness of this transition region rather than actual ripples on the droplet surface. The solid splat morphology history is shown in Figure 5.9. The final splat has a radius of 92 Mm and is 15 Mm thick at its highest point (on the axis of symmetry).

Liquid jet overflow [149] is not predicted in the base case. However for larger droplets and, therefore, smaller impact velocities this mechanism is still present. For instance, a 148 Mm droplet with an impact velocity of 31 m/s (Re=22600, We=886) was found to experience liquid-jet overflow. The predicted behavior is then similar to the results that were previously [149] obtained with tungsten for instance. In the present case, a first overflow occurs at $t \approx 2 \mu s$ (for a total spreading time of 10 µs). The interaction of the spreading liquid layer with the ring thus created eventually results in the gap being completely filled because, at this point of the spreading process, the downward velocity component is still significant. A second overflow occurs at $t \approx 3.7 \mu s$. At this point, however, the downward velocity component is significantly smaller than the radial component, as evidenced by Figure 5.10, and the gap still exist at the end of the spreading process.

The factors which determine whether or not liquid-jet overflow occurs are still not fully understood. Delplanque and Rangel [162] have shown using a simplified disk spreading model that the Re/We ratio plays an important role in the balance between kinetic energy, potential energy and viscous dissipation, and, indeed, the case described above where liquid-jet overflow was observed correspond to a value of this ratio 25% larger than in the base case. A more complete parametric study is needed that is not within the scope of this paper. Work in this area is continuing.

5.3.4. Evaluation of the Numerical Model Validity

A precise evaluation of the numerical prediction validity would require the measurement of the size, impact velocity, and temperature of the droplet which produced a particular splat. This is obviously unrealistic in a practical spray configuration such as the one used here. Such tests can however be performed using a single droplet deposition facility. Nevertheless, it is possible to assess the validity of the numerical model by attempting to estimate the initial size and impact velocity of the droplet which produced a given splat.
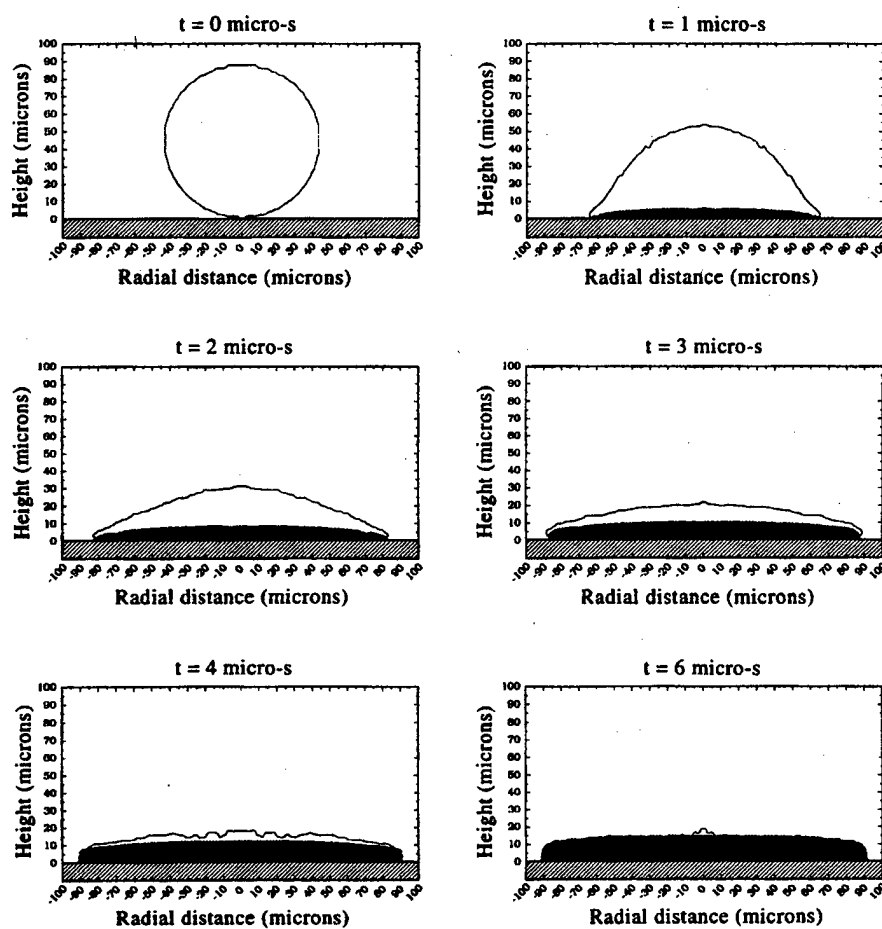
Figure 5.8. Ta-Fe droplet solidification sequence.
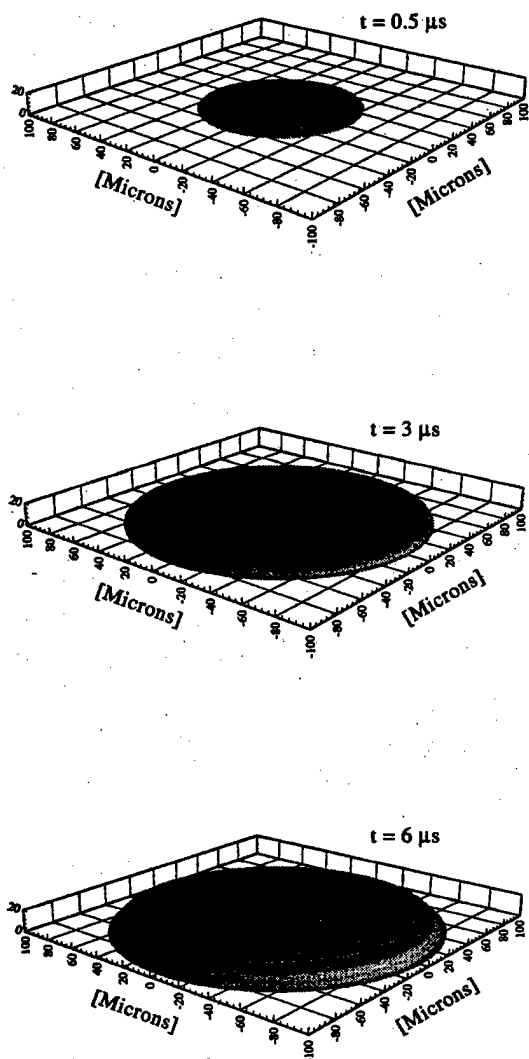
Figure 5.9.   Ta-Fe splat (solid only) morphology history.
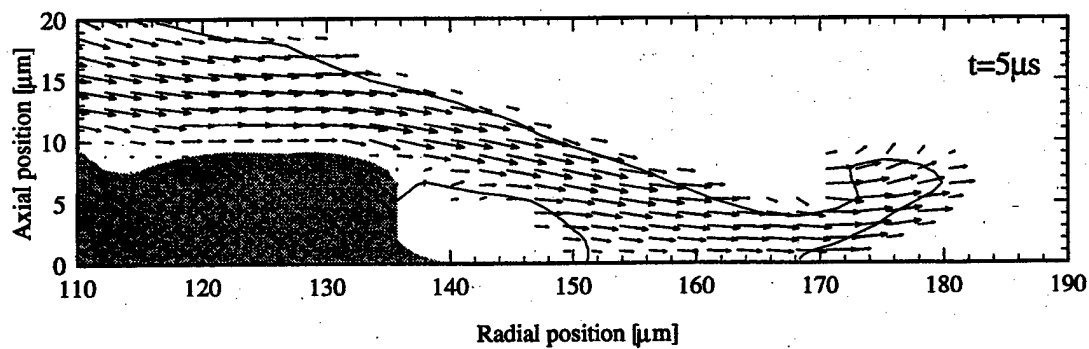
Figure 5.10.   Liquid-jet overflow in a spreading and solidifying Ta-Fe droplet.

Micrographic of three typical splats (top and side views) were obtained. One of these splats is roughly axisymmetric (see Figures 5.3(b) and 5.3(a)). The two others are actually half-splats (fractured) and are very irregular (Figure 5.11). Since the numerical model assumes an Asymmetric splat, comparison requires the definition of an Idealized Equivalent Axisymmetric Splat (IEAS) having the same volume and project area as the actual splat. To this end, the micrographs were scanned and digitized. The resulting silhouettes were integrated to yield the top area (AT), top perimeter (PT), cross-section area *(As)*, and cross-section perimeter (Ps). The volume of the IEAS is then defined as

$$V = A_T b \text{ with } b = \frac{P_s - \sqrt{P_S^2 - 16A_S}}{4} \tag{5.7}$$

and its diameter is $D = \sqrt{4A_T/\pi}$. Note that $I = DP_T/4A_t$ an index of the splat irregularity; I= I corresponding to an asymmetric splat. The diameter of the corresponding incident droplet is given by

$$D_l = \left[\frac{6V}{\pi}\right]^{\frac{1}{3}} \tag{5.8}$$

Equation 5.6 can then be solved to determine the impact velocity, Vimp.

The corresponding cases were simulated and the numerically predicted splat dimensions compared to the IEASs. Figure 5.12 shows that the predictions match the data reasonably well given the approximations that were made in the estimation of the droplet state at impact and the imprecision in the alignment of the line of sight with the normal to the surface being measured in the micrographs. The predicted splat radius for the 257 μm droplet is to be taken with caution as computations had to be stopped at only 0.77 solid fraction. This case is indeed at the validity limit of the numerical model used here. As mentioned above, larger droplets are predicted to experience liquid-jet overflow in the last half of the spreading process. It was found that splashing also becomes important. Furthermore, numerical constraints (e.g. mesh size) are more computationally expensive with larger drops and can actually cause the total computation time to become unrealistically large.
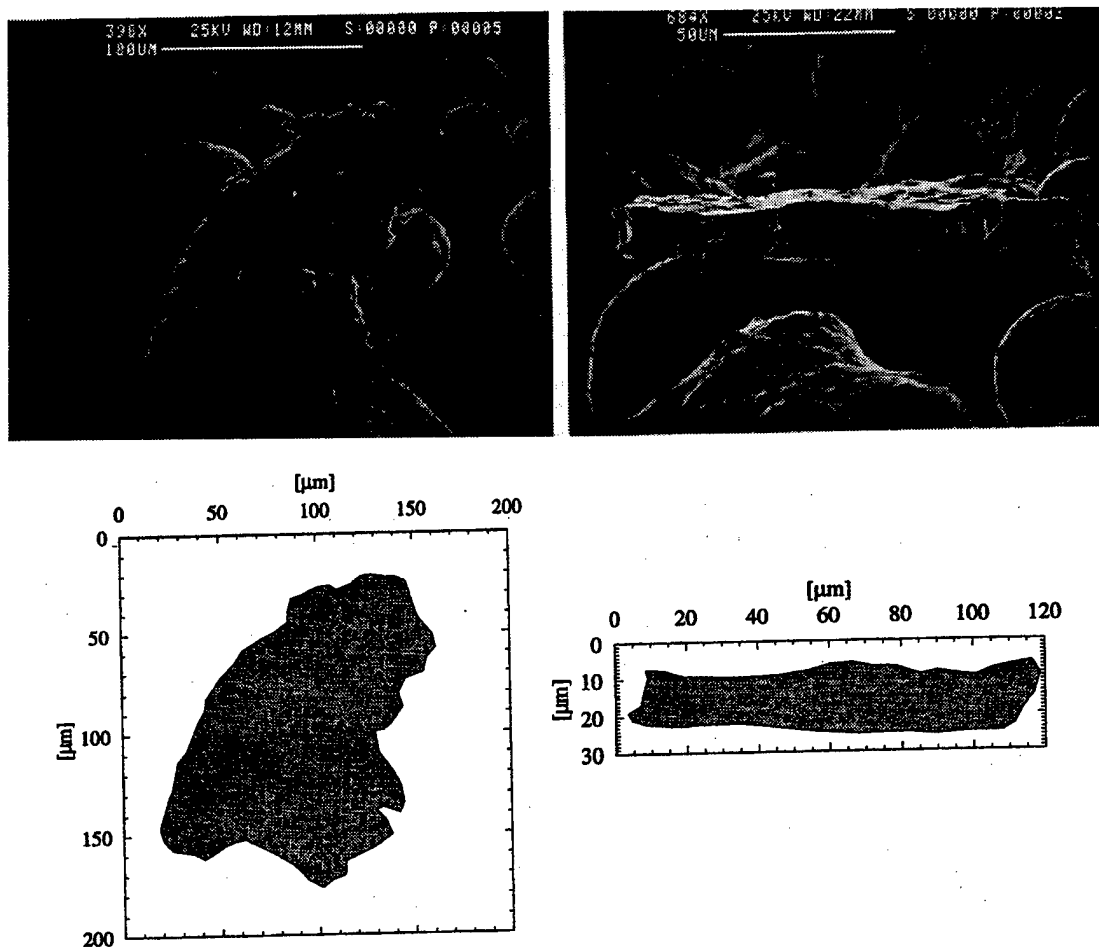
Figure 5.11. Example of splat micrographs and corresponding digitized projections used to
define the Idealized Equivalent Asymmetric Splat (IEAS).
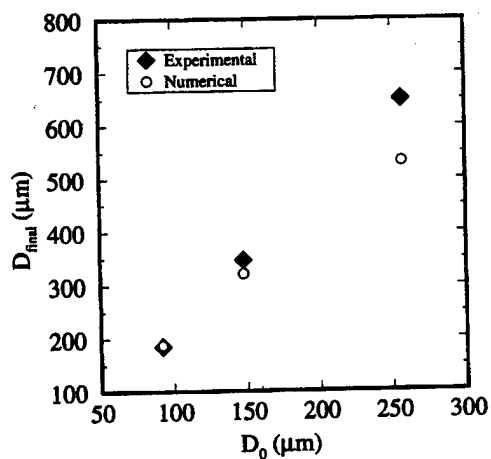
Figure 5.12. Final thickness and diameter of selected Ta-Fe splats. Comparison of numerical
predictions and experimental measurements.

VI.   LOW PRESSURE SPRAY FORMING OF 2024 ALUMINUM ALLOY

6.1.   Experimental Procedures

Low pressure spray forming (LPSF) is a technique in which the spray atomization and deposition process is performed under dynamic evacuation. The experimental procedures that are used for LPSF are described as follows. First, an alloy is charged in a graphite or ceramic crucible. Then, the atomization chamber is evacuated. Once this step is complete, the alloy is induction melted to a certain degree of superheat which is determined for each individual experiment, but usually is about 100 to 200°C above the liquidus of the alloy. The melt is then delivered through a ceramic delivery tube to an atomizer, where it is energetically disintegrated into micrometer-sized droplets using inert gas, such as Ar or N_2. The droplets then travel through the evacuated chamber and impinge on a water cooled Cu substrate to form a solid deposit. In the process, the vacuum level of the chamber decreases rapidly at the beginning of the atomization, and then remains at a stabilized vacuum level until the melt is completely atomized (Figure 6.1). The stabilized vacuum level for the chamber depends on the capacity of the vacuum pump, the size of atomization chamber, and the atomization gas flow rate.
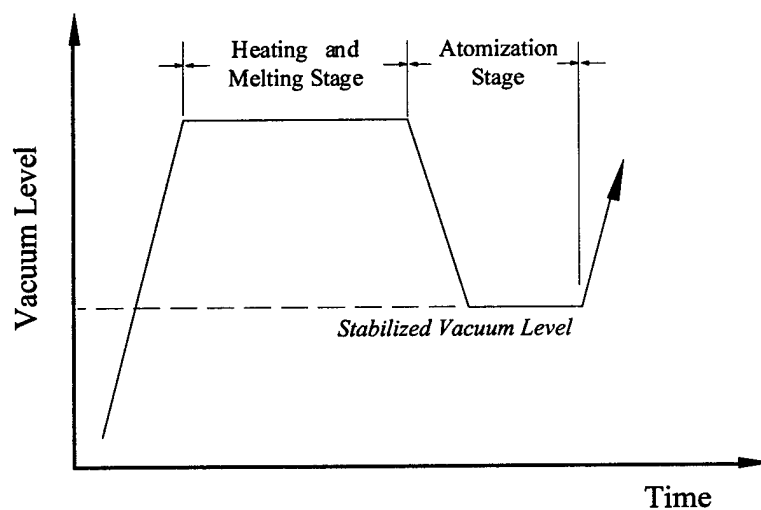
Figure 6.1.   Schematic diagram showing the variation of chamber vacuum level during LPSF.

In the present study, a 2024 Al alloy was selected for experimental study of the LPSF technique. The alloy was supplied as rods (Ø 19 mm x 305 mm, approximately). The alloy was induction melted and superheated to 850°C and then spray atomized and deposited. A mechanical pump (with a displacement of about 0.04 m^3/s and an ultimate vacuum of 10^{-3} torr) was used. In

this case, the stabilized vacuum level was 12 to 15 torr when the atomization gas pressure used was 1.2 MPa. During the heating and melting stages, the vacuum was maintained at a level of 0.2 to 0.3 torr. For comparison, a conventional spray forming (i.e., without dynamic evacuation) experiment on the same alloy was conducted with almost identical processing parameters as those used in the LPSF experiment (Table 6.1). The gas flow rate was estimated on the basis of the pressure drop in the gas cylinders, whereas the melt flow rate was estimated on the basis of charge weight and atomization time. From Table 6.1, it is noted that the gas to metal flow rate ratio is higher for LPSF than for CSF, which may be attributed to the difference in pressure drop across the atomization nozzle used in the two experiments. The backfill gas used in CSF, as well as the atomization gas used in both experiments, was N_2.

Table 6.1. The processing parameters

	LPSF	CSF
Atomization Pressure (MPa)	1.2	1.2
Atomization Gas	N_2	N_2
Deposition Distance (mm)	356	356
Melt Temperature (°C)	850	850
Nozzle diameter (mm)	3	3
Gas to metal flow rate ratio	1.6	0.8

The shape of the deposited materials processed by both LPSF and CSF is schematically shown in Figure 6.2. A representative sample was sectioned from each deposited material to conduct the microstructural examination and porosity evaluation (Figure 6.2). To accomplish this, the samples were further sectioned into 9 to 10 pieces (Figures. 6.3 and 6.4) and then mechanically ground and polished. Once this procedure was completed, the densities were determined by using Archimedes' principle. In this study, the nominal density, 2.78 g/cm^3 for 2024 Al [163] was taken as its theoretical density. Optical microscopy was used to examine the microstructure of the as-deposited materials as a function of distance from the substrate. Accordingly, a sample, labeled A in Figure 6.2, was removed from the center of the deposited materials, and prepared by using standard metallographic methods. The etchant used was Keller's agent (1 ml HF, 1.5 ml HCl, 2.5 ml HNO_3, and 95 ml H_2O). The grain size was determined according to ASTM standard (E112). The pore size distribution was determined using computerized image analysis. Scanning electron microscopy (SEM) was used to document the location and morphology of the porosity present in the deposited materials. X-ray diffraction analysis for detection of any possible reaction products between the melt and the atomizing gas during spray forming was conducted using a SIEMENS D5000 diffractometer. To determine the compositional variation during spray forming, chemical

analysis of the as-sprayed materials, for both LPSF and CSF was performed. Moreover, the amount of nitrogen and oxygen was also measured by inert gas fusion method (conducted by using a LECO TC-436 Nitrogen/Oxygen Determinator at Metals Technology, Northridge, California).
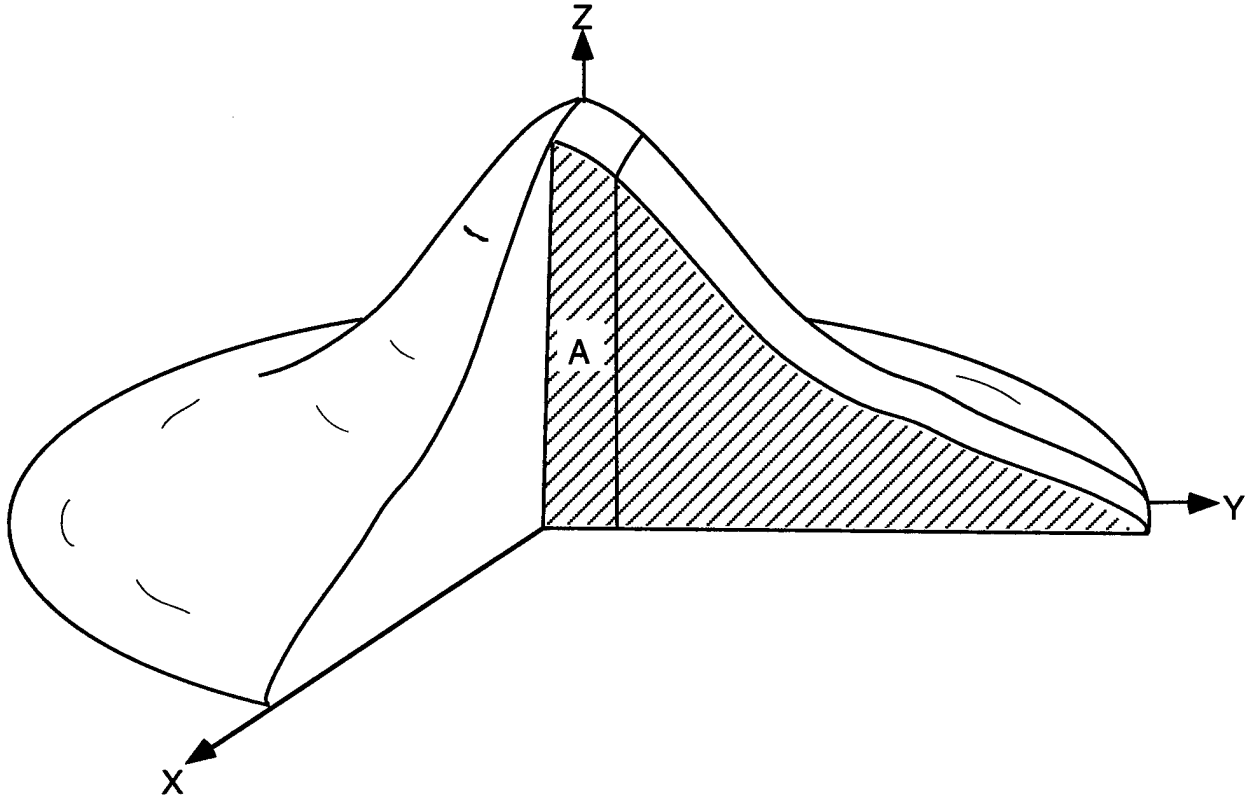
Figure 6.2.   The geometry of the deposited materials for both LPSF and CSF, and the location of samples examined.

6.2.   Results and Discussion

6.2.1.   Density and Porosity of As-deposited 2024 Al Alloys

The geometry of deposited materials produced by low pressure spray forming (LPSF) and conventional spray forming (CSF) was nearly Gaussian (Figure 6.3 and 6.4), which may be described by the following equation [164]

$$Z(x,y) = Z_o \exp\left[-\xi\left(x^2 + y^2\right)\right] \qquad (6.1)$$

where Z_o is the height of the deposited material as measured at the spray axis (x=0 and y=0), and ξ is a coefficient whose value depends upon the profile (i.e., flatness) of the deposited material. The smaller the value of β is, the flatter the profile of the deposited material becomes. In the

present study, the LPSF deposited material has a base diameter of 200 mm and a spray axis height of 78 mm approximately, whereas the CSF deposited material has a base diameter of 180 mm and a height of 92 mm approximately. Accordingly, the magnitude of Z_o for the LPSF and CSF deposited materials is 78 mm and 92 mm, respectively. β was estimated from the cross sectional profile of the deposited materials (Figure 6.3 and 6.4); 0.00027 mm^{-2} for LPSF and 0.00037 mm^{-2} for CSF. The Gaussian shaped profiles exhibited by the spray formed materials in present study are consistent with available experimental studies involving close-coupled atomizers [40, 93, 110, 111].

The spatial distribution of density and porosity of the LPSF formed 2024 Al alloy is shown in Figure 6.3. The density ranges from 2.70 to 2.77 g/cm^3 across the deposited material. Moreover, if the edge area, which comprises approximately 13% of the overall cross sectional area, is ignored, the density across the deposited material is uniform around 2.76 to 2.77 g/cm^3. The corresponding porosity of the LPSF material ranges from 0.26 to 0.71% (using the nominal density of 2024 Al alloy as 2.78 g/cm^3). In comparison, Figure 6.4 shows the spatial distribution of density and porosity across the deposited material processed by using CSF. The density falls between 2.45 and 2.70 g/cm^3. As is the case for LPSF, the outer edge section exhibits a lower density (2.45 to 2.63 g/cm^3), whereas the other sections have nearly uniform density across the deposited material (2.66 to 2.70 g/cm^3) with corresponding porosity of 2.65 to 4.30%. These results clearly demonstrate that the use of LPSF has led to a significant decrease of porosity in as-deposited Al alloy. In this experiment, the porosity is approximately 6 to 10 times lower than that for CSF. It is worth noting that similar reductions in porosity were also documented when conducting experiments with other alloy systems, such as 5083 Al alloy. For example, the density of a LPSF spray formed 5083 Al alloy was greater than 99.2% of theoretical value. However, these results are not reported here in detail in order to narrow the scope of the present work to a single alloy composition.

It is noted that both deposited materials exhibit very porous peripheral sections (approximately greater than 15% porosity) as illustrated by the shaded areas in Figure 6.3 and 6.4. During the present LPSF experiment, it was observed that the porous peripheral area rapidly developed at a distance (about 80 to 100 mm) away from spray axis immediately after the deposition began, as schematically illustrated in Figure 6.5, and then grew gradually as the material deposited on the substrate. Numerous experimental and numerical studies have demonstrated that at the initial stage of deposition, the impinging droplets experience a rapid cooling due to quenching by the cold substrate [40, 110, 154, 165, 166]. Accordingly, the formation of the porous peripheral area at the initial stage of deposition can be explained as follows. When impinging on the cold substrate, the droplets arriving initially did not bond strongly with substrate due to the quenching effect. As a result, these impinged droplets, under the influence of the gas flow field, were then forced to move

radially, accumulate at the edge area, and form a porous region. The further build-up of this highly porous region in the periphery of the deposited material may be rationalized on the basis of the following factors. First, fine pre-solidified droplets, which typically populate the peripheral region of the spray cone accumulate during impingement. This spatial patternation of droplets in the atomization cone has been reported in various numerical [110-112, 138, 167] and experimental [159, 166, 168] studies. Second, the accumulation of a large proportion of pre-solidified droplets in the periphery is exacerbated by the bouncing of solid droplets, as well as by the dragging of fine droplets induced by the flow field's positive radial velocity component. This may be explained by the interactions between the droplets and the substrate or deposition surfaces. For example, Mathur et al. [109] argued that the solid droplets will bounce off from a solid deposition surface and partially bounce off from a mushy surface. Third, the peripheral region retains a high degree of porosity throughout deposition since there is insufficient liquid to completely fill the interstices that remain between solid droplets.

Figure 6.6 reveals the microstructure of central sections of the deposited materials processed by both LPSF and CSF. It is evident that the amount of pores present in the LPSF deposited material is much less than that present in the CSF material (Figure 6.6a and 6.6b), which is consistent with the density measurements. The distribution of pore sizes is shown in Figure 6.7 for both deposited materials. The equivalent mean pore sizes are 9.3 μm for LPSF and 10.7 μm for CSF. It is worth noting that the pore size distribution reported herein for LPSF was based on a much larger cross sectional area than for CSF, as necessitated by the much smaller amount of pores present. SEM studies revealed that two types of pores are present in the deposited materials: nearly spherical pores and irregular pores (Figure 6.8). Nearly spherical pores are generally small (less than 5 μm approximately), and often located at triple points (Figure 6.8a). Intragranular cavities were also observed (Figure 6.8a). The irregular pores observed were as small as a few microns (Figure 6.8b and 6.8c), or as large as an entire grain, i.e., approximate 10 to 30 μm (Figure 6.8b). The small irregular pores were generally located transgranularly or at triple points (Figure 6.6 and Figure 6.8c). The pores whose sizes are equivalent to the grain sizes (Figure 6.8b) were observed much more frequently in the CSF material than in the LPSF material.
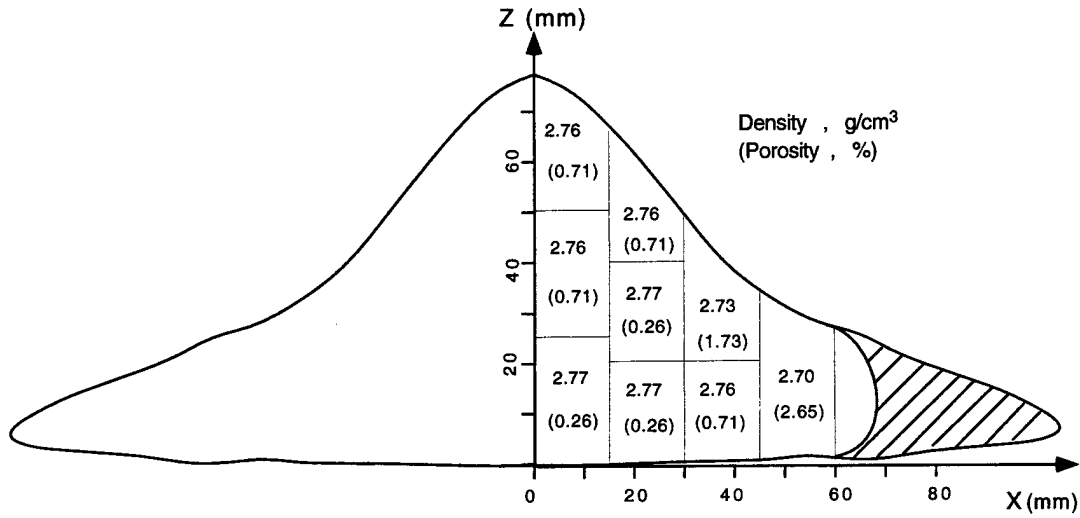
Figure 6.3.   The distribution of density and porosity on the cross section of LPSF 2024 alloy (shaded area is porous peripheral area).
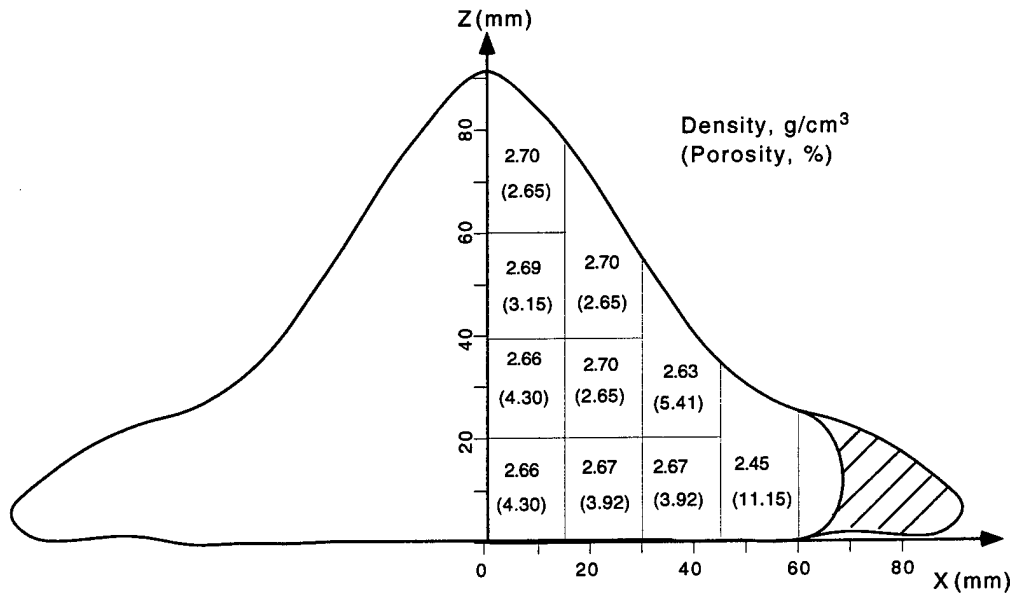
Figure 6.4.   The distribution of density and porosity on the cross section of CSF 2024 Al alloy (shaded area is porous peripheral area).
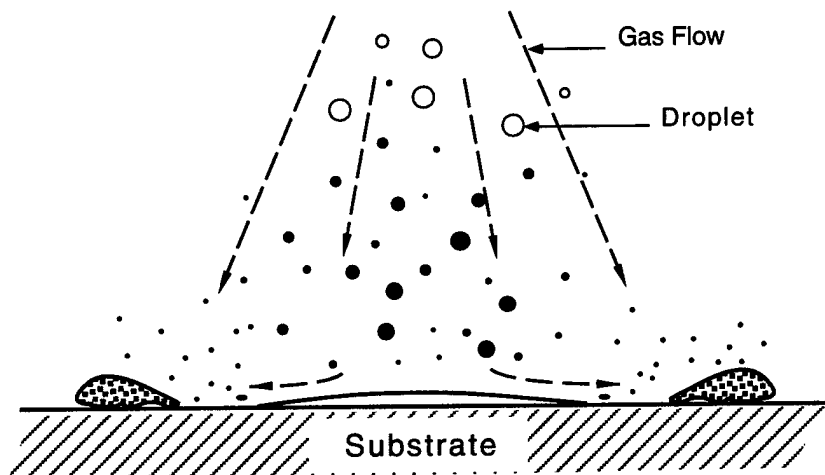
Figure 6.5.   Schematic diagram illustrating experimental observation of the build-up of porous peripheral area at the beginning of deposition.

6.2.2.   Microstructure of As-deposited 2024 Aluminum Alloy

Spatial characterization of the microstructure, conducted on samples removed from the central region of the spray formed materials (A in Figure 6.2), revealed the following findings. First, the morphology of the grains is equiaxed for both LPSF and CSF materials (Figure 6.9) and few prior droplet boundaries were noted, consistent with results from other studies [36, 96, 98, 99, 104, 108]. The origin of this microstructure has been rationalized on the basis of one or a combination of the following mechanisms: (a) the fragmentation of dendrites in the powders during impingement [37, 108]; (b) the homogenization of undeformed dendrites during impingement [155]; (c) the increase in nucleation site density that results from both dendrite fragments and pre-solidified droplets [91]. Second, for both LPSF and CSF materials, the grain size in both upper (near free surface) and lower (near substrate) regions was smaller than that present in the central region where the magnitude of the size variation was small. This is illustrated in Figure 6.10, where it is evident that the grain size of LPSF deposited material is slightly larger than that of CSF deposited material, with the exception of the region near the substrate where the converse is true, although the observed differences in grain size are relatively small. The spatial variation of grain size in deposited materials has been attributed to variations in solidification rate during spray forming [40, 96, 169], which are influenced by both the rate of enthalpy input and the rate of enthalpy extraction during deposition. The rate of enthalpy extraction during spray forming is largely determined by the conduction of thermal energy to the substrate and extraction of thermal energy by the atomization gas. For example, the numerical results of Mathur et al. [109], which were obtained using an enthalpy formulation, reveal that the cooling rate - time profile of deposited
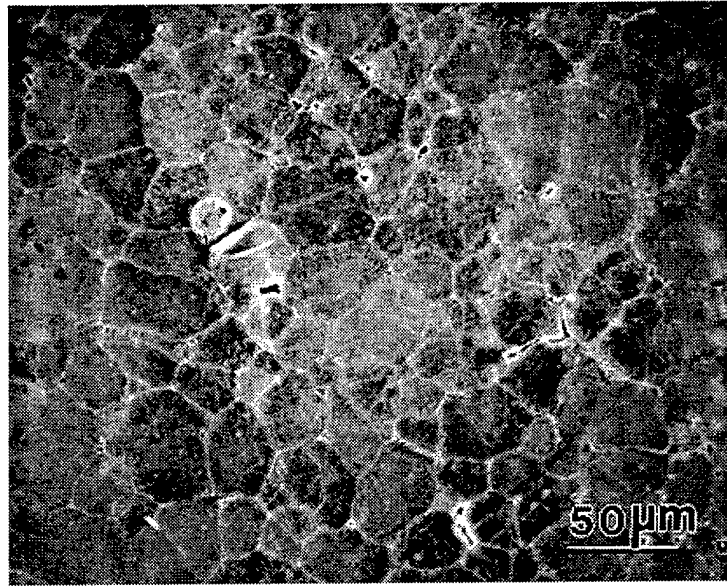
(a)
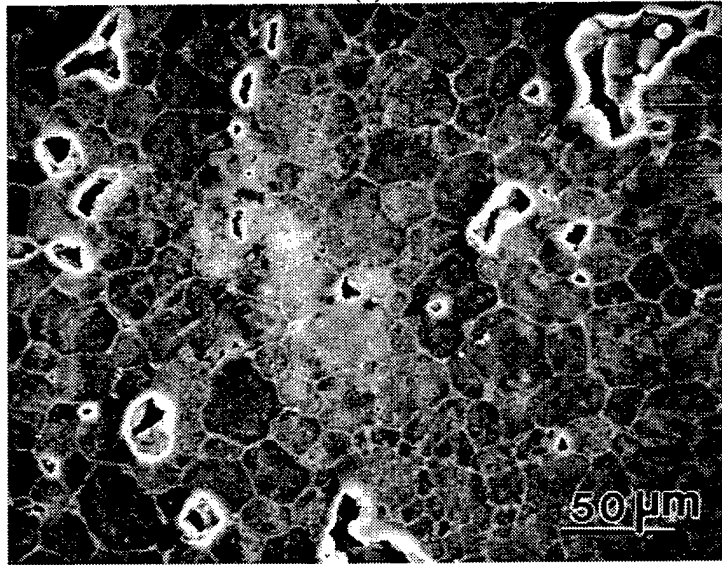
(b)

Figure 6.6.   SEM micrograph of central sections from deposited materials processed by (a) LPSF and (b) CSF.
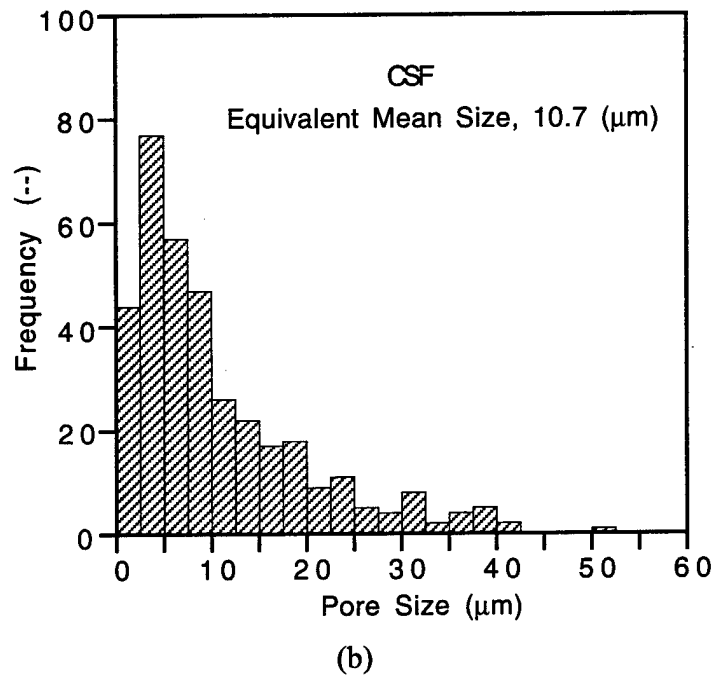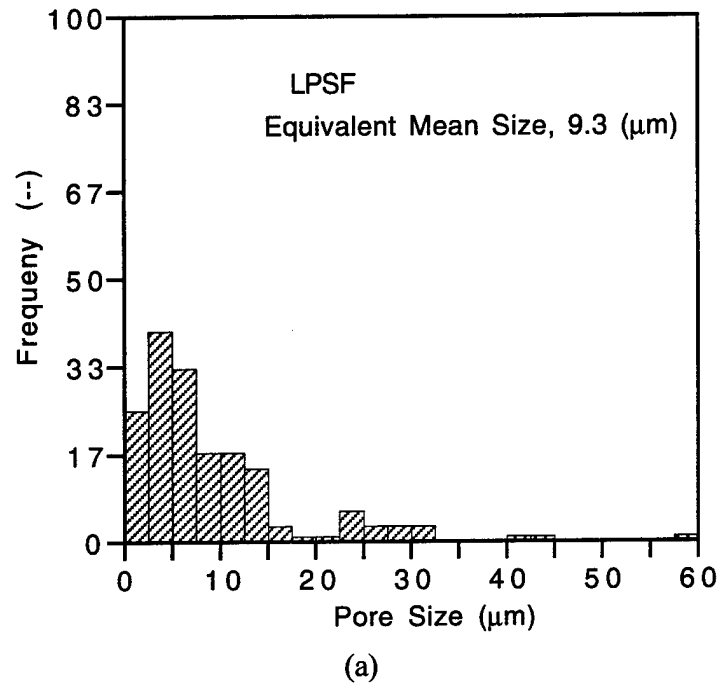
Figure 6.7.   The pore size distribution for (a) LPSF, and (b) CSF deposited 2024 Al alloy.
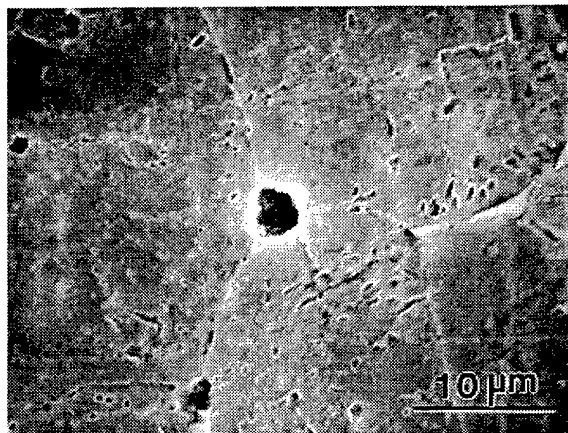
(a) nearly spherical pores at a triple point
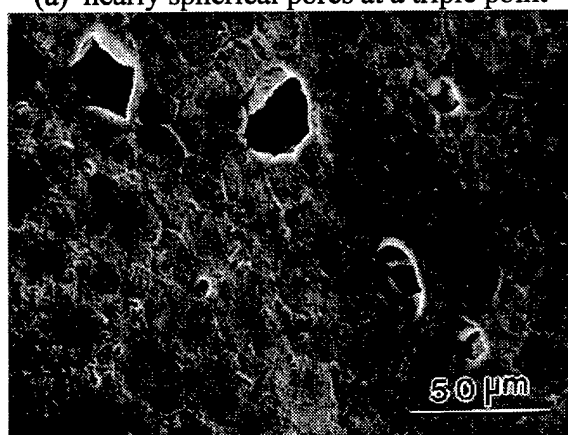
(b) large pores

(c) transgranular pores

Figure 6.8.   SEM micrograph showing the morphology and location of pores in the as-deposited 2024 aluminum alloy

Top

Middle

Bottom

(a)   (b)
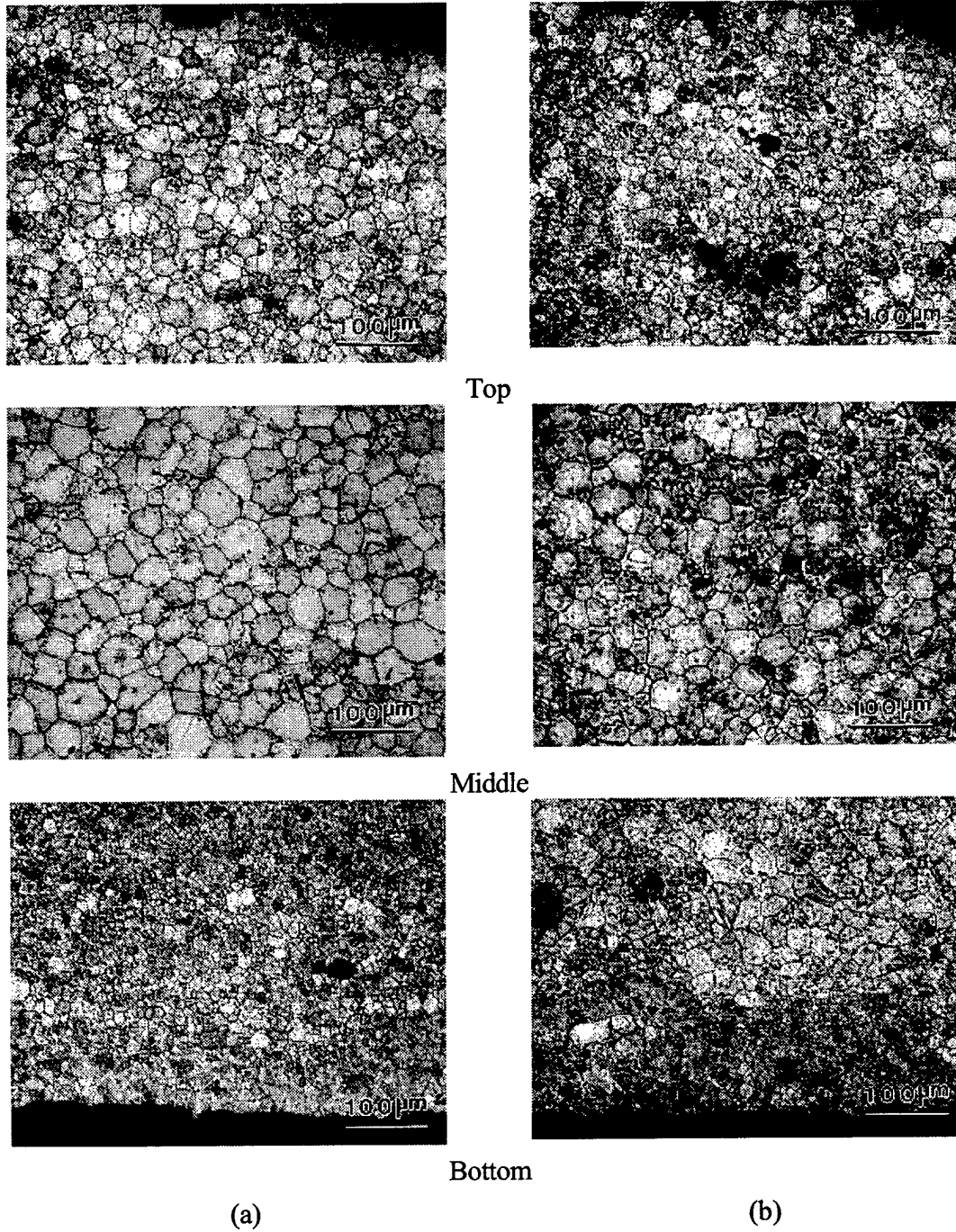
Figure 6.9.   Grain morphology of the as-deposited 2024 aluminum alloy processed by (a)
               LPSF and (b) CSF, from substrate to upper section of the deposited materials
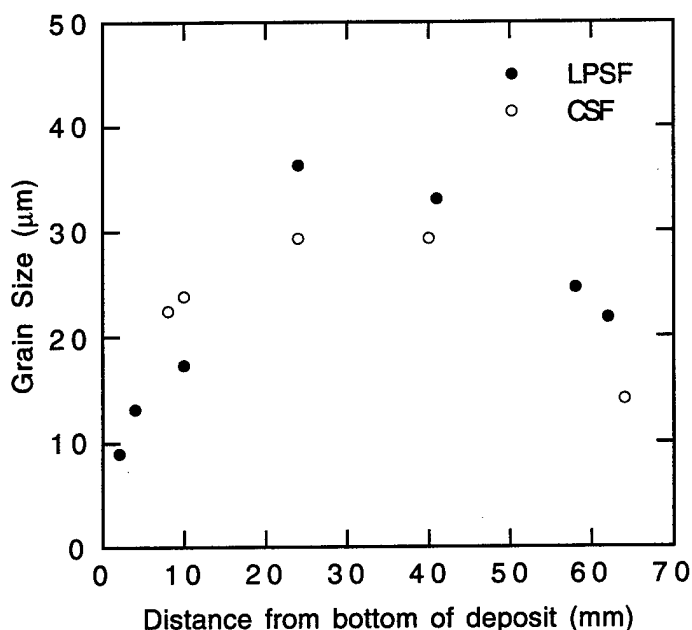
Figure 6.10.   Grain size distribution from the lower section to the upper section of deposited
materials processed by LPSF and CSF.

materials during deposition consists of three stages: initial transient stage, steady state stage, and final stage. During the initial transient stage, thermal conduction to the substrate is rapid as a result of the large temperature gradient. For example, Mathur et al. [40] indicated the heat transfer coefficient at the deposit-substrate interface is about 10^5 w/(m^{2}K) at the start of deposition for an Al-4.5Cu alloy. In related numerical results reported by Wang and Matthys [165], it was shown that the magnitude of the interfacial heat transfer coefficients rapidly increases at the initial stage of deposition. As the deposition progresses, on the one hand, the substrate temperature gradually increases, and on the other hand, an air gap forms at the interface between substrate and deposited materials [40], due to incomplete bonding between the deposited material and the substrate resulting from the quenching effects experienced by the droplets impinging on the cold substrate [166]. As a result of these two effects, the magnitude of the deposit-substrate interfacial heat transfer coefficient decreases rapidly [165]. Once the deposit-substrate interfacial heat transfer coefficient reaches a relatively constant value, a steady state stage is achieved. In the case of an Al-4.5Cu alloy, for example, the magnitude of the steady state interfacial heat transfer coefficient has been estimated to be 500 w/(m^2 K) [40]. During the steady state stage, the rate of thermal energy input from the impinging spray is balanced by the rate of the thermal energy dissipation into the substrate and surrounding gas environment. Once deposition is completed and there is no more enthalpy input, the deposited materials experience a final stage, in which thermal energy is rapidly dissipated into the substrate and surrounding environment [37, 40, 110, 169]. The presence of the

three aforementioned stages has been confirmed on the basis of other numerical [37, 156-158] and experimental [91, 159, 160] studies. For example, the infrared thermal image analyses on the surface temperature of deposited materials showed that for a Sn-38Pb alloy, the top surface temperature increased rapidly (20 to 30 K/s) at the beginning of deposition; after about 15 s, the temperature became approximately constant; finally when melt delivery was discontinued, the surface temperature quickly decreased [159].

In the work of Liang et al. [155], the influence of cooling rate on grain size during spray forming was described using the following equation

$$d = a\dot{T}^{-b} \tag{6.2}$$

where a and b are constants whose values depend on the material selected. From this equation, it is obvious that the higher the cooling rate, the smaller the grain size. Accordingly, the spatial variation of grain size as observed in the present study can be construed on the basis of three stages of cooling during deposition as described above. During the initial transient stage, the cooling rate decreases with time, resulting in a transient grain size variation from smaller to larger in the deposited materials. Once the steady state cooling rate is achieved, the deposited materials exhibit a nearly uniform grain size. Finally, the grain size becomes smaller again when the cooling rate increases during the final stage.

6.2.3. Evaporation of Alloying Elements During Low Pressure Spray Forming

The results of chemical analysis for the as-deposited materials are listed in Table 5.1. The compositions of both deposited materials are comparable except for the element Mg. The content of Mg is lower for LPSF than for CSF, suggesting that loss of Mg occurred during spray forming. Intuitively, this should be attributed to the high vapor pressure of Mg. Figure 6.11 shows the vapor pressure of principal alloying elements that are contained in 2024 Al alloy; Mg has a much higher vapor pressure than the other alloying elements, such as Mn and Cu. During spray forming, the melting and atomization stages are most likely the stages when Mg evaporation occurs. As previously stated, the vacuum level was 0.2 to 0.3 torr during heating and melting stage and about 15 torr during the atomization and deposition stage. Thus, during heating and melting, the vacuum level was lower than the vapor pressure of Mg and serious evaporation of Mg should be expected. However, the presence of an oxide layer on the melt prevented excessive loss of Mg. During atomization and deposition, the temperature of the droplets decreases rapidly so that excessive vaporization of magnesium should not be expected. However, when considering the large amount of surface area created during atomization, certain amount of the evaporation of magnesium should occur. Accordingly, suitable precautions need to be taken when LPSF is used to process alloys that contain high vapor pressure elements, such as increasing the content of high

vapor pressure elements in the master alloys or applying the vacuum only at the beginning of the atomization so that the vaporization of these elements may be minimized. Because of the much lower vapor pressure, as compared with the vacuum level of the chamber, excess vaporization of other elements, such as Cu and Mn was not observed during spray forming, as demonstrated in Table 6.2.

Table 6.2.　　Composition of As-deposited 2024 Aluminum Alloy

	Cu	Mg	Mn	O_2	N_2
	(wt.%)			(ppm)	
LPSF	3.90	1.03	0.64	12	20
CSF	3.98	1.41	0.66	22	19
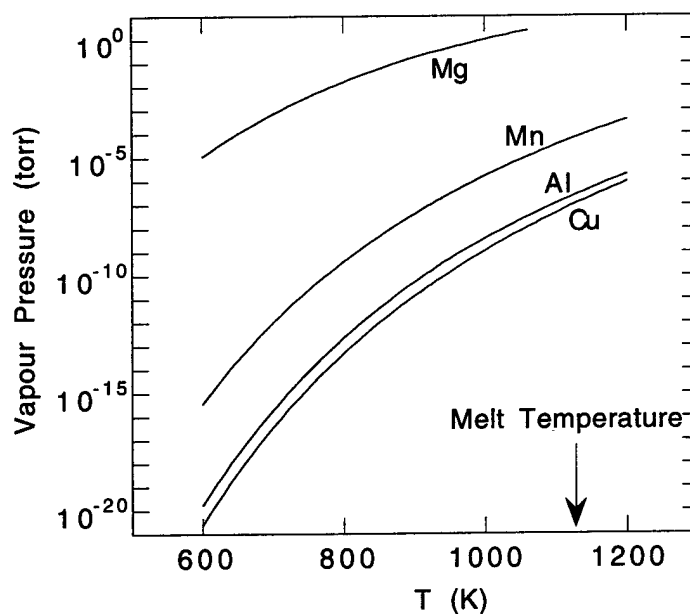
Figure 6.11.　　Vapor pressure of principal alloying elements in 2024 Al alloy [170].

6.2.4.　　Oxygen Content of As-deposited Alloy

In order to provide insight into the extent of oxygen contamination during spray forming, the oxygen content in samples from LPSF and CSF was measured by using the inert gas fusion method. The results of this study are shown in Table 5.1. It is interesting to note that the LPSF material exhibits only about 50% of the oxygen content of the CSF material. In view of complex chemistry of 2024 Al alloys (principal alloying elements: Cu, Mg, and Mn), it is difficult to ascertain the particular chemistry of the oxide phases present in the spray formed materials.

However, available thermochemical data reveals that two oxides are most likely to form during spray forming: Al_2O_3 and MgO. For example, at 1000K, Gibbs free energies for following reactions are:

$$2Al + \frac{3}{2}O_2 = Al_2O_3 \qquad\qquad \Delta G^o = -1312.00 \text{ kJ/mole}$$

$$Mg + \frac{1}{2}O_2 = MgO \qquad\qquad \Delta G^o = -505.67 \text{ kJ/mole}$$

Quantitative study of the chemistry of the oxides present in the LPSF and CSF materials is outside the scope of the present study. However, in view of the high negative Gibbs free energy of the reactions, it is likely that one or a combination of these oxides would form during spray forming regardless of whether it is CSF or LPSF. Hence it is probable that the low oxygen content measured for the LPSF material may be attributed to a decrease in oxygen gas entrapment either during atomization, or subsequently during deposition.

6.2.5.   Gas Entrapment

Entrapment of gas is thought to be partially responsible for the formation of porosity in spray deposition processes [37, 40, 109-111]. To provide insight into the mechanisms that govern gas entrapment during spray forming, the content of atomization gas (N_2) in the deposited materials was measured and the results are summarized in Table 5.1. It is evident from these results that the measured amount of atomization gas (N_2) is almost identical for both LPSF and CSF materials; 20 ppm and 19 ppm respectively. To estimate the possible contribution of the gas content to porosity, following relationship between porosity (P) and gas content is established on the basis of weight balance:

$$P = \left(\frac{AC_g}{1+AC_g} \right) \times 100 \qquad\qquad (6.3)$$

where

$$A = \frac{\rho_m}{\rho_g} - 1 \qquad\qquad (6.4)$$

and C_g is gas content in weight percent, ρ_m and ρ_g are the metal density and the gas density, respectively. Now, if one assumes that the gas present in the deposited materials is at 1 atm (0.1MPa) and 300K. Then, the estimated porosity in the deposited materials is about 4.2% for 20 ppm nitrogen content. Clearly, a small amount of gas content may contribute to a relatively large

amount of pores.

Gas entrapment during spray forming processes can occur during the melting, atomization, and/or deposition stages. The small difference in the nitrogen gas content between the LPSF and the CSF materials (see Table 5.1) suggests that the dissolution of gas in the liquid metal during melting and superheating was not significant, since melting during the CSF experiment was conducted under an over-pressure of N_2, whereas melting during the LPSF experiment was conducted under a vacuum. The entrapment of atomization gas during deposition, may occur as individual droplets impinge and deform, initially against the deposition surface and subsequently on each other [37]. Under extreme conditions, the presence of excess liquid at the deposition surface can exacerbate gas entrapment as the atomization gas disrupts the deposition surface [171]. The extent of gas entrapment during atomization is discussed in detail below.

A number of experimental studies on atomized powders have reported the formation of internal pores during atomization [36, 39, 172, 173]. For example, L'Estrade et al. [172] indicated that atomized metal powders always contained porosity regardless of the chemistry of the atomization gas or melting process used. In related studies, Benz et al. [36] reported that during the atomization of a superalloy using argon, gas bubbles were produced within the powders. In the work of Janowski et al. [39], hollow powders were observed when the atomizing gases used had low solubility in the melt. In the present study, similar experimental evidence was observed in oversprayed powders of various sizes. Figure 6.12 shows an example of a spherical pore present in a spherical oversprayed powder. Moreover, the gas entrapment during spray forming is supported by the preliminary results of HIPing experiments. A sample sectioned from CSF processed Al alloy was heat treated at 475°C for 2 to 28 h in Ar atmosphere following HIPing. The porosity was evaluated. The results reveal that the porosity was reduced from 3.92% to less than 0.5% after HIPing. However, when HIPed sample was subjected to heat treatment, the porosity increases accordingly with increasing time of the heat treatment (Figure 6.13). Moreover, some gas bubbles were observed on the sample surface. Apparently, this phenomena could explained only by the gas expansion during heat treatment. It should be indicated that the aforementioned results did not imply that the HIPing can not eliminate the pores even in the Al alloys. Actually, once appropriate
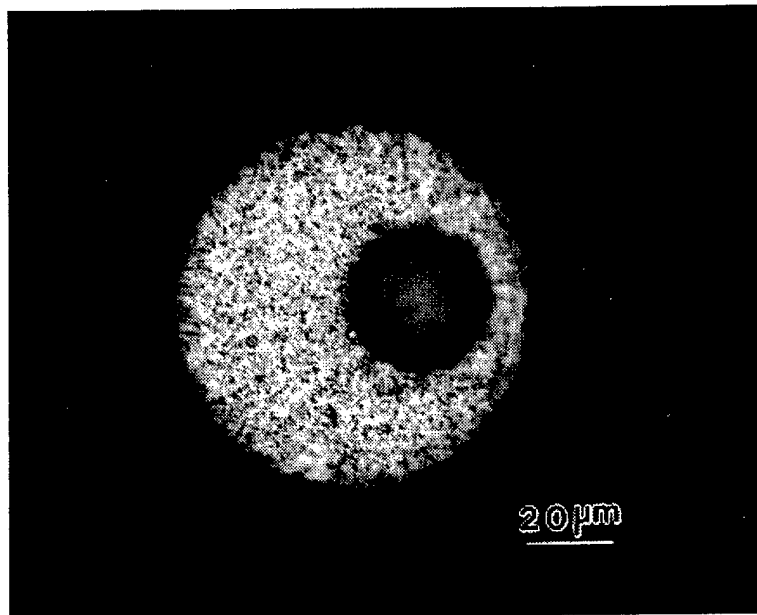
Figure 6.12.   A spherical pore present in an oversprayed powder from LPSF.
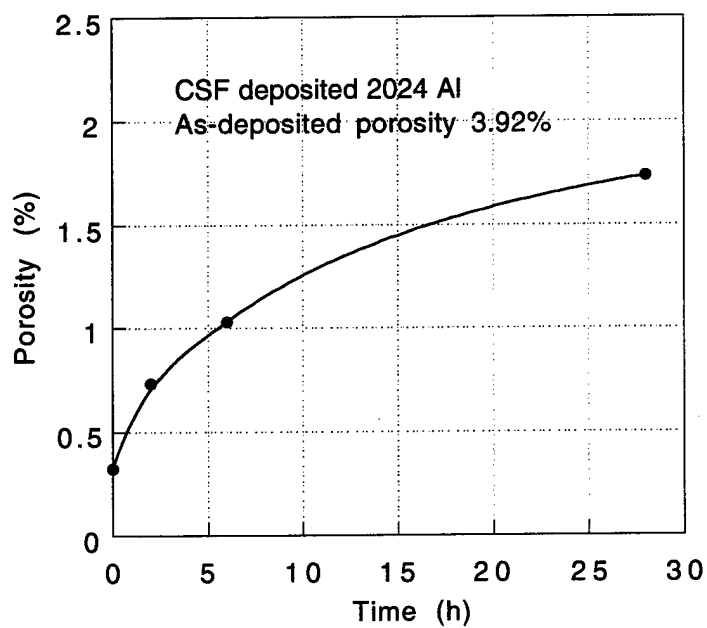
Figure 6.13.   Variation of porosity with heat treatment time for deposited 2024 Al alloy after HIPing.

processing conditions are selected, the pores can be almost completely eliminated.

Atomization generally consists of three stages: primary droplet formation; primary droplet break-up and droplet solidification, the exception involving conditions of very low melt to gas relative velocity (Rayleigh regime) where only the first stage is involved [174-176]. The mechanisms of primary droplet break-up depend on the Weber number, a dimensionless parameter used to describe melt disintegration. For low Weber numbers, the primary droplet break-up is governed by the bag break-up mechanism, whereas for high Weber numbers it is governed by ligament break-up mechanism [175, 176]. These two droplet break-up mechanisms have been suggested to be related to gas entrapment during atomization [172, 173]. L'Estrade et al. [172] indicated that during the evolution from ligament to droplet, parachute like membranes form, which sometimes instead of breaking up into small droplets, collapse on themselves forming hollow particles, thereby leading to gas entrapment. Furthermore, Rabin et al. [173] pointed out that during the bag break-up process, due to the high viscosity of liquid metals, a thick wall bag may not break up into smaller droplets; instead it may collapse and form a gas containing hollow particles.

It is difficult to ascertain the precise relationship between gas entrapment in the atomized droplets and the presence of porosity in spray formed materials. Nevertheless, it is highly probable that the origin of the pore formation mechanisms will depend on the relevant thermodynamic (i.e., gas solubility in the materials) and kinetic (i.e., chemical reactions leading to nitride formation in the presence of nitrogen [36]) characteristics of the system. When the gas is insoluble in liquid and solid phases, the gas contained in the pores will not diffuse out. However, if the gas exhibits a high solubility and diffusivity in the liquid and solid phases, the gas pressure in the internal cavity could be dissipated by diffusion, possibly leading to the disappearance of the cavity. In cases where there exists a driving force for a chemical reaction to occur between the atomization gas and liquid/solid phase, the partial pressure of the gas in the pores will decrease as secondary phases are formed, which eventually may leads to the collapse of the gas filled pores.

In the present study, certain amount of entrapped gas remained in the deposited materials, as shown in Table 5.1, which is most likely caused by the low solubility of N in Al and the weak tendency of AlN formation. It has been reported that the solubility of nitrogen in liquid Al ranges from 0.0052 wt. % to 0.0006 wt. % (from 1280 K to 975K) [177], and in solid Al ranges from 0.0002 to 0.001 wt. % [178]. It is evident that the solubility of N in Al is smaller than the measured amount of N in the deposited materials. Consequently, it is unlikely that all internal porosity present will disappear by dissolution of the entrapped gas. The reaction between Al and atomization gas N_2:

$$2Al + N_2 = 2AlN$$
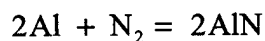
is thermodynamically favorable (ΔG^o, for example, is -215 kJ/mol at 973 K), but kinetically unfavorable [179]. As a result, it is unlikely that a significant amount of AlN would form during atomization. Moreover, X-ray diffraction results showed no detectable amount of AlN present in the deposited materials. Accordingly, it can be concluded that a proportion of pores in the droplets, which results from gas entrapment, may remain following impingement on the deposition surface and contribute to the overall porosity of the deposited materials.

6.2.6.   Flow Straightening Effects

Interstitial porosity is widely reported to be significantly responsible for most of the porosity present in spray formed materials [40, 96, 108-111]. The porosity usually forms when individual droplets overlap each other during impingement, forming interstices which are not subsequently filled by liquid. The formation of interstitial porosity depends strongly on the characteristics of the spray upon the impingement on the substrate, such as the fraction of solid and the droplet size distribution.

The amount of enthalpy extracted from the droplets in flight prior to impingement depends strongly on the droplet size [108, 110, 154]; the smaller the droplet size, the higher the heat extraction rate. In the case of Al-4 wt. % Cu for example, numerical studies [137] showed that the mean heat transfer coefficient and the mean cooling rate for a 10 μm droplet are 11.45×10^{-3} W/(m²K) and 3.3×10^5 K/s, respectively with an initial axial gas velocity of 330 m/s, whereas for a 80 μm droplet they are 3.85×10^{-3} W/m²K and 2.6×10^4 K/s, respectively. Furthermore, the distribution of droplet sizes at a given axial location is Gaussian [112, 168]. Consequently, at a given flight distance, coarser droplets can still be in a fully molten state, while finer droplets are already fully solidified, and droplets with an intermediate size are partially solidified or undercooled.

Many investigators [40, 109, 159, 171] have indicated that the fraction of solid is critical to the amount of porosity in deposited materials. For high fractions of solid, there is not enough liquid to fill the droplet interstices present on the deposition surface, which leads to the formation of interstitial porosity. On the other hand, a low fraction of solid has a dual effect. First, interactions between the excess liquid and the atomization gas cause splashing and whipping of the liquid, thus leading to gas entrapment in the liquid [171]. Second, when the liquid fraction is too high, solidification shrinkage can promote the formation of pores in deposited materials [40, 98, 108, 109, 159]. This suggests that there is an optimal value of fraction of solid upon the impingement, corresponding to the case where there is just enough liquid to fill the interstices between the droplets previously deposited, which minimizes porosity in the deposited materials. An approximation of fraction of solid ($\overline{f_s}$) upon the impingement has been established by Grant et

al. [180]:

$$\overline{f_s} = a_1 + a_2 \Delta T_s + a_3 \frac{v_{go} z^{2/3}}{\dot{M}}$$
(6.5)

where v_{go} is the initial atomizing gas velocity, $\dot{M}$ is the melt mass flow rate, ΔT_s is the superheat above the liquidus, z is the axial distance, and a_1, a_2 and a_3 are constants whose values depend on the particular material of interest. Eq. 5.5 demonstrates that for a given distribution of droplets, the fraction of solid is controlled by four processing parameters, that is the initial atomizing gas velocity, the melt mass flow rate, the superheat above the liquidus, and the axial distance (deposition distance). Ideally, the optimal fraction of liquid can be achieved by carefully adjusting these parameters during the processing. There are, however, other phenomena, such as droplet bouncing off the deposition surface (see section 5.2.1), that have a significant effect on the fraction of solid. Comparisons of the results obtained with LPSF and CSF in the present study suggest that the nature of the flow field is also an important factor.

To clearly elucidate the effects of the flow field on the fraction of solid, the atomizing chamber above the substrate and below the nozzle tip is divided into three zones (Figure 6.14). Zone I and Zone II represent the spray cone. Zone I contains the droplets that eventually impinge on the substrate and predominately contribute to the deposit build-up. Zone II is right next to Zone I and contains the droplets that miss the substrate. Zone III is the region outside the spray cone (Figure 6.14). The extent of Zone II depends on the factors that affect the droplet trajectories and the size of the substrate. Numerical predictions of droplet trajectories demonstrated that droplet dispersion from the spray axis could be as much as 60°, and smaller droplets have the greater radial dispersion than larger droplets [111, 112, 138]. Furthermore, a number of experimental and numerical investigations have shown that the droplet size decreases radially outward [110, 112, 138, 159, 166, 167]. For example, the results of Uhlenwinkle and Bauckhage [167] showed that the mass median diameter of droplets decreases with increasing radial distance. Consequently, the spatial density of larger droplets in Zone I decreases from the center to the edge, whereas the spatial density of smaller droplets is higher at the edge. Hence, it follows that Zone II is dominated by smaller droplets. Furthermore, for a given droplet size, the droplet velocity along the spray axis is larger than that at the periphery of the spray cone [112]. Therefore, for a given droplet size, droplets are more likely to be fully solidified at the periphery than along the spray axis because of the induced difference in flight time. As discussed above, small droplets are more likely to be fully solid upon impingement, whereas large droplets are expected to be fully liquid or semi-solid. In summary, droplets in Zone I can be fully solidified, partially solidified, or fully liquid, but small droplets are predominant at the periphery. Zone II is dominated by fully solid small droplets. Ideally, there is no interaction among the three zones. Then, when the optimal fraction of solid is
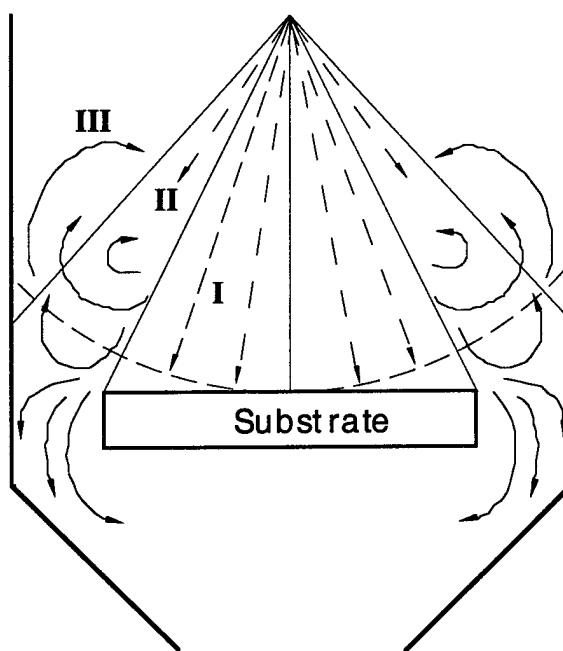
(a)
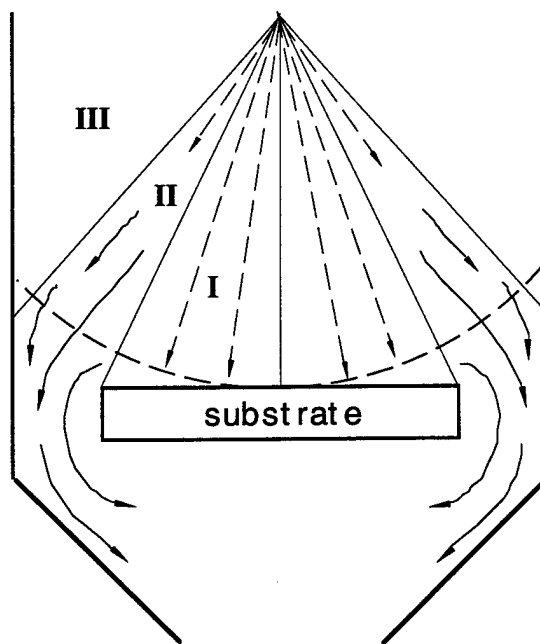
(b)

Figure 6.14.Schematic diagram showing the flow field in the atomizing chamber for (a) CSF, and (b) LPSF.

achieved in Zone I, the lowest porosity in the deposited materials can be obtained. However, the flow field perturbs this ideal case. In CSF, a shear layer develops between the atomization gas and the stagnant ambient gas eventually resulting in the creation of a toroidal recirculation vortex. When solidified droplets impinge on the deposition surface in Zone I, some of them, especially at the periphery, bounce off and are carried by recirculating flow gas into Zone II and Zone III. On the other hand, most droplets in Zone II impinge on the chamber wall, and a proportion of them rebound from the wall and are carried by recirculating flow gas into Zone III and Zone I (Figure 6.14a). As a result, a proportion of droplets in the Zone II and Zone III randomly enters into Zone I, which alters the optimal fraction of solid in Zone I and leads to a larger amount of porosity present in the deposited materials. In the case of LPSF, however, the lower pressure reduces the density of the initially stagnant ambient gas. This results in a significantly weak shear layer and, consequently, a weak recirculation vortex. This flow field modification diminishes significantly the recirculation of droplets from both Zone I and Zone II. Instead, these droplets travel down to the bottom of the chamber to the exit (Figure 6.14b). In this case, few droplets are present in Zone III, which is in agreement with the experimental observation that the recirculation region corresponding to Zone III is much cleaner than that for CSF. Therefore, the droplet trajectories and gas flow are straighter and the amount of droplets that could get into Zone I by recirculation is minimized, which keeps the optimal fraction of solid in Zone I nearly unaffected, and hence low porosity is achieved in the deposited materials.

The fraction of solid upon the impingement is not uniform across the substrate because of droplet size distribution on Zone I. Even if the optimal fraction of solid is achieved at the spray axis, there would be a gradual deviation from the optimal fraction of solid with increasing distance from the spray axis. Therefore, more pores are present at the edge. As a result, deposited materials exhibit higher porosity at the edges than at center as shown in Figure 6.3 and 6.4.

VII. MODELING OF POROSITY DURING SPRAY ATOMIZATION AND DEPOSITION

7.1. Formulation

7.1.1. Porosity Model

Three major mechanisms of porosity formation during spray forming have been proposed, that is, gas porosity; interstitial porosity; and solidification shrinkage [37, 40, 109-111]. Consequently, porosity present in as-deposited materials can be described as the sum of gas porosity, porosity from solidification shrinkage and interstitial porosity. However, since it is difficult to discern between gas porosity and solidification shrinkage [181-184], both types of porosity are treated as one single porosity source, i.e., a solidification porosity, in the present study. Considering that the formation of interstitial porosity is due to the lack of sufficient liquid to fill particle interstices, whereas solidification porosity is significant, primarily when excessive liquid is present in spray upon impingement, interstitial porosity and solidification porosity may be treated as two mutually exclusive phenomena. Consequently, when interstitial porosity is predominant, solidification porosity is neglected. Conversely, when solidification porosity is predominant, interstitial porosity is neglected. On the basis of the considerations described above, a porosity model is developed to estimate the amount of porosity formed in as-deposited materials during spray forming. This model essentially incorporates two main assumptions. First, it is assumed that the droplets in the incident spray are grouped into two classes, i.e., fully liquid droplets and completely solidified droplets. Considering the breaking-up upon impingement, partially solidified droplets can be reasonably represented in both classes proportionally to their fraction. Second, it is assumed that the deposited material is built up by formation of successive layers. One layer forms on previous layer only after the latter is completely solidified. There is no interaction among layers. Each layer forms by a two stage mechanism (Figure 7.1). During the first stage, solidified droplets impinge on the previous layer and form a random dense particle packing structure (Figure 7.1a). During the second stage, liquid droplets first impinge on the resultant particle packing structure (Figure 7.1b); then liquid subsequently flows into the particle packing structure and finally solidifies (Figs. 1c and 1d). In practice, solid and liquid droplets arrive at the deposition surface simultaneously. Hence, it is further assumed that there is no resistance for liquid flowing into the particle packing structure. Moreover, it is assumed that the volumetric shrinkage during liquid solidification inside the particle packing structure can be instantaneously compensated for. On the basis of these assumptions, two cases are taken into consideration, as schematically shown in Figure 7.1c and Figure 7.1d. If the volume of liquid, once solidified, is smaller than that of the voids in the particle packing structure (Figure 7.1c),

porosity is assumed to be dominated by interstitial porosity. In this case, porosity is estimated directly from the fraction of voids that are not filled by liquid. On the other hand, if the volume of liquid, once solidified, is more than that of the voids (Figure 7.1d), porosity is assumed to be controlled by solidification of the liquid left. A detailed study on solidification porosity is outside of the scope of the present study; in order to maintain the problem tractable, solidification porosity is simply represented by a volumetric shrinkage factor during solidification. A thorough treatment of solidification porosity can be found in references [182-187].

Let V be the total volume of the incident spray, $\overline{f_s}$ its fraction of solid, V_p the total volume of the solidified particle packing structure and Γ the particle packing density (the volume fraction occupied by the particles in the packing structure). Then, the volume of solid in the spray is $V\overline{f_s}$ and the volume of voids in the particle packing structure $V_p(1-\Gamma)$. Let Ω be the sticking efficiency that is defined herein as a volume fraction of droplets that stick on the deposition surface and contribute to the build-up of deposited material. Then, conservation of volume can be written as:

$$V_p\Gamma = \Omega V\overline{f_s}$$

(7.1)

For simplicity, Ω is assumed to be 1.0 in the present study.

The fact that the volume of liquid in the incident spray, once solidified, occupies an equal or a smaller volume than the available void volume in the particle packing can be described by:

$$V_p(1-\Gamma) - V\left(1-\overline{f_s}\right)(1-\beta) \geq 0$$

(7.2)

where $V\left(1-\overline{f_s}\right)(1-\beta)$ is the volume of liquid in the incident spray after solidification and β is solidification contraction ($\beta = 1 - \rho_m/\rho_s$). Combining Eqs. 7.1 and 7.2 yields:

$$\Phi \equiv \left(\frac{1-\Gamma}{\Gamma}\right) - \left(\frac{1-\overline{f_s}}{\overline{f_s}}\right)(1-\beta) \geq 0$$

(7.3)

where Φ is defined as a porosity coefficient. In this case, porosity is dominated by interstitial porosity, whose amount corresponds to the volume of unfilled voids in the particle packing divided by the total volume of the particle packing (i.e., volume fraction of voids):

$$p = \frac{V_p(1-\Gamma) - V(1-\overline{f_s})(1-\beta)}{V_p} = \Phi\Gamma$$

(7.4)
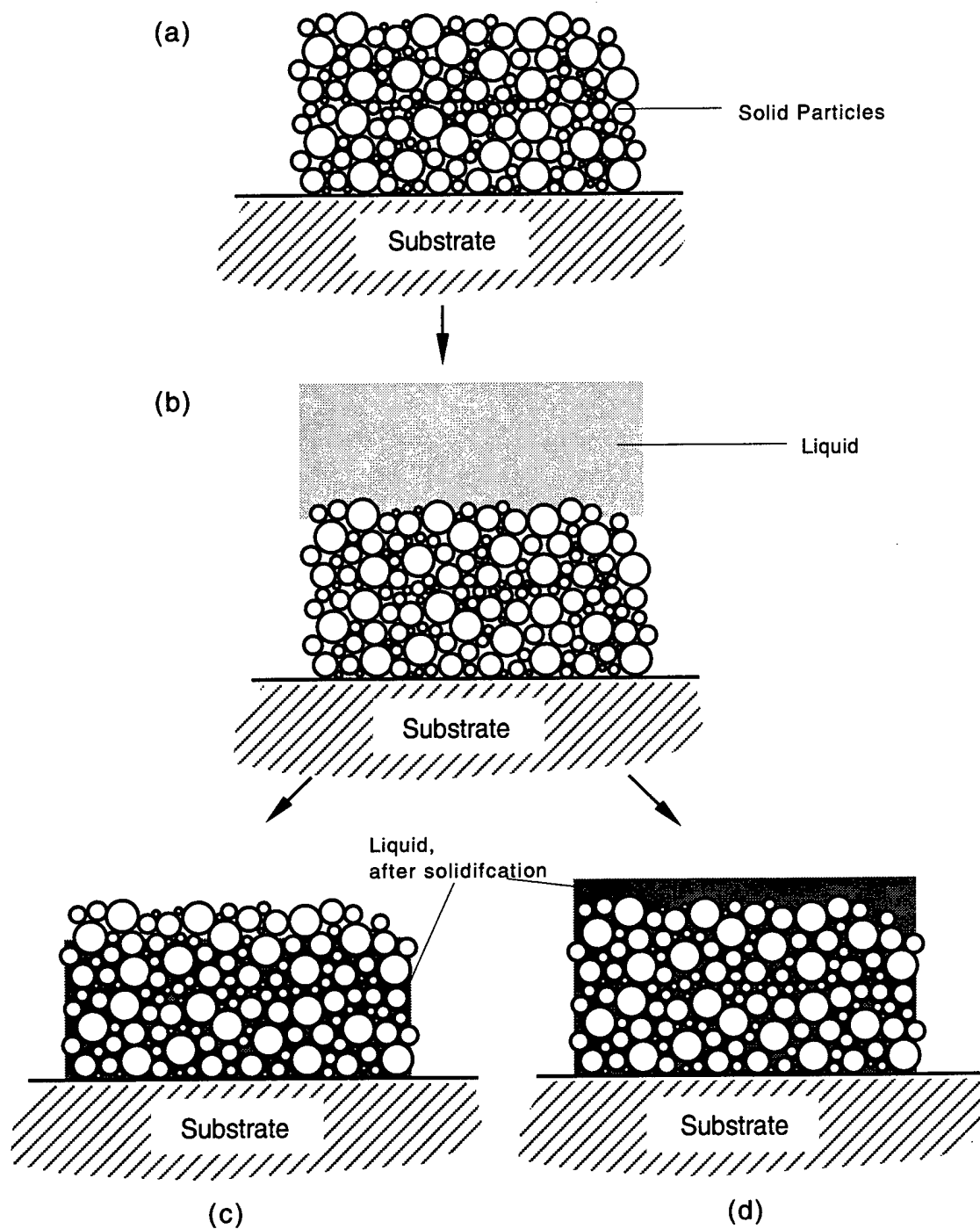
Figure 7.1. Schematic diagram showing two stage mechanism of forming a deposited material. (a) solid particles forming a random dense particle packing structure, (b) liquid droplets impinging on the particle packing structure, (c) and (d) liquid flowing into the particle packing structure and subsequently solidifying.

If $\Phi < 0$, i.e., the volume of the incident liquid, once solidified, occupies a larger volume than the available void volume in the particle packing. Hence, porosity is dominated by the voids created by solidification of any remaining liquid. Noting that the volume of liquid needed to completely fill the voids following solidification is $V_p(1-\Gamma)/(1-\beta)$, porosity can then be simply estimated on the basis of the volumetric shrinkage during solidification as:

$$p = \frac{\left[V(1-\bar{f_s}) - \frac{V_p(1-\Gamma)}{1-\beta}\right]\beta}{V_p + V(1-\bar{f_s}) - \frac{V_p(1-\Gamma)}{1-\beta}} = \frac{\Phi\Gamma\beta}{\Phi\Gamma - (1-\beta)} \qquad (7.5)$$

In summary, under the assumptions stated above, porosity can be evaluated using the following expression:

$$p = \begin{cases} \Phi\Gamma & \Phi \geq 0 \\ \dfrac{\Phi\Gamma\beta}{\Phi\Gamma - (1-\beta)} & \Phi < 0 \end{cases} \qquad (7.6)$$

where p is porosity or volume fraction of voids, Φ is defined as a porosity coefficient which characterizes the conditions for porosity formation and is a function of the average fraction of solid in the incident spray, the particle packing density and the solidification shrinkage contraction. It should be indicated that when Φ equals to zero, porosity (p) equals to zero as well, which is inconsistent with available experimental data. However, it should be noted that the present model is a simplified one; several other sources or factors are not taken into consideration in the present model. First, gas porosity actually is comprised of two components, i.e. porosity resulting from gas rejection due to the difference of solubility between solid and liquid; and porosity resulting from mechanical gas entrapment. Gas entrapment can occur during gas atomization, which is thought to be responsible for the pores observed in oversprayed powders [35], and anticipated to contribute a proportion of porosity in as-deposited materials. Second, in this model solidification porosity is neglected when interstitial porosity is predominant, and vice-versa. In practice, these two types of porosity can and probably will co-exist simultaneously. Third, porosity is also influenced by other factors such as substrate condition and flow field around spray cone [35, 40]. However, since interstitial porosity plays a critical role in spray formed materials as described previously, it is anticipated that the porosity contribution from the first two sources should be insignificant. As for factors such as substrate condition and flow field, a number of approaches can be adapted to minimize their influences. For example, interference from the flow field can be overwhelmed by applying a controlled pressure environment [35]. It should also be indicated that the present model does not taken account of the effects of microstruture evolution on porosity after

impingement.

In Eq. 7.6, β is determined by material densities. Correspondingly, in order to estimate the amount of porosity, average fraction of solid and particle packing density must be determined.

7.1.2. Average Fraction of Solid

The average fraction of solid in the incident spray can be determined as follows

$$\overline{f_s} = \int_0^\infty f_s(x,z)g(x)dx \qquad (7.7)$$

where $f_s(x,z)$ is fraction of solid for a single droplet as a function of its size (x) and the deposition distance (z); $g(x)$ is the probability density function for a given particle size distribution. To determine the fraction of solid for a single droplet, knowledge of its dynamic and thermal history during atomization is essential. Accordingly, in following sections, the size distribution of atomized particles, and the formulation of the dynamics and thermal history of single droplets are described.

7.1.3. Gas Atomized Droplet Size Distribution

During gas atomization, the melt stream is energetically disintegrated into a dispersion of droplets. The droplet size distribution for a variety of gas atomized metals and alloys has been widely reported to follow a lognormal distribution [111, 126, 171, 188-191]. Accordingly, the probability density function ($g(d)$) of droplet size distribution can be expressed as follows [192-194]:

$$g(d) = \frac{1}{\ln\sigma_g\sqrt{2\pi}}\left(\frac{1}{d}\right)\exp\left[\frac{(\ln d - \ln d_m)^2}{2\ln^2\sigma_g}\right] \qquad (7.8)$$

where d_m and σ_g are the mass median diameter and geometric standard deviation, respectively. Numerous investigations have been conducted to predict the mass mean diameter (d_m) of particles produced by gas atomization [189, 190, 194-196]. Among these, an empirical equation derived by Lubanska [188] based on experimental results for iron, steel and tin, is widely used:

$$d_m = DK\left[\frac{\eta_m}{\eta_g W}\left(1 + \frac{\dot{M}}{\dot{G}}\right)\right]^{1/2} \qquad (7.9)$$

where, D is melt stream diameter, and K constant. W is the Weber number, a dimensionless number representing the ratio of the fluid inertial forces to the surface tension forces

($W = v^2 \rho_m D / \gamma_m$), where v is gas velocity during impact of gas jets with melt stream. Lubanska's equation has been shown to agree reasonably well with experimental data for a variety of metals and alloys, such as Al and Cu [111, 190]. Therefore, this equation is used to estimate the mass median diameter in the present study. For a wide range of metals and alloys, σ_g generally decreases as d_m decreases; an empirical relation has been established as follows [189, 190]:

$$\sigma_g = a d_m^b \tag{7.10}$$

where a and b are constants. The melt flow rate, $\dot{M}$ in this study is selected as one of the input parameters. The gas velocity during impact on the melt stream (v) and gas flow rate ($\dot{G}$) depend on atomization pressure and the design of the atomizer, which can be estimated as follows. On the basis of earlier studies on atomization nozzles used in our laboratory [126], these types of nozzles can be treated as convergent-divergent ones. It is assumed that the atomizer manifold is large enough so that the velocity of gas in the manifold is considered to be nearly zero. Accordingly, the manifold pressure (atomization gas pressure) and temperature represent the stagnation pressure (P_o) and stagnation temperature (T_o), respectively. Hence, the Mach number (M_a) at the nozzle exit can be calculated by the ratio of atomization gas pressure and the exit gas pressure (P_e) following compressible fluid mechanics by assuming steady state and isentropic flow for an ideal gas [197, 198]. Moreover, to account for friction effects and the differences between the atomization nozzle used and an ideal convergent-divergent nozzle, a correlation coefficient (C_M) is introduced. Thus, the Mach number can be calculated from:

$$M_a = C_M \left\{ \frac{2}{\gamma - 1} \left[\left(\frac{P_o}{P_e} \right)^{\frac{\gamma - 1}{\gamma}} - 1 \right] \right\}^{\frac{1}{2}} \tag{7.11}$$

where γ is the ratio of specific heat of atomization gas. Assuming that the nozzle is operated at the optimal condition, i.e. $P_e = P_a$ (P_a is atomization chamber pressure), the Mach number can then be readily determined. The gas temperature at the nozzle exit (T_e) can be determined by the following relationship [199]:

$$\frac{T_o}{T_e} = 1 + \frac{\gamma - 1}{2} M_a^2 \tag{7.12}$$

and the sonic velocity v_s at the nozzle exit can be calculated:

$$v_s = \left(\gamma R T_e \right)^{\frac{1}{2}} \tag{7.13}$$

where R is gas constant. Finally, the gas velocity at the nozzle exit (v_e) is determined by:

$$v_e = M_a v_s \tag{7.14}$$

Neglecting the decay of gas velocity from the exit to the point of atomization, the gas velocity

during impact with the melt stream is then same as the exit velocity. The gas flow rate can be estimated by:

$$\dot{G} = A_e \rho_{ge} v_e \qquad (7.15)$$

7.1.4. Droplet Dynamics

Once a droplet is created during gas atomization, the velocity difference between the droplet and the atomization gas results in a drag force which causes the droplet to accelerate until the droplet velocity exceeds the gas velocity, and then to decelerate. Following the discussion in reference [197], the equation of motion for a droplet can be described as:

$$\frac{dv_d}{dt} = \frac{3}{4}\frac{C_D \rho_g}{d\rho_d}(v_g - v_d)|v_g - v_d| + g\left(1 - \frac{\rho_g}{\rho_d}\right) \qquad (7.16)$$

In this equation, the "added mass" term and "history" term have been neglected by assuming that droplet motion is affected only by the gravity force and by the drag from the adjacent fluid. The droplet drag coefficient, C_D, is estimated by [112]:

$$C_D = \begin{cases} 24/\text{Re} & 0 < \text{Re} < 1 \\ 24/\text{Re}^{0.646} & 1 \leq \text{Re} < 400 \\ 0.5 & 400 \leq \text{Re} < 3 \times 10^5 \end{cases} \qquad (7.17)$$

Based on the results of various experimental and theoretical studies, Grant et al. [111] established an approximated relation for axial gas velocity:

$$v_g = v_{go}\exp\left(-\frac{z}{\lambda}\right) \qquad (7.18)$$

where the exponential decay coefficient $\lambda = 3.04 \times 10^{-4}v_{go}^{1.24}$. Eqs. 7.16 to 7.18 are solved numerically to yield the droplet axial velocity. In these calculations, the droplet density is assumed constant for simplicity.

7.1.5. Droplet Thermal History

During the flight of a droplet towards a substrate, heat extraction from the droplet surface occurs by radiative and convective cooling. Droplet cooling is usually treated under the assumption of Newtonian cooling conditions (i.e., homogenous temperature inside of a droplet) [63, 137, 138, 156, 200-202]. The droplet cooling can be described by five respective cooling stages for an eutectic binary alloy system: liquid phase cooling; nucleation and recalescence; segregated solidification; eutectic solidification; and solid phase cooling. However, before

formulating these five cooling stages, the liquid undercooling should be estimated first.

Droplet undercooling

Liquid metal atomization has been widely regarded as a rapid solidification process. It is well known that one of the characteristics of rapid solidification is the attainment of relatively high levels of undercooling before the onset of nucleation. In practice, heterogeneous nucleation prevails for the majority of processing conditions. The nucleation frequency per unit volume for heterogeneous nucleation is given by [201]:

$$J_v(T) = 10^{40} \exp\left[-\frac{16\pi}{3k_B T} \frac{T_l^2 \gamma_{sl}^3 f_w(\theta)}{\rho_d^2 \Delta H_f^2 (T_l - T)^2}\right] \qquad (7.19)$$

where $f_w(\theta) = \frac{1}{4}(2 - 3\cos\theta + \cos^3\theta)$, which can be simplified with an assumption that $f_w(\theta)$ obeys an inverse relation with the droplet size [137]:

$$f_w(\theta) = -5.025 \times 10^{-3} + \frac{1.005 \times 10^{-6}}{d} \qquad (7.20)$$

For a continuous cooling process, the total number of nuclei formed per unit volume can be written as [203, 204]:

$$n = \int_{T_N}^{T_l} \frac{J_v(T)}{\dot{T}} dT \qquad (7.21)$$

Assuming that the formation of a single nucleus represents the onset of nucleation in a given droplet with a volume of V_d, the critical condition for onset of nucleation then can be described by:

$$V_d \int_{T_N}^{T_l} \frac{J_v(T)}{\dot{T}} dT = 1 \qquad (7.22)$$

It has been indicated that $J_v(T)$ is essentially zero except for a very narrow temperature range near T_N [203]. Hence, by introducing a correlation coefficient α ($0 < \alpha < 1$), this narrow temperature range can be assumed to be represented by $\alpha(T_l - T_N)$ in which $J_v(T)$ is equal to $J_v(T_N)$. Consequently, the critical condition becomes:

$$\frac{\alpha(T_l - T_N) J_v(T_N) V_d}{\dot{T}} = 1 \qquad (7.23)$$

Solving Eqs. 7.19 and 7.23, the nucleation temperature T_N can be determined.

Liquid phase cooling

During this stage, a droplet cools from its initial temperature (i.e., melt temperature) to the

nucleation temperature T_N. An energy balance between the thermal energy of the atomized droplets and that released to the atomization gas leads to the following equation:

$$-d C_{pl} \rho_l \frac{dT}{dt} = 6h(T - T_g) + 6\varepsilon\sigma(T^4 - T_g^4)$$ (7.24)

where, h is the convective heat transfer coefficient, which can be estimated using an experimental correlation developed by Ranz and Mashall [205]:

$$h = \frac{K_g}{d}\left(2 + 0.6 \operatorname{Re}^{\frac{1}{2}} \operatorname{Pr}^{\frac{1}{3}}\right)$$ (7.25)

During this stage, the droplets have not solidified yet, thus

$$f_s(d,z) = 0$$ (7.26)

Nucleation and Recalescence

Once the liquid temperature reaches the nucleation temperature, T_N, the recalescence process begins to occur. Since the release of latent heat ensuing the nucleation of the solid phase is so large that regardless of the quenching capacity of the surrounding environment, the released heat cannot be dissipated, a rapid increase in droplet temperature occurs during recalescence [156]. However, since recalescence is driven by undercooling, as the droplet temperature increases, the rate of latent heat release decreases. Once the rate of latent heat release is equivalent to that of heat extraction from the surface of the droplet, the recalescence process terminates. According to Levi and Mehrabian [206], the enthalpy of a semi-solid system at temperature T can be expressed as:

$$H - H_{sm} = [\Delta H_f + C_{pl}(T - T_l)](1 - f_s) + C_{ps}(T - T_l)f_s$$ (7.27)

Accordingly, at the end of recalescence (i.e., $\frac{dT}{dt} = 0$), a heat balance equation can be written:

$$d\rho_d[\Delta H_f - (C_{pl} - C_{ps})(T_l - T_r)]\frac{df_s}{dt} = 6h(T_r - T_g) + 6\varepsilon\sigma(T_r^4 - T_g^4)$$ (7.28)

Furthermore, it has been indicated that the growth rate of the solid phase in an undercooled melt can be estimated as follows [137]:

$$\frac{df_s}{dt} = R_i \frac{T_l - T}{d}$$ (7.29)

Solving Eqs. 7.28 and 7.29 yields the recalescence temperature T_r. The maximum fraction of solid f_r at the end of recalescence can be estimated by following equation [126]:

$$f_r = \left(T_l - T_N\right)\frac{C_{pl}}{\Delta H_f} \qquad (7.30)$$

Segregated solidification

Once the droplet temperature reaches the recalescence temperature T_r, segregated solidification starts. Considering the resulting latent heat release, the heat balance equation thus becomes:

$$-\rho_d d\left\{C\frac{dT}{dt} - \left[\Delta H_f - \left(C_{pl} - C_{ps}\right)\left(T_l - T\right)\right]\frac{df_s}{dt}\right\} = 6h\left(T - T_g\right) + 6\varepsilon\sigma\left(T^4 - T_g^4\right) \quad (7.31)$$

where $C = C_{ps}f_s + C_{pl}\left(1 - f_s\right)$, and the droplet density is estimated by

$$\rho_d = \rho_s f_s + \rho_l\left(1 - f_s\right) \qquad (7.32)$$

During this stage, solidification can be approximately described on the basis of the Scheil equation [181, 207]:

$$\frac{df_s}{dT} = \frac{1 - f_r}{\left(k_e - 1\right)\left(T_M - T_r\right)}\left\{\frac{T_M - T_r}{T_M - T}\right\}^{\frac{k_e - 2}{k_e - 1}} \qquad (7.33)$$

and

$$f_s = 1 - \left(1 - f_r\right)\left(\frac{T_M - T}{T_M - T_r}\right)^{\frac{1}{k_e - 1}} \qquad (7.34)$$

Eutectic solidification

When the eutectic temperature, T_E, is reached, the droplets then remain at this temperature until solidification is complete. Hence, the heat balance equation during this stage can be written as:

$$d\rho_d\left[\Delta H_f - \left(C_{pl} - C_{ps}\right)\left(T_l - T_E\right)\right]\frac{df_s}{dt} = 6h\left(T_E - T_g\right) + 6\varepsilon\sigma\left(T_E^4 - T_g^4\right) \quad (7.35)$$

where the droplet density, ρ_d is estimated using Eq. 7.32.

Solid phase cooling

Once solidification is complete, $f_s(d,z) = 1$ and the associated thermal energy balance can be written as:

$$-d\rho_s C_{ps} \frac{dT}{dt} = 6h\left(T - T_g\right) + 6\varepsilon\sigma\left(T^4 - T_o^4\right) \qquad (7.36)$$

Particle packing density

For a lognormal particle size distribution, particle packing density depends primarily on the geometric standard deviation of size distribution and the particle geometry [208-211]. The larger the geometric standard deviation, the higher the particle packing density. The particle size has no direct influence on particle packing density. Based on their experimental results, Sohn and Moreland [210] suggested a hyperbolic relationship between packing density and geometric standard deviation for a lognormal distribution:

$$\Gamma = a_1 - \frac{a_2}{\sigma_g} \qquad (7.37)$$

where a_1 and a_2 are constants which depend essentially on particle sphericity, Ψ [209, 210]. Particle sphericity is a quantitative particle shape index based on the ratio of the surface area of a sphere of equivalent volume divided by the surface area of the particle [211]. Regarding the geometry of the metal particles produced by gas atomization, it has been well documented that the particles are predominately spherical [190, 212, 213]. However, there are many factors influencing particle sphericity, such as the presence of surface satellites, which results from the collision or impingement of fine solidified particles onto coarser molten or semi-solid particles during atomization [213]; surface roughness which leads to a lower sphericity [190]; and the presence of oxides or impurities on the particle's surface, which retards droplet spheroidization during atomization [190]. Moreover, Ridder et al. [214] reported that the process parameters have a significant influence on particle shape. Consequently, it is more reasonable to consider the particles produced by gas atomization to be near-spherical (or well rounded) instead of spherical. According to Peronius and Sweeting [215], near-spherical particles have a range of sphericity from 0.7 to 1.0. Hence, for simplicity, an arithmetic mean sphericity, i.e., $\Psi = 0.85$, is used for the packing density calculations in the present study. The constants a_1 and a_2 then are determined by interpolating the data reported by Sohn and Moreland [210], which are 0.8198 and 0.2148, respectively. It should be indicated that in this study, the size distribution and geometric standard deviation for solid droplets are assumed to be the same as those of the entire droplet size distribution.

7.1.6. Model Material and Properties

N_2 and Ar are the most frequently used gases in gas atomization and spray forming of metals

and alloys. As a result, the influences of these atomization gases on the formation of porosity were investigated. The physical properties of these gases are listed in Figure 7.1. For simplicity, the temperature of atomization gas is assumed to remain constant (300 K) during the spray forming process.

Model materials that were investigated include: Al-4Cu, Cu-6Ti, Fe-8Ti, Ni-20Cr and Sn-15Pb (all in weight percent and all alloys will be simply designated as Al-Cu, Cu-Ti, Fe-Ti, Ni-Cr and Sn-Pb). There are three reasons to select these alloy systems. First, these five alloy systems all exhibit a simple phase transformation (i.e., eutectic). Second, they are selected such that a wide range of materials properties can be investigated. Finally, Al-Cu, Cu-Ti, Sn-Pb and Ni-Cr have been experimentally studied in a variety of spray forming investigations [91, 93, 109, 137, 154, 201, 216]. The properties of these alloys are listed in Tables 2 and 3. It should be noted that because of very limited data available for these alloys, most of the properties listed in Tables 2 and 3 are estimated by a rule of mixtures approach based on the data obtained from references [170, 217]. Furthermore, the viscosities used are those corresponding to the pure components (solvents). The solid-liquid interfacial energy (γ_{sl}) is estimated by a two step procedure. First, the solid-liquid interfacial energy of each pure component in an alloy system is estimated by using a correlation suggested by Turnbull [218], which can be expressed to be:

$$\gamma_{sl} = 0.45\Delta H_f \left(\frac{\rho_s^2 A}{N_A}\right)^{\frac{1}{3}}$$ (7.38)

where ΔH_f is latent heat of melt, ρ_s is density of the element, A is atomic weight of the element and N_A is Avogadro's number. Second, the solid-liquid interfacial energy of each alloy system is estimated by using a rule of mixtures approach. Equilibrium partition coefficients and phase transformation temperatures are retrieved directly from respective binary phase diagrams [219]. For simplicity, the differences of specific heats between the liquid and the solid are neglected during calculations of droplet thermal history. Calculations of the average fraction of solid are conducted starting from a droplet size of 1 μm to a size corresponding to a fraction of solid of zero at the given conditions, which generally cover a droplet size range of 1 μm to 800 μm.

The numerical assessment of correlation coefficient α in Eq. 7.23 in a range of 0.001 to 0.9 reveals that the influence of α on the resultant undercooling for a given droplet size is limited within a few degrees. Hence, α is arbitrarily taken as 0.01. The a and b are taken as 0.425 and 0.333 respectively with d_m in micrometers, from the work of Lubanska [188], which has been widely used in many numerical studies [109, 171]. The constant K is approximately taken to be 50 [171]. The total cross sectional area for gas flow at the nozzle exit (A_e) is taken as 8.21×10^{-6}, which corresponds to a 18 jet atomizer used in our laboratory. The correlation coefficient (C_M) for Mach number is estimated to be 0.549 for N_2 and 0.625 for Ar based on the reported maximum

Mach number achieved during high pressure atomization [220].

Table 7.1.   Physical Properties of Atomization Gases [170]

		N_2	Ar
ρ_g	(kg/m^3)	1.12	1.5979
μ_g	(Ns/m^2)	1.873×10^{-5}	2.29×10^{-5}
K_g	$(W/m.K)$	0.0258	0.0179
C_{pg}	$(J/kg.K)$	1043.21	520.67
g	(-)	1.40	1.67
R	$(J/kg.K)$	297	208

Table 7.2.   Model Materials Properties[170, 217, 219]

		Al-4Cu	Cu-6Ti	Fe-8Ti	Ni-20Cr	Sn-15Pb
k_e	(-)	0.166	0.3448	0.592	0.666	0.0833
T_M	(K)	933	1357	1811	1728	505
T_l	(K)	923	1293	1673	1693	485
T_E	(K)	821	1158	1562	1618	371
C_{ps}	$(J/kg\,K)$	882	394	461.76	453.8	211.57
ρ_s	(kg/m^3)	2777	8692	7600	8540	7957
ΔH_f	(J/kg)	387000	213878	251110	319200	53770
ε	(-)	0.05	0.14	0.37	0.36	0.15
γ_{sl}	(J/m^2)	0.125	0.190	0.220	0.271	0.056
C_{pl}	$(J/kg\,K)$	1080	503	787.4	652	235.3
β	(-)	0.85	0.86	0.89	0.89	0.95

Table 7.3. Materials Properties as a Function of Temperature [217]

	ρ_m (kg/m^3)	γ_m (J/m^2)	μ_m $(N\,s/m^2)$
Al-4Cu	$2385 - 0.28(T - T_l)$	$0.914 - 3.5\times10^{-4}(T - T_l)$	$1.492\times10^{-4}\exp\left(\dfrac{16500}{8.3144T}\right)$
Cu-6Ti	$7520 - 0.8110(T - T_l)$	$1.306 - 1.4\times10^{-4}(T - T_l)$	$3.001\times10^{-4}\exp\left(\dfrac{10900}{8.3144T}\right)$
Sn-15Pb	$7552 - 0.7184(T - T_l)$	$0.533 - 7.9\times10^{-5}(T - T_l)$	1.97×10^{-3}
Ni-20Cr	$7580 - 0.988(T - T_l)$	$1.762 - 3.7\times10^{-4}(T - T_l)$	$1.663\times10^{-4}\exp\left(\dfrac{50200}{8.3144T}\right)$
Fe-8Ti	$6783 - 0.8685(T - T_l)$	$1.854 - 4.72\times10^{-4}(T - T_l)$	$3.699\times10^{-4}\exp\left(\dfrac{41400}{8.3144T}\right)$

The important processing parameters during spray forming, which are considered in the simulations, include: melt superheat, deposition distance, atomization pressure, initial gas velocity, gas flow rate and melt flow rate. Among these processing parameters, melt superheat and deposition distance are independent parameters. However, atomization pressure, initial gas velocity and gas flow rate are intimately related. Generally, for a given atomizer, a certain relationship between atomization pressure and exit gas velocity exists. For example, it is reported that atomization gas pressure exponentially related to the gas velocity at 250 mm downstream from the nozzle exit [220]. The gas flow rate can be estimated by using Eq. 7.15 or a similar relationship. Accordingly, only one of them can be considered as an independent parameter. In the present study, atomization gas pressure is selected. Melt flow rate depends largely on melt height, melt stream diameter, and is also influenced by atomization gas pressure through associated aspiration phenomena present at the delivery nozzle exit for a close-coupled atomizer [189, 220, 221]. Hence, melt flow rate is considered as a quasi-independent parameter. Accordingly, these four independent or quasi-independent parameters are selected for study. The typical ranges of these four independent or quasi-independent parameters studied are: superheat of melt from 50 to 250 K; deposition distance from 0.1 m to 0.6 m, atomization gas pressure from 1 to 10 MPa; and melt flow rate from 0.001 to 0.6 kg/s.

7.2. Results

7.2.1. Average Fraction of Solid

Figures 7.2, 7.3 and 7.4 show average fraction of solid as a function of deposition distance, atomization pressure and melt flow rate for the Al-Cu. Evidently, the average fraction of solid, in all cases, varies monotonically with these parameters. The average fraction of solid increases with increasing deposition distance and atomization gas pressure (Figures 7.2 and 7.3); decreases with increasing melt flow rate (Figure 7.4). For example, the fraction of solid increases from about

0.46 to 0.78 as deposition distance increases from 0.1 to 0.6 m under melt superheat of 100 K (Figure 7.2). The average fraction of solid increases from 0.68 to 0.83 as the atomization pressure increases from 1 to 10 (Figure 7.3), and decreases from 0.90 to 0.56 as melt flow rate increases from 0.001 to 0.02 kg/s (Figure 7.4), for a melt superheat of 150 K. As shown in Figures 7.2, 7.3 and 7.4, average fraction of solid significantly decreases as melt superheat increases at a given condition. For instance, at a deposition distance of 0.3 m, average fraction of solid is 0.58 for a superheat of 250 K, whereas it is 0.66 for a superheat of 100 K.

Figure 7.5 shows the variations of average fraction of solid with melt flow rate for atomization gases of N_2 and Ar. It is shown that average fraction of solid is significantly different for N_2 and Ar. At a given melt flow rate, the average fraction of solid for N_2 is higher than that for Ar (Figure 7.5). For instance, at a melt flow rate of 0.01 kg/s, the average fraction of solid is about 0.79 for N_2 and 0.52 for Ar.

Variations of average fraction of solid with respective processing parameters for other alloy systems are similar to that of Al-Cu alloy. However, as shown in Figure 7.6, melt flow rate varies significantly with alloy composition. For example, for an average fraction of solid of 0.7, the corresponding melt flow rates are approximately 0.015 kg/s for Al-Cu, 0.026 kg/s for Fe-Ti, 0.05 kg/s for Ni-Cr, 0.125 kg/s for Sn-Pb and 0.35 kg/s for Cu-Ti.

7.2.2. Packing Density

The particle packing density decreases noticeably with increasing atomization gas pressure; and with decreasing melt flow rate, as shown in Figures 7.7 and 7.8. For example, packing density decreases from 0.73 to 0.713 as atomization pressure increases from 1 to 10 MPa; and increases from 0.70 to 0.73 as melt flow rate increases from 0.001 to 0.02 kg/s, at melt superheat of 150 K. Deposition distance has no effects on packing density, simply because deposition distance has no influence on mass median diameter and geometric standard deviation (Lubanska's correlation). The influences of melt superheat on packing density are shown in Figures 7.7 and 7.8. Generally, packing density increases with decreasing melt superheat. For example, at a given condition such as a deposition distance of 0.4 m, an atomization pressure of 1.2 MPa and melt flow rate of 0.01 kg/s, the packing density increases from 0.717 at 250 K to 0.724 at 50 K (Figure 7.7).
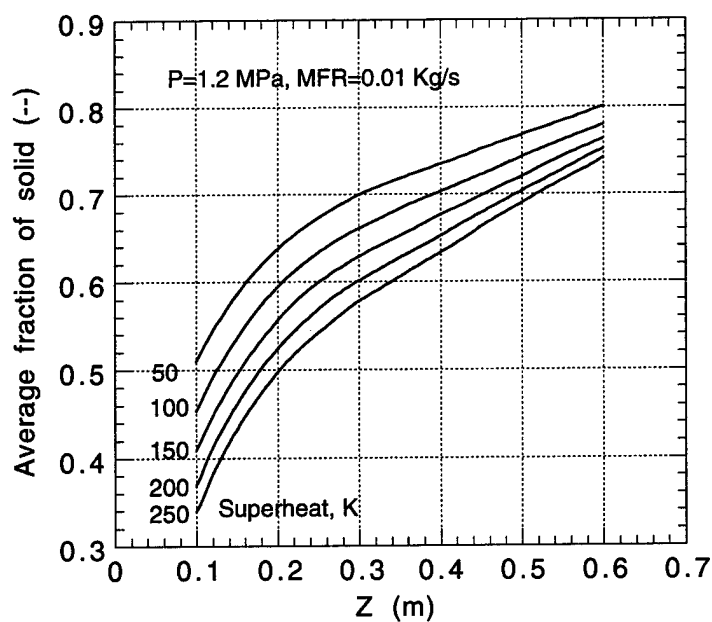
Figure 7.2. Calculated average fraction of solid as a function of deposition distance for an atomization pressure of 1.2 MPa and a melt flow rate of 0.02 kg/s.
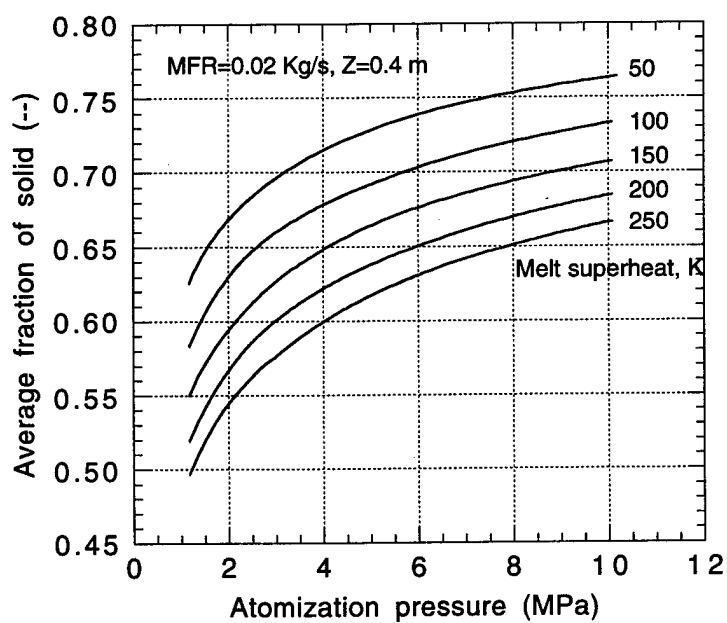
Figure 7.3. Calculated average fraction of solid as a function of atomization gas pressure for a deposition distance of 0.4 m and melt flow rate of 0.01 kg/s.

Figure 7.4. Average fraction of solid as a function of melt flow rate for an atomization pressure of 1.2 MPa and a deposition distance of 0.4 m.

Figure 7.5. A comparison of average fraction of solid as a function of melt flow rate between atomization gases of N_2 and Ar.
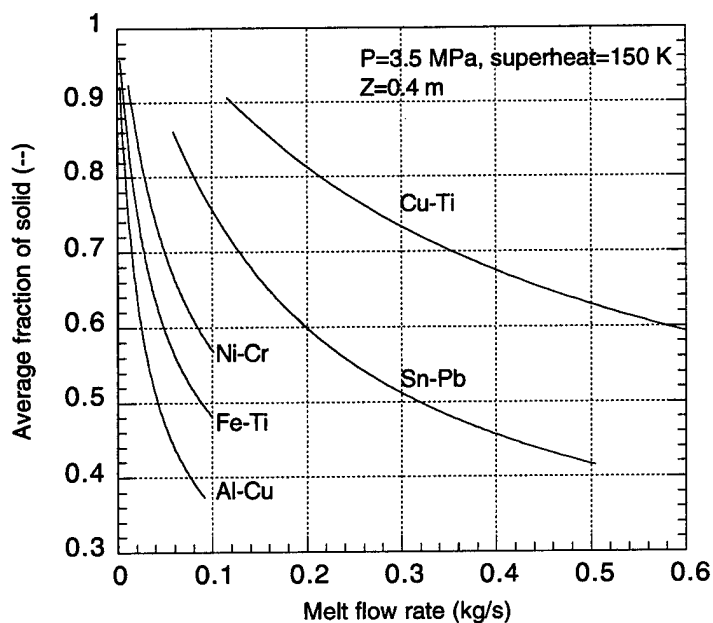
Figure 7.6.   Average fraction of solid as a function of melt flow rate for five alloy systems.
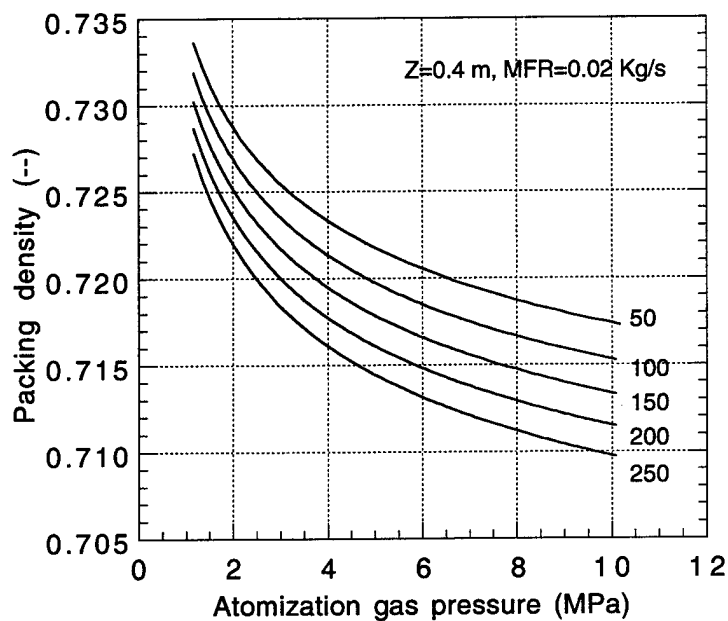
Figure 7.7. Particle packing density as a function of atomization gas pressure for a deposition
distance of 0.4 m and a melt flow rate of 0.02 kg/s.

Figure 7.8.   Packing density as a function of melt flow rate for an atomization pressure of 1.2 MPa and a deposition distance of 0.4 m.

The influence of atomization gas chemistry on packing density is shown in Figure 7.5. The packing density is significantly different for N_2 and Ar. For instance, at a flow rate of 0.01 kg/s, the packing density for Ar is about 0.717 and for N_2 is 0.700.

The variations of packing density for other alloy systems studied here are similar to that of the Al-Cu alloy. However, there are two significant differences. First, the influence of melt superheat on packing density for Cu-Ti alloy is less significant than that in the cases of Al-Cu, Fe-Ti and Ni-Cr. Furthermore, melt superheat appears to have no effect on packing density for the Sn-Pb alloy. These observations can be explained based on effects of melt superheat on melt viscosity. It has been indicated that melt viscosity has significant effects on geometric standard deviation (Lubanska's correlation). As a result, changes in melt viscosity with temperature will definitely affect geometric standard deviation. As shown in Figure 7.3, the viscosity of Cu-Ti is less sensitive to temperature than that of Al-Cu, Fe-Ti and Ni-Cr, whereas the viscosity data for Sn-Pb as a function of temperature is not available and hence was assumed to be constant. Accordingly, it can be concluded that the influence of viscosity on geometric standard deviation is more significant than that of surface tension. Second, it is noted that the melt flow rate for different alloy systems varies over a wide range, a trend that is similar to that observed for the average fraction of solid. One example is shown in Figure 7.9. It is observed that to achieve the same level of packing density, the magnitude of melt flow rate required depends strongly on alloy composition.

Figure 7.9. Comparison of packing density as a function of melt flow rate for five alloy systems at an atomization pressure of 3.5 MPa, a melt superheat of 150 K and a deposition distance of 0.4 m.

7.2.3. Porosity

Figures 7.10, 7.11 and 7.12 show the porosity as a function of deposition distance, atomization gas pressure and melt flow rate, respectively. The distinct "V" shaped variations are evidently demonstrated. As the values of these parameters increase, porosity decreases continuously until minimum values of porosity are achieved; beyond these points, porosity starts to increase sharply with increasing deposition distance and atomization pressure (Figures 7.10 and 7.11), whereas increase gradually with increasing melt flow rate (Figure 7.12). The significant influences of melt superheat on porosity are clearly shown in Figures 7.10 to 7.12. It is observed in Figure 7.10 and 7.11 that when deposition distance and atomization pressure are lower than certain values that correspond to a minimum value of porosity, porosity increases as melt superheat increases. Conversely, when deposition distance and atomization pressure are higher than certain values that correspond to a minimum value of porosity, porosity increases as melt superheat decreases. On the contrary, the variation of porosity with melt superheat with respect to melt flow rate is opposite to the cases with respect to deposition pressure and atomization pressure (Figure 7.12). In addition, it is observed that attaining a minimum value of porosity strongly depends on melt superheat (Figures 7.10 to 7.12). For example, in Figure 7.10, at a melt superheat of 50 K, a minimum amount of porosity is achieved at a deposition distance of 0.28 m, whereas at 150 K, it

occurs at 0.43 m. In Figure 7.11, it can be seen that for the given conditions, a minimum amount of porosity is achieved with atomization gas pressure of 2.8, 4.6, 6.7 and 9.2 MPa corresponding to melt superheat of 50, 100, 150 and 200 K, respectively. When the melt superheat is higher than 250 K, a minimum amount of porosity can not be achieved for the given conditions. In Figure 7.12, for the given condition, the minimum value of porosity is achieved at 0.0077, 0.0084, 0.0095, 0.0107 and 0.013 kg/s, corresponding to melt superheat values of 250, 200,150, 100 and 50 K, respectively. It is also noted that in Figure 7.12, when melt flow rate is very small (<0.003), the influence of melt superheat is significantly diminished.

The influence of atomization gas chemistry is shown in Figure 7.13. The variation of porosity with melt flow rate again follows the V-shaped behavior for both N_2 and Ar (Figure 7.13). However, it is observed that melt flow rate corresponding to a minimum amount of porosity for Ar is one order of magnitude lower than that for N_2. For example, it is 0.003 kg/s for Ar and 0.016 kg/s for N_2, approximately.

Variations of porosity with respect to processing parameters for other alloy systems are similar to those of Al-Cu. Once again similar to the behavior of average fraction of solid and packing density, the dependence of porosity on melt flow rate exhibits a wide range of values for the alloy compositions studied (Figure 7.14). Accordingly, the melt flow rate corresponding to a minimum amount of porosity is much different for different alloy systems. For instance, for an atomization pressure of 3.5 MPa, a deposition distance of 0.4 m and a melt superheat of 150 K, a minimum amount of porosity is attained at a melt flow rate of 0.016 kg/s for Al-Cu, 0.03 kg/s for Fe-Ti, 0.05 kg/s for Ni-Cr, 0.13 kg/s for Sn-Pb and 0.35 kg/s for Cu-Ti.

7.3. Discussion

In the present model, the porosity is solely determined by the average fraction of solid and the particle packing density (Eq.7.6). Accordingly, the effects of various factors on porosity can be attributed to their respective effects on the average fraction of solid and the packing density. Packing density depends only on the geometric standard deviation, and therefore only on the mass median diameter for a given particle sphericity (Eqs. 7.37 and 7.10). The average fraction of solid is determined by Eq. 7.7, indicating that it is controlled by the fraction of solid of single droplets and the respective droplet distribution probability function. The droplet distribution probability can be exclusively determined by the mass median diameter and geometric standard deviation (Eq. 7.8). Regarding Eq. 7.10, it is concluded that the governing factors for the average fraction of solid are mass median diameter, and fraction of solid for single droplets. Accordingly, the effects of various factors on average fraction and particle packing density can be attributed to their respective effects on the mass median diameter and fraction of solid for single droplets.
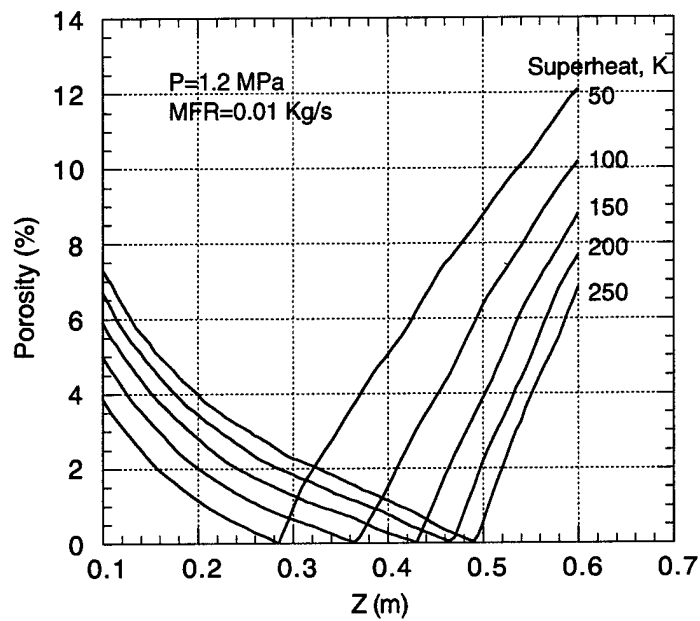
Figure 7.10.   Porosity as a function of deposition distance for an atomization gas pressure of 1.2 MPa and a melt flow rate of 0.01 kg/s.
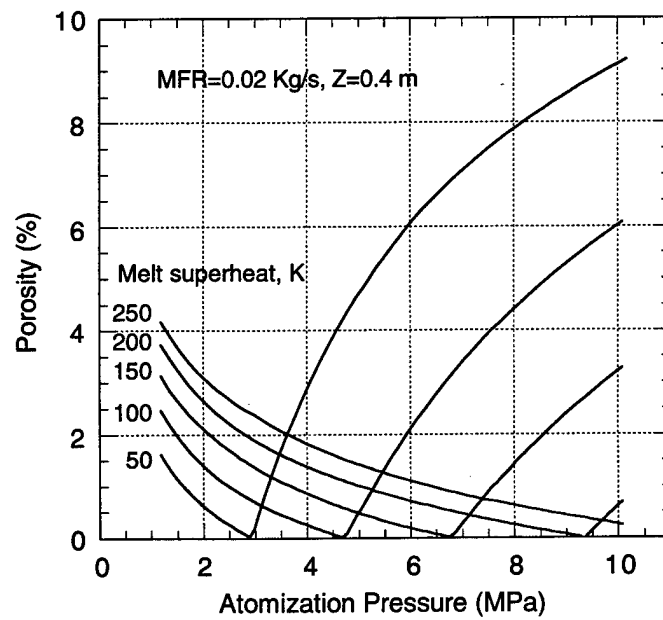
Figure 7.11.   Porosity as a function of atomization gas pressure for a melt flow rate of 0.02 kg/s and a deposition distance of 0.4 m.
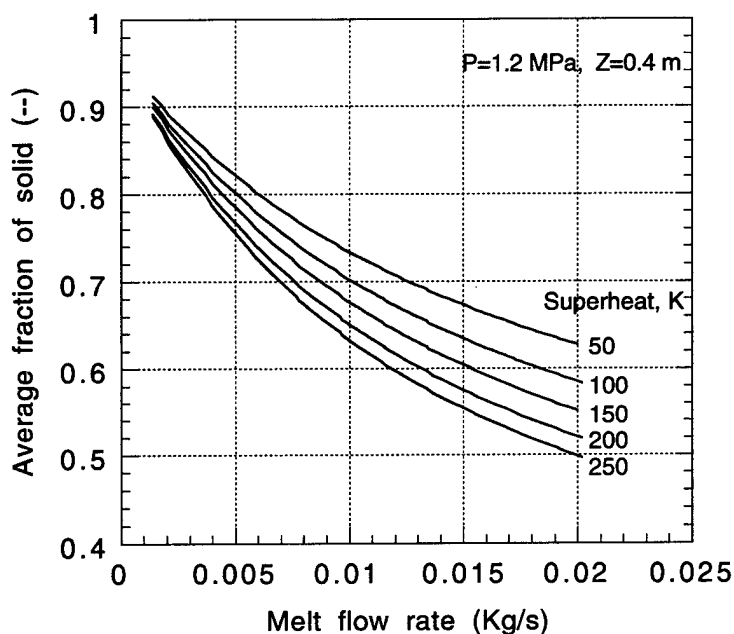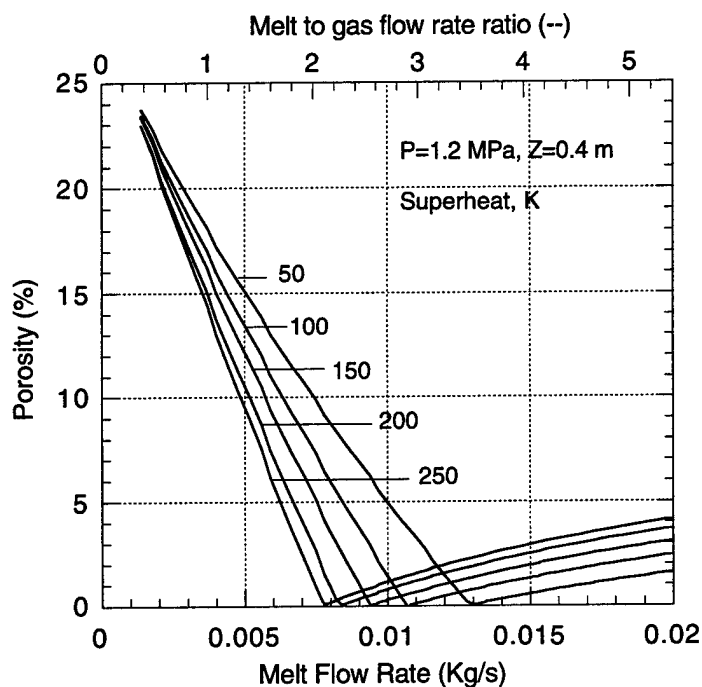
Figure 7.12.   Porosity as a function of melt flow rate for an atomization pressure of 1.2 MPa and a deposition distance of 0.4 m.
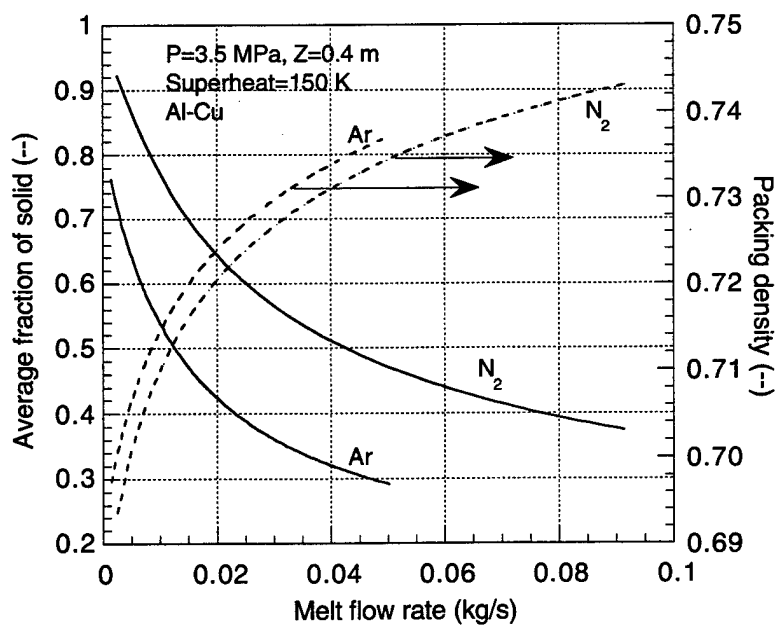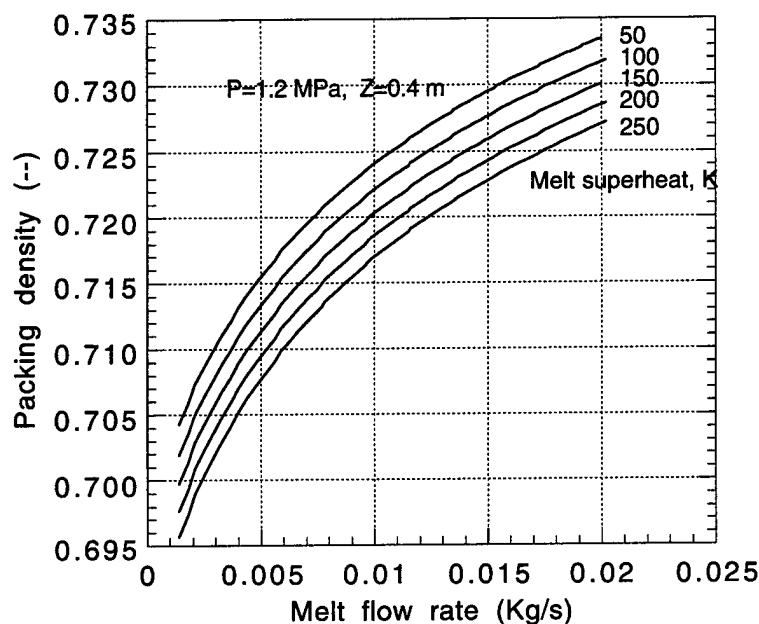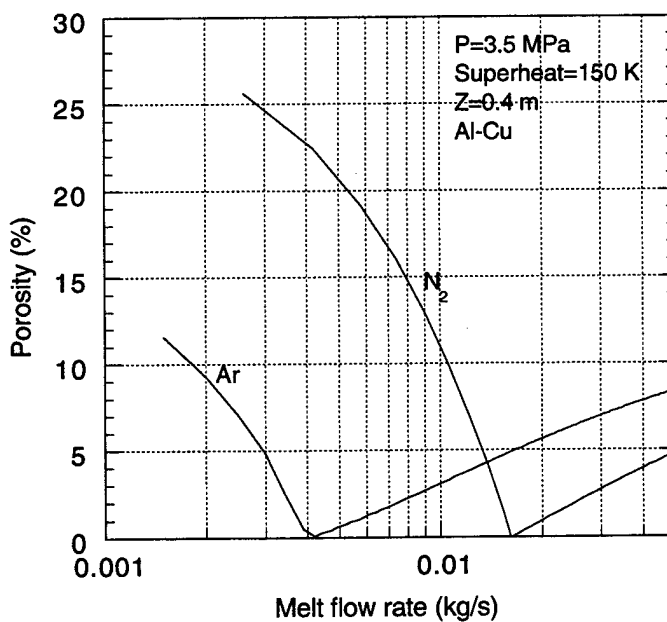

Figure 7.13.   The influence of atomization gas chemistry on porosity for the Al-Cu.

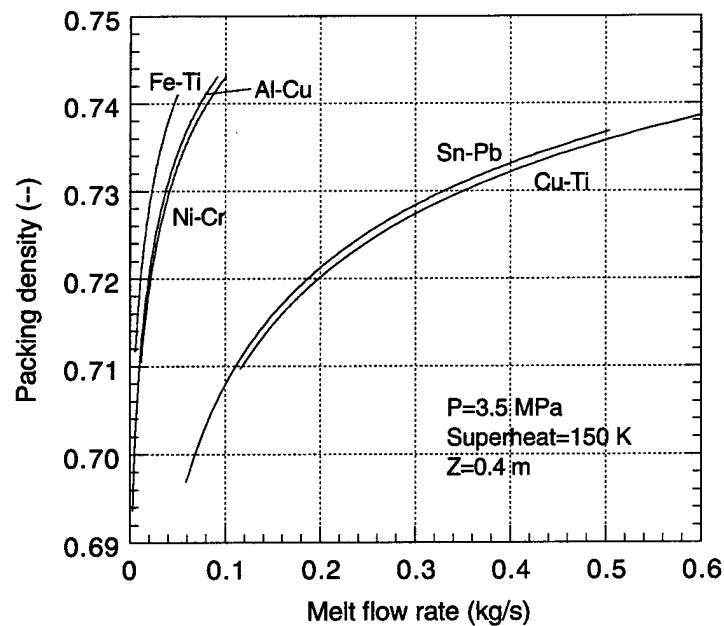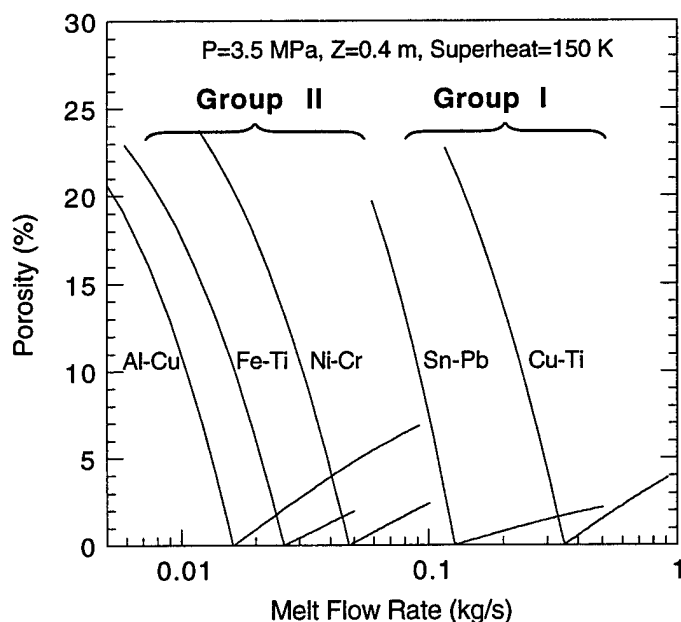Figure 7.14.   Calculated porosity as a function of melt flow rate for five alloy systems at an atomization pressure of 3.5 MPa, a melt superheat of 150 K and a deposition

7.3.1. Effects of Processing Parameters on Porosity

The processing parameters that influence the mass median diameter are: melt flow rate, gas flow rate and gas exit velocity (Eq. 7.9, both are determined by atomization gas pressure for a given nozzle design). Moreover, melt superheat also influences the mass median diameter, which occurs through temperature dependence of melt surface tension and melt viscosity. The fraction of solid of single droplets is determined by droplet size, droplet dynamics and droplet thermal history. Hence, the melt superheat, the gas exit velocity (or atomization pressure) and the deposition distance are the three most important governing parameters for the fraction of solid for single droplets.

The mass medium diameter increases with increasing melt flow rate, and decreases with increasing atomization pressure (Eq. 7.9). Accordingly, packing density increases with increasing melt flow rate (Figure 7.8), but decreases with increasing atomization pressure (Figure 7.7). The melt surface tension and viscosity generally decrease with increasing temperature. Therefore, increasing melt temperature leads to a decrease of mass median diameter, which certainly results in a decrease of packing density (Figures 7.7 and 7.8).

The large mass median diameters correspond to a low average fraction of solid at a given set of processing conditions. Accordingly, the average fraction of solid decreases with increasing melt flow rate (Figure 7.4). The effect of deposition distance on average fraction of solid is

straightforward. A longer deposition distance implies that more heat is extracted from droplets and therefore a higher average fraction of solid is attained, as shown in Figure 7.2. On the contrary, a higher melt superheat implies that more heat needs to be dissipated. Accordingly, average fraction of solid increases as melt superheat decreases (Figures 7.2 to 7.4). Even though a higher melt superheat results in a lower mass median diameter, this effect apparently can not compete with the associated increase of the thermal energy. The effects of atomization gas pressure on average fraction of solid are related to gas velocity and gas flow rate. The gas velocity increases with increasing atomization pressure (Eqs. 7.11 to 7.14) and the gas flow rate is proportional to the atomization gas pressure (Eq. 7.15). Accordingly, an increase of atomization gas pressure leads to a decrease in mass median diameter (Eq. 7.9), and consequently an increase in the average fraction of solid. It is worth noting that the increase of gas velocity due to the increase of atomization gas pressure also leads to an increase in droplet velocity, which produces two opposite effects on the average fraction of solid. First, an increase in droplet velocity results in an increase in the magnitude of the heat transfer coefficient and therefore an increase in the cooling rate (Eq. 7.25), which leads to an increase of the average fraction of solid. Second, an increase in the droplet velocity results in a short cooling time, and consequently a decrease in the average fraction of solid during impingement. However, this inverse effect of short cooling time is weaker than other effects [171]. Consequently, the average fraction of solid increases with increasing the atomization pressure, as shown in Figure 7.3.

7.3.2. Effects of Atomization Gas Chemistry

The results presented in Figures 7.5 and 7.13 reveal that variations in average fraction of solid, packing density and porosity with melt flow rate are notably influenced by the chemistry of atomization gas. For a given material and processing conditions, Lubanska's correlation (Eq. 7.9) can be rewritten as:

$$d_m = A \left[\frac{1}{\mu_g R} \left(\rho_g + \frac{C}{\sqrt{R}} \right) \right]^{\frac{1}{2}}$$

(7.39)

where A and C are parameters that are independent t of gas properties. Evidently, the mass median diameter is governed by gas properties such as density, viscosity and values of the gas constant. According to the data listed in Figure 7.1, μ_g and R are smaller, ρ_g is higher for Ar than that for N_2. Accordingly, for the same conditions, the mass median diameter is larger for Ar than that of N_2. It has been indicated that average fraction of solid decreases as mass median diameter increases. As a consequence, the average fraction of solid is higher for N_2 than that for Ar for the same processing conditions. Alternatively, for a given average fraction of solid, the corresponding

melt flow rate is higher for N_2 than that of Ar (Figure 7.5). According to Eqs. 7.9 and 7.10, the influence of gas properties on the geometric standard deviation is exactly the same as on the mass medium diameter. The larger the value of the geometric standard deviation the higher the particle packing density. Consequently, packing density in the case of Ar is higher than that in the case of N_2 (Figure 7.5). Note that the magnitude of variation in the particle packing density with melt flow rate is much less than that of the average fraction of solid. Apparently, the average fraction of solid will play a predominant role in determining the amount of porosity. Inspection of Eq. 7.3 reveals that the average fraction of solid that corresponds to $\Phi=0$ is a constant value if the variation in the magnitude of particle packing density is neglected. It has been shown that in Figure 7.5 that for a constant average fraction of solid, the melt flow rate for Ar is lower than that for N_2. Accordingly, the melt flow rate that corresponds to a minimum amount of porosity (or $\Phi=0$) for Ar is lower than that for N_2, as shown in Figure 7.13. In summary, the influence of atomization gas chemistry on porosity is associated with gas properties such as gas density, viscosity and gas constant.

7.3.3. Effects of Alloy Composition

A common phenomenon observed in Figure 7.6 and 7.9 is that the five alloy systems can be divided into two groups on the basis of the variations of average fraction of solid and particle packing density with melt flow rate. Group I includes Sn-Pb and Cu-Ti alloys, and Group II includes Fe-Ti, Al-Cu and Ni-Cr alloys. For a given average fraction of solid or packing density, the magnitude of melt flow rates for Group II is ten times (one order of magnitude) higher than that for Group I (Figure 7.6 and 7.9). This grouping phenomenon can be rationalized as follows. As discussed above, both of average fraction of solid and particle packing density are significantly influenced by the mass median diameter. Inspection of Lubanska's correlation (Eq. 7.9) reveals that melt viscosity, surface tension and density are the material related factors that influence mass median diameter and geometric standard deviation. Further, it is noted that the values of the material property factor, $\mu_m \gamma_m / \rho_m^2$ differentiate the two alloy system groups (Figure 7.4). For Group I this factor is on the order of 10^{-11}, whereas for Group II it is on the order of 10^{-10}. Accordingly, it can be concluded that such grouping of alloy systems is attributed to the different values of the material property factor, $\mu_m \gamma_m / \rho_m^2$. It is obvious that mass median diameter is proportional to $\mu_m \gamma_m / \rho_m^2$ (Eq. 7.9). Again from Eq. 7.9, it is seen that mass median diameter increases as melt flow rate increases. Hence, to achieve a given mass median diameter, the corresponding melt flow rate for Group I should be higher than that for Group II due to the value of $\mu_m \gamma_m / \rho_m^2$. Since particle packing density is solely determined by the mass medium diameter, particle packing density certainly follows the same pattern, i.e., for a given packing density, the

corresponding melt flow rate for Group I is higher than that for Group II. Similarly, since the mass median diameter has a significant influence on the average fraction of solid, the average fraction of solid should also follows the same pattern. For achieving a given average fraction of solid, the magnitude of melt flow rate for Group I will be higher than that for Group II. Finally, it should be noted that the constant K in Lubanska's correlation is assumed to be constant for all alloy systems in the present study. However, since K is generally reported to be in a small range of 40 to 50 [188, 189], the above grouping and the argument should be valid independent of the magnitude of K used.

Table 7.4.   The Material Factor of $\mu_m \gamma_m / \rho_m^2$ at the Melt Superheat of 150 K

	Alloy System	$\mu_m \gamma_m / \rho_m^2$
Group I	Sn-Pb	1.8522×10^{-11}
	Cu-Ti	1.7468×10^{-11}
Group II	Fe-Ti	2.2883×10^{-10}
	Al-Cu	1.4877×10^{-10}
	Ni-Cr	1.3590×10^{-10}

In Figure 7.9, it is observed that for a given melt flow rate, the sequential order of the magnitude for the particle packing density coincides with the sequential order of the magnitude of $\mu_m \gamma_m / \rho_m^2$ (Figure 7.9 and Figure 7.4). For example, in Group II, for a given melt flow rate, the particle packing density for Fe-Ti is the highest, followed by Al-Cu and then Ni-Cr. This phenomenon can be readily attributed to the fact that the particle packing density is solely determined by the geometric standard deviation for a given particle sphericity. Obviously, for a given melt flow rate, the particle packing density is actually solely determined by the values of $\mu_m \gamma_m / \rho_m^2$. Nevertheless, the sequential order of the magnitude for the average fraction of solid is different from that for particle packing density (Figure 7.6). For example, in Group II, for a given melt flow rate, the average fraction of solid in the spray for Ni-Cr is highest, followed by Fe-Ti and then Al-Cu. To understand this phenomenon, the influence of fraction of solid of single droplets needs to be taken into consideration. From Eq. 7.7, it is evident that the average fraction of solid is determined by the mass median diameter (associated with the distribution probability function, $g(d)$) as well as fraction of solid of single droplets. The fraction of solid for single droplets for different alloy systems is differentiated by the liquidus temperature, melting point of solvent and equilibrium partition coefficient (Figure 7.15 and Table 7.2). Coincidentally, the average fraction of solid for the alloy systems in each group is also differentiated by these factors. For example, in Group II, for a given melt flow rate, the average fraction of solid in the spray for

the Ni-Cr is highest, followed by Fe-Ti and then Al-Cu, with corresponding values of equilibrium partition coefficient of 0.666, 0.592 and 0.166, respectively (Figure 7.6 and Figure 7.2). In summary, regarding the variation of average fraction of solid with melt flow rate, the alloy systems studied can be divided into two groups on the basis of the values of the material property factor, $\mu_m \gamma_m / \rho_m^2$. In each group, the magnitude of the average fraction of solid for a given melt flow rate can be further differentiated by three materials parameters, i.e., liquidus temperature, melting point of solvent and equilibrium partition coefficient.
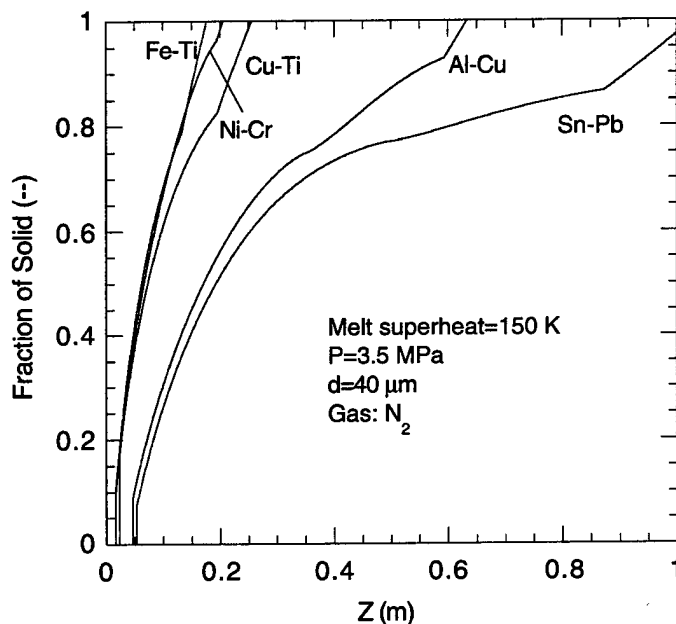
Figure 7.15.   Fraction of solid for single droplets as a function of deposition distance for five alloy systems.

From Figure 7.14, it is evident that the melt flow rate has a significant influence on the minimum amount of porosity that can be attained by each alloy. Obviously, this influence can be readily explained by considering the influence of melt flow rate on packing density and average fraction of solid. As indicated previously, the average fraction of solid plays a predominant role in determining the magnitude of porosity in the deposited materials. Accordingly, in regard to the variation of porosity with melt flow rate, alloy systems are divided into two groups by the material factor of $\mu_m \gamma_m / \rho_m^2$ just like for the variation of average fraction of solid with melt flow rate. Following the same argument used in the previous section regarding the influence of gas chemistry, if the variation of particle packing density with melt flow rate is neglected, the average fraction of solid that corresponds to $\Phi=0$ is a constant value (Eq. 7.3). From Figure 7.6, for a given average fraction of solid, the corresponding value of melt flow rate for Group I is higher than that for Group II. Following the same pattern, the values of melt flow rate corresponding to

$\Phi=0$ or a minimum porosity for Group I is higher than that for Group II. In each group, the values of melt flow rate corresponding to $\Phi=0$ or a minimum porosity is determined by liquidus temperature, melting point of the solvent and the values of equilibrium partition coefficient. The higher liquidus temperature, melting point of solvent and the values of equilibrium partition coefficient correspond to higher melt flow rate, leading to $\Phi=0$. Let us define an optimal melt flow rate to be that which corresponds to a minimum amount porosity (or $\Phi=0$) for given conditions, and then plot as a function of liquidus temperature, melting point of solvent and equilibrium partition coefficient. Then, the above argument becomes more evident. One example is shown in Figure 7.16 for the equilibrium partition coefficient of the alloy systems. It is evident that the optimal melt flow rate is in the range of 0.1 to 0.5 kg/s for the alloys in Group I, whereas it is in the range of 0.01 to 0.08 kg/s for the alloys in Group II. In each group, the optimal melt flow rate increases with increasing the values of equilibrium partition coefficient.
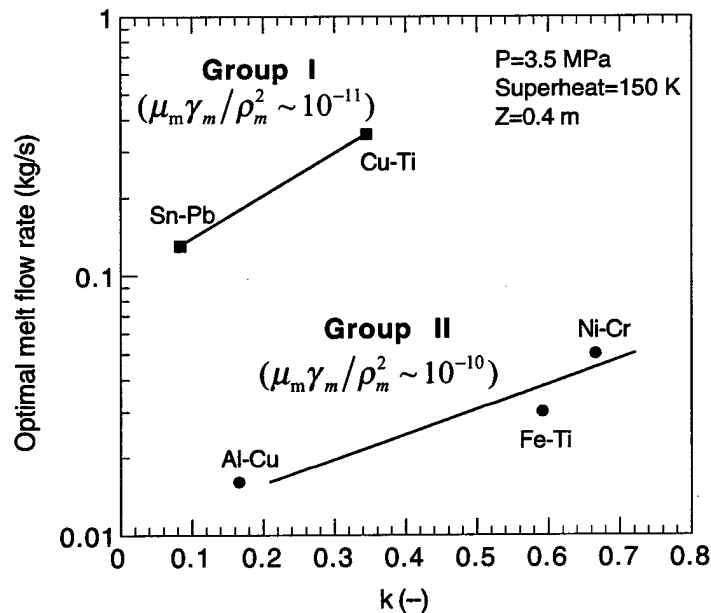
Figure 7.16.   Calculated melt flow rate that corresponds to a minimum amount of porosity (optimal melt flow rate) as a function of equilibrium partition coefficient at an atomization pressure of 3.5 MPa, a melt superheat of 150 K and a deposition distance of 0.4 m.

7.3.4. Optimal Processing Parameters

On the basis of the calculated results on the influences of various parameters on porosity described above, it is relatively straightforward to find optimal processing parameters for spray forming, by which low porosity in the deposited materials can be attained. However, it is worth

noting that the optimal parameters are calculated from a small proportion of the combination of the above described parameters. Accordingly, a large number of optimal parameter combinations can be obtained. However, it should be emphasized that the optimal parameters discussed herein are only associated with the minimum amount of porosity in the deposited materials. In practice, other issues have to be take into consideration, such as fine microstructures as well as economic issues. Consequently, in practice, there are additional factors that influence the selection of a particular set of parameters. Moreover, it should be pointed out that predicting the optimal parameters by using present model depends largely on the correlation for the mass median diameter. Even though the Lubanska's correlation is widely used, discrepancies with experimental results have been reported by some investigators, such as Cheng et al. [216] for Cu-6Ti alloy and Antipas et al. [196] for Al-Cr alloys. Therefore, it is imperative to develop more accurate particle size correlation.

VIII. INVESTIGATION OF CREEP BEHAVIOR IN AL ALLOYS AND SIC-AL COMPOSITE MATERIALS

8.1. Correlation Between Creep Behavior in Al-Based Solid Solution Alloys and Powder Metallurgy Al Alloys

The creep characteristics of Al-based solid solution alloys and powder metallurgy (PM) Al alloys are reviewed. Consideration of available information shows that the creep behavior of PM Al alloys is different from that of Al-based solid solution alloys with regard to the stress dependence of creep rate as inferred from the value of the stress exponent, n, and the temperature dependence of creep rate as measured by the value of the activation energy, Q. For example, according to well-documented experimental evidence, the activation energies for creep in Al based solid solution alloys, whether they behave as Class I (alloy Class, n = 3) or Class II (metal Class, n = 5), are close to that for self-diffusion in Al. By contrast, the apparent activation energies for creep in PM Al alloys are not only much higher than those reported for Al-based solid solution alloys but also variable. It is suggested that the aforementioned differences arise from the presence of a threshold stress for creep in PM Al alloys; that the origin of such a threshold stress is related to the interaction between moving dislocations and oxides particles which are present as a result of processing these alloys by powder metallurgy; and that by incorporating the threshold stress and its temperature dependence in the analysis, the true creep characteristics of PM Al alloys become similar to those of Al-based solid solution alloys. The consistency between this suggestion and experimental trends for two PM Al alloys, PM 6061 Al and PM 2124 Al, is examined.

8.2. On Creep Behavior in Powder Metallurgy 6061 Al

An analysis of recent creep data on PM 6061 Al in terms of creep rate against effective stress suggests that the creep behavior of the alloy exhibits a transition from viscous glide to a high-stress region whose advent is related to the breakaway of dislocations from their solute atom atmospheres. This suggestion is supported by the following: (a) the close correspondence between activation energies estimated from experimental data and those reported for Al-based solid-solution alloys, (b) the good agreement between theory and experiment in the viscous glide region, and (c) the consistency between experimental data and the glide/climb criterion. On the basis of the present analysis, it is predicted that a transition in the creep behavior of PM Al alloys and their discontinuous composites from that of Class I (alloy Class) to that of Class II (metal Class) may

occur when the effective stress is reduced below a critical value. This critical value for the effective stress is in part determined by the value of the threshold stress for creep which in turn is controlled by the volume fraction of oxide particles introduced in PM Al alloys and their discontinuous composites by powder metallurgy. In general, the above prediction should also be valid for solid-solution alloys that contain nanometer-scale stable particles.

8.3. On the Creep Strengthening of SiC Particulates in SiC-Al Composites

A comparison between the steady-state creep rates of 10 vol.% SiC-2124 Al composite and those of the unreinforced matrix alloy, 2124 Al, reveals that, for constant temperature, strengthening arising from SiC particulates is eliminated at high strain rates. An examination of the microstructure of deformed samples suggests that the loss of strengthening at high strain rates is due to the occurrence of debonding between SiC particulates and 2124 Al (interfacial debonding). This suggestion is supported by the observation that no significant interfacial debonding is detected in 30 vol.% SiC-6061 Al composite which exhibits better creep resistance than 6061 Al over the entire strain rate range measured (no loss of the creep strengthening at high strain rates).

8.4. An Investigation of Creep Behavior in an SiC-2124 Al Composite

The creep behavior of powder metallurgy (PM) 10 vol.% silicon carbide particulate reinforced 2124 aluminum (SiCp-2124 Al composite) was studied under experimental conditions identical with those used in an earlier investigation on the unreinforced matrix alloy, PM 2124 Al. The results show that the creep behavior of PM 10 vol.% SiCp-2124 Al composite is similar to that of PM 2124 Al with regard to: (a) the variation in both the apparent stress exponent and the apparent activation energy for creep with applied stress, (b) the value of the true stress exponent (n = 4.5), (c) the value of the true activation energy for creep ($Q_c \grave{o} Q_D$), (d) the interpretation of creep in terms of a threshold stress, (e) the temperature dependence of the threshold stress. These similarities indicate that deformation in the matrix alloy, 2124 Al, controls the creep of the composite, 10 vol.% SiCp-2124 Al composite; and that SiC particulates are not directly responsible for the threshold stress behavior in the composite. A comparison between the creep rates of the composite and those of the unreinforced matrix alloy reveals that, for constant temperature, strengthening arising from SiC particulates is eliminated at high strain rates and the creep strength of PM 10 vol.% SiCp-2124 Al composite becomes essentially equal to that of the unreinforced matrix alloy, PM 2124 Al.

8.5. Effect of Threshold Stress Processes on Creep Behavior

The operation of a threshold stress process signifies that the high temperature mechanical behavior of the material is not driven by the total applied stress but rather by an effective stress. By incorporating a threshold stress for creep, which depends strongly on temperature, in basic deformation processes proposed for metals and simple alloys, it is demonstrated that the creep behavior of powder metallurgy Al alloys and PM discontinuous SiC-Al composites can be predicted from information and analyses documented for solid- solution alloys.

IX. SUMMARY

On the basis of the experimental and theoretical results obtained in this research program, some concluding remarks may be summarized as following:

(1)   The macro-axial stress at the center of the deposited material is in a compressive state, and the magnitude decreases with increasing deposition thickness from the bottom. The magnitude of the residual stresses from X-ray diffraction is found to be greater than that from finite element analysis. The difference in magnitude could be attributable to the fact that the X-ray diffraction measurement yielded the total residual stresses and that the samples for the X-ray measurement were exposed to the HIP process whereas the finite element model did not take the HIP process into account. Nonetheless, the residual stress distribution from X-ray diffraction and finite element analysis are in a very good agreement. The macro-radial stress distribution is very distinct for the aluminum and the SiC rich layers. The macro-radial stress is found to be tensile in the aluminum layers and compressive in the SiC rich layers due to the tensile state in the aluminum layers and the compressive state in the SiC rich layers in order to maintain continuity between layers during cool down. At the upper center region of the deposited material, the aluminum layers have higher macro-von Mises' stress as compared with that of the SiC rich layers. The spray deposited material exhibits the highest macro-von Mises' stress at the outer edge of the deposited material due to the fastest cooling rate exerted on that region. The micro-radial stress is found to be compressive in the entire SiC particulate. The aluminum matrix in the vicinity of the SiC particulate exhibits compressive micro-radial stress and this compressive micro-radial stress becomes tensile for the aluminum matrix farther away from the SiC particulate. The SiC particulate exhibits compressive micro-hoop stress, whereas the aluminum matrix exhibits tensile micro-hoop stress. The stress state of the micro-radial and hoop stresses in the SiC particulate and the aluminum matrix can be explained by the fact that the aluminum matrix must stretch in order to maintain continuity with the SiC particulate after shrinkage caused by a temperature decrease. The micro-von Mises' stress has the highest value at the interface between the SiC particulate and the aluminum matrix and it decreases as the distance from the interface increases. It is also found that the micro-von Mises' stress decreases significantly in the regions where the thickness of aluminum matrix surrounding the SiC particulate is large.

(2)   An intermetallic matrix composite $TiAl/TiB_2$ was spray formed with co-injection using an induction skull melting/spray forming technique. The volume percentage of reinforcement in the bulk, spray formed materials is approximately 35%. The microstructure of the spray

formed composite is characterized by fine grained equiaxed fully lamellar structures, with average grain size of approximately 40 μm. The distribution of TiB_2 in the composite exhibits layered characteristic. On the basis of experimental observations of TiB_2 distribution in oversprayed powders and related numerical analysis, this phenomenon was attributed to the segregation of TiB_2 particles to the exterior region of the droplets and the subsequent deformation of the droplets along the direction normal to the substrate during impingement. Numerical analysis suggests that the most likely approach to improve the homogeneity of the distribution of TiB_2 in the deposit is to decrease the co-injector/atomizer distance.

(3) A tantalum alloy was successfully atomized and spray-deposited. Comparison of the microstructure in the upper section of the spray-formed Ta-Fe alloy deposit to that in the lower section indicates that rapid cooling occurs in the latter. The relative scarcity of secondary dendrite arms in the lower region was attributed to dendrite arm fragmentation. The phases present in the spray-formed Ta-Fe alloy were identified as Ta, μ phase (FeTa), and iron carbide. Numerical simulation of the impact and solidification of a Ta-Fe droplet corresponding to the measured mean size (90 μm) revealed a spreading behavior qualitatively simple. Liquid-jet overflow was shown to occur for droplet larger than the mean size. Comparisons of the measured and calculated final splat sizes showed that the numerical model gives a good estimate of the final droplet spreading.

(4) The newly developed LPSF technique significantly reduced the porosity in as-deposited 2024 Al alloy. As compared with CSF material, a significant reduction in porosity was achieved. SEM studies revealed that the pores whose sizes equivalent to grain sizes were much less frequently observed in the LPSF material than in the CSF material. The microstructural characterization showed that the grain morphology of LPSF material is the same as that of CSF material, with a slightly larger average grain size. The grain size in both upper (near free surface) and lower (near substrate) regions was smaller than that present in the central region where the magnitude of the size variation was small. It is argued that reduced pressure during spray forming minimize the flow recirculation in the atomization chamber, which leads to droplet trajectory and gas flow straightening. Consequently, an optimal fraction of solid condition is maintained in spray cone and porosity in the deposited materials is minimized. Gas entrapment during atomization stage may contribute to a proportion of the overall porosity in the deposited materials, which appears to be supported by two experimental results. First, gas filled pores were observed in oversprayed 2024 Al alloy powders. Second, an amount of atomization gas (N_2) was present in the deposited materials.

(5) On the basis of particle packing theory, flow mechanics and droplet thermal history, a porosity model for spray forming has been established. By using the model, the amount of porosity in as-deposited materials can be estimated on the basis of average fraction of solid and solidified particle packing density. The values of porosity vary with melt flow rate, atomization gas pressure and deposition distance by V-shaped behavior. The mass median diameter of particle size distribution plays an important role on the amount of porosity in as-deposited materials. The values of a material property factor, $\mu_m \gamma_m / \rho_m^2$ characteristically differentiate the behavior of the alloy systems studied. With a low value of $\mu_m \gamma_m / \rho_m^2$, the alloy system shows a high melt flow rate that corresponds to a minimum amount of porosity. Conversely, with a high value of $\mu_m \gamma_m / \rho_m^2$, the alloy system shows a low value of melt flow rate in order to achieve a minimum amount of porosity.

NOMENCLATURE

A.   Nomenclature for Section V

F	volume of fluid function
$\overline{F_g}$	body forces
$\overline{g}$	gravity acceleration
h_{sf}	latent heat of solidification
k	thermal conductivity
p	pressure
s	curvilinear coordinate
S	thickness of solidified layer
Ste	$= k\Delta T / \left(\alpha \rho h_{sf} \right)$ Stefan number
T	temperature
t	time
$\overline{V}$	velocity vector
x	radial coordinate
y	axial coordinate

Greek symbols

α	thermal diffusivity
θ	volume fraction open to flow
λ	solidification constant
ρ	density

Subscripts

i	initial
l	liquid
m	at the melting point
s	solid

Diacritics

$-$	vector

B.   Nomenclature for Section VII

A_t	total cross sectional area for gas flow at atomizer exit	m^2
C_{pl}, C_{ps}, C_{pg}	specific heat of liquid, solid and gas, respectively	$J/kg\ K$
H_{sm}	enthalpy at melting point	J/kg
k_e	equilibrium partition coefficient	-
K_g	thermal conductivity of gas	$W/m\ K$
Pr	Prandtl number, defined as $\mu_g C_{pg}/K_g$	-
Re	Reynold number, defined as $\rho_g \left| v_g - v_d \right| d / \mu_g$	-
R_i	liquid-solid interface mobility	$m/s\ K$
T_M	melting point of pure component (solvent)	K
T_g	gas temperature	K
T_l	metal melt temperature	K
T_N	nucleation temperature	K
T_r	droplet temperature at end of recalescence	K
T_E	eutectic temperature	K
$\dot{T}$	cooling rate	K/s
v_d	droplet velocity	m/s
v_g	gas velocity	m/s
v_{go}	initial gas velocity	m/s
V_d	volume of a single droplet	m^3
ε	surface emissivity	-
γ_m	surface tension of melt	N/m
η_m, η_g	kinematic viscosity of melt and gas, respectively	m^2/s
μ_g	dynamic viscosity of gas	$N\ s/m^2$
ρ_m, ρ_s	density of melt and solid	Kg/m^3
ρ_g	density of gas at 0.1 MPa	kg/m^3
ρ_{ge}	density of gas at a nozzle exit	kg/m^3
ρ_d	density of droplet	kg/m^3
σ	Stephen-Boltzmann constant (5.669×10^{-8})	$W/m^2\ K^4$

REFERENCES

1   P. K. Rohatgi, R. Asthana and S. Das, *Inter. Mater. Rev.* **31**, 115 (1986).

2   I. A. Ibrahim, F. A. Mohamed and E. J. Lavernia, *J. Mater. Sci.* **26**, 1137 (1991).

3   M. G. Mckimpson, E. L. Pohlenz and S. R. Thompson, *JOM* **45**, 26 (1993).

4   Y. Wu and E. J. Lavernia, *Metall. Trans.* **23A**, 2923 (1992).

5   P. Lengsfeld, J. A. Juarez-Islas, W. A. Cassada and E. J. Lavernia, *Int. J. Rapid Solidif.* **8**, 237 (1995).

6   P. Kumar, *J. Met.* **10**, 24 (1988).

7   R. W. Balliett, M. Coscia and F. J. Hunkler, *J. Met.* **9**, 25 (1986).

8   A. Bose and R. M. German, *Metall. Trans. A* **21**, 1325 (1990).

9   D. Han and J. J. Mecholsky, *J. Mater. Sci.* **25**, 4949 (1990).

10   R. M. German, L. L. Bourguignon and B. H. Rabin, *J. Met.* **37**, 36 (1985).

11   S. C. Yang and R. M. German, *Metall. Trans. A* **22**, 786 (1991).

12   L. M. Shepard, *Am. Ceram. Soc. Bull* **71**, 617 (1992).

13   R. G. Ford, *Mater. Processing Report* **7**, 1 (1992).

14   K. Atarashiya, K. Kurokawa and N. Tadao, *Ceram. Eng. Sci. Proc.* **13**, 400 (1992).

15   E. J. Lavernia, J. D. Ayers and T. S. Srivatsan, *Int. Mater. Rev.* **37**, 1 (1992).

16   M. Wu, T. S. Srivatsan, J. R. Picken and E. J. Lavernia, *Scr. Metall. Mater.* , 761 (1992).

17   M. Es-Souni, A. Bartels and R. Wagner, *Acta Metall. Mater.* **43**, 153 (1995).

18   S. L. Semiatin and P. A. Mcquay, *Metall. Trans.* **23A**, 149 (1992).

19   K. S. Chan and Y. M. Kim, *Acta Metall. Mater.* **43**, 439 (1995).

20   S. L. Kampe, P. Sadler, L. Christodoulou and D. E. Larson, *Metall.&Mater. Trans.* **25A**, 2181 (1994).

21   K. S. Kumar and M. S. DiPietro, *Scripta Metall. mater.* **32**, 793 (1995).

22   Q. Ma, L. C. Liang, D. R. Clarke and J. W. Hutchinson, *Acta Metall. Mater.* **42**, 3299 (1994).

23   S. M. Jeng and J.-M. Yang, *J. Mater. Res.* **8**, 905 (1993).

24   T. S. Srivatsan, T. S. Sudarshan and E. J. Lavernia, *Prog. Mater. Sci.* **39**, 317 (1995).

25   J. Zhang, R. J. Perez and E. J. Lavernia, *Acta Metall. Mater.* **42**, 395 (1994).

26   X. Liang and E. J. Lavernia, *Mater. Sci.&Eng.* **153A**, 646 (1992).

27   D. G. Morris, M. A. Morris, S. Gunter, M. Leboeuf and G. Hollrigl, *Scr. Metall. Mater.* **27**, 1645 (1992).

28   D. G. Morris, S. Gunter and M. Leboeuf, *Phil. Mag.* **69A**, 527 (1994).

29   T. P. Johnson, M. H. Jacobs, R. M. Ward and J. M. Young, in *2nd International Conference on Spray Forming* (*Proc. Conf.*), p. 183, Swansea (1993).

30   B. Li, W. Cai and E. J. Lavernia, *J. Mater. Synth. Process.* **4**, 35 (1996).

31   J. W. Sears, in *1992 Powder Metallurgy World Congress* (edited by J. M. Capus and R. M. German), , MPIF/APMI, Princeton, NJ. (1992).

32   A. Hirose, D. Ozamoto, R. Aoki and K. F. Kobayashi, *Zeitschrift Fur Metallkunde* **86**, 580 (1995).

33   J. A. Decock, Y. A. Chang, M.-X. Zhang and O. Y. Chen, *MRS Symp. Proc.* **170**, 173 (1990).

34   J. H. Norman, G. H. Reynolds and L. Brewer, *MRS Symp. Proc.* **194**, 369 (1990).

35   W. D. Cai, J. Smugeresky and E. J. Lavernia, *Mater. Sci. Eng. A* **241**, 60(1997).

36   M. G. Benz, T. F. Sawyer, W. T. Carter, R. J. Zabala and P. L. Dupree, *Powder Metall.* **37**, 213 (1994).

37   E. J. Lavernia and Y. Wu, *Spray Atomization and Deposition*, John Wiley & Sons, Inc., New York (1996).

38   J. Zhang, M. N. Gungor and E. J. Lavernia, *J. Mater. Sci.* **28**, 1515 (1993).

39   G. M. Janowski, F. S. Biancaniello, G. E. Hicho, R. J. Fields and S. D. Ridder, in *P/M in Aerospace, Defense and Demanding Applications* (edited by F. H. Froes), p. 363, MPIF, Princeton, NJ (1993).

40   P. Mathur, S. Annavarapu, D. Apelian and A. Lawley, *JOM* **41**, 23 (1989).

41   S. Hariprasad, S. M. L. Sastry, K. L. Jerina and R. J. Lederich, *Metall. Trans. A* **24**, 865 (1993).

42   H. Liu, E. J. Lavernia and R. H. Rangel, *Acta Metall. Mater.* **43**, 2053 (1995).

43   S. P. Andrew, R. D. Caligiuri and L. E. Eiselstein, in *Tungsten and Tungsten Alloys - Recent Advances* (edited by A. Crowson and E. S. Chen), p. 141, TMS, Warrendale, PA. (1991).

44   L. Ekbom, L. Holmberg and A. Persson, in *Tungsten & Tungsten Alloys - 1992* (edited by A. Bose and R. J. Dowding), p. 551, MPIF, Princeton, NJ. (1992).

45   L. S. Magness, in *Tungsten & Tungsten Alloys - 1992* (edited by A. Bose and R. J. Dowding), p. 15, MPIF, Princeton, NJ. (1992).

46   R. J. Dowding, in *P/M in Aerospace, Defense and Demanding Applications* (edited by F. H. Froes), p. 25, MPIF, Princeton, NJ (1993).

47   T. W. Penrice, in *Progress in Powder Metallurgy* (edited by M. S. Nayar, S. M. Kaufman and K. E. Meiners), p. 507, MPIF, Princeton, NJ. (1984).

48   T. W. Penrice, in *Proceedings of the Fourth International Tungsten Symposium* (*Proc. Conf.*), p. 140, Vancouver, Canada (1987).

49   C. J. Osborn and R. L. Woodward, in *Strength of Metals and Alloys* (edited by R. C. Gifkins), p. 467, Pergamon, NJ., Oxford, UK (1983).

50   G. Pageau, R. Vaziri and A. Poursartip, in *Proc. of the 23rd Inter. SAMPE Technical Conference* (*Proc. Conf.*), p. 639, (1991).

51   S. A. Mariano, D. Kokidko and S. J. Bless, in *Proc. of the 24th Inter. SAMPE Technical Conference* (*Proc. Conf.*), p. 500, (1992).

52   R. A. Muldoon, 1987, *MTL TR 87-34*, US Army Mater. Tech. Laboratory.

53   E. S. C. Chin, J. C. Beck, P. J. Huang and R. R. Biederman, in *Proc. of the 25th Inter. SAMPE Technical Conference* (*Proc. Conf.*), p. 197, (1993).

54   M. J. Forrestal, *J. Appl. Mech, Trans. ASME* **55**, 755 (1988).

55   J. G. Hetherington and B. P. Rajagopalan, *Inter. J. Impact Eng.* **11**, 33 (1991).

56   H. Matsumoto and T. Shiranita, *J. Mater. Sci. Lett.* **9**, 476 (1990).

57   A. Fujiwara and T. Kadono, *Japan J. Appl. Phy.* **29**, 1620 (1990).

58   J. B. Lambert, *Metals Handbook*, p. 557, ASM, Materials Park, Ohio (1990).

59   D. Raabe, G. Schlenkert, H. Weisshaupt and K. Lucke, *Mater. Sci. Technol.* **10**, 299 (1994).

60   J. B. Clark, R. K. Garrett, T. L. Jungling and R. I. Asfahani, *Metall. Trans. A* **23**, 2183 (1992).

61   S. I. Wright, G. T. Gray and A. D. Rollett, *Metall. Trans. A* **25**, 1025 (1994).

62   A. R. E. Singer and S. Ozbek, *Powder Metall.* **28**, 72 (1985).

63   X. Liang and E. J. Lavernia, *Metall. Trans.* **25A**, 2341 (1994).

64   E. J. Lavernia and X. Liang, *Reviews in Particulate Materials* **4**, (1994).

65   T. S. Srivatsan and E. J. Lavernia, *J. Mater. Sci.* **27**, 5965 (1992).

66   M. Gupta, F. A. Mohamed and E. J. Lavernia, *Metall. Trans. A* **23A**, 845 (1992).

67   Y. Wu and E. J. Lavernia, *Metall. Trans. A* **23**, 2923 (1992).

68   M. Wu, T. S. Srivatsan, J. R. Pickens and E. J. Lavernia, *Scr. Metall. Mater.* **27**, 761 (1992).

69   Y. Wu and E. J. Lavernia, *JOM* **43**, 16 (1991).

70   A. R. E. Singer, *Mater. Sci. Eng.* **135A**, 13 (1991).

71   Y. Wu and E. J. Lavernia, *Scr. Metall. Mater.* **27**, 173 (1992).

72   P. Mathur, D. Apelian and A. Lawley, *Powder Metall.* **34**, 109 (1991).

73   J. B. Holt, *Functionally Gradient Materials*, American Ceramic Society, Westerville, Ohio (1993).

74   N. Cherradi, A. Kawasaki and M. Gasik, *Compos. Eng.* **4**, 883 (1994).

75   C.-Y. Lin, H. B. McShane and R. D. Rawlings, *Mater. Sci. Technol.* **10**, 659 (1994).

76   J. H. Abboud, D. R. F. West and R. D. Rawlings, *J. Mater. Sci.* **29**, 3393 (1994).

77   A. Bishop, C.-Y. Lin, M. Navaratnam, R. D. Rawlings and H. B. McShane, *J. Mater. Sci. Lett* **12**, 1516 (1993).

78   M. M. Gasik and K. R. Lilius, *Computational Materials Science* **3**, 41 (1994).

79   M. Wu, J. J. Zhang, W. H. Hunt, J. J. Lewandowski and E. J. Lavernia, in *Processing and Fabrication of Advanced Materials IV. Proceedings of a Symposium held during Materials Week '95 Proceedings of Processing and Fabrication of Advanced Materials IV* (*Proc. Conf.*), p. 441, Cleveland, OH, USA (1995).

80   M. Manoharan, L. Ellis and J. J. Lewandowski, *Scr. Metall. Mater.* **24**, 1515 (1990).

81   C. K. Syn, D. R. Lesuer and O. D. Sherby, in *Advanced Synthesis of Engineering Materials* (edited by J. J. Moore, E. J. Lavernia and F. Froes), p. 149, ASM International, Materials Park, OH (1993).

82   T. M. Osman, P. M. Singh and J. J. Lewandowski, *Scr. Metall. Mater.* **31**, 607 (1994).

83   Y. Flom and R. J. Arsenault, *Mater. Sci. & Engin.* **77**, 191 (1986).

84   T. F. Klimowicz and X. S. Vecchino, in *Fundamental Relationships Between Microstructures and Mechanical* (edited by P. K. Liaw and M. N. Gungor), p. 255, TMS, Warrendale, PA (1990).

85   W. E. Frazier, E. W. Lee, M. E. Donnellan and J. J. Thompson, *JOM* **41**, 22 (1989).

86   M. E. Fine, in *Dispersion Strengthened Aluminum Alloys* (edited by Y. W. Kim and W. M. Griffith), p. 103, TMS/AIME, Warrendale, PA (1988).

87   M. Gupta, J. Juarez-Islas, W. E. Frazier, F. A. Mohamed and E. J. Lavernia, *Metall. Trans. B* **23**, 719 (1992).

88   X. Liang, H. K. Kim, J. C. Earthman and E. J. Lavernia, *Mater. Sci. Eng. A* **153**, 646 (1992).

89   P. Bewlay and B. Cantor, in *Rapidly Solidified Materials* (edited by P. Lee and R. Carbonara), p. 15, ASM, Materials Park, Ohio (1986).

90   S. Annavarapu, D. Apelian and A. Lawley, *Metall. Trans. A* **19A**, 3077 (1988).

91   B. P. Bewlay and B. Cantor, *J. Mater. Res.* **6**, 1433 (1991).

92   R. P. Underhill, P. S. Grant and B. Cantor, *Mater. Design* **14**, 45 (1993).

93   P. S. Grant, W. T. Kim and B. Cantor, *Mater. Sci. Eng. A* **134**, 1111 (1991).

94   S. Ebalard and M. Cohen, *Mater. Sci. Eng. A* **133**, 297 (1991).

95   E. J. Lavernia, T. Ando and N. J. Grant, in *Rapidly Solidified Materials* (edited by P. Lee and R. Carbonara), p. 29, ASM, Materials Park, Ohio (1986).

96   S. Annavarapu and R. Doherty, *Inter. J. Powder Metall.* **29**, 331 (1993).

97   M. Gupta, J. Marinkovich, F. A. Mohamed and E. J. Lavernia, in *Advances in Powder Metallurgy* (edited by T. G. Gasbarre and J. W. F. Jandeska), p. 99, MPIF, Princeton, NJ (1989).

98   J. M. Marinkovich, F. A. Mohamed, J. R. Pickens and E. J. Lavernia, *JOM* **41**, 36 (1989).

99   K. Ogata, E. J. Lavernia, G. Rai and N. J. Grant, *Int. J. Rapid Solidif.* **2**, 21 (1986).

100   X. Duan, A. Farah, I. Ucok and N. J. Grant, in *Science and Technology of Rapid Solidification and Processing* (edited by N. A. Otooni), p. 205, Klumer Academic Publishers, Dordrecht (1994).

101   J. Duszczyk, J. L. Estrada, T. L. J. d. Haan, A. G. Leatham and A. J. W. Ogilvy, in *PM Aerospace Materials 87: Proceedings of International Conference on PM Aerospace Materials* (*Proc. Conf.*), p. 1, Luzern, Switzerland (1987).

102   E. J. Lavernia, G. Rai and N. J. Grant, *Int. J. Powder Metall.* **22**, 9 (1986).

103   M. G. Chu, D. K. Denzer, A. K. Chakrabarti and F. R. Billman, *Mater. Sci. Eng.* **98**, 227 (1988).

104   X. Duan, Y. Hao, M. Yoshida, T. Ando and N. J. Grant, *Inter. J. Powder Metall.* **29**, 149 (1993).

105   J. B. Plies and N. J. Grant, *Inter. J. Powder Metall.* **30**, 335 (1994).

106   J. Zhou, J. Duszczyk and B. M. Korevaar, *J. Mater. Sci.* **26**, 5275 (1991).

107   J. Baram, *Metall. Trans. A* **22**, 2515 (1991).

108   E. J. Lavernia, *Int. J. Rapid Solidif.* **5**, 47 (1989).

109   P. Mathur, S. Annavarapu, D. Apelian and A. Lawley, *Mater. Sci. Eng. A* **142**, 261 (1991).

110   P. Mathur, D. Apelian and A. Lawley, *Acta Metall.* **37**, 429 (1989).

111   P. S. Grant, *Prog. Mater. Sci.* **39**, 497 (1995).

112   H. Liu, R. H. Rangel and E. J. Lavernia, *Mater. Sci. Eng. A* **191**, 171 (1995).

113   R. D. Payne, M. A. Matteson and A. L. Moran, *Inter. J. Powder Metall.* **29**, 345 (1993).

114   J. Lu, B. Miege, J. F. Flavenot and S. Thery, *J. Comp. Tech. Res.* **12**, 232 (1990).

115   S. D. Tsai, D. Mahulikar, H. L. Marcus, I. C. Noyan and J. B. Cohen, *Mater. Sci. Eng.* **47**, 145 (1981).

116   H. M. Ledbetter and M. W. Austin, *Mater. Sci. Eng* **89**, 53 (1987).

117   S. Ho and E. J. Lavernia, *Scr. Mater.* **34**, 1911 (1996).

118   W. F. Smith, *Principles of Materials Science and Engineering*, McGraw Hill, Inc., NY (1990).

119   K. G. Budinski, *Engineering Materials: Properties & Selection*, p. 85, Prentice Hall, NJ, NJ (1989).

120   H. E. Boyer and T. L. Gall (ed.), *Metals Handbooks*, p. 187, ASM, Metals Park, OH. (1985).

121   I. Tamura, Y. Tomota and H. Ozawa, in *Proc. 3rd Int. Conf. on Strength of Metals and*

Alloys,, p. 611, Institute of Metals and Iron and Steel Institute, London (1973).

122   H. Fishmeister and B. Karlsson, *Z. Metalkde.* **68**, 311 (1977).

123   R. L. Williamson, B. H. Rabin and J. T. Drake, *J. Appli. Phys.* **74**, 1310 (1993).

124   G. L. Povirk, M. G. Stout, M. Bourke, J. A. Goldstone, A. C. Lawson, M. Lovato, S. R. Macewen, S. R. Nutt and A. Needleman, *Acta Metall.* **40**, 2391 (1992).

125   J. R. Brockenbrough, S. Suresh and H. A. Wienecke, *Acta Metall.* **39**, 735 (1991).

126   X. Liang and E. J. Lavernia, *Mater. Sci. Eng. A* **161**, 221 (1993).

127   Y. A. Bahei-el-din, G. J. Dvorak and J. F. Wu, *J. Mater. Sci.* **30**, 1 (1995).

128   W. B. Li, K. E. Easterling and M. F. Ashby, *Metall. Trans. A* **22**, 1071 (1991).

129   J. D. Eshelby, *Proc. R. Soc.* **252A**, 561 (1959).

130   J. D. Eshelby, *Proc. R. Soc.* **241A**, 376 (1957).

131   T. Mura and M. Taya, *ASTM STP 864*, p. 209, (1985).

132   S. Ho, "*Ph.D. Dissertation,*" , Tufts University, 1994.

133   M. Suery, C. Teodosiu and L. F. Menezes, *Mater. Sci. Eng.A* **176**, 97 (1993).

134   L. F. Smith, A. D. Krawitz, P. Clarke, S. Saimoto, N. Shi and R. J. Arsenault, *Mater. Sci. Eng.A* **159**, L13 (1992).

135   H. Mabuchi, H. Tsuda and Y. Nakayama, *Scripta Metall. Mater.* **32**, 253 (1995).

136   E. M. Gutierrez, E. J. Lavernia, G. M. Trapaga, J. Szekely and N. J. Grant, *Metall. Trans.* **20A**, 71 (1989).

137   P. S. Grant, B. Cantor and L. Katgerman, *Acta Metall. Mater.* **41**, 3097 (1993).

138   B. Li, X. Liang, J. C. Earthman and E. J. Lavernia, *Acta Metall. Mater.* **44**, 2409 (1996).

139   H. Liu, R. H. Rangel and E. J. Lavernia, *Mater. Sci.&Eng.* **191A**, 171 (1995).

140   R. E. Bolz and G. L. Tuve (ed.), *Handbook of Tables for Applied Engineering Science*, p. 56, CRC Press, Cleveland, OH (1973).

141   P. Ramachandrarao, *Trans. JIM* **21**, 248 (1980).

142   H. S. Chen, *J. Non-Crystalline Solids* **27**, 257 (1978).

143   T. Z. Kattamis and T. J. Piccone, *Mater. Sci.&Eng.* **131A**, 265 (1991).

144   H. Liu, E. J. Lavernia and R. H. Rangel, *Atomiz.&Sprays* **4**, 369 (1994).

145   P. G. Breig and S. W. Scott, *Mater. Manuf. Process.* **4**, 73 (1989).

146   D. S. Reed, *Indus. Heat.* **57**, 20 (1990).

147   D. B. Kothe, R. C. Mjolsness and M. D. Torrey, "RIPPLE: A Computer Program for Incompressible Flows with Free Surfaces," 1991, *LA-12007-MS, UC-000* .

148   J.-P. Delplanque, S. Dai, R. H. Rangel and E. J. Lavernia, in *Spray Forming: Experiment, Analysis, and Applications. Part of the TMS Annual Meeting (Proc. Conf.)*, p. 87, Orlando, FL, USA (1997).

149   J.-P. Delplanque, E. J. Lavernia and R. H. Rangel, *Numer. Heat Transf. A, Appl.* **30**, 1

(1996).

150   J. U. Brackbill, D. B. Kothe and C. Zemach, *J. Comp. Phys.* **100**, 335 (1992).

151   H. Liu, E. J. Lavernia and R. H. Rangel, *Atomization and Sprays* **4**, 369 (1994).

152   H. Liu, E. J. Lavernia and R. H. Rangel, *J. Phys. D: Appl. Phys.* **26**, 1900 (1993).

153   H. Liu, R. H. Rangel and E. J. Lavernia, *Acta Metall. Mater.* **42**, 3277 (1994).

154   B. P. Bewlay and B. Cantor, *Metall. Trans. B* **21**, 899 (1990).

155   X. Liang, J. C. Earthman and E. J. Lavernia, *Acta Metall. Mater.* **40**, 3003 (1992).

156   E. J. Lavernia, E. M. Gutierrez, J. Szekely and N. J. Grant, *Int. J. Rapid Solidif.* **4**, 89 (1988).

157   E. Gutierrez-Miravete, E. J. Lavernia, G. M. Trapaga and J. Szekely, *Int. J. Rapid Solidif.* **4**, 125 (1988).

158   E. Gutierrez-Miravete, E. J. Lavernia, G. M. Trapaga, J. Szekely and N. J. Grant, *Metall. Trans. A* **20A**, 71 (1989).

159   P. S. Grant, W. T. Kim, B. P. Bewlay and B. Cantor, *Scr. Metall.* **23**, 1651 (1989).

160   P. S. Grant and B. Cantor, *Powder Metall.* **33**, 144 (1990).

161   J.-P. Delplanque, E. J. Lavernia and R. H. Rangel, *International Journal of Non-Equilibrium Processing* **10**, 185 (1997).

162   J.-P. Delplanque and R. H. Rangel, *J. Mater. Sci.* **32**, 1519 (1997).

163   *Aluminum Standards and Data*, p. 42, The Aluminum Association Inc., Washington DC, (1984).

164   C. A. Tsao and N. J. Grant, *Int. J. Powder Metall.* **30**, 323 (1994).

165   G.-X. Wang and E. F. Matthys, in *Heat Transfer 1994, Proceedings of the Tenth International Heat Transfer Conference* (*Proc. Conf.*), p. 169, Brighton, UK (1994).

166   S. N. Ojha, A. K. Tripathi and S. N. Singh, *Powder Metall. Int.* **25**, 65 (1993).

167   V. Uhlenwinkle and K. Bauckhage, in *Spray Forming 2- Proceedings of the Second International Conference on Spray Forming* (*Proc. Conf.*), p. 25, Swansea, UK (1993).

168   V. G. McDonnell, E. J. Lavernia and E. J. Samuelsen, in *Synthesis and Analysis in Materials Processing: Advances in Characterization and Diagnosis of Ceramic and Metal Particulate Processing* (edited by E. J. Lavernia, H. Henein and I. Anderson), p. 13, TMS, Warrendale, PA (1989).

169   J. L. Estrada and J. Duszczyk, *J. Mater. Sci.* **25**, 1381 (1990).

170   D. R. Lide, *The CRC Chemistry and Physics Handbook*, CRC Press, Ann Arbor, MI. (1995).

171   P. S. Grant, B. Cantor and L. Katgerman, *Acta Metall. Mater.* **41**, 3109 (1993).

172   L. L'Estrade, H. Hallen and R. Ljunggren, in *Modern Developments in Powder Metallurgy* (edited by P. U. Gummeson and D. A. Gustafson), p. 187, MPIF, Princeton,

NJ. (1988).

173 B. H. Rabin, G. R. Smolik and G. E. Korth, *Mater. Sci. Eng.* **A124**, 1 (1990).

174 S. D. Ridder, F. S. Biancaniello and P. I. Espina, in *Synthesis and Analysis in Materials Processing: Advances in Characterization and Diagnosis of Ceramic and Metal Particulate Processing* (edited by E. J. Lavernia, H. Henein and I. Anderson), p. 73, TMS, Warrendale, PA (1989).

175 N. A. Chigier, in *ICLASS-91. Proceedings of the Fifth International Conference on Liquid Atomization and Spray Systems (Proc. Conf.)*, p. 1, Gaithersburg, MD (1991).

176 A. J. Yule and J. J. Dunkley, *Atomization of Melts*, p. 44, Clarendon Press, Oxford (1994).

177 C. L. Smithells, *Gases and Metals*, p. 174, John Wiley & Sons, Inc., New York, NY. (1937).

178 L. F. Mondolfo, *Aluminum Alloys: Structure and Properties*, p. 331, Butter Worths, London (1976).

179 Q. Hou, R. Mutharasan and M. Koczak, *Mater. Sci. Eng. A* **195**, 121 (1994).

180 P. S. Grant and B. Cantor, *Acta Metall. Mater.* **43**, 913 (1995).

181 M. C. Flemings, *Solidification Processing*, p. 35, McGraw-Hill, New York, NY. (1974).

182 D. Emadi, J. E. Gruzleski and J. M. Toguri, *Metall. Trans. B* **24**, 1055 (1993).

183 K. Kubo and R. D. Pehlke, *Metall. Trans. B* **16**, 359 (1985).

184 G. K. Sigworth and C. Wang, *Metall. Trans. B* **24**, 349 (1993).

185 D. R. Poirier, K. Yeum and A. L. Maples, *Metall. Trans. A* **18**, 1979 (1987).

186 P. Rousset, M. Rappaz and B. Hannart, *Metall. Mater. Trans. A* **26**, 2349 (1995).

187 A. K. Gupta, B. K. Saxena, S. N. Tiwari and S. L. Malhotra, *J. Mater. Sci.* **27**, 853 (1992).

188 K. Lubanska, *J. Met.* **32**, 45 (1970).

189 E. J. Lavernia, T. S. Srivatsan and R. H. Rangel, *Atomization and Sprays* **2**, 253 (1992).

190 A. Lawley, *Atomization: the Production of Metal Powders*, p. 74, MPIF, Princeton, NJ. (1992).

191 A. Unal, *Metall. Trans. B* **20**, 61 (1989).

192 E. L. Crow and K. Shimizu, *Lognormal Distributions: Theory and Applications*, p. 2, Marcel Dekker, New York, NY. (1988).

193 J. E. Smith and M. L. Jordan, *J. Colloid. Sci.* **19**, 549 (1964).

194 A. H. Lefebvre, *Atomizations and Spray*, p. 85, Taylor & Francis, Bristol, PA (1989).

195 C. Tornberg, in *Advances in Powder Metallurgy & Particulate Materials-1992 (Proc. Conf.)*, p. 137, San Francisco, CA (1992).

196 G. Antipas, C. Lekakou and P. Tsakiropoulos, in *Spray Forming 2- Proceedings of the*

Second International Conference on Spray Forming (Proc. Conf.), p. 15, Swansea, UK (1993).

197   J. Szekely and N. J. Themelis, *Rate Phenomena in Process Metallurgy*, Wiley-Interscience, New York, NY. (1971).

198   D. R. Poirier and G. H. Geiger, *Transport Phenomena in Materials Processing*, TMS, Warrendale, PA (1994).

199   R. W. Fox and A. T. McDonald, *Introductiion to Fluid Mechanics*, p. 633, John Wiley & Sons, Inc., New York, NY. (1992).

200   X. Liang, E. J. Lavernia, J. Wolfenstine and A. Sickinger, *J. Therm. Spray Technol.* **4**, 252 (1995).

201   E.-S. Lee and S. Ahn, *Acta Metall. Mater.* **42**, 3231 (1994).

202   T. W. Clyne, R. A. Ricks and P. J. Goodhew, *Int. J. Rapid Solidif.* **1**, 85 (1985).

203   J. P. Hirth, *Metall. Trans. A* **9**, 401 (1978).

204   W. J. Boettinger and J. H. Perepezko, in *Rapidly Solidifed Alloys: Processes, Structures, Properties, Applications* (edited by H. H. Liebermann), p. 17, Marcel Dekker, Inc., New York (1993).

205   W. E. Ranz and W. R. Marshall, *Chem. Eng. Prog.* **48**, 141 (1952).

206   C. G. Levi and R. Mehrabian, *Metall. Trans. A* **13**, 221 (1982).

207   I. Minkoff, *Solidification and Cast Structure*, p. 100, John Wiley & Sons, New York, NY. (1986).

208   A. R. Dexter and D. W. Tanner, *Nature Phys. Sci.* **238**, 31 (1972).

209   R. J. Wakeman, *Powder Technol.* **11**, 297 (1975).

210   H. Y. Sohn and C. Moreland, *The Canadian J. of Chem. Engin.* **46**, 162 (1968).

211   R. M. German, *Particle Packing Characteristics*, p. 201, MPIF, Princeton, NJ. (1989).

212   U. Backmark, N. Backstrom and L. Arnberg, *Powder Metall. Int.* **18**, 338 (1986).

213   G. Rai, E. Lavernia and N. J. Grant, *J. Met.* **37**, 22 (1985).

214   S. D. Ridder and F. S. Biancaniello, *Mater. Sci. Eng.* **98**, 47 (1988).

215   N. Peronius and T. J. Sweeting, *Powder Technol.* **42**, 113 (1985).

216   C. Cheng, S. Annavarapu and R. Doherty, in *Spray Forming 2- Proceedings of the Second International Conference on Spray Forming (Proc. Conf.)*, p. 67, Swansea, UK (1993).

217   E. A. Brandes and G. B. Brook, *Smithells Metals Reference Book*, Butterworths-Heinemann, Oxford (1992).

218   D. Turnbull, *J. Appl. Phys.* **21**, 1022 (1950).

219   T. B. Massalski (ed.), *Binary Alloy Phase Diagram*, ASM, Materials Park, OH. (1982).

220   M. K. Veistinen, E. J. Lavernia, J. C. Baram and N. J. Grant, *Inter. J. Powder Metall.*

25, 89 (1989).

221   I. E. Anderson, R. S. Figliola and H. Morton, *Mater. Sci. Eng. A* **148**, 101 (1991).

LIST OF PUBLICATIONS

A.   Journal Papers

(1)   X. Liang, E.J. Lavernia, J. Wolfenstine and A. Sickinger "Microstructure Evolution during Reactive Plasma Spraying of MoSi$_2$ with Methane", *Journal of Thermal Spray Technology*, Vol. 4 (3), pp. 252-260, 1995.

(2)   Y. Wu, X. Zeng, E.J. Lavernia and J.M. Schoenung, "Reactive Atomization of Silicon to Form In-Situ Oxide Sintering Aids", *Metallurgical and Materials Transactions*, Vol. 27A, No. 8, pp. 2115-2121, 1996.

(3)   S. Ho and E.J. Lavernia, "Thermal Residual Stresses in Functionally Graded and Layered 6061 Al/SiC", *Metallurgical and Materials Transactions*, Vol. 27A, October, pp. 3241-3249, 1996.

(4)   J.-P. Delplanque, W.D. Cai, R.H. Rangel and E.J. Lavernia, "Spray Atomization and Deposition of Tantalum Alloys", *Acta Materialia*, Vol. 45, No. 12, pp 5233-5243, 1997.

(5).   S. Ho and E.J. Lavernia, "Investigation of Thermal Residual Stresses in Layered Composite Using Finite Element Method and X-ray Diffraction", *Metallurgical and Materials Transactions*, Vol. 28B, pp. 969-978, 1997.

(6).   X. Liang, J. Wolfenstine A. Sickinger and E.J. Lavernia, and "In-Situ Carburized Coating produced by Reactive Plasma Spraying Low Carbon Steel with Methane", *Materials Science and Engineering*, Vol. A212, pp. 51-61, 1996.

(7).   M. Wu, J. Zhang, J. Lewandowski, W. Hunt and E.J. Lavernia, "Enhanced Fracture Toughness of a Layered 6061/SiCp DRA Material Produced by Spray Deposition", *Journal of Materials Synthesis and Processing* Vol. 4, No. 2, pp. 127-134, 1996.

(8).   S. Ho and E.J. Lavernia, "The Effect of Heat Transfer Coefficient on Thermal Residual Stresses in Spray Deposited Materials", *Scripta Materialia*, Vol. 36, No. 3, pp. 283-290, 1997.

(9).   W.D. Cai and E.J. Lavernia, "Modeling of Porosity During Spray Forming", *Materials Science and Engineering A*, pp. 8-12, 1997.

(10).   S.C. Lim, M. Gupta, Y.F. Leng and E.J. Lavernia, "Wear of a Spray Deposited Hypereutectic Aluminum-Silicon Alloy", *Journal of Materials Processing Technology 63*, pp. 865-870, 1997.

(11).   B.Li, N. Nordstrom and E.J.Lavernia, "Spray Forming of Zircaloy-4", *Materials Science and Engineering A237*, pp. 207-215, 1997.

(12).   B. Li and E.J. Lavernia, "Spray Forming and Co-Injection of Particulate Reinforced TeAl/TiB$_2$ Composites", *Acta Materialia*, Vol. 49, No. 12, pp. 5015-5030, 1997.

(13).   J.A. Juarez-Islas, B. Campillo, R. Perez, S. Su and E.J. Lavernia, "Characterization of a Solid Solution of Cu in Al-Cu-SiC$_p$ Metal Matrix Composites Processed by Spray Atomization and Co-Deposition", *Journal of Materials Science*, Vol. 33, No. 1, pp.259-63, 1998.

(14). W.D. Cai, J. Smugeresky and E.J. Lavernia, "Low Pressure Spray Forming of 2024 Aluminum Alloy", *Materials Science and Engineering A241, pp.60-71, 1998.*

(15). H. Choe, T. Hsieh, Y. Wu, E.J. Lavernia and J. Wolfenstine, "The Effect of Powder Processing on the Mechanical Behavior of MoSi$_2$-10 Vol% Si$_3$N$_4$ Composites", *Journal of Materials Synthesis and Processing,* Vol. 4, No. 14, pp. 235-243, 1996.

(16). W.D. Cai and E.J. Lavernia, "Numerical Simulation of Porosity Evolution During Spray Forming of Ta-2.5 wt% Fe", *Journal of Materials Synthesis and Processing,* Vol. 5, No. 1, pp. 39-44, 1997.

(17). L. Martinez, O. Flores, M. Amaya, A. Duncan, S. Viswanathan, D. Lawrynowicz and E.J. Lavernia, "The Role of Alumina Particulate in Microstructural and Forging Properties of Spray-Atomized and -Deposited Fe-Al Ordered Intermetallic Compounds", *Journal of Materials Synthesis and Processing,* Vol. 5, No. 1, pp. 65-76, 1997.

(18). W. Cai and E.J. Lavernia, "Modeling of Porosity During Spray Forming I. Effects of Processing Parameters", *Metallurgical and Materials Transactions,* in press 1998.

(19). W. Cai and E.J. Lavernia, "Modeling of Porosity During Spray Forming II. Effects of Atomization Gas Chemistry and Alloy Compositions", *Metallurgical and Materials Transactions,* in press 1998.

(20). L. Martinez, M. Amaya, J. Porcayo-Calderon and E.J. Lavernia, "High Temperature Electrochemical Testing of Spray Atomized and Deposited Iron Aluminides Alloyed with Boron and Reinforced with Alumina Particulate", Materials Science and Engineering A, in press 1998.

(21). Yong Li; Mohamed, F.A., "An investigation of creep behavior in an SiC-2124 Al composite", *Acta Materialia,* Vol.45, No.11, pp.4775-85, 1997.

(22). Li, Y.; Nutt, S.R.; Mohamed, F.A., "An investigation of creep and substructure formation in 2124 Al", *Acta Materialia,* Vol.45, No.6, pp. 2607-20, 1997.

(23) Mohamed, F.A., "Correlation between creep behavior in Al-based solid solution alloys and powder metallurgy Al alloys", *Materials Science & Engineering A,* Vol.A245, No.2, pp.242-56, 1998.

(24) Mohamed, F.A., "On creep behavior in powder metallurgy 6061 Al", *Scripta Materialia,* Vol.38, No.3, pp.457-63, 1998.

(25) Mohamed, F.A., "On the creep strengthening of SiC particulates in SiC-Al composites", *Metallurgical and Materials Transactions A,* Vol.28A, No.12, pp. 2780-2, 1997.

B.   Papers in Conference Proceedings

(1). J.-P. Delplanque, W.D. Cai, R.H. Rangel and E.J. Lavernia, "Experimental and Numerical Investigation of Porosity Evolution during Low Pressure Plasma Spray Deposition of W", conference proceedings, *International Conference on W and Refractory Metals,* November 1995, Arlington, VA.

(2). J.-P. Delplanque, W.D. Cai, R.H. Rangel and E.J. Lavernia, "Spray Atomization and Deposition of Ta Alloys", *Proceedings of the 1996 TMS Meeting,* Anaheim, CA, Feb 5-8, 1996.

(3). S.C. Lim, M. Gupta, Y.F. Leng and E.J. Lavernia, "Wear of a Spray Deposited Hypereutectic Aluminum-Silicon Alloy", *Proceedings of the 3rd Asia Pacific Conference on Materials Processing,* Singapore, July 1996.

(4). Y. Li, E.J. Lavernia and F.A. Mohamed, "High Temperature Deformation in a Ta-W Alloy", *Proceedings of the 1996 TMS Meeting,* Anaheim, CA, Feb. 5-8, 1996.

(5). L. Martinez, M. Amaya, O. Flores, D. Lawrynowicz and E.J. Lavernia, "High Temperature Fracture During Forging of FeAl Intermetallic Alloys Fabricated Using Spray Atomization and Alumina Particulate", *Proceedings of the Seventh International Conference on Creep and Fracture of Engineering Materials and Structures,* J.C. Earthman and F.A. Mohamed, eds., pp. 395-404, University of California, Irvine, August 10-15, 1997.

(6). J.-P. Delplanque, W.D. Cai and E.J. Lavernia, "Evaluating Porosity in Spray Deposited Materials", *Proceedings of the 1998 TMS Annual Meeting: Solidification and Deposition of Molten Metal Droplets,* February 15-19, 1998, San Antonio,TX.

(7). L. Martinez, M. Amaya, J. Porcayo-Calderon and E.J. Lavernia, "High-Temperature Electrochemical Testing ofSpray-Atomized and Deposited Iron Aluminides Alloyed with Boron and Reinforced with Alumina Particulates", *Proceedings of the 1998 TMS Annual Meeting: International Symposium on Iron Aluminides: Alloy Design, Processing, Properties & Applications: Powder Processing, Corrosion and Wear ,* February 15-19, 1998, San Antonio,TX.

LIST OF PARTICIPATING SCIENTIFIC PERSONNEL

1.	Dr. E. J. Lavernia	Principal Investigator, UCI, Irvine, CA
2.	Dr. F. A. Mohamed	Co-Principal Investigator, UCI, Irvine, CA
3.	Mr. I. Sauer	Laboratory Technician, UCI, Irvine, CA
4.	Dr. J.-P. Delplanque	Research Associate, UCI, Irvine, CA
5.	Dr. W. D. Cai	Ph.D degree earned, 1996, UCI, Irvine, CA
6.	Dr. Y. Li	Ph.D degree earned, 1996, UCI, Irvine, CA
7.	Dr. B. Li	Ph.D degree earned, 1998, UCI, Irvine, CA
8.	Dr. Ho	Research Associate, UCI, Irvine, CA
9.	Mr. Q. Xu	Graduate Student, UCI, Irvine, CA

LIST OF AWARDS RECEIVED BY FACULTY

Professor Farghalli A. Mohamed

1997 Fellow, Board of Trustees of ASM International	1997

Professor Enrique J. Lavernia

Chemical and Biochemical Engineering and Materials Science Teacher of the Year	1998
1998 Fellow, Board of Trustees of ASM International	1998
Maxion Howe Medal for "Best Paper", *Metallurgical Materials Transactions B,* with D. Lawrynowicz and B. Li	1997
Best Paper Award, *Journal of Thermal Spray Technology*, with X. Liang and J. Wolfenstine,	1995
Silver Medal of the Materials Science Division of ASM International	1996
Alexander Von Humboldt Fellowship from Germany	1995

Awards Received by Supervised Students

Reyna Paniagua, undergraduate, UROP-PUF Fellow at UCI, for research project: "A Research into Novel Alloy Compositions for Aerospace Applications"	1998-1999
Maggy Lau, Ph.D. candidate, The Michael Kozcak Student Paper Award for Best Paper Presentation at the TMS Powder Materials Committee-sponsored Symposia	1997
Linda Del Castillo, Ph.D. candidate, NASA Fellowship, NASA Langley	1996-1999